

Functional analysis of FSP1 and its novel inhibitors

Toshitaka Nakamura

Complete reprint of the dissertation approved by the TUM School of Medicine and Health of the Technical University of Munich for the award of the Doktor der Naturwissenschaften (Dr. rer. nat.)

Chair: Prof. Dr. Dirk H. Busch

Examiners:

1. Prof. Dr. Percy A. Knolle
2. Prof. Dr. Franz Hagn
3. Prof. Dr. Thomas Brabletz

The dissertation was submitted to the Technical University of Munich on 03 August 2023 and accepted by the TUM School of Medicine and Health on 13 March 2024.

Table of Contents

1. Abstract/ Zusammenfassung
2. List of publications
3. Introduction
 - 3.1 Ferroptosis
 - 3.2 Chemical reaction behind ferroptosis
 - 3.3 Ferroptosis suppressor protein-1 (FSP1)
 - 3.4 Phase separation
4. Material and methods
 - 4.1 Material
 - 4.2 Methods
5. Discussion
 - 5.1 Ferroptosis and phase separation
 - 5.2 Mutagenesis and precision medicine
 - 5.3 FSP1 inhibitors and applications
 - 5.4 FSP1 inhibitors vs quinone reductase inhibitors
6. Publications and summary
 - 6.1 Phase separation of FSP1 promotes ferroptosis. *Nature* 2023
 - 6.2 Integrated chemical and genetic screens unveil FSP1 mechanisms of ferroptosis regulation. *Nat. Struct. Mol Biol.* 2023
 - 6.3 DHODH inhibitors sensitize to ferroptosis by FSP1 inhibition. *Nature* 2023.
7. References
8. Curriculum vitae
9. Acknowledgments
10. Affidavit
11. Publications

1. Abstract

Since the term “ferroptosis” has been defined as a new type of necrotic cell death associated with the deleterious destruction of cell membranes by iron-dependent lipid peroxidation, it has attracted overwhelming interest because of its relevance to many diseases, such as cancer, neurodegeneration, and tissue ischemia-reperfusion injury. Glutathione peroxidase 4 (GPX4) has long been considered as the only enzyme controlling (phospho)lipid peroxidation at the expense of electrons provided by glutathione. However, recently, ferroptosis suppressor protein-1 (FSP1), encoded by apoptosis-inducing factor mitochondria-associated 2 (AIFM2), along with quinones (i.e., ubiquinone/vitamin K) and NAD(P)H/H⁺ as an electron donor, has been discovered as the second ferroptosis surveillance system, which efficiently prevents lipid peroxidation independent of the glutathione/GPX4 axis.

First, to elucidate the molecular mechanisms of FSP1 function, numerous FSP1 mutations found in cancer or identified by untargeted random mutagenesis were studied. This mutagenesis approach combined with the recent machine learning-based structure prediction tool afforded elucidation of the FAD/NAD(P)H binding site and proton transfer function of FSP1, which emerges to be evolutionally conserved among many types of NADH quinone reductases.

Second, given that ferroptosis is considered a highly promising approach to combat difficult-to-treat tumors and the knockout of FSP1(Aifm2) has no overt phenotype in mice, the development of *in vivo* active and versatile FSP1 inhibitors is timely and highly warranted. The first reported FSP1 inhibitor, iFSP1, is human-specific and its mechanism of action (MoA) has remained unclear. Thus, for the elucidation of its MoA, all amino acid residues in human FSP1 different from the mouse orthologue were individually altered to their murine counterparts and functionally investigated. This approach identified F360 as a putative iFSP1 binding site. Moreover, an additional random mutagenesis screen was performed uncovering H48N and T327K to confer resistance to iFSP1, which suggests that iFSP1 presumably targets the quinone-binding site of FSP1.

Third, since iFSP1 is not suitable for *in vivo* studies and limited to the human system because of its poor *in vivo* stability, compound screens were performed or re-evaluated, then identifying two novel classes of FSP1 inhibitors as potential next-generation FSP1 inhibitors (i.e., viFSP1 and icFSP1). The first species-independent FSP1 inhibitor, called viFSP1, was found

to directly inhibit the FSP1 enzyme activity of several species including human and mouse FSP1. Furthermore, a subsequent mutagenesis screen unveiled that viFSP1 targets the putative NADH binding pocket. Although viFSP1 also shows poor microsomal stability and poor pharmacokinetic properties, the second class of FSP1 inhibitors, called icFSP1, was identified as the first *in vivo* active FSP1 inhibitor. Notably, while icFSP1 cannot inhibit FSP1 directly, it induces phase separation of FSP1 by forcing FSP1 to dissociate from the membrane. As a proof of concept, icFSP1 was applied in an *in vivo* subcutaneous tumor model, whereby icFSP1 impaired tumor growth as well as induced FSP1 condensates in the tumor, suggesting that icFSP1 can be a potential drug candidate for cancer therapy.

Last, while investigating FSP1 inhibitors, some other ubiquinone reductase inhibitors targeting mitochondrially localized dihydroorotate dehydrogenase (DHODH) were found to also inhibit FSP1 at high concentrations. This finding, therefore, reinforces the notion that FSP1 has a broad substrate specificity and should remind us of the importance of using appropriate concentrations of inhibitors before drawing strong conclusions that might be based on potential off-target activity.

In summary, the thesis presented here provides intriguing insights into FSP1 mechanisms as well as new tools for ferroptosis research and will serve as a good example for the development of novel pharmacotherapies for diseases including cancer, where ferroptosis has been implicated.

1. Zusammenfassung

Aufgrund ihrer herausragenden Bedeutung für viele Krankheiten, wie beispielsweise Tumorerkrankungen, Neurodegeneration und Ischämie-Reperfusionsschäden von Organen, hat die Ferroptose als eine neue Art des nekrotischen regulierten Zelltods, die durch eine eisenabhängige Lipidperoxidation von Zellmembranen gekennzeichnet ist, mittlerweile ein überwältigendes Interesse auf sich gezogen. Dabei galt die Glutathionperoxidase 4 (GPX4) lange Zeit als das einzige Enzym, das zusammen mit Glutathion als Kofaktor sehr effizient vor Lipidperoxidation und der damit einhergehenden Ferroptose schützt. Kürzlich gelang es jedoch das Ferroptose-Suppressorprotein-1 (FSP1), das vom *Apoptosis Inducing Factor Mitochondria-Associated 2* (AIFM2) Gen kodiert wird, zu identifizieren, das zusammen mit Chinonen (i.e. Ubichinon/Vitamin K) und NAD(P)H/H⁺ als Elektronendonator unabhängig vom Glutathion/GPX4-System effizient vor der Lipidperoxidation schützt.

Um die molekularen Mechanismen des FSP1 Enzyms aufzuklären, wurden zunächst zahlreiche FSP1-Mutationen untersucht, die entweder bei diversen Tumoren identifiziert, oder durch gezielte Mutagenese des FSP1 Enzyms generiert wurden. Die Kombination aus gezielten Mutagenese-Studien und künstlicher Intelligenz-basierter Strukturvorhersagen ermöglichte die Entschlüsselung der FAD/NAD(P)H-Bindungsstelle und der Protonentransferfunktion des FSP1-Enzyms, die sich als evolutionär konserviert unter vielen Arten von NADH-Chinon-Reduktasen herausstellte. Da die Ferroptose als vielversprechender Ansatz zur Bekämpfung schwer behandelbarer Tumorarten erachtet wird und der Knockout des *Aifm2* Gens bei Mäusen keinen offensichtlichen Phänotyp aufweist, ist die Entwicklung von *in vivo* wirksamen und Spezies-unabhängigen FSP1-Inhibitoren ausschlaggebend. Der erste publizierte FSP1-Inhibitor iFSP1 ist spezifisch für das humane Enzym, und sein Wirkmechanismus war bislang unklar. Zur Aufklärung des Wirkmechanismus wurden daher zunächst alle Aminosäuren im menschlichen FSP1-Protein, die sich vom Maus-Ortholog unterscheiden, einzeln in die entsprechenden murinen Sequenzen mutiert und funktionell analysiert. Dadurch gelang es, F360 als mutmaßliche iFSP1-Bindungsstelle zu identifizieren. Darüber hinaus wurde ein zusätzlicher Mutagenese-Screen des FSP1 Proteins durchgeführt, wobei die FSP1-Mutanten H48N und T327 eine starke Resistenz gegen iFSP1 vermittelten. Dies deutet somit darauf hin, dass iFSP1 mutmaßlich die Chinon-Bindungsstelle von FSP1 blockiert. Da sich iFSP1 aufgrund seiner geringen metabolischen Stabilität nicht für *In-vivo*-Studien und nicht für die weitere (prä)klinische Entwicklung eignet, wurden Hits aus einem früheren Wirkstoffscreening re-

evaluiert sowie ein neues Screening durchgeführt, bei dem zwei neue Substanzklassen von FSP1-Inhibitoren als potenzielle FSP1-Inhibitoren der nächsten Generation (d. h. viFSP1 und icFSP1) identifiziert wurden. Dabei stellte sich heraus, dass der erste speziesunabhängige FSP1-Inhibitor viFSP1 die FSP1-Enzymaktivität von verschiedenen Spezies hemmt, einschließlich in Mensch und Maus. Daran anschließende Mutagenese-Studien ergaben, dass viFSP1 an die vermeintliche NADH-Bindungstasche bindet. Obwohl viFSP1 sowie iFSP1 eine schlechte mikrosomale Stabilität und unzureichende pharmakokinetische Eigenschaften aufweisen, konnte mit icFSP1 der erste *in vivo* aktive FSP1-Inhibitor identifiziert werden. Interessanterweise hemmt icFSP1 das FSP1-Enzym nicht direkt, sondern induziert eine Phasentrennung von FSP1, indem es eine Dislokalisierung von FSP1 weg von der Zellmembran erzwingt. Zum Nachweis des Proof-of-Concepts als *in vivo* wirksamer FSP1 Inhibitor wurde icFSP1 in einem subkutanen In-vivo-Tumormodell appliziert. Dabei konnte icFSP1 das Tumorwachstum abschwächen, indem es wie in Zellkultur auch FSP1-Kondensate im Tumor induzierte, was impliziert, dass icFSP1 ein potenzielles Medikament für die Krebstherapie darstellen könnte.

Schließlich konnte bei Untersuchungen anderer Ubichinon-Reduktase-Inhibitoren (z.B. Brequinar), insbesondere der mitochondrial lokalisierten Dihydroorotat-Dehydrogenase (DHODH), festgestellt werden, dass einige davon ebenfalls das FSP1 in hohen Konzentrationen effizient hemmen können. Dieser Befund untermauert somit, dass FSP1 eine breite Substratspezifität aufweist, weshalb angemessene Inhibitor-Konzentrationen in entsprechenden Studien verwendet werden müssen, bevor eindeutige Schlussfolgerungen gezogen werden, die möglicherweise auf einer potenziellen Off-Target-Aktivität beruhen könnten. Zusammenfassend lässt sich sagen, dass die hier vorgestellte Arbeit neue Einblicke in die Mechanismen des FSP1 Enzyms, sowie neue experimentelle Ansätze für die Ferroptose-Forschung liefert. Diese Studien könnten somit als Vorreiter für die Entwicklung neuer Pharmakotherapien für Krankheiten wie Krebs dienen, bei denen Ferroptose eine wesentliche Rolle spielt.

2. List of publications

1. **Nakamura T.**, Hipp C., Mourão A. S. D., Borggräfe J., Aldrovandi M., Henkelmann B., Wanninger J., Mishima E., Lytton E., Emler D., Proneth B., Sattler M. & Conrad M. Phase separation of FSP1 promotes ferroptosis. *Nature*, 2023.
2. **Nakamura T.**, Mishima E., Yamada N., Mourão A. S. D., Trümbach D., Doll S., Wanninger J., Lytton E., Sennhenn P., Silva T. N. X., Angeli J. P. F., Sattler M., Proneth B. & Conrad M. Integrated chemical and genetic screens unveil FSP1 mechanisms of ferroptosis regulation *Nat. Struct. Mol. Biol.*, 2023.
3. Mishima E.*, **Nakamura T.***, Zheng J.*, Zhang W., Mourão A. S. D., Sennhenn P. & Conrad M. DHODH inhibitors sensitize to ferroptosis by FSP1 inhibition. *Nature*, 2023
* equal contribution
4. Mishima E., Ito J., Wu Z., **Nakamura T.**, Wahida A., Doll S., Tonnus W., Nepachalovich P., Eggenhofer E., Aldrovandi M., Henkelmann B., Yamada K., Wanninger J., Zilka O., Sato E., Feederle R., Hass D., Maida A., Mourão A. S. D., Linkermann A., Geissler E., Nakagawa K., Abe T., Fedorova M., Proneth B., Pratt D. & Conrad M. A non-canonical vitamin K cycle is a potent ferroptosis suppressor. *Nature*, 2022.

3. Introduction

3. 1. Cellular stress and ferroptosis

Cells are constantly exposed to diverse stress conditions, including varying temperatures and an altered redox and metabolic status, requiring adequate responses to such extrinsic and intrinsic stresses. When cellular stress reaches a certain level, which cannot be compensated by endogenous cellular systems, cells inevitably succumb to cell death. For instance, thermal stress (heat and cold stress) can affect redox status and induce lipid reactive oxygen species (ROS)-dependent necrosis¹⁻³. Historically, cell death was first classified as either apoptosis (i.e., programmed cell death) or “unregulated” or “accidental” necrosis. However, in recent years, many types of “regulated forms” of necrosis have been identified and characterized by a caspase 3-independent and membrane-permeable form of non-apoptotic cell death⁴. Understanding their precise underlying molecular mechanisms is therefore of utmost importance for identifying therapeutic targets and developing novel pharmacotherapies for the treatment of many diseases including inflammatory diseases and cancer^{4,5}. Among these regulated cell death modalities, ferroptosis, a metabolic form of cell death characterized by iron-dependent lipid peroxidation, has been defined only quite recently⁶. Ferroptosis has attracted tremendous interest because of its high relevance to human diseases, such as cancer, neurodegenerative disorders, and tissue ischemia-reperfusion injuries⁷⁻¹⁰.

Ferroptosis can be efficiently triggered through the inhibition of the cystine-glutamate antiporter, designated system Xc⁻, a heterodimer consisting of SLC7A11 (xCT) light chain and SLC3A2 (4F2) heavy chain¹¹ (**Figure 1**). Inhibition of system Xc⁻ for instance by the small molecule compound erastin^{6,12} leads to cellular cysteine starvation, followed by exhaustion of the main intracellular antioxidant, glutathione (GSH). Cellular GSH depletion can also be achieved by direct inhibition of γ -GCL (γ -glutamylcysteine-ligase), the enzyme catalyzing the first and rate-limiting step in GSH biosynthesis using L-buthionine sulfoximine (BSO). Therefore, both mechanisms ultimately converge on the level of GSH to trigger cell death. Importantly, ferroptosis can be triggered independently of GSH depletion either through genetic deletion or pharmacological inhibition of glutathione peroxidase 4 (GPX4) using (1*S*,3*R*)-RSL3 (RSL3), ML210, and JKE-1674¹³⁻¹⁶. These studies highlighted the pivotal function of GPX4 as the rate-limiting enzyme conferring the pro-survival role of GSH.

Besides the xCT-GSH-GPX4 axis, a metabolomics approach identified another defense system consisting of mitochondrial ubiquinone that is regenerated by dihydroorotate dehydrogenase (DHODH)¹⁷. Moreover, its cognate inhibitor, brequinar (BQR), was shown to promote ferroptosis and the combination therapy of BQR and xCT inhibitor (sulfasalazine: SAS) was reported to block

tumor growth efficiently. In addition, a CRISPR activation screen previously identified GTP cyclohydrolase 1 (GCH1) as another ferroptosis suppressive system¹⁸. Mechanistically, GCH1 protects against ferroptosis via its metabolic product tetrahydrobiopterin (BH4), which can act as a radical trapping antioxidant (RTAs) and which is reduced by dihydrofolate reductase (DHFR)¹⁹.

Last, ferroptosis sensitivity highly relies on the abundance of polyunsaturated fatty acids (PUFAs) esterified in lipid membranes. PUFA-CoAs are the product of acyl-CoA synthetase long-chain family members 1/4 (ACSL1/4) with coenzyme A, which are then incorporated into the lipid membrane via lysophosphatidylcholine acyltransferase 3 (LPCAT3) and related enzymes. While membranes with a high PUFAs content are prone to undergo lipid peroxidation and are thus considered “pro-ferroptotic”, saturated or monosaturated fatty acids (SFAs and MUFAs) are “anti-ferroptotic” due to the lack of a labile H atom in conjugated dienes²⁰⁻²². Thus, lipid composition is another important factor dictating ferroptosis vulnerability.

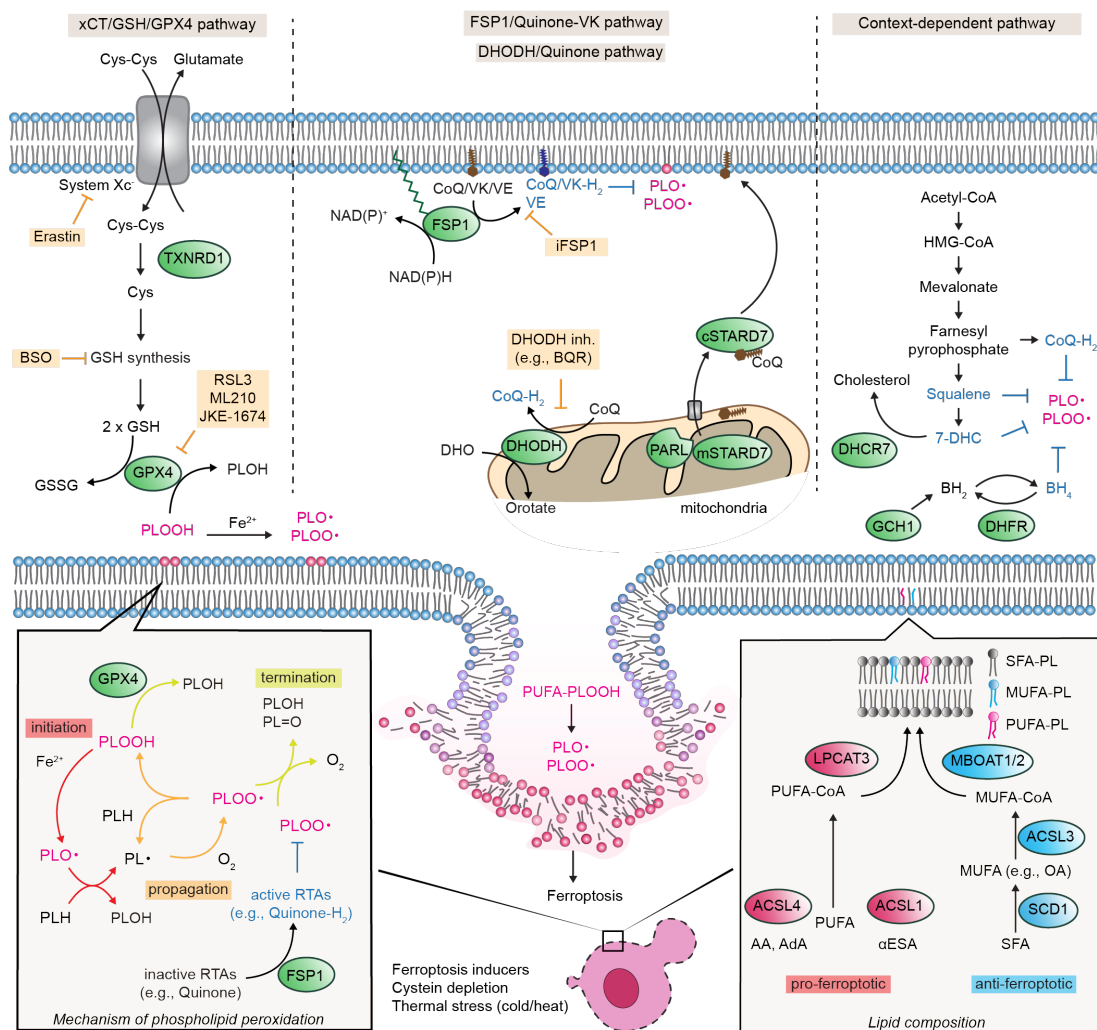


Figure 1. Overview of ferroptosis. (Left) The canonical ferroptosis regulating pathway: uptake of cystine (Cys-Cys) via the cystine-glutamate antiporter (xCT), designated system x_c^- , glutathione (GSH)- and/or thioredoxin reductase 1 (TXNRD1) mediated reduction of cystine to cysteine, GSH biosynthesis, and glutathione peroxidase 4 (GPX4)-dependent reduction of phospholipid hydroperoxides (PL-OOH) yielding the corresponding alcohols (PL-OH). Erastin inhibits system x_c^- and BSO inhibits GSH biosynthesis, whereas RSL3, ML210 and JKE-1674 inhibit GPX4. (Middle) The FSP1/ubiquinone (CoQ₁₀)-vitamin K system has been recently identified that completely protects against ferroptosis induced by pharmacological inhibition or genetic deletion of GPX4. FSP1 prevents lipid peroxidation and associated ferroptosis via the reduction of ubiquinone, vitamin E, and vitamin K, which all act as radical-trapping antioxidants (RTAs). Mitochondrially synthesized ubiquinone is shuttled from mitochondria to the cytosol by StAR-related lipid transfer domain protein (cSTARD7) after mitochondrial STARD7 (mSTARD7) is cleaved by presenilins-associated rhomboid-like protein (PARL) in mitochondria. Another defense system using mitochondrial ubiquinone reduced by dihydroorotate dehydrogenase (DHODH) was recently reported and its cognate inhibitor, brequinar (BQR), promotes ferroptosis. (Right) Alternative cell/context-dependent ferroptosis-suppressive mechanisms include squalene, 7-dehydrocholesterol (7-DHC), and tetrahydrobiopterin (BH₄)-mediated inhibition of lipid peroxidation. RTAs are shown in blue. (Lower left) Mechanisms of phospholipid peroxidation. Lipid peroxidation, the hallmark of ferroptosis, can be divided into three phases: initiation (Fenton reaction, red), propagation (The reaction between lipids and lipid peroxyl radicals, orange) and termination (the reaction by GPX4 or RTAs such as ubiquinol reduced by FSP1, light green). (Lower right) The phospholipid composition dictates ferroptosis sensitivity. Esterification of phospholipids with saturated fatty acids (SFAs) and monounsaturated fatty acids (MUFAs: oleic acid (OA)) produced by stearoyl-Coenzyme A desaturase (SCD1) has anti-ferroptotic effects, while an enrichment of phospholipids with polyunsaturated fatty acids (PUFAs, such as arachidonic acids (AA), α -eleostearic acid (α -ESA), and adrenic acid (AdA)) renders cells susceptible to ferroptosis (Abbreviations: ACSL1/3/4, acyl-CoA synthetase long chain family member 1/3/4; GCH1, GTP cyclohydrolase 1; LPCAT3 lysophosphatidylcholine acyltransferase 3; MBOAT1/2, membrane bound O-acyltransferase domain containing 1/2; DHCR7, 7-dehydrocholesterol reductase; VK, vitamin K; VE, vitamin E; DHO, dihydroorotic acid; DHFR, Dihydrofolate reductase; PLO(O)•, lipid peroxyl radicals; CoQ-H₂, ubiquinol)

3. 2. Chemical basis of ferroptosis

A small fraction of cellular iron (less than 5% of the total iron in cells, approx. 50 μM)²³ in its redox-active state might be contained in the so-called labile iron pool (LIP). LIP is still a poorly understood entity in cells, which is present mainly in mitochondria and lysosomes²⁴. Unchaperoned, redox-active free iron can produce highly reactive oxygen radicals, such as hydroxyl radical ($\cdot\text{OH}$) and peroxy lipid radical ($\text{PLOO}\cdot$), via Fenton-type of chemistry²⁵. Thereby, ferrous iron (Fe^{2+}) reacts with hydrogen peroxide (H_2O_2) or phospholipid peroxides (PLOOH), which are mainly produced by superoxide dismutases (SODs) or lipoxygenases (LOXs) and cytochrome P450 oxidoreductases (PORs), respectively, thereby generating the highly reactive hydroxyl radical or phospholipid peroxy radicals ($\text{PLOO}\cdot$).

Hydroxyl radicals and/or lipid peroxy can react with polyunsaturated fatty acid (PUFA) residues esterified in phospholipids to generate a phospholipid radical ($\text{PL}\cdot$). Upon reaction with molecular O_2 , peroxy radical ($\text{PLOO}\cdot$) is formed, which initiates lipid peroxidation. Then, lipid peroxy radicals can attack other nearby PUFA lipids to propagate the lipid peroxidation chain reaction. If radical trapping antioxidants (RTAs) such as ubiquinone^{26, 27}, vitamin K²⁸, 7-dehydrocholesterol (7-DHC)^{29, 30}, tetrahydrobiopterin (BH_4)¹⁹ and squalene³¹, enzymes to (re)generate these RTAs and/or lipid (peroxy) radicals themselves are present, this chain reaction of lipid peroxidation can be terminated to the corresponding lipid alcohol (PLOH) and/or aldehyde ($\text{PL}=\text{O}$). The reaction for all is shown in **Figure 1**.

3. 3. Ferroptosis suppressor protein-1 (FSP1)

In search of mechanisms that may suppress ferroptosis independently of the canonical system $\text{Xc}^-/\text{GSH}/\text{GPX4}$ axis, the Conrad group conducted a genetic suppressor screen to uncover genes able to compensate for GPX4 loss²⁶. For this approach, the MCF7 breast carcinoma line was selected as it shows marked resistance to ferroptosis. Upon transduction of *Gpx4* knockout cells with a cDNA library generated from MCF7 cells and robust selection for anti-ferroptotic genes, two types of cDNA expressing clones were obtained. One expressed GPX4 as expected, and the other expressed "apoptosis inducing factor mitochondria associated 2" (AIFM2). AIFM2 is a flavoprotein originally identified as a p53-responsive gene conferring a purported pro-apoptotic function³²⁻³⁴. But due to its robust anti-ferroptotic activity as shown by Doll *et al.*²⁶, it was proposed to rename the enzyme, now referred to as ferroptosis suppressor protein-1 (FSP1). Detailed mechanistic studies showed that the anti-ferroptotic function of FSP1 relies on its role in reducing ubiquinone (CoQ)/vitamin K (VK) to ubiquinol (CoQ- H_2)/VK hydroquinone (VK- H_2), which prevents uncontrolled

lipid peroxidation by trapping peroxy radicals in lipid bilayers²⁶⁻²⁸. Mitochondrially synthesized ubiquinone is shuttled from mitochondria to the cytosol by StAR-related lipid transfer domain protein (cSTARD7) after mitochondria STARD7 (mSTARD7) is cleaved by presenilins-associated rhomboid-like protein (PARL) in mitochondria³⁵. In contrast, since VK cannot be produced in mammalian cells, VK is absorbed from the diet via a transporter, Niemann–Pick C1-like 1 (NPC1L1)³⁶. Then, the side chain of VK is cleaved and distributed to each organ through the lymphatic system³⁷. After VK is transferred, UbiA prenyltransferase containing 1 (UBIAD1) elongates the side chain to re-generate VK³⁸.

The anti-ferroptotic function of FSP1 relies on its membrane binding ability via N-terminal myristoylation^{26, 27}. FSP1 localizes to the plasma membrane, endoplasmic reticulum (ER), Golgi apparatus (Golgi), the outer membrane of mitochondria, lipid droplets, and perinuclear structures^{26, 27, 39}. Among these subcellular distributions, FSP1 localization in the plasma membrane seems to be most critical in ferroptosis inhibition²⁷. N-myristoylation is achieved in a co-translational process by the activity of N-myristoyl transferases (NMTs)⁴⁰. Interestingly, ACSL1 is also proposed to stabilize myristoylated FSP1⁴¹; however, its mechanism remains unclear.

A number of cancer cell lines from different origins express FSP1 and its high expression strongly correlates with the resistance to ferroptosis inducers^{26, 27, 42}. Kirsten rat sarcoma virus (KRAS) mutational status and resulting oxidative stress conditions induce the intrinsic antioxidant system, known as kelch like ECH associated protein 1 (KEAP1)-nuclear factor erythroid 2-related factor 2 (NFE2L2 or NRF2) system⁴³. KEAP1 negatively regulates NRF2 protein levels via constant degradation of NRF2; however, under oxidative stress, cysteine residues of KEAP1 are oxidized, and KEAP1 becomes inactivated and ubiquitylated, whereupon NRF2 escapes KEAP1-dependent degradation⁴⁴. Upon stabilization, NRF2 binds to antioxidant responsive elements (ARE) in promoter regions and drives transcription of antioxidant genes. A recent study shows that the promoter region of AIFM2 (FSP1) also contains an ARE element and thus FSP1 can be considered as one of the target genes of NRF2⁴⁵. Another potential regulator of FSP1 is bromodomain and extraterminal domain protein (BET), such as bromodomain containing 4 (BRD4). BETs can recognize histone modifications, such as acetylation and methylation, and they are known to be critical for the induction of pro-survival genes in cancer⁴⁶. Several studies have shown that the BET inhibitor JQ1⁴⁷ enhances ferroptosis sensitivity⁴⁸ and downregulates FSP1 expression⁴⁹. Moreover, it is reported that CpG islands are highly methylated to repress FSP1 transcription in acute lymphatic leukemia (ALL)⁵⁰. All these studies indicate that transcription of FSP1 is modulated by stress responses, as well as epigenomic regulation. Other than transcriptional regulation, FSP1 expression might also be affected by mRNA modification. For instance, N-acetyltransferase 10 (NAT10) or

methyltransferase-like protein 3 (METTL3) modify *FSP1* mRNA to N4-acetylcytidine (ac4C) or N6-Methyladenosine (m6A), respectively^{51, 52}. However, the role of these modifications in the modulation of mRNA stability is still controversial and requires further investigations.

For the development of FSP1-specific inhibitors as potential future drugs to combat certain cancers, a screening campaign using approx. 10,000 drug-like small molecule compounds was performed²⁶. Thereby, the Conrad group identified a series of highly promising compound scaffolds of FSP1 inhibitors awaiting further development. Among them, iFSP1 was introduced as the first FSP1-specific inhibitor showing that iFSP1 efficiently killed different types of cancer cell lines in synergism with the GPX4 inhibitor RSL3²⁶. However, since iFSP1 is a human FSP1-specific inhibitor⁵³ and does not qualify for further development to become a drug⁵⁴, it is only suitable as a research tool compound. Therefore, it remained challenging to identify a new *in vivo* efficacious FSP1 inhibitor as well as a species-independent, versatile inhibitor to investigate the role of FSP1 in different species and in the *in vivo* context.

Physiologically, FSP1 is widely expressed in many tissues and especially abundant in adipose tissue^{28, 55}. After induction of brown adipose tissue (BAT) cell differentiation, FSP1 expression drastically increases, which is regulated by the cAMP response element (CRE) binding protein (CREB) by binding to its CRE motif. It is reported that upon cold stress and/or β -adrenergic stimulation, FSP1 is induced and can be translocated to mitochondria to enhance thermogenesis in BAT⁵⁵.

Vitamin K (VK) has multiple functions not merely in ferroptosis inhibition. Previously, its main function has been ascribed to blood coagulation and bone metabolism⁵⁶. As another physiologically important function, FSP1 was recently described to be the warfarin-resistant VK reductase in the canonical VK cycle^{28, 57}. The canonical vitamin K cycle is indispensable for the γ -carboxylation of VK-dependent coagulation proteins, which is known as one of the post-translational modifications of proteins mediated by γ -carboxylglutamyl carboxylase (GGCX). GGCX oxidizes VK-H₂ to VK epoxide (VKO) and simultaneously adds CO₂ to glutamate (Glu), resulting in γ -carboxylglutamate (Gla). To regenerate VK, VKO is reduced by vitamin K epoxide reductase (VKOR). The VKOR inhibitor warfarin is one of the most commonly prescribed anticoagulant medicines worldwide. High-dose VK is used as the antidote during warfarin overdosing and known to bypass the VKOR-mediated VK cycle for γ -carboxylation⁵⁸, suggesting the existence of a warfarin-resistant VK reductase. While the genes for GGCX and VKOR were identified quite some time ago, the warfarin-resistant enzyme that reduces VK back to VK-H₂ was missing for about half a century. Mishima *et al.* focused on the structural similarities of VK to CoQ and found that FSP1 could also efficiently reduce VK to VK-H₂, both in cells and in enzyme assays. Actually, in *Fsp1* KO

mice, the antidotal effect of VK in the presence of warfarin was completely lost²⁸, indicating that it is FSP1 that is the warfarin-resistant VK reductase. An overview of the recent understanding of FSP1 mechanisms for ferroptosis suppression and regulating FSP1 functions is summarized in **Figure 2**.

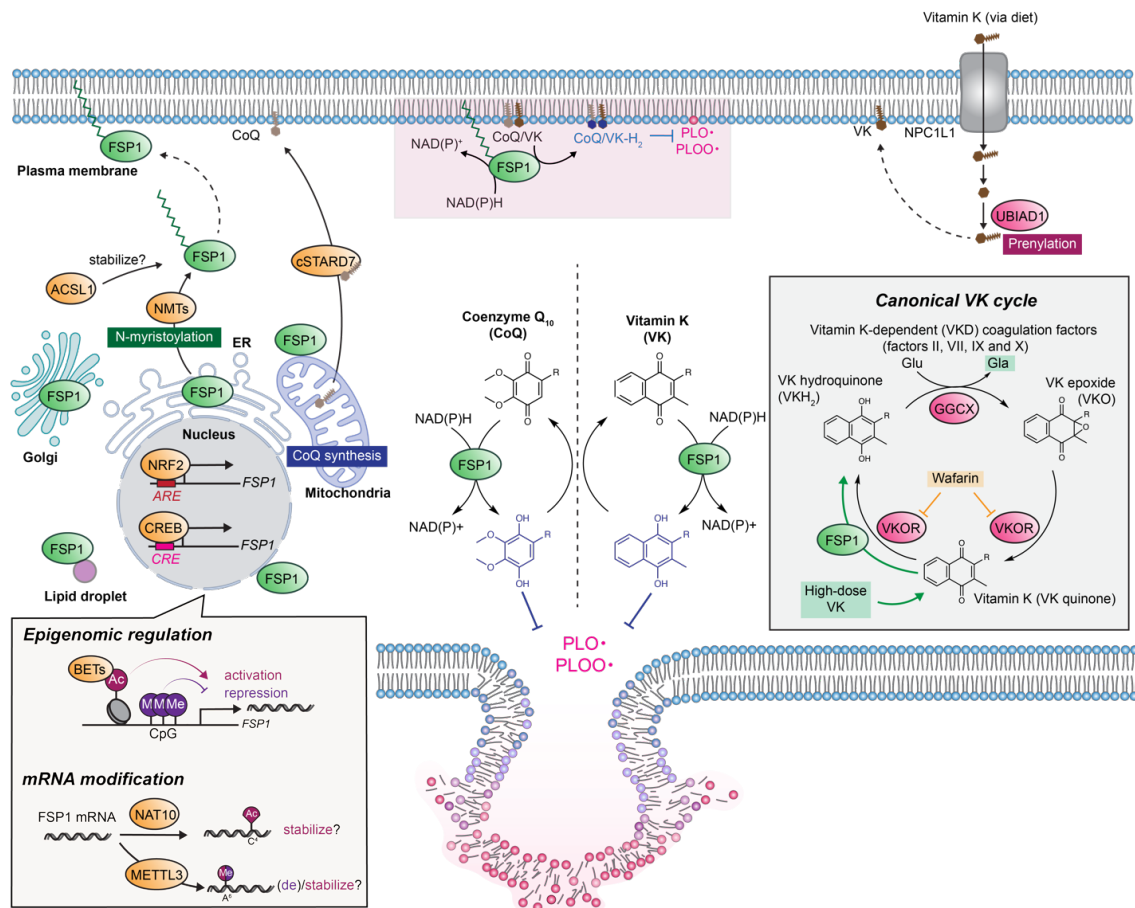


Figure 2. Overview of FSP1 functions and its regulation. FSP1 is mainly localized to the plasma membrane, endoplasmic reticulum (ER), Golgi apparatus (Golgi), the outer membrane of mitochondria, lipid droplets and perinuclear structures via its N-myristoylation accomplished by N-myristoyl transferases (NMTs). ACSL1 is proposed to stabilize myristoylated FSP1, although the precise mechanisms remain obscure. FSP1 is transcriptionally regulated by nuclear factor erythroid 2-related factor 2 (NRF2) via its antioxidant responsive element (ARE) or cAMP response element (CRE) binding protein (CREB) via its CRE motif in the promoter region. At the epigenomic level, bromodomain and extraterminal domain proteins (BETs) activate FSP1 transcription. The hypermethylation in CpG island represses FSP1 transcription. N-acetyltransferase 10 (NAT10) or

methyltransferase-like protein 3 (METTL3) regulates FSP1 mRNA stability. Enzymatically, FSP1 reduces coenzyme Q₁₀ (CoQ₁₀) and vitamin K (VK) to the corresponding hydroquinones (CoQ/VK-H₂), which can act as radical trapping antioxidants (RTAs), at the expense of nicotinamide adenine dinucleotide (phosphate) (NAD(P)H) as electron donors. CoQ₁₀ is synthesized at mitochondria and distributed via the cytosolic form of STARD7. VK is absorbed from the diet in the intestine, cleaved, and re-regenerated via multiple steps. As a second enzymatic function, FSP1 is found as a long sought-after warfarin-resistant vitamin K reductase in the canonical VK cycle. VK-H₂ is used for the γ -carboxylation of VK-dependent (VKD) proteins including some blood coagulation factors by γ -carboxyglutamyl carboxylase (GGCX). VK epoxide (VKO) is then regenerated by vitamin K epoxide reductase (VKOR), which is the target enzyme of warfarin. In the presence of warfarin, coagulation factors are depleted, while supplementation of high-dose vitamin K (the antidote of warfarin poisoning), FSP1 can bypass this VKOR inhibition. Abbreviation: Glu, glutamate; Gla, γ -carboxyglutamate; PLO(O)•, phospholipid peroxy radicals; UBIAD1, UbiA prenyltransferase containing 1; Me, methylated, Ac, acetylated. Organelle images are obtained from Biorender.com. Proteins related to the functions of FSP1 (orange) or vitamin K biology (red) are shown.

3. 4. Phase separation

Biological condensates of proteins detected as membrane-less organelles play essential roles in many biological processes⁵⁹, such as transcription^{60, 61}, stress signaling^{62, 63}, protein homeostasis^{64, 65}, development⁶⁶, and cell death⁶⁷. Nowadays, several proteins have been reported to undergo condensate formation in a process, known as (liquid-liquid) phase separation. Phase separation is a physicochemical phenomenon separating proteins and inducing intracellular membrane-less compartmentation, in analogy to the separation of oil and water⁶⁸. To achieve spatiotemporal segregation of one protein from the others, classic organelles (e.g., the endoplasmic reticulum, Golgi apparatus, endosomal/lysosomal small particles, or nucleus, etc.) physically separate and sort proteins by their membrane. In contrast, many compartments or signal transduction sites without membranes are also present in cells. For instance, P granules in germ cells of *Caenorhabditis elegans* (*C. elegans*) were found as the first indicator of liquid-like condensates driven by phase separation⁶⁹. P granules can fuse with each other in a spherical shape, exchange rapidly within and outside of condensates after photobleaching, and flow with high mobility under shear stress. Since P granules were found to be phase-separated condensates, other compartments, such as stress granules⁷⁰, DNA damages and repair sites⁷¹, and membrane clusters at signal transduction⁷², were also found. Then, biomolecular condensates driven by phase separation have been highlighted. Recent advances in the last couple of years have allowed us to generalize "biomolecular

condensates", which means both membrane-less and membrane-bound granules with the ability to concentrate biomolecules and comprise protein condensates⁷³. Biomolecular condensates in cells and their role in the many cellular processes in response to stress are summarized in **Figure 3**.

For the induction of phase separation of proteins in cells, multiple factors have been identified that contribute to this highly sophisticated process. First, multivalent interactions, such as protein-protein interactions via intrinsic disordered regions (IDRs: flexible and linear motifs without any higher order structure such as α -helix or β -sheet) or low complexity regions (LCRs: domains rich in glycine and serine or other amino acids repeat sequence) are the main driving forces of phase separation⁷³. These interactions are usually mediated by charges, charge- π , π - π , dipolar and hydrogen bonds, or protein-protein interactions via spacer-sticker interactions. Second, multivalent tandem structures⁷⁴, such as RNA recognition motifs (RRMs)⁷⁵, Src homology 2/3 domains (SH2/3)⁷⁴, and poly-ubiquitination^{65, 76} drive phase separation as well. Last, small molecules and posttranslational modifications also dictate condensates mediated by phase separation. For instance, phosphorylation, poly (ADP)ribose (PAR), or sodium ion (Na^+) can regulate the liquidity of condensates under hyperosmotic stress^{62, 77}. Other than natural small molecules, some anti-cancer drugs, such as cisplatin and tamoxifen, also accumulate in biomolecular condensates along with oncogenic transcription factors in the nucleus⁷⁸. The selective accumulation of these drugs at the oncogenic super-enhancer region is considered to be a potential therapeutic target to enhance the local concentrations of these drugs, resulting in the specificity of targeting cancers⁷⁹. While biomolecular condensates at the oncogenic super-enhancer region can be a promising target for cancer therapy, neurodegenerative diseases-associated aggregates can also be potential targets for phase separation⁸⁰. Neurodegenerative diseases-associated proteins, such as fused in sarcoma (FUS), TAR DNA-binding protein 43 (TDP-43), alpha-synuclein (a-syn), and microtubule-associated protein (Tau), are prone to form condensates in cells and *in vitro*. This may result in pathological aggregates as a consequence of phase transition from liquid-like to gel-/solid-like condensates. Remarkably, these proteins are associated with frontotemporal lobar degeneration, amyotrophic lateral sclerosis, Parkinson's disease and Alzheimer's diseases, respectively; thus, inhibiting these condensate-derived aggregates may be a potential therapeutic strategy in the future⁸⁰.

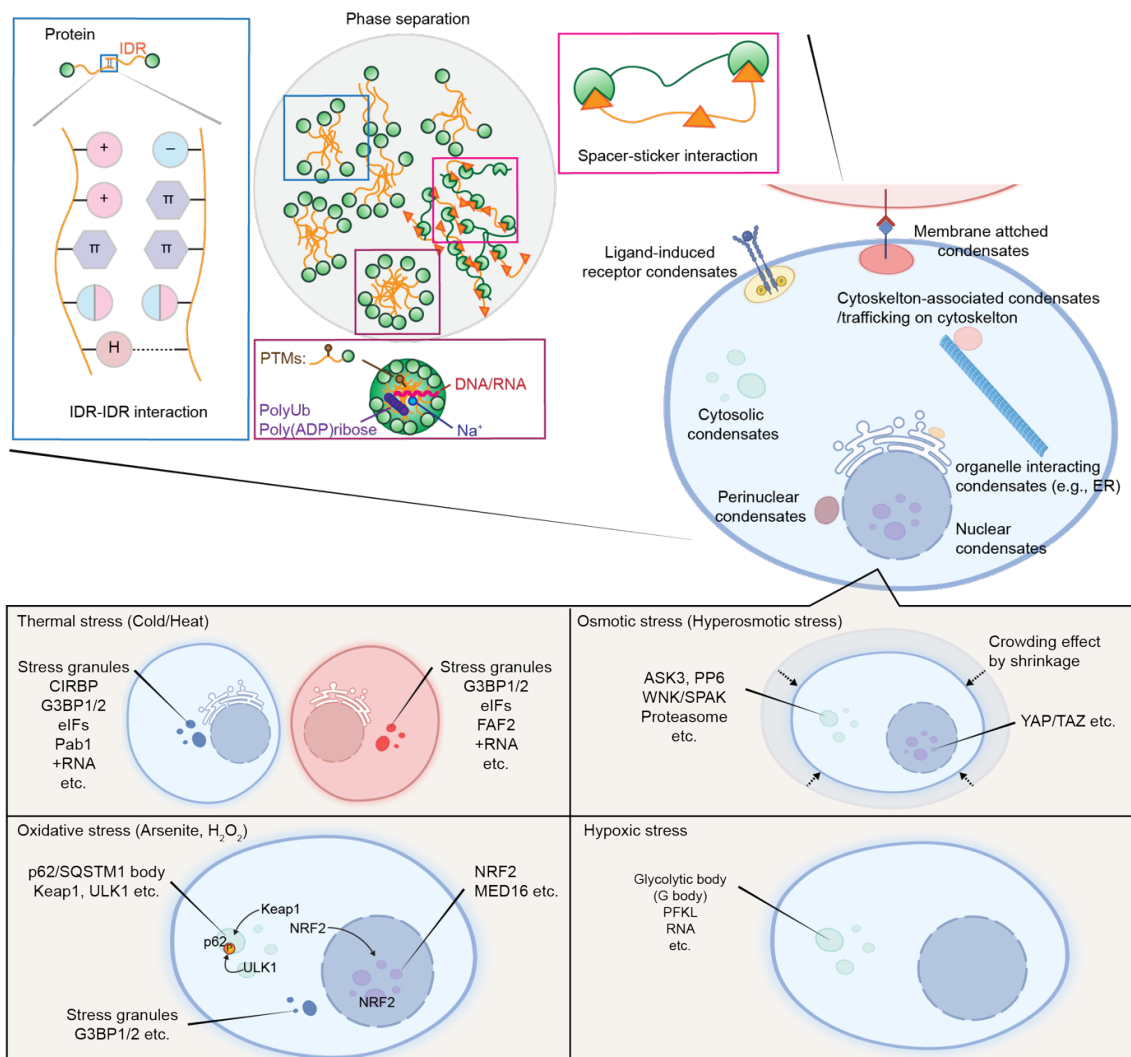


Figure 3. The basic principle of phase separation. (upper left) Biomolecular condensate formation via protein intrinsic disorder regions (IDRs). IDR-IDR interactions are mediated by charges, charge- π , π - π , dipolar and hydrogen bonds. Another protein-protein interaction is mediated by a spacer and sticker interaction. These biomolecular condensates and their property are associated with multiple factors: post-translational modifications (PTMs), poly ubiquitination (polyUb), poly (ADP)ribose (PAR), nucleic acids (DNA/RNA) and sodium ions (Na^+), etc. (upper right) Spatial distribution of biomolecular condensates. The most commonly known condensates are located in the cytosol, perinuclear or nuclear. Some condensates appear upon exogenous stimuli, such as a ligand or cell-cell contact, and are also attached to organelles, such as the endoplasmic reticulum

(ER) and traffic to the cytoskeleton. (bottom) Ferroptosis-related stimuli can induce phase separation. Thermal stress (cold or heat) induces stress granule formation in eukaryotic and yeast cells. Stress granules contain G3BP stress granule assembly factor1/2 (G3BP1/2)⁷⁰, eukaryotic initiation factors, cold inducible RNA binding protein (CIRBP)⁸¹, yeast poly(A)-binding protein (Pab1)⁸², FAS associated factor 2 (FAF2)⁸³ and RNAs. Osmotic stress (hyperosmolarity) induces cell volume shrinkage, triggering the crowding of the content of cells including proteins. Apoptosis signal-regulating kinase 3 (ASK3), protein phosphatase 6 (PP6)⁷⁷, with-no-lysine (WNK) kinases, serine-threonine kinase 39 (SPAK)⁸⁴, proteasome subunits, Yes-associated protein (YAP)⁶¹, and WW-domain-containing transcription regulator (TAZ)⁶⁰ are shown to be phase separated upon osmotic stress. Oxidative stress induced by arsenate and hydroperoxide (H₂O₂) triggers phase separation of the p62 body (sequestosome 1; SQSTM1). Unc-51-like kinase 1 (ULK1) phosphorylates p62 and induces subsequent KEAP1 dissociation from NRF2⁸⁵. Then, NRF2 is activated and translocated to the nucleus to form droplets⁸⁶. Hypoxia induces glycolytic body (G body)^{87, 88}, which contains glycolytic enzymes and RNAs.

4. Material and Methods

4. 1. Materials

Chemicals

Lipoxstatin-1 (Lip-1: Selleckchem, S7699), doxycycline (Dox: Sigma, D9891), (1S,3R)-RSL3 (RSL3: Cayman, 19288); L-buthionine sulfoximine (BSO, Sigma, B2515); iFSP1 (ChemDiv, 8009-2626); icFSP1 (ChemDiv, L892-0224, or custom synthesis by Intonation Research Laboratories), viFSP1 (Vistas-lab, STK626779), erastin (Merck, 329600), ML210 (Cayman, Cay23282-1), FIN56 (Cayman, Cay25180-5), FINO2 (Cayman, Cay25096-1), deferoxamine mesylate salt (DFO: Sigma, 138-14-7), ferrostatin-1 (Fer-1: Sigma, SML0583), zVAD-FMK (zVAD: Enzo Life Sciences, ALX-260-02), necrostatin-1s (Nec-1s: Enzo Life Sciences, BV-2263-5), MCC950 (Sigma, 5381200001), olaparib (Selleckchem, S1060), staurosporine (STS: Cayman, 81590), recombinant human TNF α (R&D Systems, NBP2-35076), Smac mimetic (BV-6) (Selleckchem, S7597), nigericin (Thermo Fisher, N1495), IMP-1088 (Cayman, Cay25366-1), lipopolysaccharide (LPS: Sigma, L2880), and JKE-1674 (Cayman, Cay30784-1) were used in this study. Custom-made compounds were obtained from Intonation Research Laboratories, Andhra Pradesh, India.

Mice

Five to six-weeks-old female C57BL6/J and athymic nude mice were obtained from Charles River and six to seven weeks-old mice were used for experiments. All mice were kept under SPF-IVC standard conditions with water and food *ad libitum* and in a controlled environment ($22 \pm 2^\circ\text{C}$, $55 \pm 5\%$ humidity, 12 h light/dark cycle) in the animal facility of Helmholtz Munich. All animal experiments have been approved by the government of Upper Bavaria (ROB-55.2-2532.Vet_02-17-167) and were performed in compliance with the German Animal Welfare Law.

Cell lines

Murine immortalized 4-hydroxytamoxifen (TAM)-inducible *Gpx4* knockout (KO) fibroblasts (referred to as Pfa1) were reported previously¹⁴. Genomic *Gpx4* deletion can be achieved by TAM-inducible Cre recombinase using the CreERT2/LoxP system. HT-1080 (CCL-121), 786-O (CRL-1932), A375 (CRL-1619), A549 (CCL-185), B16F10 (CRL-6475), LLC1 (CRL-1642), MDA-MB-436 (HTB-130), SW620 (CCL-227), HT-29 (HTB-38), HEK293T (CRL-3216), NCI-H460 (HTB-177) and 4T1 (CRL-2539) cells

were obtained from ATCC. LOX-IMVI was obtained from NCI/NIH. SKOV3 (91091004) and primary peripheral blood mononuclear cells (PBMC) were obtained from Sigma-Aldrich. HEC151 cells (JCRB1122-A) were obtained from Tebubio. MC38 cells were kindly gifted from Dr. Patrizia Agostinis (KU Leuven, Belgium). Huh7 cells were kindly gifted from Dr. Robert Schneider (Helmholtz Munich). SUDHL5, SUDHL6, DOHH2, and OCI-Ly19 cells were kindly gifted from Dr. Stephan Hailfinger (University of Münster). Rat1 cells were gifted from Medizinische Hochschule Hannover.

Pfa1, HT-1080, 786-O, A375, HT-29, SW620, Huh7, Rat1, MC38, LLC and B16F10 cells were cultured in DMEM-high glucose (4.5 g glucose/L) with 10% fetal bovine serum (FBS), 2 mM L-glutamine, and 1% penicillin/streptomycin. H460, MDA-MB-436, SKOV3, HEC151, THP-1, PBMC, SUDHL5, SUDHL6, DOHH2 and 4T1 cells were cultured in RPMI GlutaMax with 10% FBS, and 1% penicillin/streptomycin. OCI-Ly19 cells were cultured in IMDM with 10% FBS and 1% penicillin/streptomycin. For generating stably overexpressing cell lines, appropriate antibiotics (puromycin 1 µg/mL, blasticidin 10 µg/mL and G418 0.5-1 mg/mL) were used. GPX4 KO A375, SW620 and H460 cells were cultured in the presence of 1 µM Lip-1 for normal maintenance. *DHODH* KO cells and *Dhodh* KO Pfa1 cells were maintained in a medium containing uridine (100 and 50 µM, respectively). All cells were cultured at 37 °C with 5% CO₂ and verified to be negative for mycoplasma.

4. 2. Methods

Cell viability assay

Cells were seeded on 96-well plates and cultured overnight (2,000 - 20,000 cells/well for ferroptosis inducers and 500 cells/well for TAM) or 384-well plates (800 cells/well). On the next day, the medium was changed to the medium containing the following compounds: RSL3, ML210, JKE-1674, erastin, FIN56, FINO2, BSO, iFSP1, icFSP1, viFSP1 Lip-1, DFO, Fer-1, zVAD, Nec-1s, MCC950, olaparib, STS, TNFα, Smac mimetic or nigericin at the indicated concentrations. For *Gpx4* or *Aifm2* gene deletion by TAM or doxycycline (Dox), cells were seeded with compounds at the same time. Cell viability was determined 1 h (for nigericin), 24 – 48 h (for RSL3, ML210, JKE-1674, erastin, FIN56, FINO2, iFSP1, icFSP1, viFSP1, STS, TNFα, Smac mimetic, and zVAD) or 72 h (for BSO, icFSP1, TAM, and Dox) after treatment using AquaBluer (MultiTarget Pharmaceuticals, 6015) or 0.004 % resazurin (dissolved in PBS, Sigma, R7017) as an indicator of viable cells. For the induction of apoptosis, HT-1080 cells were treated with different concentrations of STS for 24 h. For the induction of necroptosis, HT-29 cells were treated with different concentrations of TNFα with Smac mimetic (400 nM) and zVAD (30 µM) for 24 h. For the induction of pyroptosis, LPS (1 µg/mL, 2 h)-

preconditioned THP-1 cells were treated with nigericin for 1 h. For the induction of ferroptosis, cells were treated with ferroptosis inducers for 24-72 h.

As readout, the fluorescence was measured at Ex/Em = 540/590 nm using a SpectraMax M5 microplate reader with SoftMax Pro v7 (Molecular devices) after 4 - 6 hours of incubation in normal cell culture conditions.

LDH release assay

Pfa1 cells (2,500 cells per well) were seeded on 96-well plates and cultured overnight. On the next day, medium was changed to the one with FSP1 inhibitors and cultured for another 24 h. Necrotic cell death was assessed using the Cytotoxicity Detection kit (LDH) (Roche, 11644793001). In brief, cell culture supernatant was harvested as medium sample, then cells were lysed using 100 μ L of 0.1% Triton X-100 in PBS as lysate sample. Medium and lysate samples were individually loaded with reagents onto microplates, and the absorbance was measured at 492 nm using SpectraMax M5 microplate reader after 15-30 min incubation at room temperature. Cell death ratio was calculated using medium values divided by the sum of medium and lysate values.

Screening of FSP1 inhibitors

Pfa1 *Gpx4* WT and *Gpx4* KO cells stably overexpressing human FSP1 (hFSP1) or murine FSP1 (mFSP1) were seeded on separate 384-well plates (500 cells per well) and screened with a library of small molecule inhibitor compounds as reported previously²⁶. Cell viability was assessed 48 h after treatment as above, and compounds showing selective lethality in Pfa1 *Gpx4* KO cells stably overexpressing human or murine FSP1 were considered as hit compounds.

Lipid peroxidation assay

Pfa1 cells (100,000 cells per well) were seeded on 12-well plates one day prior to the experiments. On the next day, cells were treated with 2.5 μ M iFSP1 or icFSP1, or 10 μ M viFSP1 for 3 h, and subsequently incubated with 1.5 μ M C11-BODIPY 581/591 (Invitrogen, D3861) for 30 min in a 5% CO₂ atmosphere at 37°C. Then, cells were washed with PBS, trypsinization, and then resuspended in 500 μ L PBS. Cells were passed through a 40 μ m cell strainer and analyzed on a flow cytometer (CytoFLEX, Beckman Coulter) equipped with a 488-nm laser for excitation. Data were collected

using CytExpert v2.4 (Beckman Coulter) from the FITC detector (oxidized BODIPY) with a 525/40 nm bandpass filter and from the PE detector (reduced BODIPY) with a 585/42 nm bandpass filter. At least 10,000 events (viable cells) were analyzed per sample. Data were analyzed using FlowJo Software (v10, FlowJo LLC). Lipid peroxidation (the ratio of fluorescence of C11-BODIPY 581/591[FITC/PE ratio (oxidized / reduced ratio)]) were calculated using median values³.

Oxilipidomics analysis

Two million cells were seeded on 15 cm dishes one day prior to the experiments. On the next day, cells were treated with 5 μ M icFSP1 for 5 hours. Then, cells were harvested and sampled to liquid nitrogen and stored at -80°C . Lipids from cells were extracted using the methyl-tert-butyl ether (MTBE) method⁸⁹. In brief, cells were collected in antioxidant buffer (100 μ M dibutylhydroxytoluene (BHT) and 100 μ M diethylenetriamine pentaacetate (DTPA) in PBS). 2.5 μ L of SPLASH[®] LIPIDOMIX[®] (Avanti Polar Lipids Inc.) were mixed with cells and incubated on ice for 15 min. Subsequently, ice-cold methanol (375 μ L) and MTBE (1250 μ L) were added, and samples were thoroughly mixed using a vortexer and incubated for 1 h at 4 $^{\circ}\text{C}$ (Orbital shaker, 32 rpm). After adding milliQ water (375 μ L), the samples were vortexed, incubated for 10 min at 4 $^{\circ}\text{C}$ (Orbital shaker, 32 rpm), and centrifuged to separate the organic and aqueous phases (10 min, 4 $^{\circ}\text{C}$, 1500 x g). The organic phase was carefully harvested and dried in the vacuum evaporator and then redissolved in 100 μ L of isopropanol. Lipid extracts were finally transferred into glass vials for LC-MS analysis.

Reversed phase liquid chromatography (RPLC) was performed by Shimadzu ExionLC equipped with an Accucore C30 column (150 x 2.1 mm; 2.6 μ m, 150 \AA , Thermo Fisher Scientific). Gradient elution with solvent A (acetonitrile/water, 1:1, v/v) and B (isopropanol/acetonitrile/water, 85:15:5, v/v) both containing 5 mM NH_4HCO_2 and 0.1% (v/v) formic acid separated lipids from the samples at 50 $^{\circ}\text{C}$ with a flow rate of 0.3 mL/min using following gradient: 0-20 min – 10 to 86 % B (curve 4), 20-22 min – 86 to 95 % B (curve 5), 22-26 min – 95 % isocratic, 26-26.1 min – 95 to 10 % B (curve 5) followed by 5 min re-equilibration at 10% B6. Mass spectrometry analysis was carried out on a Sciex 7500 system equipped with an electrospray (ESI) source and operated in negative ion mode. Products were analyzed in MRM mode monitoring transitions from the parent ion to daughter ion with the following parameters: TEM 500 $^{\circ}\text{C}$, GS1 40, GS2 70, CUR 40, CAD 9, IS – 3000 V.

The area under the curve (AUC) for the parent ion to daughter ion was integrated and standardized by appropriate lipid species, PC (15:0/18:1(d7)) or PE(15:0/18:1(d7)), from SPLASH LIPIDOMIX Mass Spec Standard (Avanti). Normalized peak areas were further log-transformed and auto-scaled in

MetaboAnalyst online platform v5.0 (<https://www.metaboanalyst.ca>)⁹⁰ and shown by GraphPad Prism 9 as the heat maps. Zero values were replaced by 0.2 × the minimum values detected for a given oxidized lipid within the samples and oxidized lipids showing a significant difference (ANOVA, adjusted P-value (false discovery rate (FDR < 0.05)) between samples were used.

Cell lysis and immunoblotting

Cells were lysed in LCW lysis buffer (20 mM Tris-HCl, 0.5% Triton-X-100, 30 mM Sodium pyrophosphate tetrabasic decahydrate, 10 mM EDTA, 0.5% sodium deoxycholate salt, 150 mM NaCl) supplemented with inhibitor cocktail (cOmplete and phoSTOP, Roche, 04693116001 and 4906837001), and centrifuged at 20,000 x g, 4 °C for 0.5 - 1 h. The supernatants were resolved in 6 x SDS sample buffer (0.03% bromophenol blue, 375 mM Tris-HCl, 9% SDS, 50% glycerol, 9% β-mercaptoethanol, pH 6.8). After heating at 98 °C for 3 min, the samples were separated on 12% SDS-PAGE gels (Bio-Rad, 4568043 or 4568046) and subsequently electroblotted onto PVDF membrane (Bio-Rad, 170-4156). The membranes were blocked with 5% skim milk (Roth, T145.2) in TBS-T (150 mM NaCl, 20 mM Tris-HCl, and 0.1% Tween-20), then probed with the primary antibodies against valosin containing protein (VCP, 1:10000, Abcam, ab11433 or ab109240), GPX4 (1:1000, Abcam, ab12506), HA tag (1:1000, clone 3F10, homemade), Flag tag (1:5000, Cell Signaling Technology, 2368S), human FSP1 (1:1000, Santa Cruz, sc-377120, AMID or 1:10, clone 6D8, rat IgG2a), mouse FSP1 (1:500, clone AIFM2 1A1 rat IgG2a or 1:5, clone AIFM2 14D7 rat IgG2b, developed in-house), ACSL4 (1:1000, clone A-5, Santa Cruz, sc-271800), human SLC7A11 (1:10; Rat IgG2a monoclonal antibody against an N-terminal peptide of hXCT (SLC7A11), clone 3A12-1-1, developed in-house), DHODH (1:1000, Santa Cruz, sc-166348), mouse SLC7A11 (1:1000, Cell Signaling Technology, 98051S), or against β-actin-HRP (1:50000, Sigma, A3854) diluted in BSA or milk buffer (TBS-T with 5% BSA and 0.1% NaN₃ (Sigma, S2002)) overnight. After washing the membranes once and exposure to the appropriate secondary antibodies diluted in 5% skim milk in TBS-T, antibody-antigen complexes were detected by the ChemiDoc Imaging System with Image Lab v6.0 (BioRad). Representative immunoblot images are shown after the adjustment to the appropriate brightness and angle using the ImageJ/Fiji software (v1.52 & 1.53).

Expression and sgRNA plasmid construction

All plasmids for this thesis were constructed by standard molecular biology techniques, and confirmed by sequencing as follows: A human *FSP1* cDNA (NM_001198696.2, C>T:1008) and

codon-optimized *Mus musculus* (mouse) *Fsp1* (NP_001034283.1) were cloned from the vectors previously reported²⁶. Codon-optimized *Rattus norvegicus* (rat) *Fsp1* (NP_001132955.1), and *Gallus gallus* (chicken) *FSP1* (XP_421597.1), and *Xenopus laevis* (Frog) *FSP1* (NP_001091397.1) were cloned in the p442 vector. Human *DHODH* (NP_001352.2, codon-optimized) with a C-terminal HA tag was synthesized by Twist Bioscience and subcloned in pLV-EF1a-IRES-Neo (85139, Addgene). Human *FSP1* (NP_001185625.1, codon-optimized) and mouse *Fsp1* (NP_001034283.1, codon-optimized) were obtained from TWIST Bioscience and subcloned in 141-IRES-puro vectors. For generating *FSP1* mutants or subcloning, desired DNAs were amplified by polymerases such as KOD One (Sigma, KMM-201NV) and PrimeSTAR Max DNA polymerase master mix (Takara Bio, R045A), and resulting PCR products were purified by Wizard SV Gel&PCR Clean-up System (Promega, A9285) according to the manufacturer's protocols. PCR products or sgRNA duplex were ligated with digested vectors by T4 ligase (NEB, M0202L) or in-Fusion cloning enzymes (Takara Bio, 639649 or 638948) according to manufacturer's protocols with minor optimization. Reaction mixtures were transformed into competent *E.coli* cells (NEB, C3040H or developed in-house). After overnight culture, plasmids were isolated using QIAprep Spin Miniprep Kit (QIAGEN, 27106) according to the manufacturer's protocols. Sequencing of the plasmids was performed by Eurofins.

Lentiviral production and transduction

The ecotropic envelope protein of the murine leukemia virus (MLV) or the amphotropic envelope protein VSV-G were used for transducing mouse or human cells, respectively. A third-generation lentiviral packaging system consisting of transfer plasmids of the interest, envelope plasmids (pEcoEnv-IRES-puro or pHCMV-EcoEnv (ecotropic particles) or pMD2.G (pantropic particles)) and packaging plasmids (pMDLg_pRRE/pRSV_Rev, or psPAX2) were co-lipofected into HEK293T cells using transfection reagents (PEI MAX (Polysciences, 24765) or X-tremeGENE HP agent (Roche, 06366236001)) for lentiviral production. Supernatants containing viral particles were harvested at 48-72 h post-transfection and filtered through a 0.45 µm PVDF filter (Millipore, SLHV033RS) and stored at -80 °C until use.

Cells were seeded on 12 or 6 well plates with a medium with 10 µg/ml protamine sulfate to enhance the transduction efficiency. Lentivirus particles were added to the cells at the same time. On the next day, the cell culture medium was replaced with fresh medium containing respective antibiotics, such as blasticidin (Invitrogen, A1113903; 10 µg/ml), puromycin (Gibco, A11138-03; 1 µg/ml), or G418 (Invitrogen, 10131-035; 1 mg/mL) and cultured until non-transduced cells were dead.

CRISPR/Cas9-mediated gene knockout

Single guide RNAs (sgRNA) were designed to target exons of the genes of interest with VBC score⁹¹, and gene knockouts (KO) were confirmed by Western blotting and/or reading the genome sequences. The sgRNAs were ligated into the *BsmBI*-digested lentiCRISPRv2-blast, lentiCRISPRv2-puro, lentiGuide-neo vectors (Addgene, 98293, 98290 and 139449) as described above.

To generate KO cells, MDA-MB-436, 786-O, A375, H460, B16F10 and 4T1 cells were transiently co-transfected with the desired sgRNAs expressing lentiCRISPRv2-blast or -puro using the X-tremeGENE HP agent as described previously^{28, 53}. One day after transfection, cell culture medium was replaced with appropriate antibiotics, such as puromycin (1 µg/mL) and blasticidin (10 µg/mL). After selection for 2-3 days, single-cell clones were isolated by serial dilution and knockout clones were validated.

To generate Dox-inducible KO cells, pCW-Cas9-blast (Addgene, 83481) plasmid was transduced in HT-1080 cells and single-cell clones were isolated. Dox-inducible Cas9 expression was confirmed by immunoblotting. Then, the lentivirus with lentiGuide-neo vectors harboring sgRNAs targeting *FSP1* were transduced with HT-1080 pCW-Cas9-blast cells and selected with neomycin (G418). Loss of FSP1 expression upon dox treatment was confirmed by immunoblotting.

To generate scalable FSP1-EGFP expressing cells, H460 *FSP1* KO cells were infected with lentivirus containing pCW-FSP1WT or Q319K-EGFP-blast. Re-expression of FSP1 in a dox concentration-dependent manner was confirmed by immunoblotting.

Stable expression of genes by transfection

4T1 *Gpx4* KO cells and B16F10 *Gpx4 KO/Fsp1* KO cells were lipo-transfected with 141-IRES-puro, 141-hFSP1-IRES-puro, and 141-mFsp1-IRES-puro vectors with the X-tremeGENE HP agent. One day after transfection, cells were selected with puromycin (1 µg/mL), and/or Lip-1 removal and maintained under this condition until they showed stable FSP1 expression.

Production and isolation of FSP1 enzyme

Recombinant human FSP1 protein (non-myr-FSP1) was produced in the *E.coli* strain BL21. In brief, codon optimized FSP1 was cloned in a small ubiquitin-like modifier (SUMO) fusion expression plasmid (pETSUMO) and transformed into cells to produce protein. After cells reached the optimal

density, protein was lysed by lysis buffer (300 mM NaCl, 50 mM TRIS, 20 mM Imidazol, 10 mM β -mercaptoethanol, pH8). Then, protein was purified by affinity chromatography with a Ni-NTA system. Size-exclusion chromatography (SEC) was performed using HiLoad 16/60 Superdex 75 at room temperature as reported previously²⁶.

For protein isolation by Strep pulldown, HEK293T cells were seeded on 10 or 15 cm dishes and transfected with EGFP-Strep-tagged constructs by PEI MAX. After washing with PBS, the cells were lysed in lysis buffer containing protease and phosphatase inhibitor cocktail and 1 mM dithiothreitol (DTT). The cells were harvested with cell scrapers and centrifuged at 20,000 x g, 4 °C for 1 h. The supernatants were transferred to new tubes and incubated with MagStrep "type3" XT beads (Biozol, 2-4090-002) at 4°C for 1-2 hrs. The beads were washed twice with washing buffer (100 mM Tris-HCl, 150 mM NaCl, 1 mM EDTA) and Strep-tagged proteins were eluted in elution buffer (100 mM Tris-HCl, 150 mM NaCl, 1 mM EDTA, 50 mM Biotin). The protein concentration was estimated from the absorbance at 280 nm with Spectrophotometer UV5Nano (Mettler Toledo) using the coefficient values which were calculated by ExPASy ProtParam (<https://web.expasy.org/protparam/>). Lastly, the protein was diluted to 3 μ M using TBS buffer (50 mM Tris-HCl, 150 mM NaCl).

Myristoylated FSP1 protein was purified by co-expression of N-myristoyltransferase 1 (hsNMT1, petCDF vector - spectinomycin resistency) with FSP1 (FSP1-EGFP with a C terminal 6-histidine tag, petM13 – kanamycin resistance) in BL21 cells in the same way as for wildtype FSP1 with a final step being gel filtration chromatography. Pure protein was confirmed by SDS-PAGE myristoylation and confirmed by mass-spectrometry, LC-ESI-MS (Waters Synapt XS). The protein was separated on a ACQUITY UPLC Protein BEH C4 Column (0.4 mL/min, buffer A: 0.1% formic acid in H₂O and buffer B: 0.1% formic acid in CH₃CN) and analyzed by Masslynx V4.2 (Waters).

FSP1 enzyme activity and inhibition assay

For the resazurin reduction assay, 15-200 nM non-myr-hFSP1 or mFSP1, 200 μ M NADH and the inhibitors (iFSP1, icFSP1, viFSP1) in TBS buffer (50 mM Tris-HCl, 150 mM NaCl) or PBS were prepared. After the addition of 100 μ M resazurin sodium salt (Sigma, R7017), fluorescent intensity (FL, Ex/Em = 540/590 nm) was measured every 0.5-1 min using SpectraMax M5 or SpectraMaxiD5 microplate reader with SoftMax Pro v7 (Molecular devices) at 37 °C. Reactions with the equivalent volume of DMSO and without resazurin were used to calculate IC₅₀ values. Curve fitting and calculating IC₅₀ values were done using GraphPad Prism v9.

For the NADH consumption assay, 25 nM non-myr-hFSP1, 200 μ M menadione (Sigma, M5625) or 200 μ M CoQ₀ (Sigma, D9150) and the inhibitors (iFSP1 and icFSP1) in PBS (Gibco, 14190094) were prepared. After the addition of 200 μ M NADH, absorbance at 340 nm at 37 °C was monitored every 30 sec using SpectraMax M5 Microplate Reader (Molecular devices). Reactions without NADH/without enzyme were used for normalization. Subsequent curve fitting was analyzed by GraphPad Prism9.

***In vitro* FSP1 condensation assays**

The isolated EGFP-Strep or hFSP1-EGFP-Strep-tagged proteins from HEK cells were diluted in TBS buffer (supplemented with 1 mM DTT) to the desired final concentrations. Then, purified proteins were mixed with polyethylene glycol 3350 (PEG, Sigma, P3640) and/or icFSP1; final concentrations of the proteins, PEG, and icFSP1 are described in each figure legend. For confocal microscopy analysis, samples were immediately transferred onto objective slides and EGFP signals were quickly acquired using LSM880 microscope with ZEN Black software (v2.3, ZWISS) with a 63x water immersion objective. The confocal microscopy images of 15 μ M recombinant C-terminally GFP-tagged non-myr-hFSP1 and myr-FSP1 in PBS (pH 7.4, 300 mM NaCl) or 10 μ M proteins in PBS (pH 7.4, 150 mM NaCl) were obtained using a Leica TCS SP8 confocal microscope with a 63x water immersion objective and GFP filter set.

For turbidity measurements, 10 μ L of different concentrations of non-myr-hFSP1 and PEG were mixed in a 384-well plate and the absorbance at 600 nm was immediately measured using SpectraMaxiD5 microplate reader (Molecular devices). For visualizing non-myr-FSP1 condensations with or without PEG in tubes, images were taken using a smartphone. Representative bright field images of non-myr-FSP1 condensates on the objective slide were acquired with Eclipse Ts2 Microscope (Nikon) with a 40x objective.

For sedimentation assays, recombinant non-myr-hFSP1 was reconstituted with the same amount of zero or 20% PEG in TBS with 1 mM DTT. Samples were then centrifuged at 2,500 x g for 5 min. The supernatants were collected in new tubes and the pellets were resolved in TBS supplemented with 1 mM DTT. Supernatant and pellet fractions of non-myr-hFSP1 were directly mixed with 6 x SDS sample buffer, and proteins were subsequently separated by SDS-PAGE. One gel was subjected to Western blotting using a FSP1 antibody (1:1000, Santa Cruz, sc-377120, AMID). The other gel was immediately soaked in Coomassie staining solution (1 mg/mL Coomassie Brilliant Blue G-250 [Sigma, 1154440025], 50% methanol, 10% acetic acid) for 15 min and subsequently

washed with washing buffer (70% methanol, 7% acetic acid). The washing buffer was microwaved, and the buffer was replaced, and the procedure was repeated until the protein bands showed clear signals.

***In vitro* saturation transfer difference experiments**

Saturation transfer difference (STD) experiments were performed with a Bruker Avance III HD spectrometer at 600 MHz ¹H frequency using a H/N/C triple resonance cryogenic probe. Spectra were recorded at 10 °C with 5 μM recombinant non-myr-hFSP1 and its mutants, and 100-fold molar excess of icFSP1 in PBS with 150 mM NaCl, 1% (v/v) DMSO-d₆ and 10% (v/v) D₂O for deuterium-lock. Saturation time was 2.5 sec and on- and off-frequencies were 0.68 and -17 ppm, respectively. NMR spectra were processed by Topspin 4.0.6 (Bruker).

Immunocytochemistry

All confocal microscopy images were recorded on a LSM880 microscope (ZEISS) with a 63x objective, and the corresponding appropriate filter sets for each fluorophore and analyzed by ZEN Blue software (v3.2, ZWISS) or ImageJ/Fiji. Cells were seeded on μ-Slide 8 well (ibidi, 80826) one day prior to experiments. On the next day, the medium was changed to a fresh cell culture medium containing 2.5 μM FSP1 inhibitors. After incubation for the indicated times, cells were washed with PBS. Fixation and staining were performed as follows: fixation with 4% paraformaldehyde for 5-10 min; permeabilization and blocking for 15 min with 0.3% Triton X-100 and 10 mg/mL BSA in PBS; staining at 4°C overnight with the primary antibodies. Antibody dilutions were as follows: 1:10 for anti-YPYDVPDYA-tag (HA; Clone 3F10), and 1:100 for anti-calnexin (Abcam, ab22595), anti-GM130 (Clone: EP892Y, Abcam, ab52649), anti-EEA1 (Clone: C45B10, Cell Signaling Technology, 3288S), and anti-LAMP1 (Clone: H4A3, Santa Cruz, sc20011) in primary antibody dilution buffer, and undulation for anti-AIFM2 (FSP1; Clone: 14D7, homemade). The cells were further incubated with the appropriate fluorophore-conjugated secondary antibodies (1:500) and DAPI (1:10,000) in TBS-T or PBS for 1-2 hours at room temperature in the dark. Finally, all samples were mounted with Aqua/poly Mount (Polysciences, 18606-20) and stored at 4°C overnight. Mitochondria, lipid droplets and aggresomes were stained with MitoTracker Red CMXRos (20 nM, Invitrogen, M7512), LipidSpot 610 (1:1000, Biotium, 70069-T), and Proteostat detection kit (1:10,000, Enzo, ENZ-51035-0025), respectively, according to the manufacturers' protocols.

Fluorescence recovery after photobleaching assay (FRAP)

Pfa1 cells (2×10^4 cells) were seeded on μ -Slide VI 0.4 (Ibidi, 80606) one day prior to the experiments. On the next day, the medium was changed to DMEM-high glucose supplemented with 10% FBS, 2 mM L-glutamine, 1% penicillin/streptomycin, 2.5 μ M icFSP1 and 10 mM HEPES. After incubation with icFSP1 for 2 - 4 hours, 2-5 rectangular areas containing several FSP1 condensates were chosen as bleaching areas. Then, one image before bleaching was considered as time "0". Subsequently, selected areas were photobleached by the maximum intensity of the laser and the fluorescent signals were measured at minimum intervals (~5 sec) with a LSM880 microscope (ZEISS).

For quantification of the FRAP rate, the region of interest (ROI) of each condensate (i) in the photobleached area and one condensate (c) in a non-photobleached area was determined by ImageJ/Fiji, then the mean value of fluorescent signals of condensate i at time t, $f_i(t)$ was analyzed. After retrieving each time of fluorescence value, $f_i(t)$ was normalized by the value of $f_i(0)$ to obtain relative fluorescence ($Rf_i(t)$) of each bleached condensates. To reflect the quenching effects during acquisition processes, each $Rf_i(t)$ was standardized by the corresponding time of relative value of non-bleached condensates ($f_c(t)/f_c(0)$) as follows: $Fi(t) = Rf_i(t) / Rf_c(t) = [f_i(t) / f_i(0)] / [f_c(t) / f_c(0)]$. Finally, the FRAP rate [%] at time t in the particles was evaluated as the mean of $Fi(t) \times 100$ as described⁶³.

Live cell imaging

For co-staining or washout analyses, Pfa1 cells ($1.5 - 3 \times 10^4$ cells) were seeded on μ -Dish 35 mm low (Ibidi, 80136), and incubated overnight. On the next day, the medium was replaced to FluoroBrite DMEM (Gibco, A1896701) supplemented with 10% FBS, 2 mM L-glutamine, and 1% penicillin/streptomycin. Live cell imaging was carried out using 3D Cell Explorer (Nanolive) equipped with Eve v1.8.2 software with the corresponding appropriate filter sets. During imaging, the cells were maintained at 37°C and 5% CO₂ atmosphere in a temperature-controlled incubation chamber. For co-staining analysis, cells were pre-treated with 5 μ M Liperfluo (Dojindo, L248-10) for 1 h, then changed to the FluoroBrite DMEM medium containing 0.2 μ g/mL propidium iodide (PI, Sigma, P4170) and started acquisition using Nanolive. After recording one image, a 100-fold concentration of icFSP1 was dropped to the dishes (final concentration was 10 μ M), while continuing recording images. Images were taken every 10 mins for more than 4 hours with GFP, BFP and RFP filter sets for acquiring fluorescent signals.

For washout experiments, after recording a few images, a 100-fold concentration of icFSP1 in FluoroBrite DMEM was dropped to dishes (final concentration was 2.5 μ M) and the recording of images continued for 4 h. The dishes were then carefully washed once with fresh FluoroBrite DMEM, and the medium was replaced with fresh one without icFSP1. Thereafter, image acquisition was resumed immediately. The images were recorded with 5 mins intervals for one more hour, i.e. the total duration was around 5 h.

For determining the number of condensates in cells, Pfa1 cells (approx. 2×10^4 cells) were seeded on μ -Slide 8 well (Ibidi, 80826) and incubated overnight. On the next day, the medium was changed to the normal medium containing 2.5 μ M icFSP1 and Hoechst. Immediately thereafter, the focus was adjusted and the acquisition of Hoechst and EGFP were started with an Axio Observer Z1 imaging system with VisView v4.0 (Visitron Systems, ZWISS) with 20x air objective and a CCD camera (CoolSnap ES2, Photometrics) with the corresponding filter sets. During imaging, the cells were maintained at normal conditions described above with a temperature-controlled incubation chamber. The imaging software ImageJ/Fiji and CellProfiler (v4.1.3, Broad Institute) were used for the analysis of condensates per cells.

Subcutaneous tumor model

All mice were purchased from Charles River. For the syngeneic subcutaneous tumor experiments, *Gpx4* KO/Fsp1 KO B16F10 cells stably overexpressing hFSP1-HA (1×10^6 cells in 100 μ L PBS) were transplanted subcutaneously into the right flank of 7-week-old female C57BL6/J mice. After tumors reached a size of approximately 25-50 mm^3 , mice were randomized and assigned to two groups. Then, mice were treated with vehicle (45% PEG E 300 and 55% PBS) or icFSP1 (50 mg/kg, Intonation) by i.p. injections twice per day. For comparison of WT and Q319K mutant, *Gpx4*KO/Fsp1KO B16F10 cells stably expressing hFSP1-WT-HA or hFSP1-Q319K-HA (1×10^6 cells in 100 μ L PBS) were transplanted subcutaneously into the right flank of 7-week-old female C57BL6/J mice. After tumors reached a size of approximately 50-150 mm^3 , mice were randomized and treated with vehicle or icFSP1 (50 mg/kg, Intonation) by i.p. injections twice per day.

For the xenograft subcutaneous tumor experiments, *GPX4* KO A375 and *GPX4* KO H460 cells (5×10^6 cells in 100 μ L PBS) were transplanted subcutaneously into the right flank of 6 or 7-week-old female athymic nude mice. After tumors reached a size of approximately 25-100 mm^3 , mice were randomized and treated with vehicle or icFSP1 (50 mg/kg, Intonation) by i.p. injections twice per day for the first 4 days and afterward once daily.

Vehicle and icFSP1 were mixed in 45% PEG E 300 (Sigma, 91462-1KG) and 55% PBS (Gibco, 14190094). Tumors were measured with a caliper every day and tumor volume was calculated by the following formula: Tumor volume = length x width² x 0.52. When tumor sizes were either tumors became necrotic or larger than 1000 mm³ at measurement, tumors were considered to be human endpoints. When tumors became human endpoints, the experiment was stopped at that point and no further experiments were performed.

Tumor tissue staining

Tumor tissues were fixed with 4% paraformaldehyde dissolved in PBS overnight at 4°C. The fixed samples were transferred and soaked in 20% sucrose in PBS overnight at 4°C, followed by embedding in OCT mounting compound (Tissue Tek, Sakura) on dry ice and stored at -80°C. The cryosections were produced from the tumor samples in 5 µm thick sections using a Cryostat Microm HM 560 (Thermo Fisher Scientific) at -30°C. The sections were post-fixed in 1% paraformaldehyde in PBS for 10 min and subsequently in 67% ethanol and 33% acetic acid for 10 min. Sections were incubated with blocking solution (5% goat serum, 0.3% Triton X-100 in PBS) for 30 min, and probed with primary antibodies (anti-HA (clone: 3F10, 1:10, developed in-house), anti-4HNE (JaICA, HNEJ-2, 1:50), anti-AIFM2 (FSP1, clone:14D7, undiluted, developed in-house)) in blocking solution overnight at 4 °C. On the next day, sections were washed with PBS and incubated with appropriate fluorophore-conjugated secondary antibodies (goat anti-rat Alexa Fluor 488 IgG (H+L) (1:500, A-11006, Invitrogen), goat anti-mouse IgG H&L Alexa Fluor 647 (1:500, ab150115, Abcam), and donkey anti-rat IgG Alexa fluor 555 (1:500, ab150154, Abcam)) in secondary dilution buffer (1% BSA and 0.3% Triton X-100 in PBS) for 2 h at room temperature. DNA was stained by DAPI for 5 min, and slides were mounted in Aqua/poly Mount. Confocal images were obtained with an LSM880 microscope (ZEISS) and analyzed by ZEN Blue and ImageJ/Fiji software.

Pharmacokinetics (PK) and metabolic stability and analysis

PK and microsomal stability studies were performed by Bienta/Enamine Ltd., Kiev, Ukraine.

Mutational screens

Randomly mutated *FSP1* cDNAs (NM_001198696.2, C>T:1008) with the adapter sequence (Kozak and HA-tag) for p442 were amplified from the expression vector, p442-hFSP1-IRES-Blast, using error-prone PCR, GeneMorph II Random Mutagenesis Kits (Agilent 200550). The optimal mutagenesis rate (3-5 DNA mutations/gene) was achieved by the following condition: [1] 95°C for 120 sec, [2] 95 °C 30 sec, [3] 60°C 30 sec, [4] 72 °C for 75 sec, [5] 72°C 10 min and the cycle from 2 to 4 was repeated for 25 times. After the isolation of PCR products by agarose electrophoresis and clean-up with Wizard SV Gel&PCR Clean-up System, FSP1 fragments were ligated in *Bam*H/*Xho*I digested p442-IRES-blast vectors with seamless cloning enzyme (Takara, 639649) under the following condition: 0.4 µg DNA insert, 0.2 µg vector and 8 µL enzyme in 40 µL reaction at 50 °C for 15 min. Then, the mixture of insert-vector was transformed into *E.coli* competent cells, and cells were pre-incubated at 37°C for 1 hour. Then, cells were applied to 8 plates (Thermo Fisher, 240835) and cultured under an ampicillin selection medium at 30 °C overnight. On the next day, colonies were harvested and DNA was isolated using QIAGEN Plasmid Maxi Kit (Qiagen, 12163) according to the manufacture's protocol.

As described above, a third-generation lentiviral packaging system consisting of *FSP1* mutant library plasmids, envelope (pEcoEnv-IRES-puro) and packaging (pMDLg_pRRE and pRSV_Rev) plasmids were co-transfected into HEK 293T cells using transfection reagents (X-tremeGENE HP agent). Cell culture supernatants including viral particles were collected 2 days after post-transfection and passed through a 0.45 µm PVDF filter, and then stored at -80°C until usage.

Pfa1 cells were seeded into 10 x T-175 flasks (1.0×10^6 cells per flask, 2.0×10^7 cells in total) with medium containing 10 µg/ml protamine and lentivirus of pooled FSP1 mutants and transduced with extremely low infection efficiency (MOI = approx. 0.1, calculated as described⁹²). On the next day, the selection was started using blasticidin (12.5 µg/mL) and puromycin (1 µg/mL). After selection for 3 days, 10 million cells were collected as a control group and 20 million cells were seeded into 5 flasks (2.0×10^6 cells per flask, 2.0×10^7 cells in total) with 500 nM of RSL3. After induction of ferroptosis by RSL3 for 2 days, 10 million cells were collected as the RSL3-treated group. Then, 10 million cells per condition were co-treated with individual FSP1 inhibitors (5 µM for the first 5 days and 10 µM thereafter) and with 500 nM RSL3 and 1 µM 4-OH TAM so that Pfa1 cells should become fully resistant to FSP1 inhibitors with cells expressing mutant but functional FSP1. Then, surviving Pfa1 *Gpx4* KO cells overexpressing FSP1 mutants resistant to individual FSP1 inhibitors were expanded and at least 10 million cells per condition were collected and stored at -80°C.

After collecting cells from all conditions, cells were lysed in lysis buffer (50 mM Tris, 50 mM EDTA, 1 % SDS, pH8) and proteins were digested by proteinase K (100 µg/mL) at 55 °C overnight. On the next day, RNase A (50 µg/mL) was mixed and incubated for 30 min at 37 °C to digest RNA. Then, DNA mixtures were mixed with the equivalent volume of phenol/chloroform/isoamyl alcohol (25:24:1) (Roth, A156.2) and centrifugated for 10 min at 16,000 x g to separate DNA from RNA and proteins. The top phase of DNA containing fraction was carefully transferred to the new tubes and DNA was precipitated after the addition of the 2 x volumes of 75 mM NaCl in ethanol and the following centrifugation for 10 min at 16,000 x g. The pellet was then washed with 70 % ethanol and centrifuged again. After drying the remaining ethanol, the pellet was resolved in 200 µL TE buffer and incubated at 65 °C for 1 h to dissolve the DNA completely. Finally, the DNA of the *FSP1* region (approx. 1.5 kbp) was amplified by DNA polymerase (KOD one) and purified as described above.

The NGS library preparation was conducted using ThruPLEX DNA-Seq HV PLUS kit (Takara, R400782) with minor optimization. After library preparation, DNA was purified with NucleoMag NGS Clean-up and Size Select (Th. Geyer, 11833159) for subsequent Next Generation Sequencing (NGS). NGS was carried out at the core facility of Helmholtz Munich.

NGS data analysis of human FSP1 cDNA

Paired-end sequencing was carried out by an Illumina NovaSeq 6000 instrument using ThruPLEX DNA-Seq HV PLUS kit from different conditions. The program FastQC (v0.11.7) (<http://www.bioinformatics.babraham.ac.uk/projects/fastqc>) was applied to the resulting FASTQ files to search for sequences that were overrepresented (Illumina adapter) in order to remove them from further analysis. We used Trimmomatic V.0.39 tool⁹³ with the following options (ILLUMINACLIP:TruSeq2-PE_extended.fa:2:30:10 LEADING:3 TRAILING:3 SLIDINGWINDOW:4:15 MINLEN:36) to trim for paired-end data. Trimmed paired-end reads (originally length 151 bp) were aligned to the reference human *FSP1* cDNA sequence of 1210 bp with the Burrows-Wheeler Alignment Tool (BWA), v0.7.17-r1188⁹⁴. Firstly, an index was produced for the reference sequence with the command "bwa index". Then, by applying the subcommand "mem", BWA shows the final alignment as the SAM (Sequence Alignment/Map) format. Aligned reads were converted to the BAM (Binary Alignment Map) format and sorted by leftmost chromosomal coordinates with the program SAMtools, v1.2⁹⁵ with the command "samtools view" and "samtools sort", respectively. From sorted BAM files, the coverage information per base for the *FSP1* reference sequence was extracted by applying IGVtools of the Integrative Genomics Viewer (IGV), v2.11.9⁹⁶. The command

"igvtools count" with the options (-w 1 and --bases) was used to generate an output file in the WIG (wiggle) format for each sorted BAM file. The mutation frequency at each position (Xi) of the *FSP1* reference sequence was evaluated from the sum of mutated nucleotides at the corresponding position of the reference sequence in the alignment divided by the sum of all nucleotides (A,C,G,T,N) at this location. The count information per base assigned in the wiggle files served as input for a custom-written R script for the calculation of the mutation frequency. The tab-delimited output file of the R script contains the number of each nucleotide, deletions, and insertions as well as the sum of all nucleotides and the mutation frequency from the alignment (columns) at each position of the FSP1 sequence (rows).

$$\text{Mutation frequency (Xi)} = N_{\text{mut}}(\text{Xi}) / N_{\text{all}}(\text{Xi})$$

(N_{mut} : sum of mutated nucleotides at Xi, N_{all} : sum of all nucleotides at Xi)

The Z-score was calculated using mean (μ) and standard deviation (σ) as follows:

$$Z = [X_i - \mu_{\text{RSL3 or iFSP1s}}] / \sigma_{\text{RSL3 or iFSP1s}}$$

$$\mu_{\text{RSL3}} = \text{Mean (Mutation frequency}_{\text{RSL3}} / \text{Mutation frequency}_{\text{ctrl}})$$

$$\mu_{\text{iFSP1s}} = \text{Mean (Mutation frequency}_{\text{iFSP1s}} / \text{Mutation frequency}_{\text{RSL3}})$$

$$\sigma_{\text{RSL3}} = \text{Standard Deviation (Mutation frequency}_{\text{RSL3}} / \text{Mutation frequency}_{\text{ctrl}})$$

$$\sigma_{\text{iFSP1s}} = \text{Standard Deviation (Mutation frequency}_{\text{iFSP1s}} / \text{Mutation frequency}_{\text{RSL3}})$$

(iFSP1s: iFSP1 or viFSP1; Xi is position of FSP1; ctrl: control)

Then, amino acid mutations were considered for possible DNA alternation considering the codon table.

***In silico* modeling and structural analysis**

Predictive human or mouse FSP1 structures were mined from AlphaFold2 database (<https://alphafold.ebi.ac.uk>)⁹⁷. The structure of the FSP1 orthologue, type II NADH:quinone oxidoreductase or alternative NADH dehydrogenase, NDH-2 (PDB: 4G73⁹⁸ or 5NA1⁹⁹), was aligned to FSP1 using Pymol v2.5.2 (Schrödinger), and the position of flavin adenine dinucleotide (FAD), NADH and ubiquinone were superimposed onto the FSP1 structure⁵³ or another NDH-2 (PDB: 4NWZ¹⁰⁰). The *in silico* modeling for FSP1 inhibitors (iFSP1, viFSP1, Brequinar) was performed by

modeling software seeSAR v12.1 (BioSolveIT). For docking simulation, the number of poses for each molecule was set to 500, and clash tolerance was set high enough to obtain comparably tolerant poses. The subsequent HYDE scoring function within SeeSAR was used for optimizing the docking poses. Favorable torsion quality and docking poses with unfavorable intra- and intermolecular clashes were removed to obtain the candidate docking poses. The structures were visualized by Pymol.

Protein alignment of FSP1 orthologues

Human FSP1 sequence and its orthologues were retrieved from UniProt (<https://www.uniprot.org>), NCBI (<https://www.ncbi.nlm.nih.gov/gene/>), and PDB (<https://www.rcsb.org>), aligned and highly conserved residues were colored with JalView (v2.11.2.6)¹⁰¹.

Genome DNA extraction and sequencing

Genomic DNA extraction was performed with DNAzol (Fisher Scientific, 15413379) according to the manufacturer's protocol from SKOV3 cells. DNA sequence was read by Eurofins genomics.

qPCR analysis

Total mRNA was extracted from the cells with an RNeasy Mini kit (Qiagen, 74104) and followed by genomic DNA digestion using DNase (Qiagen, 79254). Then, cDNA was synthesized by the QuantiTect Reverse Transcription Kit (Qiagen, 5001473). Human testis mRNA (Takara-bio, 636533) as control was reverse-transcribed. Quantitative RT-PCR (qPCR) was carried out by PowerUp SYBR Green Master Mix (Thermo Fisher Scientific, A25778) using qTOWER³ G (Analytikjena). All samples were performed with technical triplicates with the following PCR condition: [1] 50 °C for 2 min; [2] 95 °C for 2 min; [3] 95 °C for 15 sec; [4] 59.5 °C for 15 sec; [5] 72°C for 1 min; [6] 95°C 1 sec - cycle from 3 to 5 was repeated 40 times. Sequences of the primers were the following: 5'-TGCTCTGTGGGGCTCTG -3' and 5'- ATGCCTTGGCGGAAAACCTC -3' for detecting the short and mitochondrial matrix forms of *GPX4*; and 5'- ATTGGTCGGCTGGACGAG -3' and 5'-ATGCCTTGGCGGAAAACCTC -3' for specific detection of the mitochondrial matrix form of *GPX4*. The expression ratio of (the mitochondrial matrix form)/(the short and mitochondrial matrix forms) of *GPX4* was evaluated by the Δ Ct method.

Expression and purification of recombinant hDHODH

The codon-optimized DNA sequence of human *DHODH* (29-395, NP_001352.2) was synthesized by IDT (Integrated DNA Technologies) and cloned in a petM11 vector containing an N-terminal 6xHis (histidine) tag. Expression and subsequent purification were performed as previously reported¹⁶. In brief, BL21 cells were transformed with the vector and cultured in Terrific Broth (TB) medium at 37°C. When the Optical Density (OD) of cells reached 2.0, DHODH expression was induced by Isopropyl-β-D-thiogalactopyranosid (IPTG: 0.5 mM) addition at 20°C overnight. After collection and resuspension of the cells in lysis buffer (PBS with 10 mM imidazol), cells were lysed with a sonicator. After centrifugation, the supernatant fraction was passed through a prepacked nickel column and washed with the lysis buffer extensively. DHODH protein was eluted with 350 mM imidazole in PBS and concentrated, then finally purified on a size exclusion chromatography column pre-equilibrated with PBS. Protein was snap-frozen in liquid nitrogen and stored at -80°C until further usage.

DHODH enzyme inhibitor assay

Enzymatic activity of DHODH was measured as previously described¹⁷. The enzymatic reaction was performed at 32°C in a buffer at pH 8.0 containing 0.1% Triton X-100, 50 mM Tris, 150 mM NaCl, 25 nM recombinant human DHODH enzyme, 100 μM coenzyme Q₀, 500 μM L-dihydroorotic acid, and 120 μM 2,6-dichloroindophenol (DCIP) with several inhibitors. DHODH activity was kinetically monitored as a function of decreasing the absorbance of DCIP at 600 nm.

Cell proliferation assays

Cells (HT-1080 and Pfa1) were seeded on 96-well plates (200 cells/well) and treated with 0 μM or 50-100 μM uridine for 5 days. Relative cell numbers were measured using AquaBluer.

Statistical analysis

All data shown represents the mean ± SEM or mean ± SD, and the number (n) in each figure legend are shown as biological or technical replicates. All experiments (except for some experiments described in legends) were independently performed at least twice. Mouse experiments were performed once or twice, and the number of animals was shown in each figure

legend. Two-tailed Student's t-test, one-way or two-way ANOVA followed by Bonferroni's, Dunnett's, Sidak's or Tukey's multiple comparison tests were used for statistical analysis with GraphPad Prism 9. p values are also shown in figure legends and p values < 0.05 were considered statistically significant.

5. Discussion

5.1 Ferroptosis and phase separation

To identify and characterize *in vivo* active FSP1 inhibitors, Doll *et al.* previously performed a small molecule compound library screen²⁶. These efforts led to the identification of iFSP1 as the first FSP1 inhibitor; however, iFSP1 is not suitable for *in vivo* use because of its low metabolic stability and poor pharmacokinetic properties *in vivo*. Thus, after a careful re-assessment of this earlier screen, I now report on a yet-unrecognized class of *in vivo* efficacious hFSP1 inhibitors (i.e., 3-phenylquinazolinones, alias icFSP1) as new anti-cancer drugs. icFSP1 displays a unique MoA by promoting ferroptosis via the dissociation of FSP1 from cellular membranes and by driving FSP1 condensate formation through phase separation. The biomolecule condensates formed via (liquid-liquid) phase separation have recently emerged as a fundamental phenomenon underlying the mechanism of the spatiotemporal coordination of a myriad of biological activities in cells. For instance, phase separation plays an essential role in signal transduction (e.g., mitogen-activated protein kinase (MAPK) pathways^{62, 63, 102}), autophagy or proteasome-mediated proteolysis^{64, 65}, cyclic GMP–AMP synthase (cGAS)–stimulator of interferon genes (STING) pathway in anti-viral response¹⁰³ and transcriptional processes^{78, 104, 105}. Moreover, aberrant phase separation is associated with several human diseases, such as neurodegenerative diseases⁸⁰ (e.g., fused in sarcoma (FUS), TAR DNA-binding protein 43 (TDP-43), alpha-synuclein (a-syn) and microtubule-associated protein (Tau)), and some rare genetic diseases including high mobility group protein B1 (HMGB1)¹⁰⁶. Most of the proteins undergo phase separation via multivalent interactions with themselves or by interacting with other binding partners, such as DNA and RNA, via so-called structurally disordered domains. Intrinsic disorder domains (IDR) or low complexity domains (LCD) are indispensable for protein condensation, and their interaction is mediated by amino acids with charge, charge- π , π - π , dipolar and hydrogen bonds.

Regarding FSP1, this thesis now shows that several molecular features in hFSP1, such as N-terminal myristoylation, distinct amino acid residues (S187, L217, Q319), IDRs and LCD of hFSP1, are required for icFSP1-mediated phase separation, thereby inducing lipid peroxidation and ferroptosis in synergism with cognate ferroptosis inducing agents. Although an experimentally determined 3-D structure of hFSP1 and its binding state of icFSP1 to hFSP1 are absent, Alphafold2^{107, 108} enabled me to predict the structure of hFSP1. This prediction showed that the globular fold prediction has high confidence in IDR1, which is indeed annotated as an uncertain region and that S187, L217 and Q319 are all located on the surface of hFSP1. Moreover, icFSP1 initiates condensate formation of hFSP1, including the plasma membrane-localized mutant lyn11-hFSP1. Since I further found that

icFSP1 itself cannot induce condensate formation of myristoylated FSP1 *in vitro*, icFSP1 may initiate condensates via coordinating FSP1-membrane interactions, thereby buffering membrane binding affinity of hFSP1, similar to the KRAS inhibitor Cmpd2¹⁰⁹ and other modulators (e.g., Ca²⁺ for recoverin¹¹⁰) for myristoyl-ligand switches. By this mechanism, hydrophobic myristoylation tails may gather with each other to trigger FSP1 condensates. In support of this hypothesis, a predicted 3-D structural model of hFSP1^{107, 108} shows that Q319 is particularly close to the expected membrane-binding surface. Of note, myristoylation is found to be essential for initiating this process. Analysis of cells expressing myristoylated and non-myristoylated FSP1 with two differently labeled tags in the same cells revealed that while icFSP1 triggered phase separation of myristoylated FSP1, non-myristoylated FSP1 (G2A) failed to form condensates even when FSP1 condensates of the wildtype enzyme were present. Hence, this data strongly suggests that myristoylation (i.e., proper membrane localization) itself is an essential prerequisite for inducing condensation. As discussed above, charged and polar residues can affect protein-protein interactions during phase separation¹¹¹, thus changing S187 to C187, L217 to R217, and Q319 to K319, respectively, will enhance positive surface charge or reduce polarity, impairing phase separation of FSP1 in cells.

The concept that ligands modulate the driving forces for phase separation is considered as polyphasic linkage^{112, 113}. This concept is explained by the preferential interaction of proteins with small molecules via multiple spacer/sticker regions. Based on this, icFSP1 would conceptually modulate the phase separation of hFSP1 through interactions involving some residues (S187, L217, and Q319), IDR/LCRs, and myristoylation. Furthermore, the phase boundary would be altered by site-directed mutagenesis. Besides, the interaction between myristoylation and its potential function as a sticker in concert with icFSP1 as a ligand might be indispensable for the phase separation of FSP1 in cells. However, to describe in more detail the mechanism of icFSP1-FSP1 interactions, an experimental 3D structure with proper membrane-binding environments, such as liposomes, bi-cells, or nanodiscs, would be required for future in-depth studies.

FSP1 is reported as the first example of inducing ferroptosis via phase separation; however, other ferroptosis-related proteins might also be related to phase separation-induced ferroptosis. Cellular iron content is one of the most critical factors in ferroptosis, and its availability relies on iron uptake via transferrin/CD44-mediated endocytosis or ferritin degradation via ferritinophagy¹¹⁴. In particular, ferritinophagy requires nuclear receptor coactivator 4 (NCOA4) to recruit ferritin (FTH) to autophagosome and increase iron concentrations in cells. Recently, it has been reported that ferritin-NCOA4 forms liquid condensates through IDRs in NCOA4, and the formation of the condensate is responsible for FTH degradation¹¹⁵. Therefore, given that NCOA4 depletion can

suppress ferroptosis via decreased labile iron pool in cells^{116, 117}, manipulating FTH-NCOA4-mediated phase separation might induce ferroptosis.

Phase separation of FSP1 can be initiated upon icFSP1 treatment; however, generally, there are many alternative ways to trigger protein phase separation under specific conditions, such as thermal stress (heat or cold)⁸³, oxidative stress, osmotic stress^{62, 63} and light activation¹¹⁸. Among them, one proteomic approach showed that FSP1 (AIFM2) is enriched in heat shock-induced stress granules⁸³. As discussed in the introduction sections, thermal stress is one of the triggers for ferroptosis¹⁻³. Besides, osmotic stress enhances ferroptosis^{119, 120}, and NRF2 regulates FSP1 expression⁴⁵; thus, phase separation of FSP1 may play some roles in the induction of ferroptosis under these stressed conditions. In addition, future studies should investigate whether other stimuli including ischemia/reperfusion would trigger phase separation of FSP1 or other ferroptosis-related proteins.

Small molecules inside biomolecular condensates have been demonstrated to dictate the property of condensates (e.g., liquidity and solidity). For instance, a recent study suggests that sodium ion (Na⁺) is required for the liquidity of several protein condensates⁶². Interestingly, it was recently suggested that the uptake of cations (Na⁺ and Ca²⁺) enhances ferroptosis. Oxidation of lipids increases the membrane tension and an increased cation influx via piezo-type mechanosensitive ion channel component 1 (Piezo1) and transient receptor potential (TRP) channels have been reported to be involved in ferroptosis execution¹¹⁹. Moreover, I previously showed that cold stress also increases Ca²⁺ uptake via transient receptor potential member 8 (TRPM8) and calcium chelation completely suppresses cold-induced ferroptosis³. Thus, cations (Na⁺/Ca²⁺) may play some roles in the phase separation of FSP1. As another potential binding partner, it has been demonstrated that FSP1 can bind to DNA *in vitro* and can change its localization to the nucleus upon some stimuli^{121, 122}. Strikingly, icFSP1 also induces FSP1 condensations in the nucleus under specific conditions (unpublished data). DNA is also a well-known molecule to be involved in phase separation⁷³; therefore, the relationship between phase-separated FSP1 and other binding partners should be investigated in the future.

5.2 Mutagenesis and precision medication

By taking advantage of a number of targeted and untargeted chemical and genetic screens, I uncovered new insights into the contribution of the NAD(P)H/FAD binding motif and the proton transfer function to FSP1 enzyme activity. Among them, several point mutations of FSP1, identified in cancer patients as somatic mutations (G244D, E160D/stop, K355R, and D285N), were shown to

be dysfunctional. Thus, cancer cells harboring these somatic mutations (heterozygous mutations) are expected to be more sensitive to ferroptosis and might be a good target for ferroptosis-based therapies. Besides, Depmap analysis (<https://depmap.org/portal/>, v23Q2) revealed that endometrial/uterine cancer cells (RL952 cells) and ovarian cancer cells (SKOV3 cells) harbor S6L and G337D mutations in FSP1, respectively. Considering that S6 is part of the myristoylation consensus motif (MGXXXS)⁴⁰, and that G337D fails to protect against ferroptosis, these cancer cell lines might be more susceptible to ferroptosis.

Here, I further identified the MoA of the first human-specific FSP1 inhibitor (iFSP1)²⁶. By using a combination of an *in silico* simulation⁵³ and several site-directed mutagenesis approaches, I found that iFSP1 targets the quinone-binding site. This was also very recently confirmed in an independent study using a similar approach¹²³. Besides, I reported the 2nd generation human-specific FSP1 inhibitor (icFSP1) and uncovered the molecular mechanism of icFSP1. However, unfortunately, both iFSP1 and icFSP1 are specific for the human enzyme. Therefore, I further introduce here viFSP1 as the first species-independent FSP1 inhibitor which targets the NADH binding pocket surrounding residues A153, F328, M294 and T327 of FSP1. This new and useful tool will be most suitable to functionally explore FSP1 orthologues across many different species. Extensive mutagenesis approaches *in cells/vitro* and a bioinformatic analysis on cancer patients indicate that certain cancer patients, such as those with T327M mutations in FSP1¹²⁴, might be resistant to these FSP1 inhibitors. Thus, in the near future (once the first FSP1 inhibitors will be approved for clinical use), this set of data derived from the mutagenesis studies presented herein might be extremely valuable for personalized treatment approaches when applying FSP1 inhibitors.

By exploiting random mutagenesis screens using error-prone PCR, I succeeded in identifying the binding pocket of FSP1 inhibitors. In theory, the screening strategy described herein can be applied to other small molecules or other antibody binding sites when searching for the binding mechanism of the respective target protein¹²⁵. Prediction tools, such as AlphaFold2 and other docking simulations, might allow us to identify the binding sites/pockets of pharmacological inhibitors and antibodies with high accuracy and reliability without any experimental 3-D structure. As a showcase, I applied these genetics and bioinformatics approaches to FSP1 and uncovered many mutations, which dictate the sensitivity of (cancer) cells to ferroptosis. This kind of integrated *in silico* and *in cells* approaches may set the groundwork for pharmacological studies in other forms of therapies, as well as for individual patients in clinical settings to predict therapy success in the near future.

5.3 FSP1 inhibitors and applications

Although inhibition of FSP1 alone is generally not sufficient to trigger cancer cell death via ferroptosis^{26, 42}, a subset of cancer cell lines can be potentially sensitive to FSP1 inhibition alone under certain conditions, such as fibrosarcoma cells lines (HT-1080 cells) and some lymphoma cell lines (SUDHL6 and DOHH2 cells). In this respect, database analysis (<https://depmap.org/portal/v23Q2>) might be useful to predict the sensitivity of FSP1 inhibition to these cancers.

Given earlier studies using tamoxifen-inducible whole-body *Gpx4* KO mice (excluding brain) that cause acute kidney failure¹³, targeting GPX4 in the tumor context might be limited by inducing severe off-target effects. In contrast, FSP1 is regarded as a more attractive target for tumor treatment because (i) *Fsp1* knockout mice are fully viable^{28, 126}; (ii) FSP1 inhibitors (viFSP1 and icFSP1) treatment does not show any off-target activity in cells; and (iii) icFSP1 does not affect body weight even under high concentrations *in vivo*. Taking into account that low cell densities render cells much more vulnerable to ferroptosis^{127, 128}, non-solid tumors, such as lymphoma or myeloid tumors, might profit best from targeting FSP1 alone as shown using SUDHL6 cells. Another potential target could be dedifferentiated cancer cells that have undergone epithelial-mesenchymal transition (EMT). In fact, the ferroptosis vulnerability was shown to be highly correlated with the activity of EMT-activating transcription factor Zeb1 or mesenchymal states¹²⁹. To target solid tumors, it likely requires synergistic approaches co-targeting the cyst(e)ine/GSH/GPX4 axis. In particular, GPX4 inhibitors are the strongest inducers for ferroptosis; however, it should be ideally delivered in a cancer cell in a cell type- and site-specific manner at carefully controlled concentrations since most types of neurons, certain immune cells, hepatocytes, and endothelial cells show a strong dependence on GPX4¹³⁰. Besides, considering that some cancer cells are resistant to GPX4 inhibition-induced ferroptosis²⁶, and that FSP1 inhibitors sensitize most cancer cells to ferroptosis induced by sublethal GPX4 inhibition, the combination therapy of FSP1 inhibitors with cognate ferroptosis inducers, given ideally in a tumor-specific manner, could be a highly promising anticancer therapy.

Except for cancer treatment, FSP1 inhibitors may also be considered as a rodenticide in warfarin-poisoning resistant rodents¹³¹. For instance, there are many warfarin-poisoning resistant rats harboring mutations in VKORC1 in Japan¹³². Given that FSP1 is a vitamin K reductase and *Fsp1* KO mice show high lethality when exposed to warfarin^{28, 57}, co-treatment of FSP1 inhibitors with warfarin may be a suitable combination for controlling resistant rodents in cities. A better understanding of the specificity of FSP1 inhibitors (iFSP1 and icFSP1, which only inhibit the human enzyme, while viFSP1 inhibits human and mouse/rat) is still required to design FSP1 inhibitors

targeting distinct species, such as rats; however, this application may have another important implication beyond cancer treatment.

5.4 FSP1 inhibitors vs quinone reductase inhibitors

As shown in this study, FSP1 inhibitors might serve as valid drugs for anti-cancer therapies. However, as we reported very recently several DHODH inhibitors including brequinar (BQR) may also render cancer cells highly vulnerable to ferroptosis via FSP1 inhibition and not its canonical target, DHODH, at high concentrations. These findings reinforce the notion that appropriate concentrations and the MoA should be taken into account in related studies in order to avoid potential off-target effects. Nonetheless, this study also implies that alternative quinone reductase inhibitors could in principle be applied as FSP1 inhibitors as the substrate specificity of FSP1 emerges to be broad. As indicated in previous studies, FSP1 can bind ubiquinone, vitamin K, and resazurin²⁶⁻²⁸ and can be inhibited by many inhibitors with varying chemical structures (NPD4928, FSEs and HQNO)^{57, 133, 134} besides iFSP1, viFSP1 and icFSP1. In the clinical setting, a number of DHODH inhibitors have been or are currently being developed against certain types of tumors¹³⁵. In addition, DHODH inhibitors and/or other potential quinone reductase inhibitors may also target FSP1, thus, such chemical structural information should be exploited to develop/design new powerful FSP1 inhibitors.

6. Publications and summary

6.1. Phase separation of FSP1 promotes ferroptosis. *Nature*, 2023

The first FSP1-specific inhibitor, called iFSP1, had already been reported by Doll *et al.*²⁶. However, it is known that iFSP1 is not suitable for *in vivo* application and exhibits off-target effects at high concentrations. Thus, *in vivo* efficacious ferroptosis inducers targeting FSP1 are highly demanded. In this paper, I discovered a new class of compounds, i.e. 3-phenylquinazolinones (alias icFSP1), as potent FSP1 inhibitors. Unlike iFSP1, icFSP1 does not inhibit FSP1 enzyme directly, but icFSP1 triggers subcellular localization changes, that is, dissociation from the membrane to induce condensation of FSP1 in a process, generally known as phase separation. Furthermore, icFSP1-induced FSP1 condensations require distinct structural components, such as intrinsic disorder regions, low complexity regions, distinct amino acids (i.e., S187, L217, and Q319), and N-terminal myristoylation, as demonstrated by using recombinant FSP1 proteins as well as different cell lines overexpressing FSP1 mutants. I further demonstrate that icFSP1 impairs tumor growth and induces FSP1 condensates in tumors. Hence, this study suggests that icFSP1 displays a unique mechanism-of-action (MoA) and provides the rationale for targeting FSP1-dependent phase separation as an efficient anti-cancer therapy. Moreover, this study may present a showcase for the development of novel therapeutic strategies to treat diseases including cancer where ferroptosis/phase separation has been implicated. Besides, this study establishes for the first time a link between ferroptosis and phase separation, which should incite future investigations on the role of phase separation in the basic principles of biology.

Almost all experiments herein were performed and conceptualized by me except for the following experiments:

Clara Hipp performed mass spec analysis for myristoylation of FSP1 and some phase separation imaging (Extended Data Fig. 6d & 6e). Dr. André Santos Dias Mourão produced recombinant FSP1 enzyme from *E. coli*. Jan Borggräfe performed NMR analysis (Extended Data Fig. 7f). Dr. Maceler Aldrovandi and Bernhard Henkelmann performed oxi-lipidomics (Fig.1g). Jonas Wanninger performed a compound screen as described before²⁶. Dr. Eikan Mishima generated HT-1080 pCW-Cas9 and MDA-MB-436, 786-O FSP1 KO cells as used in Extended Data Fig. 1f, 1g, 1k and 1l. Elena Lytton supported me in isolating clones for mini-prep/DNA isolation used in Extended Data Fig. 7d. David Emler helped to validate the FSP1 antibody for Western blotting. Besides me, Drs. Bettina Proneth, Prof. Michael Sattler and Marcus Conrad conceived the study and wrote the manuscript.

6.2. Integrated chemical and genetic screens unveil FSP1 mechanisms of ferroptosis regulation. *Nat. Struct. Mol. Biol.*, 2023.

In this paper, I studied a large number of FSP1 mutations present in certain types of cancer or that were identified by random mutagenesis screens in this work. This extensive mutational analysis unveiled the FAD/NAD(P)H binding site and proton transfer function of FSP1, which emerge to be evolutionarily conserved among different NADH quinone reductases. Furthermore, I introduce a new class of compounds (alias viFSP1) as potent species-independent FSP1 inhibitors. Unlike iFSP1 or icFSP1, which are human-specific FSP1 inhibitors, I further show that viFSP1 directly inhibits FSP1 enzyme activity in human, mouse and other species, such as rat and chicken. Moreover, I established several random mutational screens to identify the binding pocket of iFSP1 and viFSP1. Subsequent validation revealed that iFSP1 targets the putative quinone-binding pocket, whereas viFSP1 targets the putative NADH-binding pocket of FSP1. In summary, this study provides novel insights into the molecular function of FSP1 and its regulation in ferroptosis, knowledge to be used in the rational design of FSP1 inhibitors targeting cancer cells.

All experiments herein were performed and conceptualized by me except for the following experiments:

Dr. Eikan Mishima performed *in vitro* enzymatic assays in Fig. 3f, 4e-f, 5c, and Extended Data Fig. 4d and 7b. Dr. Naoya Yamada performed some cell viability assays in Fig. 3c, and Extended Data Fig. 6i-j. Dr. André Santos Dias Mourão produced recombinant human and mouse FSP1 enzymes and some mutants from *E. coli*. Jonas Wanninger performed the small molecule compound screen. Drs. Dietrich Trümbach and Sebastian Doll helped me to analyze the NGS data. Elena Lytton helped to isolate some clones for mini-prep/DNA isolation used in Fig. 2b. Dr. Peter Sennhenn helped me to conduct *in silico* docking simulation used in Fig. 3g and 5d. Thamara Nishida Xavier da Silva and Dr. Prof. José Pedro Friedmann Angeli provided Pfa1 cells overexpressing murine FSP1 for the compound screen used in Fig. 4a. Besides me, Drs. Bettina Proneth, Prof. Michael Sattler and Marcus Conrad helped me to conceive the study and to write the manuscript.

6.3. DHODH inhibitors sensitize to ferroptosis by FSP1 inhibition. *Nature* 2023.

Mao *et al.*¹⁷ previously reported mitochondrially localized dihydroorotate dehydrogenase (DHODH) as a new ferroptosis suppressor by reducing ubiquinone (CoQ₁₀) to ubiquinol in mitochondrial membranes in analogy to what was previously reported for FSP1 in regenerating extra-mitochondrial ubiquinone²⁶⁻²⁸. In the study by Mao *et al.*, the canonical DHODH inhibitor brequinar (BQR) was used to show synergistic effects with RSL3 (GPX4 inhibition)-induced ferroptosis. However, Mao *et al.* used 500 μ M BQR throughout their study, which is extremely high when compared to the reported inhibitory concentration (IC₅₀) of BQR required for DHODH inhibition (IC₅₀: 7 nM). Given that DHODH is a CoQ₁₀-reducing flavoprotein like FSP1, it was hypothesized that the synergistic killing effect of BQR with ferroptosis inducers might result from FSP1 inhibition instead of DHODH. To clarify BQR sensitizing effect on ferroptosis, cell-based and cell-free assays using BQR were carefully analyzed. Thereby, it could be concluded that while around 0.1 μ M was sufficient to inhibit DHODH in cells and *in vitro* enzyme assays, BQR concentrations higher than 70 - 100 μ M (500 μ M BQR was used in that study¹⁷), were sufficient to inhibit FSP1 as well. To further investigate whether other DHODH inhibitors besides BQR may also inhibit FSP1, multiple DHODH inhibitors were tested *in vitro* and in cells. Interestingly, DHODH inhibitors, such as vidofludimus and ASLAN003, were also found to inhibit FSP1. DHODH inhibitors were initially contemplated as anti-tumor agents owing to the role of DHODH in synthesizing orotate from dihydroorotate for the *de novo* pyrimidine biosynthesis, which is essential for cell proliferation. Therefore, DHODH has been considered an attractive target for cancer therapy, and indeed some of its inhibitors are currently under clinical trials. Considering that various DHODH inhibitors can also act as FSP1 inhibitors, the knowledge from these chemical structures might be helpful in designing new FSP1 inhibitors with appropriate *in vivo* stability.

Half of the experiments in this study were performed by me, and the following experiments were performed by others:

Dr. Eikan Mishima performed most of the remaining experiments in cells and *in vitro* enzymatic assays in Fig. 1b (left), 1c, 1e-f, 1h and Extended Data Fig. 1d-e, 2a-c, 2e-f, 3a, and 3d-f. Weijia Zhang performed Extended Data Fig. 2d and 3c. Dr. André Santos Dias Mourão produced recombinant human and mouse FSP1 and human DHODH enzymes from *E. coli*. Dr. Peter Sennhenn and I performed *in silico* docking simulation used in Fig. 1g and Extended Data Fig. 2i. Besides me and Weijia Zhang, Drs. Eikan Mishima, Jiashuo Zheng, and Marcus Conrad conceived the study and wrote the manuscript.

7. References

1. Distéfano, A.M. *et al.* Heat stress induces ferroptosis-like cell death in plants. *Journal of Cell Biology* **216**, 463-476 (2017).
2. Hattori, K. *et al.* Cold stress-induced ferroptosis involves the ASK1-p38 pathway. *EMBO reports* **18**, e201744228-e201744228 (2017).
3. Nakamura, T. *et al.* The mitochondrial Ca²⁺ uptake regulator, MICU1, is involved in cold stress-induced ferroptosis. *EMBO reports* **22**, e51532-e51532 (2021).
4. Galluzzi, L. *et al.* Molecular mechanisms of cell death: Recommendations of the Nomenclature Committee on Cell Death 2018. *Cell Death and Differentiation* **25**, 486-541 (2018).
5. Conrad, M., Angeli, J.P.F., Vandenabeele, P. & Stockwell, B.R. Regulated necrosis: Disease relevance and therapeutic opportunities. *Nature Reviews Drug Discovery* **15**, 348-366 (2016).
6. Dixon, S.J. *et al.* Ferroptosis: An iron-dependent form of nonapoptotic cell death. *Cell* **149**, 1060-1072 (2012).
7. Angeli, J.P.F., Shah, R., Pratt, D.A. & Conrad, M. Ferroptosis Inhibition: Mechanisms and Opportunities. *Trends in Pharmacological Sciences* **38**, 489-498 (2017).
8. Friedmann Angeli, J.P., Krysko, D.V. & Conrad, M. Ferroptosis at the crossroads of cancer-acquired drug resistance and immune evasion. *Nature Reviews Cancer* **19**, 405-414 (2019).
9. Nakamura, T., Naguro, I. & Ichijo, H. Iron homeostasis and iron-regulated ROS in cell death, senescence and human diseases. *Biochimica et Biophysica Acta (BBA) - General Subjects* **1863**, 1398-1409 (2019).
10. Stockwell, B.R. *et al.* Ferroptosis: A Regulated Cell Death Nexus Linking Metabolism, Redox Biology, and Disease. *Cell* **171**, 273-285 (2017).
11. Parker, J.L. *et al.* Molecular basis for redox control by the human cystine/glutamate antiporter system xc(). *Nat Commun* **12**, 7147 (2021).
12. Yan, R. *et al.* The structure of erastin-bound xCT-4F2hc complex reveals molecular mechanisms underlying erastin-induced ferroptosis. *Cell Res* **32**, 687-690 (2022).
13. Friedmann Angeli, J.P. *et al.* Inactivation of the ferroptosis regulator Gpx4 triggers acute renal failure in mice. *Nature Cell Biology* **16**, 1180-1191 (2014).
14. Seiler, A. *et al.* Glutathione peroxidase 4 senses and translates oxidative stress into 12/15-lipoxygenase dependent- and AIF-mediated cell death. *Cell metabolism* **8**, 237-248 (2008).
15. Yang, W.S. *et al.* Regulation of ferroptotic cancer cell death by GPX4. *Cell* **156**, 317-331 (2014).

16. Eaton, J.K. *et al.* Selective covalent targeting of GPX4 using masked nitrile-oxide electrophiles. *Nature Chemical Biology* **16** (2020).
17. Mao, C. *et al.* DHODH-mediated ferroptosis defence is a targetable vulnerability in cancer. *Nature* **593**, 586-590 (2021).
18. Kraft, V.A.N. *et al.* GTP Cyclohydrolase 1/Tetrahydrobiopterin Counteract Ferroptosis through Lipid Remodeling. *ACS Central Science* **6**, 41-53 (2020).
19. Soula, M. *et al.* Metabolic determinants of cancer cell sensitivity to canonical ferroptosis inducers. *Nature chemical biology* (2020).
20. Magtanong, L. *et al.* Exogenous Monounsaturated Fatty Acids Promote a Ferroptosis-Resistant Cell State. *Cell Chemical Biology* **26**, 420-432.e429 (2019).
21. Tesfay, L. *et al.* Stearoyl-CoA Desaturase 1 Protects Ovarian Cancer Cells from Ferroptotic Cell Death. *Cancer Res* **79**, 5355-5366 (2019).
22. Liang, D. *et al.* Ferroptosis surveillance independent of GPX4 and differentially regulated by sex hormones. *Cell* **186**, 2748-2764 e2722 (2023).
23. Kakhlon, O. & Cabantchik, Z.I. The labile iron pool: characterization, measurement, and participation in cellular processes(1). *Free Radic Biol Med* **33**, 1037-1046 (2002).
24. Petrat, F., de Groot, H., Sustmann, R. & Rauen, U. The chelatable iron pool in living cells: A methodically defined quantity. *Biological Chemistry* **383**, 489-502 (2002).
25. James P, K. The Haber–Weiss reaction and mechanisms of toxicity. *Toxicology* **149**, 43-50 (2000).
26. Doll, S. *et al.* FSP1 is a glutathione-independent ferroptosis suppressor. *Nature* **575**, 693-698 (2019).
27. Bersuker, K. *et al.* The CoQ oxidoreductase FSP1 acts parallel to GPX4 to inhibit ferroptosis. *Nature* **575**, 688-692 (2019).
28. Mishima, E. *et al.* A non-canonical vitamin K cycle is a potent ferroptosis suppressor. *Nature* **608**, 778-783 (2022).
29. Yamada, N. *et al.* DHCR7 as a novel regulator of ferroptosis in hepatocytes. *bioRxiv* (2022).
30. Angeli, J.P.F. *et al.* 7-Dehydrocholesterol is an endogenous suppressor of ferroptosis. *Research Square* (2021).
31. Garcia-Bermudez, J. *et al.* Squalene accumulation in cholesterol auxotrophic lymphomas prevents oxidative cell death. *Nature* **567**, 118-122 (2019).
32. Mei, J., Webb, S., Zhang, B. & Shu, H.B. The p53-inducible apoptotic protein AMID is not required for normal development and tumor suppression. *Oncogene* **25**, 849-856 (2006).

33. Marshall, K.R. *et al.* The human apoptosis-inducing protein AMID is an oxidoreductase with a modified flavin cofactor and DNA binding activity. *Journal of Biological Chemistry* **280**, 30735-30740 (2005).
34. Wu, M., Xu, L.G., Li, X., Zhai, Z. & Shu, H.B. AMID, an apoptosis-inducing factor-homologous mitochondrion-associated protein, induces caspase-independent apoptosis. *Journal of Biological Chemistry* **277**, 25617-25623 (2002).
35. Deshwal, S. *et al.* Mitochondria regulate intracellular coenzyme Q transport and ferroptotic resistance via STARD7. *Nat Cell Biol* **25**, 246-257 (2023).
36. Takada, T. *et al.* NPC1L1 is a key regulator of intestinal vitamin K absorption and a modulator of warfarin therapy. *Science Translational Medicine* **7**, 275ra223 LP-275ra223 (2015).
37. Hirota, Y. *et al.* Menadione (vitamin K3) is a catabolic product of oral phylloquinone (vitamin K1) in the intestine and a circulating precursor of tissue menaquinone-4 (vitamin K2) in rats. *J Biol Chem* **288**, 33071-33080 (2013).
38. Nakagawa, K. *et al.* Identification of UBIAD1 as a novel human menaquinone-4 biosynthetic enzyme. *Nature* **468**, 117-121 (2010).
39. Fedoryshchak, R.O. *et al.* Discovery of lipid-mediated protein–protein interactions in living cells using metabolic labeling with photoactivatable clickable probes. *Chemical Science* **14**, 2419-2430 (2023).
40. Meinel, T., Dian, C. & Giglione, C. Myristoylation, an Ancient Protein Modification Mirroring Eukaryogenesis and Evolution. *Trends Biochem Sci* **45**, 619-632 (2020).
41. Zhang, Q. *et al.* ACSL1-induced ferroptosis and platinum resistance in ovarian cancer by increasing FSP1 N-myristylation and stability. *Cell Death Discov* **9**, 83 (2023).
42. Zheng, J. *et al.* Sorafenib fails to trigger ferroptosis across a wide range of cancer cell lines. *Cell Death and Disease* **12** (2021).
43. Muller, F. *et al.* Elevated FSP1 protects KRAS-mutated cells from ferroptosis during tumor initiation. *Cell Death Differ* **30**, 442-456 (2023).
44. Sies, H. *et al.* Defining roles of specific reactive oxygen species (ROS) in cell biology and physiology. *Nat Rev Mol Cell Biol* **23**, 499-515 (2022).
45. Koppula, P. *et al.* A targetable CoQ-FSP1 axis drives ferroptosis- and radiation-resistance in KEAP1 inactive lung cancers. *Nat Commun* **13**, 2206 (2022).
46. Fujisawa, T. & Filippakopoulos, P. Functions of bromodomain-containing proteins and their roles in homeostasis and cancer. *Nature Reviews Molecular Cell Biology* **18**, 246-262 (2017).
47. Filippakopoulos, P. *et al.* Selective inhibition of BET bromodomains. *Nature* **468**, 1067-1073 (2010).

48. Verma, N. *et al.* Synthetic lethal combination targeting BET uncovered intrinsic susceptibility of TNBC to ferroptosis. *Science Advances* **6** (2020).
49. Schmitt, A. *et al.* BRD4 inhibition sensitizes diffuse large B-cell lymphoma cells to ferroptosis. *Blood* (2023).
50. Pontel, L.B. *et al.* Acute lymphoblastic leukemia necessitates GSH-dependent ferroptosis defenses to overcome FSP1-epigenetic silencing. *Redox Biol* **55**, 102408 (2022).
51. Zheng, X. *et al.* N-acetyltransferase 10 promotes colon cancer progression by inhibiting ferroptosis through N4-acetylation and stabilization of ferroptosis suppressor protein 1 (FSP1) mRNA. *Cancer Commun (Lond)* **42**, 1347-1366 (2022).
52. Li, N. *et al.* Targeting Ferroptosis as a Novel Approach to Alleviate Aortic Dissection. *Int J Biol Sci* **18**, 4118-4134 (2022).
53. Mishima, E. *et al.* DHODH inhibitors sensitize to ferroptosis by FSP1 inhibition. *Nature* **619**, E9-E18 (2023).
54. Nakamura, T. *et al.* Phase separation of FSP1 promotes ferroptosis. *Nature* **619**, 371-377 (2023).
55. Nguyen, H.P. *et al.* Aifm2, a NADH Oxidase, Supports Robust Glycolysis and Is Required for Cold- and Diet-Induced Thermogenesis. *Molecular Cell* **77**, 600-617.e604 (2020).
56. Mishima, E., Wahida, A., Seibt, T. & Conrad, M. Diverse biological functions of vitamin K: from coagulation to ferroptosis. *Nat Metab* **5**, 924-932 (2023).
57. Jin, D.Y. *et al.* A genome-wide CRISPR-Cas9 knockout screen identifies FSP1 as the warfarin-resistant vitamin K reductase. *Nat Commun* **14**, 828 (2023).
58. Tie, J.K. & Stafford, D.W. Functional Study of the Vitamin K Cycle Enzymes in Live Cells. *Methods Enzymol* **584**, 349-394 (2017).
59. Hirose, T., Ninomiya, K., Nakagawa, S. & Yamazaki, T. A guide to membraneless organelles and their various roles in gene regulation. *Nat Rev Mol Cell Biol* **24**, 288-304 (2023).
60. Lu, Y. *et al.* Phase separation of TAZ compartmentalizes the transcription machinery to promote gene expression. *Nature Cell Biology* **22**, 453-464 (2020).
61. Cai, D. *et al.* Phase separation of YAP reorganizes genome topology for long-term YAP target gene expression. *Nat Cell Biol* **21**, 1578-1589 (2019).
62. Morishita, K., Watanabe, K., Naguro, I. & Ichijo, H. Sodium ion influx regulates liquidity of biomolecular condensates in hyperosmotic stress response. *Cell Rep*, 112315 (2023).
63. Watanabe, K. *et al.* Cells recognize osmotic stress through liquid-liquid phase separation lubricated with poly(ADP-ribose). 1-27 (2020).
64. Fujioka, Y. *et al.* Phase separation organizes the site of autophagosome formation. *Nature* **578**, 301-305 (2020).

65. Yasuda, S. *et al.* Stress- and ubiquitylation-dependent phase separation of the proteasome. *Nature* **578**, 296-300 (2020).
66. Bose, M., Lampe, M., Mahamid, J. & Ephrussi, A. Liquid-to-solid phase transition of oskar ribonucleoprotein granules is essential for their function in *Drosophila* embryonic development. *Cell* **185**, 1308-1324 e1323 (2022).
67. Lee, S.A. *et al.* OASL phase condensation induces amyloid-like fibrillation of RIPK3 to promote virus-induced necroptosis. *Nat Cell Biol* **25**, 92-107 (2023).
68. Alberti, S., Gladfelter, A. & Mittag, T. Considerations and Challenges in Studying Liquid-Liquid Phase Separation and Biomolecular Condensates. *Cell* **176**, 419-434 (2019).
69. Brangwynne, C.P. *et al.* Germline P Granules Are Liquid Droplets That Localize by Controlled Dissolution/Condensation. *Science* **324**, 1729-1732 (2009).
70. Yang, P. *et al.* G3BP1 Is a Tunable Switch that Triggers Phase Separation to Assemble Stress Granules. *Cell* **181**, 325-345 e328 (2020).
71. Altmeyer, M. *et al.* Liquid demixing of intrinsically disordered proteins is seeded by poly(ADP-ribose). *Nat Commun* **6**, 8088 (2015).
72. Su, X. *et al.* Phase separation of signaling molecules promotes T cell receptor signal transduction. *Science* **352**, 595-599 (2016).
73. Banani, S.F., Lee, H.O., Hyman, A.A. & Rosen, M.K. Biomolecular condensates: Organizers of cellular biochemistry. *Nature Reviews Molecular Cell Biology* **18**, 285-298 (2017).
74. Li, P. *et al.* Phase transitions in the assembly of multivalent signalling proteins. *Nature* **483**, 336-340 (2012).
75. Molliex, A. *et al.* Phase Separation by Low Complexity Domains Promotes Stress Granule Assembly and Drives Pathological Fibrillization. *Cell* **163**, 123-133 (2015).
76. Sun, D., Wu, R., Zheng, J., Li, P. & Yu, L. Polyubiquitin chain-induced p62 phase separation drives autophagic cargo segregation. *Cell Research* **28**, 405-415 (2018).
77. Watanabe, K. *et al.* Cells recognize osmotic stress through liquid-liquid phase separation lubricated with poly(ADP-ribose). *Nat Commun* **12**, 1353 (2021).
78. Klein, I.A. *et al.* Partitioning of cancer therapeutics in nuclear condensates. *Science* **368**, 1386-1392 (2020).
79. Kilgore, H.R. & Young, R.A. Learning the chemical grammar of biomolecular condensates. *Nat Chem Biol* (2022).
80. Zbinden, A., Pérez-Berlanga, M., De Rossi, P. & Polymenidou, M. Phase Separation and Neurodegenerative Diseases: A Disturbance in the Force. *Developmental Cell* **55**, 45-68 (2020).

81. Lenard, A.J. *et al.* Phosphorylation Regulates CIRBP Arginine Methylation, Transportin-1 Binding and Liquid-Liquid Phase Separation. *Front Mol Biosci* **8**, 689687 (2021).
82. Bukau, B., Hofmann, S., Stoecklin, G., Bankhead, P. & Cherkasova, V. Translation suppression promotes stress granule formation and cell survival in response to cold shock. *Molecular Biology of the Cell* **23**, 3786-3800 (2012).
83. Gwon, Y. *et al.* Ubiquitination of G3BP1 mediates stress granule disassembly in a context-specific manner. *Science* **372**, eabf6548-eabf6548 (2021).
84. Boyd-Shiwerski, C.R. *et al.* WNK kinases sense molecular crowding and rescue cell volume via phase separation. *Cell* **185**, 4488-4506 e4420 (2022).
85. Ikeda, R. *et al.* Phosphorylation of phase-separated p62 bodies by ULK1 activates a redox-independent stress response. *EMBO J*, e113349 (2023).
86. Lu, Y. *et al.* Activation of NRF2 ameliorates oxidative stress and cystogenesis in autosomal dominant polycystic kidney disease. *Sci Transl Med* **12** (2020).
87. Jin, M. *et al.* Glycolytic Enzymes Coalesce in G Bodies under Hypoxic Stress. *Cell Rep* **20**, 895-908 (2017).
88. Fuller, G.G. *et al.* RNA promotes phase separation of glycolysis enzymes into yeast G bodies in hypoxia. *Elife* **9** (2020).
89. Matyash, V., Liebisch, G., Kurzchalia, T.V., Shevchenko, A. & Schwudke, D. Lipid extraction by methyl-tert-butyl ether for high-throughput lipidomics. *J Lipid Res* **49**, 1137-1146 (2008).
90. Chong, J., Wishart, D.S. & Xia, J. Using MetaboAnalyst 4.0 for Comprehensive and Integrative Metabolomics Data Analysis. *Curr Protoc Bioinformatics* **68**, e86 (2019).
91. Michlits, G. *et al.* Multilayered VBC score predicts sgRNAs that efficiently generate loss-of-function alleles. *Nat Methods* **17**, 708-716 (2020).
92. Pan, D. *et al.* A major chromatin regulator determines resistance of tumor cells to T cell-mediated killing. *Science (New York, N.Y.)* **359**, 770-775 (2018).
93. Bolger, A.M., Lohse, M. & Usadel, B. Trimmomatic: a flexible trimmer for Illumina sequence data. *Bioinformatics* **30**, 2114-2120 (2014).
94. Li, H. Aligning sequence reads, clone sequences and assembly contigs with BWA-MEM. *arXiv preprint arXiv:1303.3997* (2013).
95. Li, H. *et al.* The sequence alignment/map format and SAMtools. *bioinformatics* **25**, 2078-2079 (2009).
96. Robinson, J.T. *et al.* Integrative genomics viewer. *Nature biotechnology* **29**, 24-26 (2011).
97. Varadi, M. *et al.* AlphaFold Protein Structure Database: massively expanding the structural coverage of protein-sequence space with high-accuracy models. *Nucleic Acids Research* **50**, D439-D444 (2022).

98. Feng, Y. *et al.* Structural insight into the type-II mitochondrial NADH dehydrogenases. *Nature* **491**, 478-482 (2012).
99. Sena, F.V. *et al.* Type-II NADH:quinone oxidoreductase from *Staphylococcus aureus* has two distinct binding sites and is rate limited by quinone reduction. *Molecular Microbiology* **98**, 272-288 (2015).
100. Heikal, A. *et al.* Structure of the bacterial type II NADH dehydrogenase: a monotopic membrane protein with an essential role in energy generation. *Molecular Microbiology* **91**, 950-964 (2014).
101. Waterhouse, A.M., Procter, J.B., Martin, D.M.A., Clamp, M. & Barton, G.J. Jalview Version 2—a multiple sequence alignment editor and analysis workbench. *Bioinformatics* **25**, 1189-1191 (2009).
102. Tulpule, A. *et al.* Kinase-mediated RAS signaling via membraneless cytoplasmic protein granules. *Cell* **184**, 2649-2664.e2618 (2021).
103. Du, M. & Chen, Z.J. DNA-induced liquid phase condensation of cGAS activates innate immune signaling. *Science* **361**, 704-709 (2018).
104. Wei, M.T. *et al.* Nucleated transcriptional condensates amplify gene expression. *Nat Cell Biol* **22**, 1187-1196 (2020).
105. Hnisz, D., Shrinivas, K., Young, R.A., Chakraborty, A.K. & Sharp, P.A. A Phase Separation Model for Transcriptional Control. *Cell* **169**, 13-23 (2017).
106. Mensah, M.A. *et al.* Aberrant phase separation and nucleolar dysfunction in rare genetic diseases. *Nature* **614**, 564-571 (2023).
107. Jumper, J. *et al.* Highly accurate protein structure prediction with AlphaFold. *Nature* **596**, 583-589 (2021).
108. Mirdita, M. *et al.* ColabFold: making protein folding accessible to all. *Nat Methods* **19**, 679-682 (2022).
109. Marshall, C.B. *et al.* Inhibition of K-RAS4B by a Unique Mechanism of Action : Stabilizing Membrane-Dependent Occlusion of the Effector-Binding Site Article Inhibition of K-RAS4B by a Unique Mechanism of Action : Stabilizing Membrane-Dependent Occlusion of the Effector-Binding. *Cell Chemical Biology* **25**, 1327-1336.e1324 (2018).
110. Ames, J.B. *et al.* Molecular mechanics of calcium–myristoyl switches. *Nature* **389**, 198-202 (1997).
111. Boeynaems, S. *et al.* Protein Phase Separation: A New Phase in Cell Biology. *Trends in Cell Biology* **28**, 420-435 (2018).
112. Wyman, J. & Gill, S.J. Ligand-linked phase changes in a biological system: applications to sickle cell hemoglobin. *Proc Natl Acad Sci U S A* **77**, 5239-5242 (1980).

113. Ruff, K.M., Dar, F. & Pappu, R.V. Polyphasic linkage and the impact of ligand binding on the regulation of biomolecular condensates. *Biophys Rev (Melville)* **2**, 021302 (2021).
114. Rodriguez, R., Schreiber, S.L. & Conrad, M. Persister cancer cells: Iron addiction and vulnerability to ferroptosis. *Molecular Cell*, 1-13 (2021).
115. Ohshima, T., Yamamoto, H., Sakamaki, Y., Saito, C. & Mizushima, N. NCOA4 drives ferritin phase separation to facilitate macroferritinophagy and microferritinophagy. *J Cell Biol* **221** (2022).
116. Gryzik, M., Asperti, M., Denardo, A., Arosio, P. & Poli, M. NCOA4-mediated ferritinophagy promotes ferroptosis induced by erastin, but not by RSL3 in HeLa cells. *Biochim Biophys Acta Mol Cell Res* **1868**, 118913 (2021).
117. Fang, Y. *et al.* Inhibiting Ferroptosis through Disrupting the NCOA4-FTH1 Interaction: A New Mechanism of Action. *ACS Cent Sci* **7**, 980-989 (2021).
118. Ruff, K.M. *et al.* Sequence grammar underlying the unfolding and phase separation of globular proteins. *Mol Cell* **82**, 3193-3208 e3198 (2022).
119. Hirata, Y. *et al.* Lipid peroxidation increases membrane tension, Piezo1 gating, and cation permeability to execute ferroptosis. *Curr Biol* **33**, 1282-1294 e1285 (2023).
120. Riegman, M. *et al.* Ferroptosis occurs through an osmotic mechanism and propagates independently of cell rupture. *Nat Cell Biol* **22**, 1042-1048 (2020).
121. Gong, M., Hay, S., Marshall, K.R., Munro, A.W. & Scrutton, N.S. DNA binding suppresses human AIF-M2 activity and provides a connection between redox chemistry, reactive oxygen species, and apoptosis. *Journal of Biological Chemistry* **282**, 30331-30340 (2007).
122. Miriyala, S. *et al.* Novel role of 4-hydroxy-2-nonenal in AIFm2-mediated mitochondrial stress signaling. *Free Radic Biol Med* **91**, 68-80 (2016).
123. Xavier da Silva, T.N., Schulte, C., Alves, A.N., Maric, H.M. & Friedmann Angeli, J.P. Molecular characterization of AIFM2/FSP1 inhibition by iFSP1-like molecules. *Cell Death Dis* **14**, 281 (2023).
124. Tate, J.G. *et al.* COSMIC: the Catalogue Of Somatic Mutations In Cancer. *Nucleic Acids Research* **47**, D941-D947 (2018).
125. Stockwell, B.R. Chemical genetics: ligand-based discovery of gene function. *Nat Rev Genet* **1**, 116-125 (2000).
126. Tonnus, W. *et al.* Dysfunction of the key ferroptosis-surveilling systems hypersensitizes mice to tubular necrosis during acute kidney injury. *Nat Commun* **12**, 4402 (2021).
127. Wu, J. *et al.* Intercellular interaction dictates cancer cell ferroptosis via NF2-YAP signalling. *Nature* (2019).

128. Yang, W.H. *et al.* The Hippo Pathway Effector TAZ Regulates Ferroptosis in Renal Cell Carcinoma. *Cell Rep* **28**, 2501-2508 e2504 (2019).
129. Viswanathan, V.S. *et al.* Dependency of a therapy-resistant state of cancer cells on a lipid peroxidase pathway. *Nature* **547**, 453-457 (2017).
130. Conrad, M., Lorenz, S.M. & Proneth, B. Targeting Ferroptosis: New Hope for As-Yet-Incurable Diseases. *Trends in molecular medicine* (2020).
131. Thijssen, H.H.W. Warfarin-Based Rodenticides - Mode of Action and Mechanism of Resistance. *Pesticide Science* **43**, 73-78 (1995).
132. Tanaka, K.D. *et al.* The genetic mechanisms of warfarin resistance in *Rattus rattus* found in the wild in Japan. *Pesticide Biochemistry and Physiology* **103**, 144-151 (2012).
133. Hendricks, J.M. *et al.* Identification of structurally diverse FSP1 inhibitors that sensitize cancer cells to ferroptosis. *Cell Chem Biol* (2023).
134. Yoshioka, H. *et al.* Identification of a Small Molecule That Enhances Ferroptosis via Inhibition of Ferroptosis Suppressor Protein 1 (FSP1). *ACS Chem Biol* **17**, 483-491 (2022).
135. Zhang, L. *et al.* Recent advances of human dihydroorotate dehydrogenase inhibitors for cancer therapy: Current development and future perspectives. *Eur J Med Chem* **232**, 114176 (2022).

9. Acknowledgements

This dissertation was demanding, hard and extensive work, but overall it was an interesting and wonderful experience for me. The successful completion of this work would not have been possible without the support, assistance and encouragement of many people.

First, I would like to express my deepest gratitude to Dr. Marcus Conrad for giving me such an outstanding opportunity to research enthusiastically with a tremendous passion as well as pursue my career as a researcher in the field of molecular biology and biochemistry. Moreover, his thoughtful comments from multidirectional perspectives has enabled me to broaden my view toward biology incredibly.

Second, I would like to deeply thank my supervisors Prof. Dr. Percy A. Knolle and Prof. Dr. Franz Hagn for their important suggestions and fruitful discussions at my annual thesis committee meetings.

Third, I would like to thank Prof. Dr. Michael Sattler and Clara Hipp, and his other lab members for guiding me to understand and to interpret the complicated mechanisms of FSP1 in phase separation and giving me many structural and molecular biological insights.

Forth, I would like to thank Dr. Bettina Proneth, Dr. Eikan Mishima, Dr. Sebastian Doll, Dr. Dietrich Trümbach, Dr. Jiashuo Zheng, Dr. Maceler Aldrovandi, Dr. Naoya Yamada, Dr. Adam Wahida, Bernhard Henkelmann, Jonas Wanninger and all other former and present lab members for sharing their experience, knowledge and passion, as well as for their many supports and fruitful discussion.

I would like to thank Dr. André Santos Dias Mourão for providing me with a number of recombinant enzymes for the *in vitro* analyses.

I would like to thank my collaborators Dr. Peter Sennhenn, Prof. Dr. Jose Pedro Friedman Angeli and his team for providing me with important knowledge and skills for data analysis.

I would like to greatly thank to my wife Saya Nakamura for supporting my life outside the laboratory from all aspects and being patient for the last 3 years.

Lastly, I would like to express my deepest thanks to my family for their constant and tremendous support and for providing me to research abroad.

Phase separation of FSP1 promotes ferroptosis


<https://doi.org/10.1038/s41586-023-06255-6>

Received: 23 August 2022

Accepted: 24 May 2023

Published online: 28 June 2023

Open access

 Check for updates

Toshitaka Nakamura¹, Clara Hipp^{2,3}, André Santos Dias Mourão², Jan Borggräfe^{2,3}, Maceler Aldrovandi¹, Bernhard Henkelmann¹, Jonas Wanninger¹, Eikan Mishima^{1,4}, Elena Lytton¹, David Emler¹, Bettina Proneth¹, Michael Sattler^{2,3} & Marcus Conrad^{1,5✉}

Ferroptosis is evolving as a highly promising approach to combat difficult-to-treat tumour entities including therapy-refractory and dedifferentiating cancers^{1–3}. Recently, ferroptosis suppressor protein-1 (FSP1), along with extramitochondrial ubiquinone or exogenous vitamin K and NAD(P)H/H⁺ as an electron donor, has been identified as the second ferroptosis-suppressing system, which efficiently prevents lipid peroxidation independently of the cyst(e)ine–glutathione (GSH)–glutathione peroxidase 4 (GPX4) axis^{4–6}. To develop FSP1 inhibitors as next-generation therapeutic ferroptosis inducers, here we performed a small molecule library screen and identified the compound class of 3-phenylquinazolinones (represented by icFSP1) as potent FSP1 inhibitors. We show that icFSP1, unlike iFSP1, the first described on-target FSP1 inhibitor⁵, does not competitively inhibit FSP1 enzyme activity, but instead triggers subcellular relocalization of FSP1 from the membrane and FSP1 condensation before ferroptosis induction, in synergism with GPX4 inhibition. icFSP1-induced FSP1 condensates show droplet-like properties consistent with phase separation, an emerging and widespread mechanism to modulate biological activity⁷. N-terminal myristoylation, distinct amino acid residues and intrinsically disordered, low-complexity regions in FSP1 were identified to be essential for FSP1-dependent phase separation in cells and in vitro. We further demonstrate that icFSP1 impairs tumour growth and induces FSP1 condensates in tumours in vivo. Hence, our results suggest that icFSP1 exhibits a unique mechanism of action and synergizes with ferroptosis-inducing agents to potentiate the ferroptotic cell death response, thus providing a rationale for targeting FSP1-dependent phase separation as an efficient anti-cancer therapy.

Ferroptosis, a metabolic form of non-apoptotic cell death characterized by iron-dependent lipid peroxidation, has been defined only recently^{1,8}. Ferroptosis has attracted tremendous interest because of its high relevance to human diseases such as neurodegenerative disorders, tissue damage during cold exposure, ischaemia–reperfusion injury and cancer^{9–12}. In particular, triggering ferroptosis in the context of malignancies has emerged as a highly promising approach that shows synergistic effects with cancer immunotherapy and even kills therapy-resistant and metastatic cancers^{2,3,13–15}. We recently showed that FSP1 represents a powerful backup system for the guardian of ferroptosis, known as GPX4, rendering tumours resistant to inhibition of this node^{5,6}. However, because the first described FSP1-specific inhibitor iFSP1 (ref. 5) does not qualify to be further developed as an anti-cancer drug, owing to its limited potential for medicinal chemistry development in terms of an unfavourable structure and substitution pattern¹⁶, next-generation, efficacious in vivo FSP1 inhibitors for tumour treatment are urgently required.

icFSP1 triggers ferroptosis

To identify possible in vivo-applicable FSP1-specific inhibitors as potential future drugs to combat difficult-to-treat cancers, we carefully revalidated hit compounds from ~10,000 drug-like small molecule compounds (as described previously³) in terms of their potential for medicinal chemistry development, using cheminformatics tools¹⁷ for the prediction of physicochemical properties and drug-likeness. Hit validation studies identified the class of 3-phenylquinazolinones (represented by the lead compound icFSP1) as a class of potent pharmacological inhibitors of FSP1 (Fig. 1a). Preliminary structure–activity relationship studies have yet to identify compounds with substantial improvement over icFSP1 (Extended Data Fig. 1a). Treatment with icFSP1 caused marked lipid peroxidation and associated ferroptotic cell death in 4-hydroxytamoxifen (TAM)-inducible *Gpx4*-knockout mouse Pfa1 cells¹⁸ stably overexpressing human FSP1 (hFSP1) and in the human fibrosarcoma HT-1080 cell line (Fig. 1b–g and Extended

¹Institute of Metabolism and Cell Death, Molecular Targets and Therapeutics Center, Helmholtz Munich, Neuherberg, Germany. ²Bavarian NMR Center, Department of Bioscience, School of Natural Sciences, Technical University of Munich, Garching, Germany. ³Institute of Structural Biology, Molecular Targets and Therapeutics Center, Helmholtz Munich, Neuherberg, Germany. ⁴Division of Nephrology, Rheumatology and Endocrinology, Tohoku University Graduate School of Medicine, Sendai, Japan. [✉]e-mail: marcus.conrad@helmholtz-munich.de

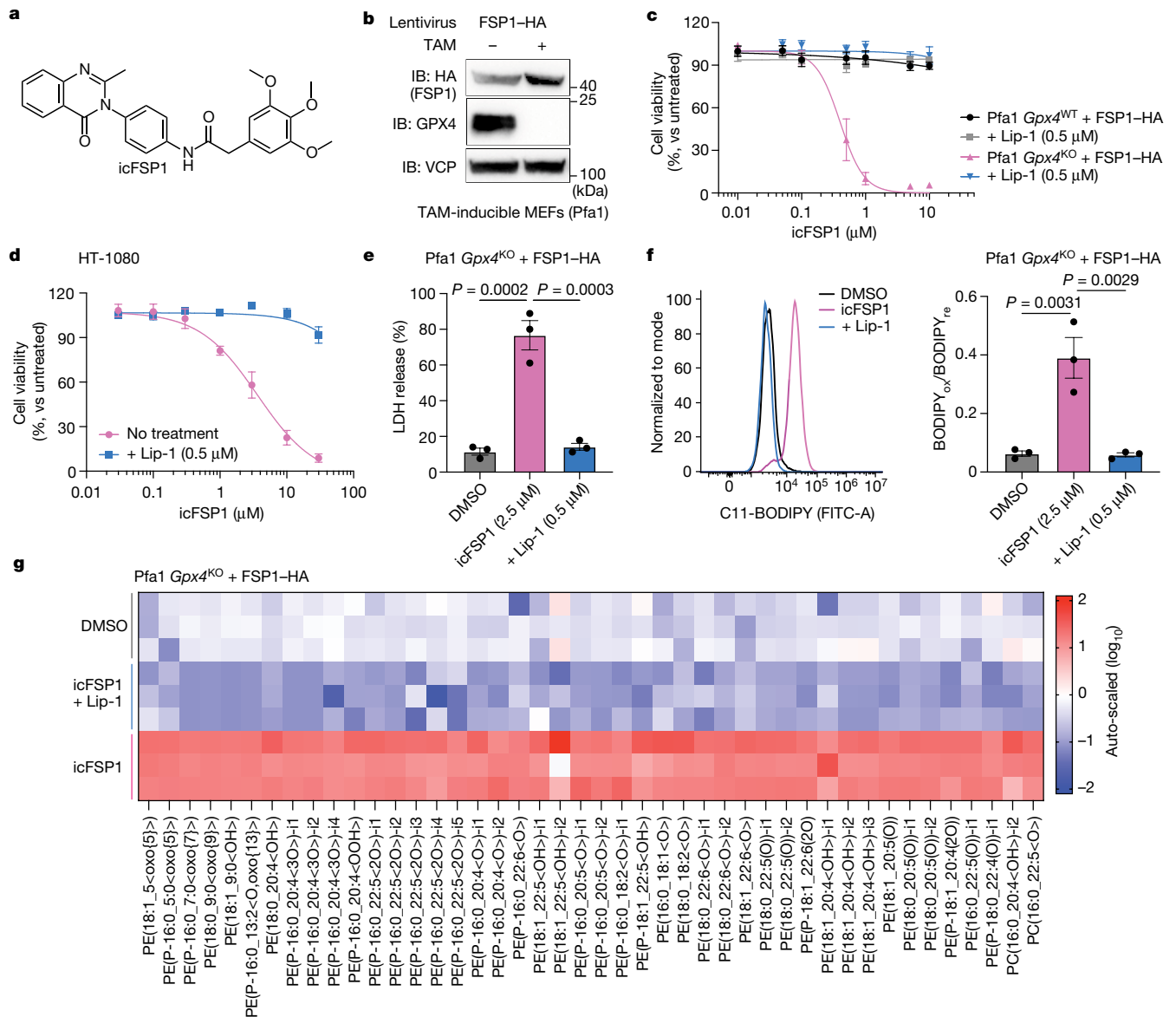


Fig. 1 | icFSP1 induces ferroptosis in synergy with GPX4 inhibition.

a, Chemical structure of icFSP1. **b**, Representative immunoblot (IB) analysis of GPX4, HA (FSP1) and VCP expression in TAM-induced *Gpx4*-knockout mouse embryonic fibroblasts (MEFs; Pfa1 cells) stably overexpressing HA-tagged hFSP1 from one of two independent experiments. **c**, Cell viability of wild-type or knockout *Gpx4* (*Gpx4*^{WT} or *Gpx4*^{KO}, respectively) Pfa1 cells stably expressing HA-tagged hFSP1 treated with icFSP1 alone or in combination with the ferroptosis inhibitor liproxstatin-1 (Lip-1; 0.5 μM) for 48 h. **d**, Cell viability of HT-1080 cells treated with icFSP1 and 0.5 μM Lip-1 for 72 h. **e**, Lactate dehydrogenase (LDH) release determined after treating *Gpx4*-knockout Pfa1 cells overexpressing HA-tagged hFSP1 with DMSO, 2.5 μM icFSP1, or 2.5 μM icFSP1 + 0.5 μM Lip-1 for 24 h. **f**, Lipid peroxidation evaluated by

581/591 staining after treating *Gpx4*-knockout cells stably overexpressing HA-tagged hFSP1 with DMSO, 2.5 μM icFSP1, or 2.5 μM icFSP1 + 0.5 μM Lip-1 for 3 h. Representative plots of one of three independent experiments (left) and quantified median values of three independent experiments (right) are shown. BODIPY_{ox}/BODIPY_{re} ratio of oxidized to reduced BODIPY. Data represent the mean ± s.e.m. of three (**c, e, f**) or four (**d**) independent experiments. *P* values were calculated by one-way ANOVA followed by Tukey's multiple-comparison test (**e, f**). **g**, Lipid peroxidation profiles measured by liquid chromatography and tandem mass spectrometry (LC-MS/MS) after treatment of *Gpx4*-knockout Pfa1 cells stably overexpressing HA-tagged hFSP1 with DMSO, 5 μM icFSP1, or 5 μM icFSP1 + 0.5 μM Lip-1 for 5 h. The heat map shows three technical replicates from one of two independent experiments.

Data Fig. 1b). icFSP1-induced cell death was rescued by ferroptosis inhibitors, but not by inhibitors targeting other forms of cell death, thus confirming its specificity for ferroptosis. Killing of (cancer) cells by targeting FSP1 usually requires co-treatment with other types of canonical ferroptosis inducers^{5,19}, such as the system X_c⁻ inhibitor erastin, the glutamate cysteine ligase (GCL) inhibitor L-buthionine sulfoximine (BSO), and the GPX4 inhibitors (1*S*,3*R*)-RSL3 (RSL3), ML210 and FIN56, as well as the iron oxidation compound FINO2

(refs. 1,5,20–22), but not with compounds inducing other forms of cell death (Extended Data Fig. 1c–e). Thus, it was surprising that treatment of HT-1080 cells, the primary cell model in ferroptosis research, with icFSP1 alone or doxycycline-inducible *FSP1* knockout for 72 h was sufficient to trigger ferroptosis (Fig. 1d and Extended Data Fig. 1f–h), in contrast to a panel of different human cancer cell lines (Extended Data Fig. 1c). To address whether icFSP1 may have off-target effects, HT-1080 and HEK293T cells and primary peripheral blood mononuclear cells

(PBMCs) were exposed to the FSP1 inhibitors (icFSP1 and iFSP1) for 72 h and 24 h, respectively. In these experiments, icFSP1 did not show off-target effects even at higher concentrations as compared with iFSP1 (Extended Data Fig. 1h–j). Apart from this, *FSP1*-knockout cells treated with increasing concentrations of icFSP1 did not show any additional synergistic effects when cells were co-incubated with a GPX4 inhibitor (Extended Data Fig. 1k,l), indicating that icFSP1 should be considered to be a selective FSP1 inhibitor.

To investigate whether icFSP1 also induces death in non-human cells, we included two different mouse cell lines and one rat fibroblast cell line in our study (that is, 4T1, B16F10 and Rat1, respectively), showing that co-treatment with RSL3 or *Gpx4* knockout failed to synergistically kill these cells (Extended Data Fig. 2a–g). In line with this, lipid peroxidation and cell viability were not affected by icFSP1 in *Gpx4*-knockout Pfa1 cells stably overexpressing mouse FSP1 (mFSP1; Extended Data Fig. 2h,i), suggesting that icFSP1 specifically inhibits the human isoform. Additionally, we tested other orthologues of FSP1 in Pfa1 cells, overexpressing FSP1 from *Gallus gallus* (chicken) and *Xenopus laevis* (frog). Although FSP1 expression (except for that from *X. laevis*) fully prevented RSL3-induced ferroptosis, icFSP1 reduced cell viability only in cells overexpressing hFSP1 (Extended Data Fig. 2j–l). These data therefore reinforce the notion that icFSP1 is an hFSP1-specific inhibitor.

icFSP1 induces FSP1 condensation

To investigate the mechanism of action of these next-generation FSP1 inhibitors, the direct inhibitory activity of FSP1 was measured *in vitro* by using an established assay with recombinant hFSP1 enzyme (Fig. 2a). Whereas the enzymatic activity of hFSP1 was inhibited by iFSP1 in a cell-free system, as reported^{5,6}, icFSP1 did not inhibit hFSP1 activity in the low-micromolar range, although it clearly affected cell viability and lipid peroxidation in Pfa1 cells overexpressing hFSP1 (Fig. 2b and Extended Data Fig. 3a–k). In fact, the estimated half-maximal inhibitory concentration (IC_{50}) of icFSP1 in the *in vitro* assay (enzyme) was more than 100-fold higher than the half-maximal effective concentration (EC_{50}) observed in Pfa1 cells (Fig. 2b and Extended Data Fig. 3i). These results strongly argue that icFSP1, as compared with iFSP1, uses a different mechanism of action to inhibit hFSP1 activity in cells.

To shed light on the mechanism of action, we first analysed whether icFSP1 may decrease the expression levels of hFSP1. Immunoblotting of hFSP1-expressing H460 or HT-1080 cells after icFSP1 treatment for 48 h and 72 h showed that expression levels of hFSP1 were not affected by icFSP1 treatment (Extended Data Fig. 3l–n). Next, we considered that icFSP1 might change the subcellular localization of hFSP1 by detaching it from lipid membranes, thereby preventing its anti-ferroptotic function of scavenging phospholipid radicals through ubiquinone and/or vitamin E or K^{4-6} . To this end, hFSP1 fused to enhanced green fluorescent protein and streptavidin (hFSP1–EGFP–Strep) was stably overexpressed in Pfa1 cells and its localization was monitored in response to icFSP1 treatment. Unlike iFSP1, icFSP1 markedly changed the subcellular localization of hFSP1–EGFP–Strep, as illustrated by the appearance of distinct foci and cellular condensates (Fig. 2c, Extended Data Fig. 3o and Supplementary Video 1). These condensates accumulated in cells in a time-dependent manner (Fig. 2d) and only occurred in cells expressing hFSP1 and not in those expressing mFSP1 (Extended Data Fig. 3p), corroborating that icFSP1 is specific for the human orthologue. To test whether the change in subcellular localization of hFSP1 causes induction of ferroptosis, *Gpx4*-knockout Pfa1 cells stably overexpressing hFSP1 fused to blue fluorescent protein (BFP) were established. hFSP1–BFP signal was monitored by live-cell imaging of cells co-stained with Liperfluo (a lipid hydroperoxide sensor) and propidium iodide, which can only stain nuclei when the plasma membrane becomes leaky. Straight after treatment of hFSP1–BFP-expressing cells with icFSP1, condensates were induced followed by Liperfluo oxidation, whereas lipid peroxide signals gradually increased in cells until cells became

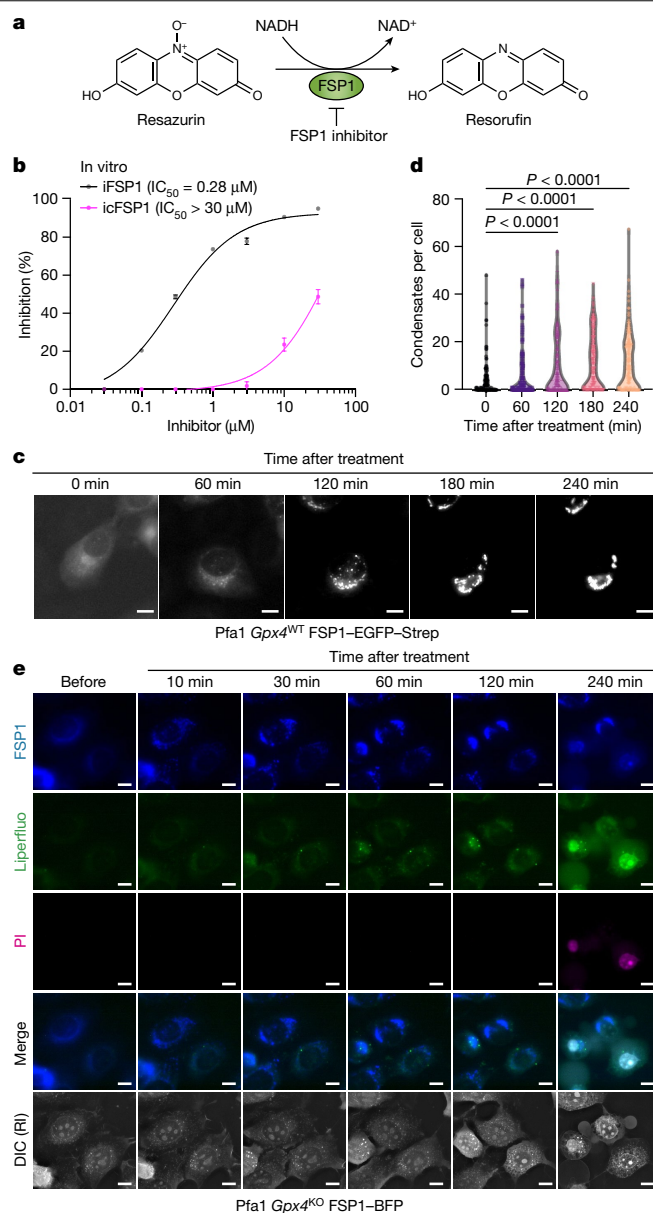


Fig. 2 | icFSP1 indirectly inhibits FSP1 by inducing condensate formation.

a, Schematic representation of the FSP1 enzyme activity assay using resazurin as the substrate. **b**, Representative dose–response curves for the effect of iFSP1 and icFSP1 on hFSP1 activity using recombinant purified hFSP1 protein. Data represent the mean \pm s.d. of 3 wells of a 96-well plate from one of three independent experiments. **c**, Representative time-lapse fluorescence images acquired immediately after treatment of wild-type *Gpx4* Pfa1 cells stably overexpressing hFSP1–EGFP–Strep with 2.5 μ M icFSP1. Scale bars, 10 μ m. Representative results from one of three independent experiments. See also Supplementary Video 1. **d**, Number of condensates per cell quantified from time-lapse images at different time points (0, 60, 120, 180 and 240 min) after treatment obtained from one of two independent experiments. Dots represent each cell and n corresponds to cell number ($n = 129, 124, 130, 130$ and 134 (left to right)). P values were calculated by one-way ANOVA followed by Dunnett’s multiple-comparison test. **e**, Representative time-lapse fluorescence images before and after treatment of *Gpx4*-knockout Pfa1 cells stably overexpressing hFSP1–mTagBFP with 10 μ M icFSP1 in FluoroBrite DMEM containing propidium iodide (PI; 0.2 μ g ml⁻¹). Cells were prestained with 5 μ M Liperfluo for 1 h. Scale bars, 10 μ m. Representative results from three independent experiments. Differential interference contrast (DIC) is displayed with refractive index (RI). See also Supplementary Video 2.

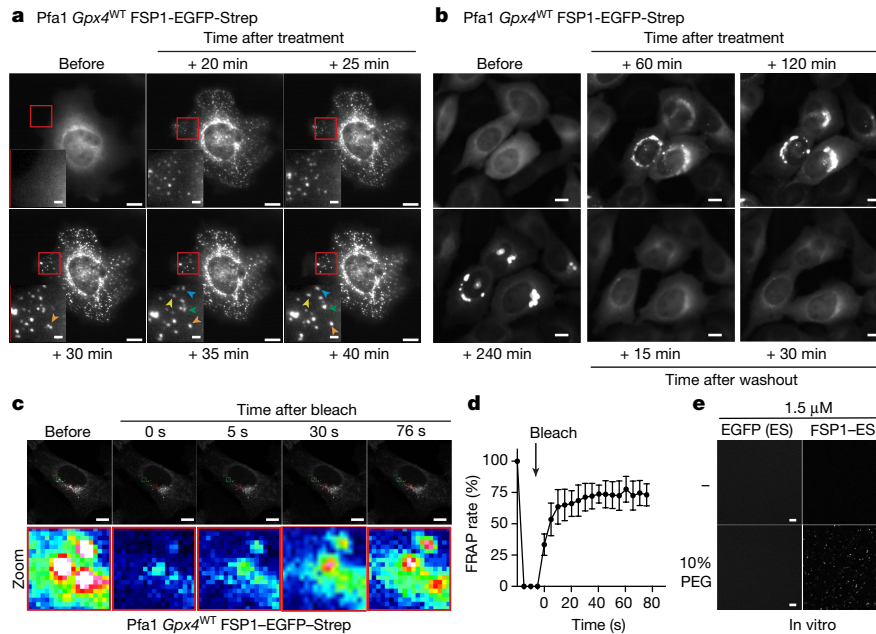


Fig. 3 | FSP1 condensates are liquid droplets. **a**, Representative time-lapse fluorescence images before and after treatment of wild-type *Gpx4* Pfa1 cells stably overexpressing hFSP1-EGFP-Strep with 2.5 μM icFSP1. Representative results are shown from one of three independent experiments. Scale bars, 10 μm (2 μm for zoomed-in images). Arrowheads indicate fusion events of individual condensates. See also Supplementary Video 3. **b**, Reversibility of hFSP1 condensates. Representative time-lapse fluorescence images before and after treatment of wild-type *Gpx4* Pfa1 cells stably overexpressing hFSP1-EGFP-Strep with 2.5 μM icFSP1. After treatment of cells with icFSP1 for 240 min, the medium was replaced with fresh medium without icFSP1 and recordings were restarted. Scale bars, 10 μm. Representative results from one of three independent experiments. See also Supplementary Video 4. **c**, FRAP assays after treatment of hFSP1-EGFP-Strep-overexpressing wild-type *Gpx4* Pfa1

cells with 2.5 μM icFSP1 for 120 min. Top, greyscale images corresponding to representative FRAP images immediately before and after photobleaching. Bottom, lookup table (LUT) images showing enlarged views of the areas in red rectangles in the top FRAP images. Scale bars, 10 μm. Representative results from one of three independent experiments. See also Supplementary Video 5. **d**, Quantified FRAP rate of each condensate. Data represent the mean ± s.d. of five condensates from **c**. Representative results from one of three independent experiments. **e**, FSP1 condensation in vitro. Representative fluorescence images of 1.5 μM EGFP-Strep and hFSP1-EGFP-Strep purified from transfected HEK293T cells were obtained immediately after mixing with or without 10% PEG. Scale bars, 10 μm. Representative results from one of three independent experiments are shown.

positive for propidium iodide as a measure for cell membrane rupture (Fig. 2e and Supplementary Video 2). These results indicate that changes in the subcellular localization of FSP1 precede lipid peroxidation and ferroptosis.

icFSP1 induces phase separation of FSP1

To interrogate whether hFSP1 condensates may localize to specific subcellular compartments, hFSP1-EGFP-Strep-expressing cells were co-stained with a number of organelle-specific markers. Reportedly, FSP1 localizes to different subcellular structures, including the endoplasmic reticulum (ER), Golgi apparatus, lipid droplets and perinuclear structures^{4,5} (Extended Data Fig. 4a). Yet, treatment of cells with icFSP1 did not induce hFSP1 condensates that clearly colocalized with any of these subcellular structures. Moreover, hFSP1 condensates did not colocalize with other cell organelles, such as endosomes, lysosomes, mitochondria, ubiquitin-dependent aggresomes or stress granules (G3BP1) (Extended Data Fig. 4b,c). Following treatment with icFSP1, these condensates were also detectable in H460 cells (expressing only endogenous hFSP1) and in cells with even lower expression levels than those of endogenous hFSP1 using doxycycline-dependent, scalable expression of hFSP1 (Extended Data Fig. 4d–g). We further noted that hFSP1 condensates dynamically and freely moved around and fused in cells in response to icFSP1 treatment (Fig. 3a, Extended Data Fig. 4h and Supplementary Video 3), which appeared to be reversible after washing out the inhibitor (Fig. 3b and Supplementary Video 4). To investigate the state of condensates in more detail, we established fluorescence

recovery after photobleaching (FRAP) analysis. These studies showed that only early-state condensates exhibited FRAP (Fig. 3c,d and Supplementary Video 5), in contrast to late-state condensates (Extended Data Fig. 5a,b and Supplementary Video 6).

On the basis of these liquid droplet-like properties of hFSP1, we considered that hFSP1 condensates might involve phase separation. Phase separation is a physicochemical process characterized by the reversible formation of biomolecular condensates⁷. These condensates are involved in the regulation of cellular signalling following stress and have been linked to human diseases, including cancer and neurodegeneration^{7,23–26}. In particular, phase separation is involved in the partitioning of target proteins in cancer tissue²⁷ and promotes the formation of aggregates of neurodegenerative disease-related proteins²⁸. Thus, we asked whether hFSP1 has the propensity to generate condensates in a cell-free system. To this end, hFSP1-EGFP-Strep was immunoprecipitated from transfected HEK293T cells using the Strep-tag to isolate natively myristoylated hFSP1 from cells. For condensate formation assays, polyethylene glycol (PEG) was used as a molecular crowding agent²⁹. Purified hFSP1 was reconstituted with 10% PEG, whereupon hFSP1 immediately formed viscoelastic material³⁰, in contrast to immunoprecipitated EGFP-Strep controls (Fig. 3e and Extended Data Fig. 5c,d). To investigate whether icFSP1 alone can initiate hFSP1 condensates, purified hFSP1 was reconstituted with PEG and/or icFSP1. However, hFSP1 could form condensates in the presence of PEG regardless of icFSP1. These differences in condensate formation are presumably due to the fact that cell-free and cellular conditions differ greatly and condensates can form viscoelastic material

as shown in cells. To reinforce our finding of hFSP1 condensation in a cell-free system through phase separation, we used recombinant hFSP1 without myristoylation (non-myr-FSP1) purified from *Escherichia coli*. Again, hFSP1 could form condensates in an FSP1 and PEG concentration-dependent manner (Extended Data Fig. 5e–h). Finally, we performed sedimentation assays to investigate whether hFSP1 condensates induced by PEG lead to stable viscoelastic material. Almost all hFSP1 could be recovered from supernatant fractions in pellets in the presence of PEG (Extended Data Fig. 5i,j), suggesting that hFSP1 has the propensity to form condensates induced by phase separation.

Structural basis of droplet formation

Phase separation can lead to formation of membrane-less compartments in cells, where multivalent interactions, typically involving intrinsically disordered regions (IDRs) and low-complexity regions (LCRs), are known to be critical⁷. Phase separation predictors³¹ revealed that hFSP1 contains two putative IDRs and one LCR in its sequence (Extended Data Fig. 6a), which may be required for condensate formation through phase separation. To analyse in detail the role of these predicted domains, the following series of hFSP1 deletion mutants was generated: Δ IDR1, Δ LCR, Δ N (Δ IDR1 and Δ LCR) and Δ IDR2 (Fig. 4a). Two additional mutants were generated in which membrane localization is known to be affected^{4,5}: (1) the G2A mutant, which is a myristoylation-defective mutant with strongly affected localization, abrogating the ferroptosis-suppressive function of FSP1 (ref. 5), and (2) the Lyn11–G2A mutant, which contains the membrane-targeting Lyn11 sequence fused N-terminally to FSP1^{G2A} and can suppress ferroptosis⁴. After icFSP1 treatment, only wild-type hFSP1 and Lyn11–hFSP1^{G2A} changed their subcellular localization to form hFSP1 condensates, and all other mutants did not undergo hFSP1 condensate formation following icFSP1 treatment (Fig. 4b). In line with this, pretreatment of cells with the myristoylation inhibitor IMP-1088 also abrogated hFSP1 condensation in cells (Extended Data Fig. 6b). To investigate whether the hFSP1 deletion mutants might have the propensity to form condensates in a cell-free system, purified hFSP1 mutants from transfected HEK293T cells were reconstituted with 10% PEG. Only wild-type hFSP1 and the G2A and Lyn11–G2A mutants formed condensates in the presence of PEG, whereas the IDR and LCR deletion mutants did not form condensates (Extended Data Fig. 6c). Next, we produced recombinant hFSP1 with myristoylation (myr-FSP1) purified from *E. coli* (Extended Data Fig. 6d) to test whether myristoylation may afford in vitro phase separation induced by PEG, lower salt concentrations and icFSP1 (Extended Data Fig. 6e,f). PEG and lower salt concentrations seemed to facilitate phase separation of myristoylated hFSP1 in vitro, whereas icFSP1 alone did not induce phase separation, suggesting that the cellular context (that is, other binding partners, the membrane environment, post-translational modifications, etc.) is important for phase separation in vitro. Furthermore, phase separation of myristoylated hFSP1 could be induced by icFSP1, whereas non-myristoylated hFSP1^{G2A} did not form condensates, even when hFSP1 condensates of the wild-type enzyme were present in Pfa1 cells (Extended Data Fig. 6g). These data imply that the presence of a myristoylation tag facilitates condensate formation, as seen for other myristoylated proteins such as the enhancer of zeste 2 (EZH2) polycomb repressive complex 2 subunit³². Moreover, myristoylation may function as a sticker enhancing polyphasic linkage^{33,34} for phase separation that is modulated by icFSP1, as a ligand.

To investigate the potential ferroptosis-suppressive functions of these mutants, cell viability experiments were performed using RSL3 and TAM-inducible *Gpx4* knockout (Extended Data Fig. 6h,i). These analyses confirmed that only wild-type hFSP1 and Lyn11–hFSP1^{G2A} could efficiently suppress ferroptosis. Hence, these data indicate that the IDRs and LCR may be required for the ferroptosis-suppressive role of FSP1, with icFSP1-induced ferroptosis triggered by hFSP1 condensation through phase separation.

S187, L217 and Q319 afford condensation

Because icFSP1 was specific for the human enzyme and did not inhibit its mouse counterpart (Extended Data Fig. 2), we addressed the underlying molecular mechanisms that may account for this species-specific inhibitory activity (Extended Data Fig. 7a). The phase separation predictor³¹ revealed that mFSP1 also harbours two predicted IDRs and an LCR with some sequence differences at its N terminus. Thus, we decided to generate a chimeric enzyme (that is, hmFSP1) consisting of the first 27 residues of hFSP1 (comprising IDR1 and the LCR) fused to residues 28–373 of mFSP1. However, hmFsp1 did not form condensates (Extended Data Fig. 7b,c), implying that other amino acids contribute to sensitizing cells to icFSP1-mediated condensate formation. On the basis of amino acid differences between the human and mouse orthologues, we generated a series of point mutations in human *FSP1* and stably expressed the corresponding mutants in Pfa1 cells (Extended Data Fig. 7d). These studies allowed us to identify the S187, L217 and Q319 residues of hFSP1 as being critical for icFSP1-dependent condensate formation and ferroptosis induction, as substitution at these sites rendered the mutant proteins resistant (Fig. 4c–e and Extended Data Fig. 7d,e). Given that (1) binding of icFSP1 to FSP1 was not affected by these substitutions (Extended Data Fig. 7f) and (2) reverse substitutions at these three positions to the human residues allowed mFSP1 to form icFSP1-dependent condensates and induce ferroptosis (Extended Data Fig. 7g–i), S187, L217 and Q319 may have critical effects on FSP1–FSP1 interactions to trigger phase separation in cells in the presence of icFSP1 (although the precise binding site of icFSP1 to wild-type hFSP1 remains to be structurally resolved).

icFSP1 impairs tumour growth in vivo

To evaluate whether icFSP1 might be applicable for in vivo use, metabolic stability and pharmacokinetics analyses were performed, showing that icFSP1 has clearly improved microsomal stability in mice and maximum concentration in mouse plasma as compared with iFSP1 (Extended Data Fig. 8a,b). Furthermore, to evaluate the efficacy of icFSP1 in a tumour-bearing mouse model, *Gpx4* and *Fsp1* double knockout B16F10 cells overexpressing hFSP1 were subcutaneously injected into female C57BL/6J mice. After tumours reached approximately 25–50 mm³ in size, mice were randomized and treated intraperitoneally with vehicle or icFSP1 twice daily. icFSP1 treatment significantly inhibited tumour growth and decreased tumour weight, without affecting body weight (Fig. 4f and Extended Data Fig. 8c). Notably, treatment of tumour-bearing mice with icFSP1 markedly increased the abundance of hFSP1 condensates and immunoreactivity to 4-hydroxynonenal (4-HNE), a lipid peroxidation breakdown product⁶ (Fig. 4g and Extended Data Fig. 8d). These data indicate that icFSP1 may trigger phase separation of hFSP1 and thereby impair tumour growth in vivo. To substantiate these findings, we established a *Gpx4* and *Fsp1* double-knockout B16F10 mutant cell line overexpressing hFSP1^{Q319K} to study condensate formation in vivo. Like the results obtained with Pfa1 and H460 cells, melanoma cell lines dependent on hFSP1^{Q319K} were resistant to icFSP1 in cultured cells and in vivo (Extended Data Fig. 8e–j); in line with this, FSP1 condensates were not observed after icFSP1 treatment in vivo (Fig. 4h and Extended Data Fig. 8h). To investigate whether icFSP1 may also work in the human context, we used a human melanoma cell line (A375) and a human lung cancer cell line (H460), which are known to express substantial levels of FSP1 (ref. 5) and which can survive after withdrawal of radical trapping agents even when *GPX4* is genetically deleted (that is, with *GPX4* knockout)³⁴. In fact, *GPX4*-knockout cells were highly sensitive to icFSP1 treatment, and the tumour growth of *GPX4*-knockout cells was substantially inhibited in the corresponding xenograft tumour model (Extended Data Fig. 9a–i). In conclusion, our results indicate that the hFSP1-specific inhibitor icFSP1 may trigger phase separation of FSP1 and synergize with canonical ferroptosis

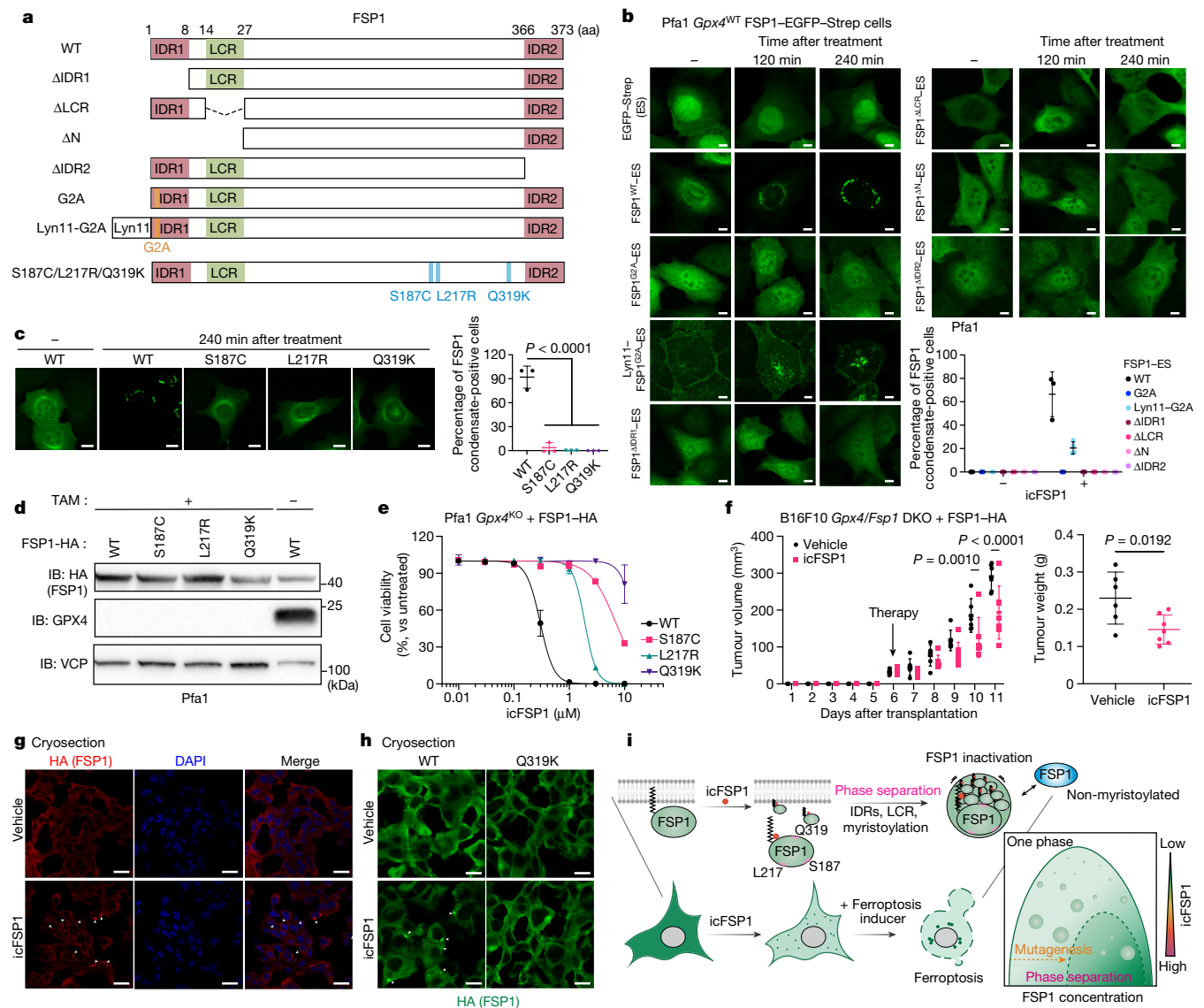


Fig. 4 | Distinct structural features of FSP1 are required for phase separation. **a**, Schematic diagram of the FSP1 mutants. **b**, Representative images of Pfa1 cells overexpressing hFSP1-EGFP-Strep mutants treated with 2.5 μM icFSP1. Scale bars, 10 μm. **c**, Representative images of Pfa1 cells overexpressing wild-type hFSP1-EGFP-Strep or the S187C, L217R or Q319K variant treated with 2.5 μM icFSP1. Scale bars, 10 μm. Data are shown as the mean ± s.d. of n = 3 or 4 different fields from one of three independent experiments (**b,c**). Statistical analysis was performed by one-way ANOVA followed by Dunnett’s multiple-comparison test (**c**). **d**, Representative immunoblot analysis of Pfa1 cells overexpressing hFSP1-HA from one of two independent experiments. **e**, Cell viability measured after treatment of *Gpx4*-knockout Pfa1 cells overexpressing wild-type hFSP1 or the S187C, L217R or Q319K variant with icFSP1 for 24 h. Data represent the mean ± s.d. of n = 3 wells from one of four independent experiments. **f**, icFSP1 inhibits tumour growth in vivo. hFSP1-HA-overexpressing

Gpx4 and *Fsp1* double knockout (*Gpx4/Fsp1* DKO) B16F10 cells were subcutaneously implanted into C57BL/6j mice. At day 6, mice were randomized and treatment was started with icFSP1 (50 mg kg⁻¹ intraperitoneally twice a day, n = 7) or vehicle (n = 6). Data represent the mean ± s.d. from one of two independent experiments. Statistical analysis was performed by two-way ANOVA followed by Bonferroni’s multiple-comparison test (left) or two-sided unpaired *t* test (right). **g**, Tumour samples from the end of the in vivo studies stained with anti-HA (hFSP1). **h**, Wild-type or Q319K hFSP1 tumour samples visualized with HA immunostaining. Representative zoomed-in images from Extended Data Fig. 8h are shown from one of three different tumour samples from one of two independent experiments (**g,h**). Arrowheads indicate FSP1 condensates (**g,h**). Scale bars, 20 μm (**g**) and 10 μm (**h**). **i**, Graphical abstract depicting icFSP1-induced FSP1 condensate formation, lipid peroxidation and ferroptosis. Image created using BioRender.com.

inhibitors to induce ferroptosis, as a viable way for efficient eradication of certain cancer entities.

Discussion

Here we report on a yet-unrecognized class of in vivo-efficacious hFSP1 inhibitors, that is, 3-phenylquinazolinones, that exhibit a unique mechanism of action in which they trigger ferroptosis through dissociation of

FSP1 from the membrane and formation of FSP1 condensates involving phase separation (Fig. 4i). Our experiments show that icFSP1-mediated phase separation requires several molecular features in hFSP1, such as N-terminal myristoylation, specific amino acid residues (S187, L217 and Q319), and the IDRs and LCR, resulting in lipid peroxidation and ferroptosis under GPX4-inhibited conditions. In the absence of an experimentally determined three-dimensional structure of FSP1, we mapped the amino acid residues that contribute to icFSP1-induced

phase separation of FSP1, on the basis of our mutational analysis, onto the structure predicted by AlphaFold2 (refs. 35,36). Although the globular fold prediction had a high-confidence IDR1 region, it was annotated as an uncertain region, in contrast to the LCR, which was predicted to exhibit an α -helical conformation with an intermediate score. The role of the LCR needs to be experimentally studied, to examine how this region may contribute to phase separation and potentially interact with the globular domain of FSP1. These interactions may well be modulated by icFSP1 and should help in understanding the underlying structural mechanisms. Moreover, considering that icFSP1 initiates formation of FSP1 condensates, including of plasma membrane-localized mutants, immediately after treatment and that icFSP1 by itself cannot trigger condensation of myristoylated FSP1 in vitro, icFSP1 may induce condensates by modulating FSP1–membrane interactions and thereby reducing the membrane-binding affinity of FSP1, similar to the KRAS inhibitor Cmpd2 (ref. 37) and other modulators (for example, Ca^{2+} for recoverin³⁸) of myristoyl–ligand switches. In support of our hypothesis, the three-dimensional structural model of FSP1 (refs. 35,36) showed that residues S187, L217 and Q319 are all located on the surface of FSP1, with Q319 in particular close to the expected membrane-binding surface. Considering the known relevance of charged and polar residues for protein–protein interactions during phase separation³⁹, changing S187 to cysteine, L217 to arginine and Q319 to lysine should increase the positive surface charge or reduce polarity and may thereby impair phase separation in cells (Extended Data Fig. 7i).

The concept in which ligands modulate the driving forces for phase separation is known as polyphasic linkage^{33,34}. Conceptually, icFSP1 would modulate the phase transition of FSP1, probably through interactions that directly or indirectly involve residues such as S187, L217 and Q319, and disruption of interactions by mutagenesis changes the phase boundary. In particular, myristoylation appears to be indispensable for this process in which icFSP1, as a ligand, preferentially binds to the myristoylated form of FSP1 (Extended Data Fig. 6g).

Although inhibition of FSP1 alone is generally not sufficient to drive cancer cell death through ferroptosis^{5,19}, a subset of cancer cell lines can potentially be sensitive to FSP1 inhibition alone under certain conditions, as was observed for HT-1080 cells. In this respect, database analysis might be helpful to predict the sensitivity of cancer cell lines to FSP1 inhibition (Extended Data Fig. 10). In light of the fact that *Fsp1*-knockout mice are fully viable⁶ and that icFSP1 does not show any observed off-target activity and does not affect body weight even at high concentrations (Extended Data Figs. 1 and 8), FSP1 should be regarded as an attractive target for tumour treatment. Thus, future studies should be geared to developing pharmacological approaches that simultaneously target both the cyst(e)ine–GSH–GPX4 node and the FSP1 system, allowing for efficient tumour cell eradication by triggering ferroptosis as a new anti-cancer paradigm.

Online content

Any methods, additional references, Nature Portfolio reporting summaries, source data, extended data, supplementary information, acknowledgements, peer review information; details of author contributions and competing interests; and statements of data and code availability are available at <https://doi.org/10.1038/s41586-023-06255-6>.

- Dixon, S. J. et al. Ferroptosis: an iron-dependent form of nonapoptotic cell death. *Cell* **149**, 1060–1072 (2012).
- Viswanathan, V. S. et al. Dependency of a therapy-resistant state of cancer cells on a lipid peroxidase pathway. *Nature* **547**, 453–457 (2017).
- Hangauer, M. J. et al. Drug-tolerant persister cancer cells are vulnerable to GPX4 inhibition. *Nature* **551**, 247–250 (2017).
- Bersuker, K. et al. The CoQ oxidoreductase FSP1 acts parallel to GPX4 to inhibit ferroptosis. *Nature* **575**, 688–692 (2019).
- Doll, S. et al. FSP1 is a glutathione-independent ferroptosis suppressor. *Nature* **575**, 693–698 (2019).

- Mishima, E. et al. A non-canonical vitamin K cycle is a potent ferroptosis suppressor. *Nature* <https://doi.org/10.1038/s41586-022-05022-3> (2022).
- Alberti, S., Gladfelter, A. & Mittag, T. Considerations and challenges in studying liquid–liquid phase separation and biomolecular condensates. *Cell* **176**, 419–434 (2019).
- Jiang, X., Stockwell, B. R. & Conrad, M. Ferroptosis: mechanisms, biology and role in disease. *Nat. Rev. Mol. Cell Biol.* <https://doi.org/10.1038/s41580-020-00324-8> (2021).
- Stockwell, B. R. et al. Ferroptosis: a regulated cell death nexus linking metabolism, redox biology, and disease. *Cell* **171**, 273–285 (2017).
- Angeli, J. P. F., Shah, R., Pratt, D. A. & Conrad, M. Ferroptosis inhibition: mechanisms and opportunities. *Trends Pharmacol. Sci.* **38**, 489–498 (2017).
- Friedmann Angeli, J. P., Krysko, D. V. & Conrad, M. Ferroptosis at the crossroads of cancer-acquired drug resistance and immune evasion. *Nat. Rev. Cancer* **19**, 405–414 (2019).
- Nakamura, T. et al. The mitochondrial Ca^{2+} uptake regulator, MICU1, is involved in cold stress-induced ferroptosis. *EMBO Rep.* **22**, e51532 (2021).
- Ubellacker, J. M. et al. Lymph protects metastasizing melanoma cells from ferroptosis. *Nature* <https://doi.org/10.1038/s41586-020-2623-z> (2020).
- Rodriguez, R., Schreiber, S. L. & Conrad, M. Persister cancer cells: iron addiction and vulnerability to ferroptosis. *Mol. Cell* <https://doi.org/10.1016/j.molcel.2021.12.001> (2021).
- Wang, W. et al. CD8⁺ T cells regulate tumour ferroptosis during cancer immunotherapy. *Nature* **569**, 270–274 (2019).
- Lovering, F., Bikker, J. & Humblet, C. Escape from flatland: increasing saturation as an approach to improving clinical success. *J. Med. Chem.* **52**, 6752–6756 (2009).
- Sander, T., Frey, J., von Korff, M. & Rufener, C. DataWarrior: an open-source program for chemistry aware data visualization and analysis. *J. Chem. Inf. Model.* **55**, 460–473 (2015).
- Seiler, A. et al. Glutathione peroxidase 4 senses and translates oxidative stress into 12/15-lipoxygenase dependent- and AIF-mediated cell death. *Cell Metab.* **8**, 237–248 (2008).
- Zheng, J. et al. Sorafenib fails to trigger ferroptosis across a wide range of cancer cell lines. *Cell Death Dis.* **12**, 698 (2021).
- Shimada, K. et al. Global survey of cell death mechanisms reveals metabolic regulation of ferroptosis. *Nat. Chem. Biol.* **12**, 497–503 (2016).
- Gaschler, M. M. et al. FINO2 initiates ferroptosis through GPX4 inactivation and iron oxidation. *Nat. Chem. Biol.* **14**, 507–515 (2018).
- Eaton, J. K. et al. Selective covalent targeting of GPX4 using masked nitrile-oxide electrophiles. *Nat. Chem. Biol.* **16**, 497–506 (2020).
- Xiao, Q., McAtee, C. K. & Su, X. Phase separation in immune signalling. *Nat. Rev. Immunol.* <https://doi.org/10.1038/s41577-021-00572-5> (2021).
- Zbinden, A., Pérez-Berlanga, M., De Rossi, P. & Polyimenidou, M. Phase separation and neurodegenerative diseases: a disturbance in the force. *Dev. Cell* **55**, 45–68 (2020).
- Boija, A., Klein, I. A. & Young, R. A. Biomolecular condensates and cancer. *Cancer Cell* **39**, 174–192 (2021).
- Watanabe, K. et al. Cells recognize osmotic stress through liquid–liquid phase separation lubricated with poly(ADP-ribose). *Nat. Commun.* <https://doi.org/10.1038/s41467-021-21614-5> (2021).
- Klein, I. A. et al. Partitioning of cancer therapeutics in nuclear condensates. *Science* **368**, 1386–1392 (2020).
- Boyko, S. & Surewicz, W. K. Tau liquid–liquid phase separation in neurodegenerative diseases. *Trends Cell Biol.* **32**, 611–623 (2022).
- Annunziata, O. et al. Effect of polyethylene glycol on the liquid–liquid phase transition in aqueous protein solutions. *Proc. Natl Acad. Sci. USA* **99**, 14165–14170 (2002).
- Mittag, T. & Pappu, R. V. A conceptual framework for understanding phase separation and addressing open questions and challenges. *Mol. Cell* **82**, 2201–2214 (2022).
- Piovesan, D. et al. MobiDB: intrinsically disordered proteins in 2021. *Nucleic Acids Res.* **49**, D361–D367 (2021).
- Zhang, J. et al. Myristoylation-mediated phase separation of EZH2 compartmentalizes STAT3 to promote lung cancer growth. *Cancer Lett.* **516**, 84–98 (2021).
- Wyman, J. & Gill, S. J. Ligand-linked phase changes in a biological system: applications to sickle cell hemoglobin. *Proc. Natl Acad. Sci. USA* **77**, 5239–5242 (1980).
- Ruff, K. M., Dar, F. & Pappu, R. V. Polyphasic linkage and the impact of ligand binding on the regulation of biomolecular condensates. *Biophys. Rev.* **2**, 021302 (2021).
- Jumper, J. et al. Highly accurate protein structure prediction with AlphaFold. *Nature* **596**, 583–589 (2021).
- Mirdita, M. et al. ColabFold: making protein folding accessible to all. *Nat. Methods* **19**, 679–682 (2022).
- Marshall, C. B. et al. Inhibition of K-RAS4B by a unique mechanism of action: stabilizing membrane-dependent occlusion of the effector-binding site. *Cell Chem. Biol.* **25**, 1327–1336 (2018).
- Ames, J. B. et al. Molecular mechanics of calcium–myristoyl switches. *Nature* **389**, 198–202 (1997).
- Boeynaems, S. et al. Protein phase separation: a new phase in cell biology. *Trends Cell Biol.* **28**, 420–435 (2018).

Publisher's note Springer Nature remains neutral with regard to jurisdictional claims in published maps and institutional affiliations.



Open Access This article is licensed under a Creative Commons Attribution 4.0 International License, which permits use, sharing, adaptation, distribution and reproduction in any medium or format, as long as you give appropriate credit to the original author(s) and the source, provide a link to the Creative Commons licence, and indicate if changes were made. The images or other third party material in this article are included in the article's Creative Commons licence, unless indicated otherwise in a credit line to the material. If material is not included in the article's Creative Commons licence and your intended use is not permitted by statutory regulation or exceeds the permitted use, you will need to obtain permission directly from the copyright holder. To view a copy of this licence, visit <http://creativecommons.org/licenses/by/4.0/>.

© The Author(s) 2023

Article

Methods

Chemicals

Lip-1 (Selleckchem, cat. no. S7699), doxycycline (Dox; Sigma, cat. no. D9891), RSL3 (Cayman, cat. no. 19288), BSO (Sigma, cat. no. B2515), iFSP1 (ChemDiv, cat. no. 8009-2626), icFSP1 (ChemDiv, cat. no. L892-0224 or custom synthesis by Intonation Research Laboratories), erastin (Merck, cat. no. 329600), ML210 (Cayman, cat. no. Cay23282-1), FIN56 (Cayman, cat. no. Cay25180-5), FINO2 (Cayman, cat. no. Cay25096-1), deferoxamine mesylate salt (DFO; Sigma, cat. no. 138-14-7), ferrostatin-1 (Fer-1; Sigma, cat. no. SML0583), zVAD-FMK (zVAD; Enzo Life Sciences, cat. no. ALX-260-02), necrostatin-1s (Nec-1s; Enzo Life Sciences, cat. no. BV-2263-5), MCC950 (Sigma, cat. no. 5381200001), olaparib (Selleckchem, cat. no. S1060), staurosporine (STS; Cayman, cat. no. 81590), recombinant human tumour necrosis factor (TNF; R&D Systems, cat. no. NBP2-35076), Smac mimic (BV-6; Selleckchem, cat. no. S7597), nigericin (Thermo Fisher, cat. no. N1495), IMP-1088 (Cayman, cat. no. Cay25366-1) and lipopolysaccharide (LPS; Sigma, cat. no. L2880) were used in this study.

Mice

Five- to six-week-old female C57BL/6J and athymic nude mice were obtained from Charles River, and 6- to 7-week-old mice were used for the experiments. All mice were kept under standard conditions with water and food provided ad libitum and in a controlled environment (22 ± 2 °C, $55\% \pm 5\%$ humidity, 12-h light/12-h dark cycle) in the Helmholtz Munich animal facility under SPF-IVC standard conditions. All experiments were performed in compliance with the German Animal Welfare Law and were approved by the institutional committee on animal experimentation and the government of Upper Bavaria (ROB-55.2-2532.Vet_02-17-167).

Cell lines

TAM-inducible *Gpx4*-knockout mouse immortalized fibroblasts (referred to as Pfa1 cells) were reported previously¹⁸. Genomic *Gpx4* deletion can be achieved by TAM-inducible activation of Cre recombinase using the CreER^{T2}/*loxP* system. HT-1080, 786-O, A375, NCI-H460 (H460), MDA-MB-436, HT-29, B16F10, and 4T1 cells were purchased from ATCC. THP-1 cells were obtained from DSMZ. Human PBMC cells were purchased from Tebu-bio (cat. no. 088SER-PBMC-F). SUDHL5, SUDHL6, DOHH2 and OCI-Ly19 cells were a gift from S. Hailfinger. Rat1 cells were a gift from Medizinische Hochschule Hannover. Pfa1, HT-1080, 786-O, A375, HT-29, Rat1 and B16F10 cells were cultured in high-glucose DMEM (4.5 g l^{-1} glucose) with 10% FBS, 2 mM L-glutamine and 1% penicillin-streptomycin. H460, MDA-MB-436, THP-1, PBMC, SUDHL5, SUDHL6, DOHH2 and 4T1 cells were cultured in RPMI GlutaMax with 10% FBS and 1% penicillin-streptomycin. OCI-Ly19 cells were cultured in IMDM with 10% FBS and 1% penicillin-streptomycin. To generate cell lines with stable overexpression, appropriate antibiotics ($1 \mu\text{g ml}^{-1}$ puromycin, $10 \mu\text{g ml}^{-1}$ blasticidin and $0.5\text{--}1.0 \text{ mg ml}^{-1}$ G418) were used. *GPX4*-knockout human A375 and H460 cells were cultured in the presence of $1 \mu\text{M}$ Lip-1 for maintenance. All cells were cultured at 37 °C with 5% CO₂ and verified to be negative for mycoplasma.

Cell viability assays

Cells were seeded on 96-well plates and cultured overnight. All cell number conditions for each cell line are described in Supplementary Table 1. The next day, the medium was changed to medium containing the following compounds: RSL3, ML210, erastin, FIN56, FINO2, BSO, iFSP1, icFSP1, Lip-1, DFO, Fer-1, zVAD, Nec-1s, MCC950, olaparib, STS, TNF, Smac mimic or nigericin at the indicated concentrations. For TAM and Dox treatment, cells were seeded with compounds at the same time. Cell viability was determined 1 h (for nigericin), 24–48 h (for RSL3, ML210, erastin, FIN56, FINO2, iFSP1, icFSP1, STS, TNF, Smac mimic and zVAD) or 72 h (for BSO, icFSP1, TAM and Dox) after the start of treatment

using AquaBluer (MultiTarget Pharmaceuticals, cat. no. 6015) as an indicator of viable cells according to the manufacturer's protocol. For apoptosis induction, HT-1080 cells were incubated with different concentrations of STS for 24 h. For necroptosis induction, HT-29 cells were incubated with different concentrations of TNF with Smac mimic (400 nM) and zVAD ($30 \mu\text{M}$) for 24 h. For pyroptosis induction, THP-1 cells stimulated with LPS ($1 \mu\text{g ml}^{-1}$, 2 h) were incubated with nigericin for 1 h. For ferroptosis induction, cells were incubated with ferroptosis inducers for 24–72 h.

As readout, fluorescence was measured at an excitation/emission wavelength of 540/590 nm using a SpectraMax M5 microplate reader with SoftMax Pro v.7 (Molecular Devices) after 4 h of incubation with AquaBluer in normal cell culture conditions. The relative cell viability (%) was calculated as follows: (fluorescence of samples – background)/(fluorescence of appropriate control samples – background) \times 100.

LDH release assays

Cells were seeded on 96-well plates and cultured overnight. The next day, the medium was changed to medium containing compounds and cells were incubated for another 24 h. Cell death rates were measured using the Cytotoxicity Detection Kit (LDH) (Roche, cat. no. 11644793001) in principle following the manufacturer's protocol. In brief, cell culture supernatant was collected as a medium sample. Cells were then lysed with PBS containing 0.1% Triton X-100 as a lysate sample. The medium and lysate samples were individually mixed with reagents on microplates, and the absorbance was measured at 492 nm using a SpectraMax M5 microplate reader after incubation for 15–30 min at room temperature. The cell death ratio was calculated by LDH release (%) as follows: (absorbance of medium samples – background)/((absorbance of lysate samples – background) + (absorbance of medium samples – background)) \times 100.

Screening of FSP1 inhibitors

Wild-type and *Gpx4*-knockout Pfa1 cells stably overexpressing hFSP1 were seeded on separate 384-well plates (500 cells per well) and screened with a library of small molecule inhibitor compounds as reported previously⁵. Cell viability of the different cell lines was assessed 48 h after the start of treatment using AquaBluer. Compounds showing selective lethality in *Gpx4*-knockout Pfa1 cells stably overexpressing hFSP1 were then validated in cell viability assays and in vitro FSP1 enzymatic assays.

Lipid peroxidation assays

For lipid peroxidation assays, 100,000 cells per well were seeded on a 12-well plate 1 day before the experiments. The next day, cells were treated with $2.5 \mu\text{M}$ icFSP1 for 3 h and then incubated with $1.5 \mu\text{M}$ C11-BODIPY 581/591 (Invitrogen, cat. no. D3861) for 30 min in a 5% CO₂ atmosphere at 37 °C. Subsequently, cells were washed once with PBS, trypsinized and then resuspended in $500 \mu\text{l}$ PBS. Cells were passed through a $40\text{-}\mu\text{m}$ cell strainer and analysed with a flow cytometer (CytOFLEX, Beckman Coulter) with a 488-nm laser for excitation. Data were collected from the FITC detector (for the oxidized form of BODIPY) with a 525/40-nm bandpass filter and from the PE detector (for the reduced form of BODIPY) with a 585/42-nm bandpass filter using CytExpert v.2.4 (Beckman Coulter). At least 10,000 events were analysed per sample. Data were analysed using FlowJo software (FlowJo). The ratio of fluorescence of C11-BODIPY 581/591 (lipid peroxidation) (FITC/PE ratio (oxidized/reduced ratio)) was calculated as follows¹²: (median FITC-A fluorescence – median FITC-A fluorescence of unstained samples)/(median PE-A fluorescence – median PE-A fluorescence of unstained samples). An example gating strategy is shown in Supplementary Fig. 1.

Oxilipidomics analysis

Two million cells were seeded on 15-cm dishes 1 day before the experiments. The next day, cells were treated with $5 \mu\text{M}$ icFSP1 to induce lipid

peroxidation. Five hours later, cells were collected, sampled to liquid nitrogen and stored at -80°C . Lipids from cells were extracted using the methyl-*tert*-butyl ether (MTBE) method⁴⁰. In brief, cell pellets collected in PBS containing dibutylhydroxytoluene (BHT; $100\ \mu\text{M}$) and diethylenetriamine pentaacetate (DTPA; $100\ \mu\text{M}$) were washed and centrifuged. SPLASH LIPIDOMIX (Avanti Polar Lipids) was added ($2.5\ \mu\text{l}$), and samples were incubated on ice for 15 min. After addition of ice-cold methanol ($375\ \mu\text{l}$) and MTBE ($1,250\ \mu\text{l}$), samples were vortexed and incubated for 1 h at 4°C (orbital shaker, 32 rpm). Phase separation was induced by adding water ($375\ \mu\text{l}$), and samples were vortexed, incubated for 10 min at 4°C (orbital shaker, 32 rpm) and centrifuged to separate the organic and aqueous phases (10 min, 4°C , $1,500g$). The organic phase was collected, dried in a vacuum evaporator and redissolved in $100\ \mu\text{l}$ isopropanol. Lipid extracts were transferred to glass vials for LC-MS analysis.

Reversed-phase LC was carried out on a Shimadzu ExionLC equipped with an Accucore C30 column ($150 \times 2.1\ \text{mm}$, $2.6\ \mu\text{m}$, $150\ \text{\AA}$; Thermo Fisher Scientific). Lipids were separated by gradient elution with solvent A (1:1 (v/v) acetonitrile/water) and solvent B (85:15:5 (v/v/v) isopropanol/acetonitrile/water), both containing $5\ \text{mM}\ \text{NH}_4\text{HCO}_2$ and 0.1% (v/v) formic acid. Separation was performed at 50°C with a flow rate of $0.3\ \text{ml}\ \text{min}^{-1}$ using the following gradient: 0–20 min, increase from 10% to 86% B (curve 4); 20–22 min, increase from 86% to 95% B (curve 5); 22–26 min, 95% isocratic; 26–26.1 min, decrease from 95% to 10% B (curve 5), which was followed by re-equilibration for 5 min at 10% B⁶. MS analysis was performed on a Sciex 7500 system equipped with an electrospray ionization (ESI) source and operated in negative-ion mode. Products were analysed in MRM mode monitoring transitions from the parent ion to the daughter ion, as described in Supplementary Table 1, with the following parameters: TEM, 500°C ; GS1, 40; GS2, 70; CUR, 40; CAD, 9; IS, $-3,000\ \text{V}$.

The area under the curve for the parent to daughter ion transition was integrated and normalized by appropriate lipid species, PC(15:0/18:1(d7)) or PE(15:0/18:1(d7)), from the SPLASH LIPIDOMIX Mass Spec Standard (Avanti Polar Lipids). Normalized peak areas were further log transformed and auto-scaled in MetaboAnalyst online platform v.5.0 (<https://www.metaboanalyst.ca>)⁴¹. Zero values were replaced by 0.2 times the minimum value detected for a given oxidized lipid in the samples. Oxidized lipids showing a significant difference (ANOVA, adjusted *P* value (false discovery rate (FDR)) cut-off of 0.05) between samples were used for the heat maps. The heat maps were created in GraphPad Prism 9. The colour scheme corresponds to auto-scaled log-transformed fold change relative to the mean log value for the samples.

Cell lysis and immunoblotting

Cells were lysed in LCW lysis buffer (0.5% Triton X-100, 0.5% sodium deoxycholate salt, $150\ \text{mM}\ \text{NaCl}$, $20\ \text{mM}\ \text{Tris-HCl}$, $10\ \text{mM}\ \text{EDTA}$ and $30\ \text{mM}\ \text{sodium pyrophosphate tetrabasic decahydrate}$) supplemented with protease and phosphatase inhibitor cocktail (cOmplete and phoSTOP; Roche, cat. nos. 04693116001 and 4906837001) and centrifuged at $20,000g$ for 1 h at 4°C . The supernatant was sampled by adding $6\times$ SDS sample buffer ($375\ \text{mM}\ \text{Tris-HCl}\ \text{pH}\ 6.8$, 9% SDS, 50% glycerol, 9% β -mercaptoethanol and 0.03% bromophenol blue). After heating at 98°C (55°C for xCT) for 3 min, the samples were resolved on 12% SDS-PAGE gels (Bio-Rad, cat. no. 4568043 or 4568046) and subsequently electroblotted onto PVDF membrane (Bio-Rad, cat. no. 170-4156). The membranes were blocked with 5% skim milk (Roth, cat. no. T145.2) in TBS-T ($20\ \text{mM}\ \text{Tris-HCl}$, $150\ \text{mM}\ \text{NaCl}$ and 0.1% Tween-20) and then probed with primary antibodies, diluted in first antibody dilution buffer (TBS-T with 5% BSA and 0.1% NaN_3 (Sigma, cat. no. S2002)), against GPX4 (1:1,000; Abcam, cat. no. ab125066), valosin-containing protein (VCP; 1:1,000; Abcam, cat. no. ab11433 or ab109240), Flag tag (1:5,000; Cell Signaling Technology, cat. no. 2368), HA tag (1:1,000; clone 3F10, homemade), hFSP1 (1:1,000;

Santa Cruz, cat. no. sc-377120, AMID), mFSP1 (1:500; clone AIFM2 1A1, rat IgG2a), hFSP1 (1:10; clone 6D8, rat IgG2a), mFSP1 (1:5; clone AIFM2 14D7, rat IgG2b), human SLC7A11 (1:10; rat IgG2a monoclonal antibody against an N-terminal peptide of human xCT, clone 3A12-1-1, developed in house), mouse SLC7A11 (1:1,000; Cell Signaling Technology, cat. no. 98051), ACSL4 (1:1,000; clone A-5, Santa Cruz, cat. no. sc-271800) or β -actin-HRP (1:50,000; Sigma, cat. no. A3854) diluted in 5% skim milk in TBS-T overnight. After membranes were washed and probed with appropriate secondary antibodies diluted in 5% skim milk in TBS-T, antibody-antigen complexes were detected with the ChemiDoc Imaging System with Image Lab v.6.0 (Bio-Rad). Representative images are shown after adjustment to the appropriate brightness and angle using ImageJ/Fiji software (v.1.52 and v.1.53).

Expression and sgRNA plasmid construction

All plasmids for this study were constructed using standard molecular biology techniques and verified by sequencing as follows. A human *FSP1* cDNA (NM_001198696.2, 1008:C>T) was cloned from previously reported vectors⁵. Codon-optimized sequences for *Mus musculus* (mouse) *FSP1* (NP_001034283.1), *Rattus norvegicus* (rat) *FSP1* (NP_001132955.1), *Gallus gallus* (chicken) *FSP1* (XP_421597.1) and *Xenopus laevis* (frog) *FSP1* (NP_001091397.1) were cloned into the p442 vector. Codon-optimized sequences for human *FSP1* (NP_001185625.1) and mouse *Fsp1* (NP_001034283.1) were synthesized by TWIST Bioscience and subcloned into 141-IRES-puro vector. To generate deletion mutants or perform subcloning, desired DNA sequences were first amplified using KOD One PCR master mix (Sigma, cat. no. KMM-201NV) or PrimeSTAR Max DNA polymerase master mix (Takara Bio, cat. no. R045A) and resulting PCR products were purified by Wizard SV Gel&PCR Clean-up System (Promega, cat. no. A9285) according to the manufacturer's protocol. Ligation reactions of PCR products or single guide RNA (sgRNA) duplexes with digested vectors were performed using T4 ligase (NEB, cat. no. M0202L) or In-Fusion cloning enzymes (Takara Bio, cat. no. 639649 or 638948) according to the manufacturer's protocol. Subsequently, reaction mixtures were transformed into stable competent cells (NEB, cat. no. C3040H). Plasmids were isolated using the QIAprep Spin Miniprep kit (Qiagen, cat. no. 27106) according to the manufacturer's protocol; the correct inserts of plasmids were confirmed by sequencing.

Lentiviral production and transduction

HEK293T cells were used to produce lentiviral particles. The ecotropic envelope protein of murine leukaemia virus (MLV) was used for mouse-derived cells, while the amphitropic envelope protein VSV-G was used for human-derived cells. A third-generation lentiviral packaging system consisting of transfer plasmids, envelope plasmids (pEcoEnv-IRES-puro or pHCMV-EcoEnv (ecotropic particles) or pMD2.G (pantropic particles)) and packaging plasmids (pMDLg_pRRE and pRSV_Rev or psPAX2) was co-lipofected into HEK293T cells using transfection reagent (PEI MAX (Polysciences, cat. no. 24765) or X-tremeGENE HP reagent (Roche, cat. no. 06366236001)). Viral particle-containing cell culture supernatant was collected 48–72 h after transfection, filtered through a $0.45\text{-}\mu\text{m}$ PVDF filter (Millipore, cat. no. SLHV033RS) and then used for lentiviral transduction.

Cells were seeded on 12- or 6-well plates in medium supplemented with $10\ \mu\text{g}\ \text{ml}^{-1}$ protamine sulfate and lentivirus was incubated with cells overnight. The next day, the cell culture medium was replaced with fresh medium containing appropriate antibiotics, such as puromycin (Gibco, cat. no. A11138-03; $1\ \mu\text{g}\ \text{ml}^{-1}$), blasticidin (Invitrogen, cat. no. A1113903; $10\ \mu\text{g}\ \text{ml}^{-1}$) or G418 (Invitrogen, cat. no. 10131-035; $1\ \text{mg}\ \text{ml}^{-1}$) and cells were cultured until non-transduced cells were dead.

CRISPR-Cas9-mediated gene knockout

sgRNAs were designed to target critical exons of the genes of interest, and gene knockout was confirmed by western blotting. sgRNAs were

Article

cloned into BsmBI-digested lentiCRISPRv2-blast, lentiCRISPRv2-puro and lentiGuide-neo vectors (Addgene, cat. nos. 98293, 98290 and 139449). All sequences for sgRNAs are listed in Supplementary Table 1.

To generate knockout cells, MDA-MB-436, 786-O, A375, H460, B16F10 and 4T1 cells were transiently co-transfected with the desired sgRNAs expressed from lentiCRISPRv2-blast and lentiCRISPRv2-puro using X-tremeGENE HP reagent as described previously^{6,42}. One day after transfection, selection was started with puromycin (1 $\mu\text{g ml}^{-1}$) and blasticidin (10 $\mu\text{g ml}^{-1}$). After selection for 2–3 days, single-cell clones were isolated, and knockout clones were validated by immunoblotting and sequencing of genomic DNA.

To generate Dox-inducible knockout cells, lentiviruses from pCW-Cas9-blast (Addgene, cat. no. 83481) were transduced into HT-1080 cells followed by selection and establishment of single-cell clones as described previously⁶. Lentiviruses generated from lentiGuide-neo vectors harbouring sgRNAs targeting FSP1 were transduced into HT-1080 pCW-Cas9-blast cells, followed by selection with G418 as above. After Dox induction, loss of FSP1 expression was confirmed by immunoblotting.

To generate Dox-inducible FSP1-EGFP-expressing cells, H460 FSP1-knockout cells were transduced with lentivirus (pCW-FSP1^{WT}-EGFP-blast or pCW-FSP1^{Q319K}-EGFP-blast). After Dox treatment of cells, scalable FSP1 expression was confirmed by immunoblotting.

Stable expression by transfection

Gpx4-knockout 4T1 cells and *Gpx4* and *Fsp1* double-knockout B16F10 cells were transfected with 141-IRES-puro, 141-hFSP1^{WT} or hFSP1^{Q319K}-IRES-puro and 141-mFsp1-IRES-puro vectors using X-tremeGENE HP reagent. One day after transfection, selection was started with puromycin (1 $\mu\text{g ml}^{-1}$) and Lip-1 was removed from the medium to select cells with stable FSP1 expression. To obtain cells with stable expression, cells were maintained under the selection condition.

Production and purification of FSP1 enzyme

Recombinant hFSP1 protein (non-myr-FSP1) was produced in BL21 *E. coli* and purified by affinity chromatography with a Ni-NTA system as described previously⁵.

For protein isolation by pulldown, HEK293T cells were seeded on 10- or 15-cm dishes and transfected with constructs encoding EGFP-Strep-tagged protein. After washing with PBS, cells were lysed in LCW lysis buffer supplemented with protease and phosphatase inhibitor cocktail and 1 mM dithiothreitol (DTT). Cell extracts were collected with a cell scraper and centrifuged at 20,000g for 1 h at 4 °C. Supernatants were incubated with MagStrep 'type3' XT beads (Biozol, cat. no. 2-4090-002) at 4 °C for 1–2 h. Beads were washed twice with washing buffer (100 mM Tris-HCl, 150 mM NaCl and 1 mM EDTA). EGFP-Strep-tagged proteins were eluted with elution buffer (100 mM Tris-HCl, 150 mM NaCl, 1 mM EDTA and 50 mM biotin), followed by dilution to 3 μM with TBS (50 mM Tris-HCl and 150 mM NaCl). Protein concentration was estimated from the absorbance at 280 nm measured with a UVNano spectrophotometer (Mettler Toledo). The coefficient was calculated by using Expasy ProtParam (<https://web.expasy.org/protparam/>).

Myristoylated protein was obtained by coexpressing *N*-myristoyltransferase 1 (hsNMT1) with FSP1. *E. coli* BL21 cells were transformed with constructs encoding hsNMT1 (petCDF vector, spectinomycin resistance) and FSP1 (FSP1-EGFP with a C-terminal His₆ tag, petM13, kanamycin resistance). Purification was performed as for wild-type FSP1 with a final step of gel filtration chromatography. Purified protein was obtained and confirmed by denaturing SDS gel. Confirmation of the presence of myristoylated protein was obtained with MS.

Mass spectrometry

Myristoylation was confirmed by LC-ESI-MS (Waters Synapt XS). Proteins were separated on an Acquity UPLC Protein BEH C4 column

(0.4 ml min⁻¹; buffer A, 0.1% formic acid in water; buffer B, 0.1% formic acid in acetonitrile), and data were analysed using Masslynx v.4.2 (Waters).

FSP1 enzyme activity and inhibition assays

For resazurin assays, enzyme reactions were prepared in TBS (50 mM Tris-HCl and 150 mM NaCl) containing 50 nM non-myr-FSP1, 200 μM NADH and inhibitor (iFSP1 or icFSP1). After the addition of 100 μM resazurin sodium salt (Sigma, cat. no. R7017), fluorescence intensity (*F*; excitation/emission wavelength of 540/590 nm) was measured every 1 min using a SpectraMax iD5 microplate reader with SoftMax Pro v.7 (Molecular Devices) at 37 °C. Reactions with an equivalent volume of DMSO and without resazurin were used to calculate IC₅₀ values. Curve fitting and calculation of IC₅₀ values were conducted using GraphPad Prism 9.

For NADH consumption assays, enzyme reactions were prepared in PBS (Gibco, cat. no. 14190094) containing 25 nM non-myr-FSP1, 200 μM menadione (Sigma, cat. no. M5625) or 200 μM CoQ₆ (Sigma, cat. no. D9150), and inhibitor (iFSP1 or icFSP1). After the addition of 200 μM NADH, absorbance at 340 nm at 37 °C was measured every 30 s using a SpectraMax M5 microplate reader (Molecular Devices). Reactions without NADH and without enzyme were used to normalize the results. Curve fitting was conducted using GraphPad Prism 9.

In vitro FSP1 condensation assays

Purified EGFP-Strep or hFSP1-EGFP-Strep tagged protein was diluted in TBS supplemented with 1 mM DTT. Purified Strep-tagged proteins were then mixed with PEG 3350 (Sigma, cat. no. P3640) and/or icFSP1; final concentrations of the proteins, PEG and icFSP1 are indicated in each figure legend. For confocal microscopy analysis, samples were immediately transferred onto objective slides and EGFP signal was quickly captured using an LSM880 microscope with Zen Black software (v.2.3, ZWISS) with a $\times 63$ water-immersion objective. For confocal microscopy analysis, recombinant C-terminally GFP-tagged FSP1 and myr-FSP1 were measured at a 15 μM protein concentration in PBS (pH 7.4; 300 mM NaCl) or at a 10 μM protein concentration in PBS (pH 7.4; 150 mM NaCl). Confocal fluorescence microscopy was performed at 255 °C on a Leica TCS SP8 confocal microscope using a $\times 63$ water-immersion objective. Samples were excited with a 488-nm laser (GFP) and imaged at 498–545 nm.

To measure turbidity, different concentrations of non-myr-FSP1 and PEG were reconstituted in 10 μl in a 384-well plate and the absorbance at 600 nm was measured using a SpectraMax iD5 microplate reader (Molecular Devices). To show non-myr-FSP1 condensation in PCR tubes, images were acquired using a smartphone. Representative bright-field images of non-myr-FSP1 condensates on an objective slide were captured using an Eclipse Ts2 microscope (Nikon) with a $\times 40$ objective.

For sedimentation assays, recombinant non-myr-FSP1 was mixed with the same amount of TBS with 0% or 20% PEG and 1 mM DTT and samples were centrifuged at 2,500g for 5 min. The supernatant was collected in a new tube and the pellet was resuspended in TBS supplemented with 1 mM DTT. Supernatant and resuspended non-myr-FSP1 were collected by adding 6 \times SDS sample buffer and subsequently resolved by SDS-PAGE. One gel was subjected to western blotting and probed with anti-FSP1 (1:1,000; Santa Cruz, cat. no. sc-377120, AMID). The other gel was immediately stained with Coomassie staining solution (1 mg ml⁻¹ Coomassie Brilliant Blue G-250 (Sigma, cat. no. 1154440025), 50% methanol and 10% acetic acid) for 15 min and then soaked in washing buffer (70% methanol and 7% acetic acid). The washing buffer was heated using a microwave, and the buffer was changed until protein bands gave clear signals.

In vitro saturation transfer difference experiments

Saturation transfer difference experiments were performed on a Bruker Avance III HD spectrometer at 600-MHz ¹H frequency using an H₁/N/C

triple-resonance cryogenic probe. Spectra were recorded at 10 °C with 5 µM recombinant hFSP1 (mutant) and 100-fold molar excess of icFSP1 in PBS containing 150 mM NaCl, 1% (v/v) DMSO-d₆ and 10% (v/v) D₂O for deuterium-lock. The saturation time was 2.5 s, and the on and off frequencies were 0.68 and -17 ppm, respectively. NMR spectra were processed using Topspin 4.0.6 (Bruker).

Immunocytochemistry

All confocal microscopy images were acquired using an LSM880 microscope (Zeiss) with a ×63 objective and the corresponding appropriate filter sets for fluorophores and analysed with Zen Blue software (v.3.2, ZWISS) or ImageJ/Fiji unless noted otherwise. Cells were seeded on µ-Slide 8-well slides (Ibidi, cat. no. 80826) 1 day before the experiments. The next day, the medium was changed to fresh cell culture medium supplemented with 2.5 µM icFSP1. After incubation for the indicated times, cells were fixed and stained according to the following procedure: fixation with 4% paraformaldehyde for 5–10 min; permeabilization and blocking for 15 min with 0.3% Triton X-100 and 10 mg ml⁻¹ BSA in PBS; and incubation at 4 °C overnight with primary antibodies or undiluted supernatant for anti-AIFM2 (FSP1; clone 14D7, homemade). Antibody dilutions were as follows: 1:10 for anti-YPYDVPDYA-tag (HA; clone 3F10) and 1:100 for anti-calnexin (Abcam, cat. no. ab22595), anti-GM130 (clone EP892Y, Abcam, cat. no. ab52649), anti-EEA1 (clone C45B10, Cell Signaling Technology, cat. no. 3288) and anti-LAMP1 (clone H4A3, Santa Cruz, cat. no. sc-20011) in primary antibody dilution buffer. Cells were further stained with appropriate fluorophore-conjugated secondary antibodies (1:500 dilution) and DAPI (1:10,000 dilution) in TBS-T or PBS for 1–2 h at room temperature, avoiding light. Finally, all samples were mounted in Aqua-/PolyMount (Polysciences, cat. no. 18606-20) and dried at 4 °C overnight. Staining of mitochondria, lipid droplets and aggresomes was performed using MitoTracker Red CMXRos (20 nM; Invitrogen, cat. no. M7512), LipidSpot 610 (1:1,000; Biotium, cat. no. 70069-T) and the Proteostat detection kit (1:10,000; Enzo, cat. no. ENZ-51035-0025), respectively, according to the manufacturer's protocol.

FRAP

Pfa1 cells (20,000 cells) were seeded on µ-Slide VI 0.4 slides (Ibidi, cat. no. 80606) 1 day before the experiments. The next day, the medium was changed to high-glucose DMEM supplemented with 10% FBS, 2 mM L-glutamine, 1% penicillin-streptomycin, 2.5 µM icFSP1 and 10 mM HEPES. After incubation with icFSP1 for 2–4 h, 2–5 rectangular areas that each contained more than three FSP1 condensates were selected as bleaching areas. One image acquired before bleaching was considered to correspond to time '0'. Subsequently, the selected areas were photobleached using the maximum intensity of the laser and FRAP was monitored at minimum intervals (-5 s) using an LSM880 microscope (Zeiss).

To quantify the FRAP rate, a region of interest (ROI) for each condensate (*i*) in the photobleached area and one condensate (*c*) in a non-photobleached area was determined using ImageJ/Fiji and the mean fluorescence intensity of condensate *i* at time *t*, $F_i(t)$ was obtained. After determining each time of fluorescence value, $F_i(t)$ was normalized by the value of $F_i(0)$ to obtain the relative fluorescence ($RF_i(t)$) of each bleached condensate area. To reflect quenching effects during observation and photobleaching, each $RF_i(t)$ value was normalized by relative fluorescence value at time *t* of condensate (*c*) in non-bleached condensate areas ($RF_c(t)$) as follows: $F_i(t) = RF_i(t)/RF_c(t) = (F_i(t)/F_i(0))/(F_c(t)/F_c(0))$. Finally, the FRAP rate (%) at time *t* in the particles was calculated as the mean of $F_i(t) \times 100$ as described previously²¹.

Live-cell imaging

For co-staining or washout analyses, Pfa1 cells (15,000–30,000 cells) were seeded on µ-Dish 35-mm low dishes (Ibidi, cat. no. 80136) and incubated overnight. The next day, the cell culture medium was changed

to FluoroBrite DMEM (Gibco, cat. no. A1896701) supplemented with 10% FBS, 2 mM L-glutamine and 1% penicillin-streptomycin. Live-cell microscopy was performed using the 3D Cell Explorer (Nanolive) with Eve v.1.8.2 software and the corresponding appropriate filter sets. During imaging, cells were maintained at 37 °C and 5% CO₂ using a temperature-controlled incubation chamber. For co-staining analysis, cells were pretreated for 1 h with 5 µM Liperfluo (Dojindo, cat. no. L248-10) and then changed to FluoroBrite DMEM containing 0.2 µg ml⁻¹ propidium iodide (Sigma, cat. no. P4170) and acquisition was started using Nanolive. After recording one image, 1 mM of icFSP1 in FluoroBrite DMEM was added to the dishes (final concentration of 10 µM) while continuing to record images. Images were acquired every 10 min for more than 4 h, and GFP, BFP and RFP filter sets were used to acquire signal. For washout experiments, high-glucose DMEM was changed to FluoroBrite DMEM before the experiments followed by data acquisition using Nanolive. After recording a few images, 0.25 mM of icFSP1 in FluoroBrite DMEM was added to the dishes (final concentration of 2.5 µM) and recording of images continued for 4 h. Thereafter, the dishes were carefully washed once with fresh FluoroBrite DMEM without icFSP1 and refilled with medium. Image acquisition was then immediately restarted. Images were recorded every 5 min for one hour; that is, the total duration of data acquisition was around 5 h.

To determine the number of condensates in cells, Pfa1 cells (15,000–20,000 cells) were seeded on µ-Slide 8-well slides (Ibidi, cat. no. 80826) and incubated overnight. The next day, the medium was changed to high-glucose DMEM supplemented with 10% FBS, 2 mM L-glutamine, 1% penicillin-streptomycin, 2.5 µM icFSP1 and Hoechst. Immediately thereafter, the focus was adjusted and Hoechst and EGFP images were recorded using an Axio Observer Z1 imaging system with VisView v.4.0 (Visitron Systems, ZWISS) with a ×20 air objective and a CCD camera (CoolSnap ES2, Photometrics) with the corresponding filter sets. During imaging, cells were maintained at 37 °C and 5% CO₂ using a temperature-controlled incubation chamber. The imaging software ImageJ/Fiji was used for visualization, and CellProfiler (v.4.1.3, Broad Institute) was used to count the condensates in each cell.

Subcutaneous tumour models

All mice were obtained from Charles River. For syngeneic subcutaneous tumour experiments, *Gpx4* and *Fsp1* double-knockout B16F10 cells stably overexpressing hFSP1-HA (1 × 10⁶ cells in 100 µl PBS) were injected subcutaneously into the right flank of 7-week-old female C57BL/6J mice. After tumours reached approximately 25–50 mm³ in size, mice were randomized and treated with vehicle or icFSP1 (50 mg kg⁻¹, Intonation) by intraperitoneal injection twice daily for 4–5 days. To generate tumour samples for staining, *Gpx4* and *Fsp1* double-knockout B16F10 cells stably expressing hFSP1^{WT}-HA or hFSP1^{Q319K}-HA (1 × 10⁶ cells in 100 µl PBS) were injected subcutaneously into the right flank of 7-week-old female C57BL/6J mice. After tumours reached approximately 25 mm³ in size, mice were randomized and treated with vehicle or icFSP1 (50 mg kg⁻¹, Intonation) by intraperitoneal injection twice daily.

For xenograft subcutaneous tumour experiments, *GPX4*-knockout A375 cells (5 × 10⁶ cells in 100 µl PBS) were injected subcutaneously into the right flank of 7-week-old female athymic nude mice. After tumours reached approximately 25–100 mm³ in size, mice were randomized and treated with vehicle or icFSP1 (50 mg kg⁻¹, Intonation) by intraperitoneal injection twice daily for the first 4 days and once daily afterwards.

For xenograft subcutaneous tumour experiments, *GPX4*-knockout H460 cells (5 × 10⁶ cells in 100 µl PBS) were injected subcutaneously into the right flank of 6-week-old female athymic nude mice. After tumours reached approximately 100 mm³ in size, mice were randomized and treated with vehicle or icFSP1 (50 mg kg⁻¹, Intonation) by intraperitoneal injection twice daily.

icFSP1 was dissolved in 45% PEG E 300 (Sigma, cat. no. 91462-1KG) and 55% PBS (Gibco, cat. no. 14190094). Tumours were measured by caliper every day, and tumour volume was calculated using the following

Article

formula: tumour volume = length × width² × 0.52. When the tumour was greater than 1,000 mm³ in size at measurement or the tumour became necrotic, tumours were considered to have reached the humane endpoint. When tumours reached the humane endpoint, the experiment was stopped and no further study was conducted.

Tumour tissue staining

Dissected tissues were fixed in 4% paraformaldehyde in PBS overnight at 4 °C. For immunofluorescence staining, fixed tissues were incubated in 20% sucrose in PBS overnight at 4 °C, followed by embedding in OCT mounting compound (TissueTek, Sakura) on dry ice and storage at –80 °C. Frozen tissues were cut into 5-µm-thick sections using a Cryostat Microm HM 560 (Thermo Fisher Scientific) at –30 °C. Tissue sections were postfixed with 1% paraformaldehyde in PBS for 10 min and subsequently fixed with 67% ethanol and 33% acetic acid for 10 min. Sections were incubated with blocking solution (5% goat serum and 0.3% Triton X-100 in PBS) for 30 min and then incubated with primary antibodies (anti-HA (clone, 3F10; 1:10; developed in house), anti-4-HNE (JalCA, cat. no. HNEJ-2; 1:50) and anti-AIFM2 (FSP1, clone 14D7; undiluted; developed in house)) diluted in blocking solution overnight at 4 °C. The next day, sections were incubated with appropriate fluorophore-conjugated secondary antibodies (goat anti-rat Alexa Fluor 488 IgG (H+L) (1:500; A-11006, Invitrogen), goat anti-mouse IgG H&L Alexa Fluor 647 (1:500; ab150115, Abcam) and donkey anti-rat IgG Alexa Fluor 555 (1:500; ab150154, Abcam)) in secondary dilution buffer (1% BSA and 0.3% Triton X-100 in PBS) for 2 h at room temperature. DNA was visualized with DAPI staining for 5 min, and slides were mounted in Aqua-/PolyMount. Images were obtained using an LSM880 microscope (Zeiss) and analysed with Zen Blue or ImageJ/Fiji software.

Pharmacokinetics and metabolic stability analyses

All studies were performed by Bienta/Enamine Ltd.

Statistical analysis

All data shown are the mean ± s.e.m. or mean ± s.d., and the number (*n*) in each figure legend represents biological or technical replicates as specified. All experiments (except those described otherwise in the legend) were performed independently at least twice. For mouse experiments, at least three animals were included per group once or twice. Two-tailed Student's *t* tests and one-way or two-way ANOVA followed by Bonferroni's, Dunnett's, Tukey's or Sidak's multiple-comparison tests were performed using GraphPad Prism 9 (GraphPad Software) (also see figure legends for more detail). The results of the statistical analyses are presented in each figure. *P* < 0.05 was considered to be statistically significant.

Reporting summary

Further information on research design is available in the Nature Portfolio Reporting Summary linked to this article.

Data availability

All data are available in the article and its Supplementary Information as well as from the corresponding author on reasonable request. Gel source images are shown in Supplementary Fig. 2. Cancer cell line data were mined from <https://depmap.org/portal/>. Prediction of the phase separation of FSP1 was conducted with <https://iupred2a.elte.hu> and <https://mobidb.bio.unipd.it>. Source data are provided with this paper.

40. Matyash, V., Liebis, G., Kurzchalia, T. V., Shevchenko, A. & Schwudke, D. Lipid extraction by methyl-*tert*-butyl ether for high-throughput lipidomics. *J. Lipid Res.* **49**, 1137–1146 (2008).
41. Chong, J., Wishart, D. S. & Xia, J. Using MetaboAnalyst 4.0 for comprehensive and integrative metabolomics data analysis. *Curr. Protoc. Bioinformatics* **68**, e86 (2019).
42. Mishima, E. et al. DHODH inhibitors sensitize to ferroptosis by FSP1 inhibition. *Nature* <https://doi.org/10.1038/s41586-023-06269-0> (2023).

Acknowledgements We are grateful to all current and former members of the Conrad laboratory for providing valuable materials and fruitful discussions. This work was supported by funding from the Deutsche Forschungsgemeinschaft (DFG) (CO 291/9-1, 461385412; and the Priority Program SPP 2306 (CO 291/9-1, 461385412; CO 291/10-1, 461507177)) to M.C. and PR 1752/3-1 to B.P., a Kekulé fellowship from the Fonds der Chemischen Industrie to C.H., the Priority Program SPP2191 to M.S., a Helmholtz Munich internal development grant and the European Research Council under the European Union's Horizon 2020 research and innovation programme (grant agreement no. GA 884754) to M.C. We thank M. Rehberg for his initial help with live-cell imaging. SUDHL5, SUDHL6, DOHH2 and OCI-Ly19 cells were kindly provided by S. Hailfinger.

Author contributions T.N., M.S., B.P. and M.C. conceived the study and wrote the manuscript. T.N. and C.H. performed in vitro phase separation experiments. T.N., D.E., J.W., E.L. and E.M. performed experiments in cells. T.N. and J.W. established and performed in vivo experiments. M.A. and B.H. performed oxilipidomic analysis. J.B. and A.S.D.M. expressed and purified recombinant FSP1 and conducted NMR experiments. All authors read and agreed on the content of the paper.

Funding Open access funding provided by Helmholtz Zentrum München - Deutsches Forschungszentrum für Gesundheit und Umwelt (GmbH).

Competing interests M.C., B.P. and T.N. hold patents for some of the compounds described herein, and M.C. and B.P. are co-founders and shareholders of ROSCUE Therapeutics GmbH. The other authors declare no competing interests.

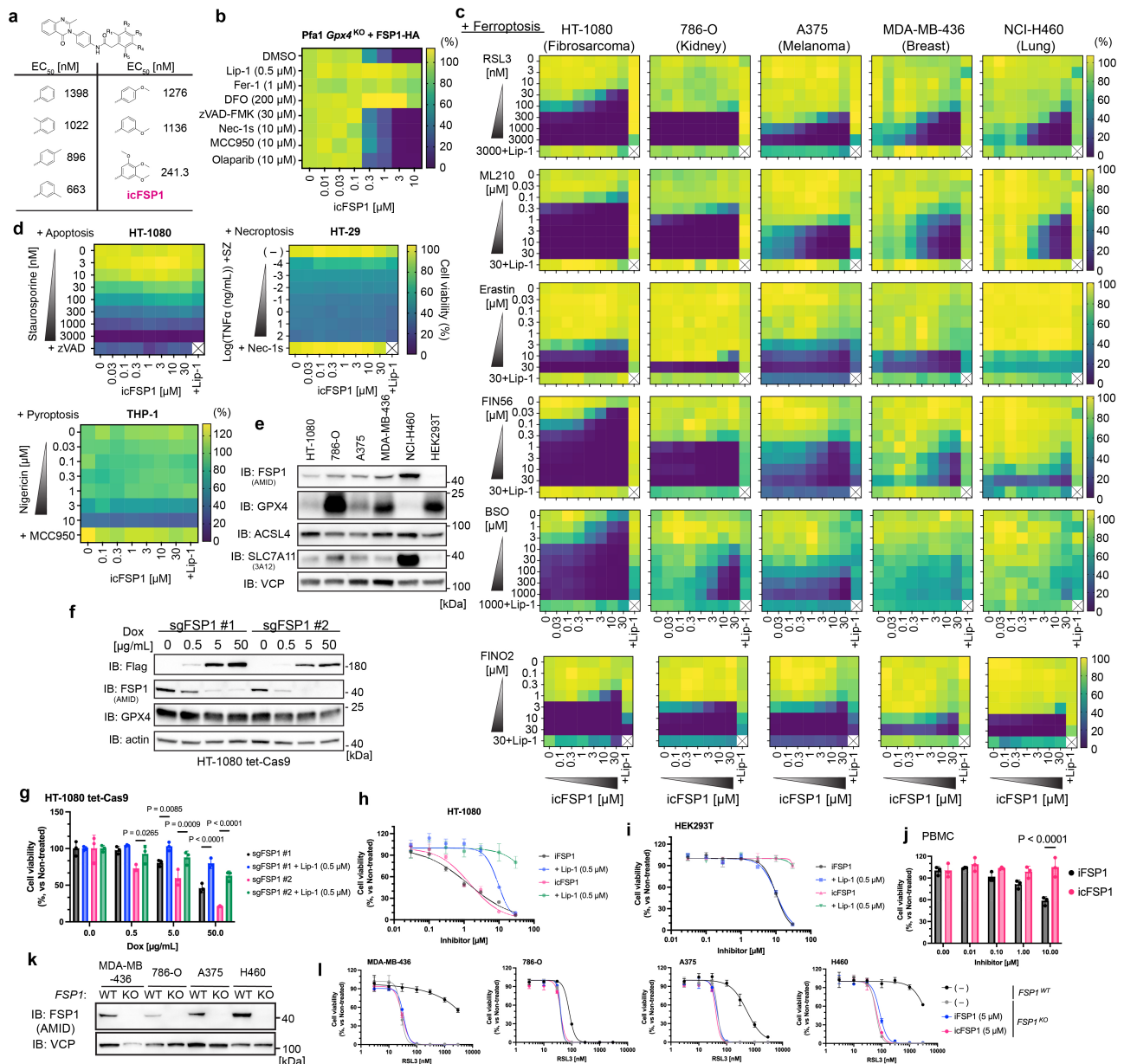
Additional information

Supplementary information The online version contains supplementary material available at <https://doi.org/10.1038/s41586-023-06255-6>.

Correspondence and requests for materials should be addressed to Marcus Conrad.

Peer review information Nature thanks Jessalyn Ubellacker and the other, anonymous, reviewer(s) for their contribution to the peer review of this work. Peer reviewer reports are available.

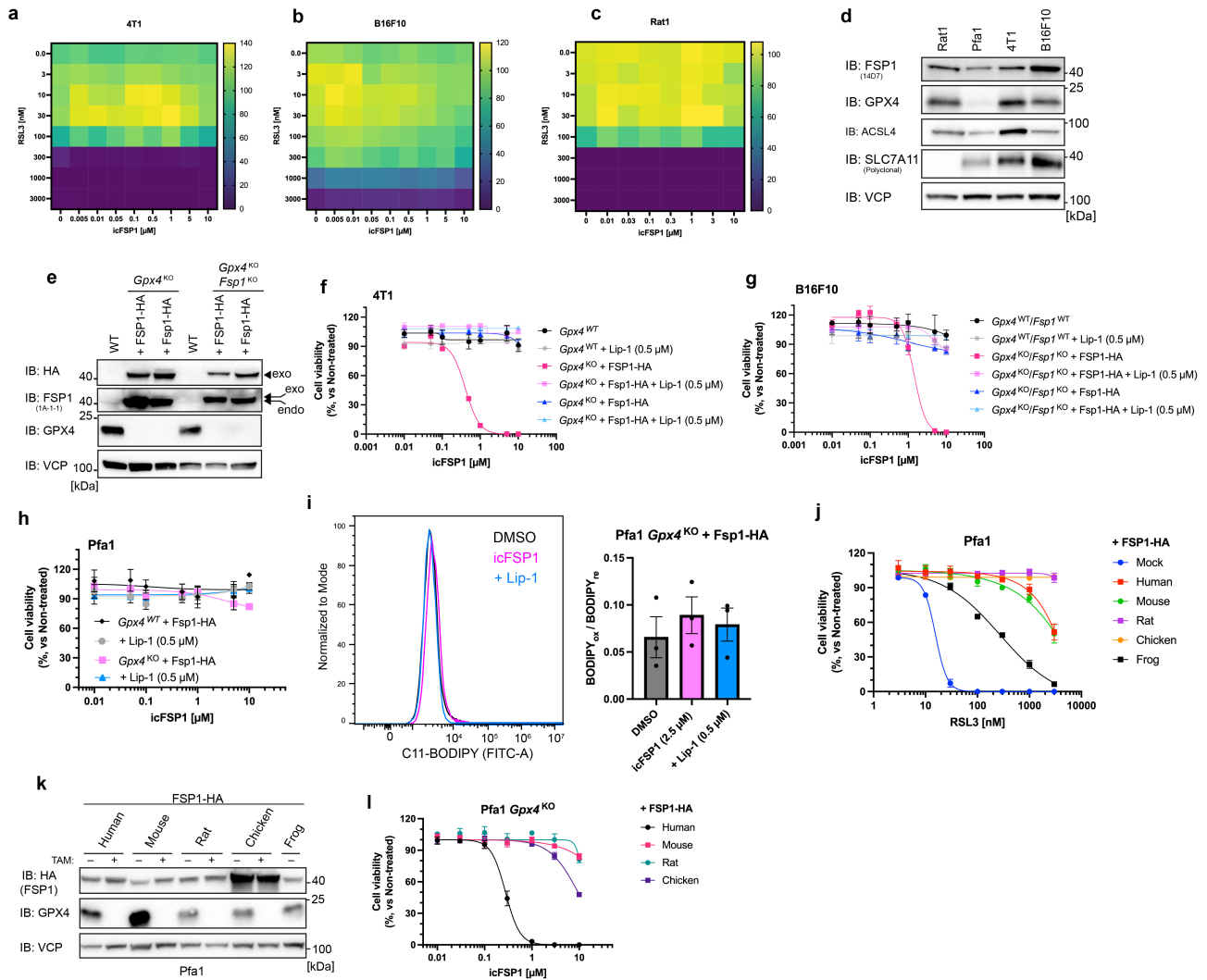
Reprints and permissions information is available at <http://www.nature.com/reprints>.



Extended Data Fig. 1 | Development of icFSP1 and synergistic effects of icFSP1 with ferroptosis inducers in a variety of human cancer cells.

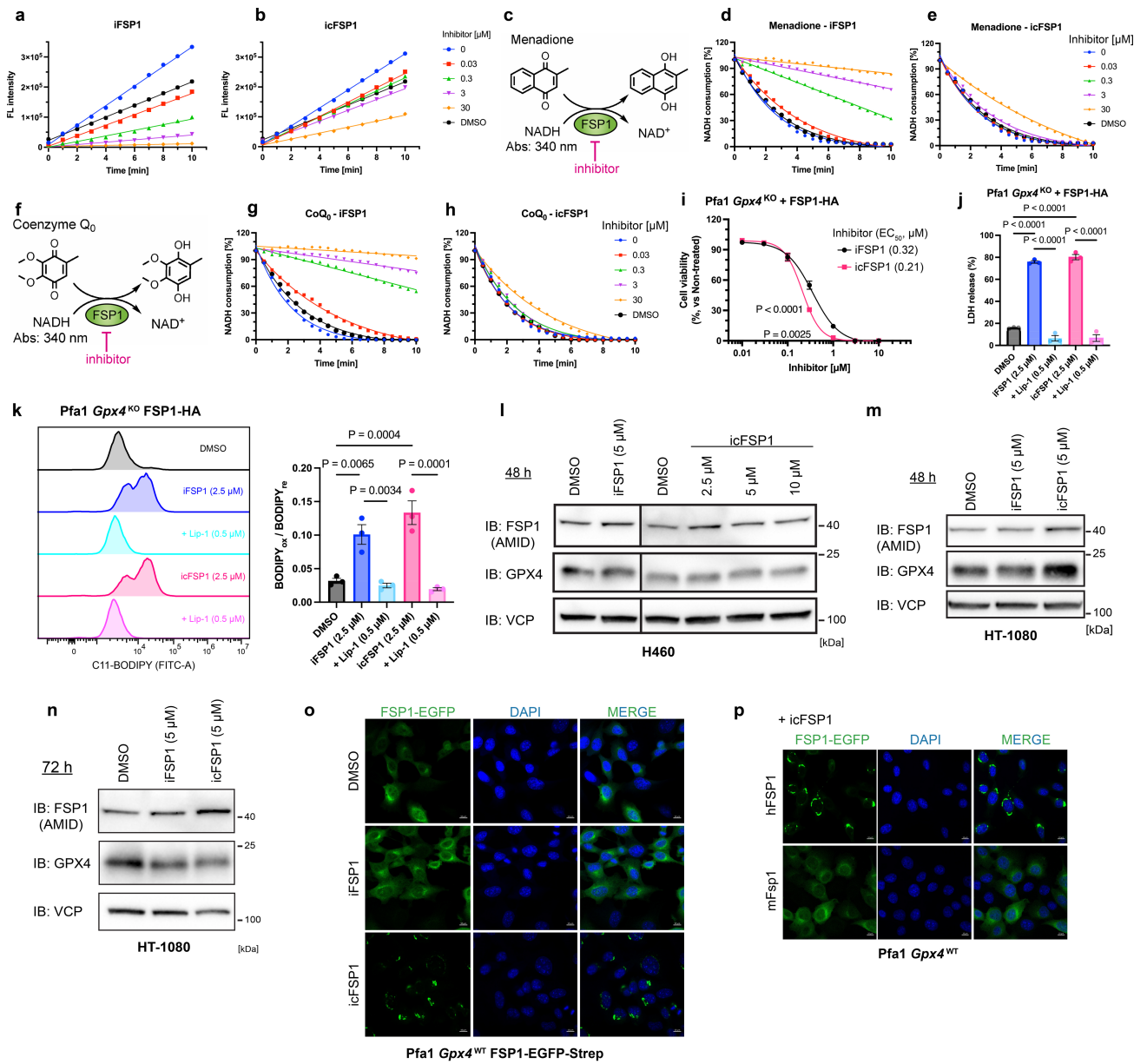
a. Structure and EC_{50} values of icFSP1 derivatives. **b.** Cell viability was measured after treating Pfa1 *Gpx4*^{KO} cells stably overexpressing FSP1-HA with icFSP1 along with different cell death inhibitors against ferroptosis (Lip-1 and ferrostatin-1 [Fer-1] or an iron chelator deferoxamine [DFO]), apoptosis (z-VAD-FMK), necroptosis (Nec-1s), pyroptosis (MCC950), and parthanatos (Olaparib). Heatmaps represent the mean of 3 wells of a 96 well plate from one out of 2 independent experiments. **c.** Cell viability was measured after treating HT-1080, A375, 786-O, MDA-MB-436 and H460 cells with different ferroptosis inducers (RSL3, ML210, erastin, FIN56 and FINO2 for 48 h, BSO for 72 h). Heatmaps represent one out of 2 independent experiments. 0.5 μ M Lip-1 was used as control. **d.** Cell viability was measured after treating HT-1080, HT-29 and THP-1 cells with icFSP1 and respective cell death inducers (staurosporine for apoptosis, TNF α + smac mimetic (S) + z-VAD-FMK (Z) for necroptosis, and nigericin for pyroptosis) for 4 h (in case of pyroptosis) or 24 h (others). Heatmaps represent one out of 2 independent experiments. 0.5 μ M Lip-1, 30 μ M z-VAD-FMK, 10 μ M Nec-1s and 10 μ M MCC950 were used as positive controls for each mode of cell death. **e.** Representative immunoblot analysis of GPX4, FSP1

(AMID), SLC7A11(3A12), ACSL4 and VCP expression in the different cell lines from one out of 2 independent experiments. **f.** Representative immunoblot analysis of GPX4, FSP1, Flag (Cas9) and actin expression in HT-1080 cells with doxycycline (Dox)-inducible expression of Flag-Cas9 and stably expressing different sgRNAs targeting FSP1 (sgFSP1) from one out of 2 independent experiments. **g.** Cell viability was measured after treating HT-1080 cells expressing dox-inducible Flag-Cas9 and stably expressing sgFSP1 with doxycycline for 72 h. 0.5 μ M Lip-1 was used as a positive control for the prevention of ferroptosis. **h.** Cell viability in HT-1080 cells treated with iFSP1 or icFSP1 and 0.5 μ M Lip-1 for 72 h. **i.** Cell viability in HEK293T cells treated with iFSP1 or icFSP1 and 0.5 μ M Lip-1 for 72 h. **j.** Cell viability in human PBMC cells treated with iFSP1 or icFSP1 for 24 h. **k.** Representative immunoblot analysis of FSP1 and VCP expression in WT and *FSP1*^{KO} different cancer cell lines from one out of 2 independent experiments. **l.** Cell viability in *FSP1*^{WT} or *FSP1*^{KO} MDA-MB-436, 786-O, A375, H460 cells treated with 5 μ M iFSP1 or icFSP1 for 48 h. Data represents the mean \pm SD of 3 wells of a 96 well or 384 well plates from one out of 2 independent experiments (g-i) or a single experiment (j). Two-way ANOVA followed by Tukey's multiple comparison tests (g, j).



Extended Data Fig. 2 | icFSP1 fails to inhibit mouse FSP1. **a.** Cell viability was measured after treating 4T1 cells with icFSP1 and RSL3 for 48 h. **b.** Cell viability was measured after treating B16F10 cells with icFSP1 and RSL3 for 48 h. **c.** Cell viability was measured after treating Rat1 cells with icFSP1 and RSL3 for 48 h. **d.** Representative immunoblot analysis of GPX4, FSP1 (14D7), SLC7A11, ACSL4 and VCP expression in different cell lines from one out of 2 independent experiments. **e.** Representative immunoblot analysis of GPX4, FSP1, and VCP expression of 4T1 *Gpx4*^{WT} cells, 4T1 *Gpx4*^{KO} cells stably overexpressing hFSP1-HA or mFsp1-HA, B16F10 *Gpx4*^{WT}/*Fsp1*^{WT} cells, B16F10 *Gpx4*^{KO}/*Fsp1*^{KO} cells stably overexpressing hFSP1-HA or mFsp1-HA from one out of 2 independent experiments. **f.** Cell viability was measured after treating 4T1 *Gpx4*^{WT} cells, 4T1 *Gpx4*^{KO} cells stably overexpressing hFSP1-HA or mFsp1-HA with icFSP1 and 0.5 μM Lip-1 for 48 h. **g.** Cell viability was measured after treating B16F10 *Gpx4*^{WT}/*Fsp1*^{WT} cells, B16F10 *Gpx4*^{KO}/*Fsp1*^{KO} cells stably overexpressing hFSP1-HA or mFsp1-HA with icFSP1 and 0.5 μM Lip-1 for 48 h. **h.** Cell viability was measured after treating Pfa1 *Gpx4*^{WT} and *Gpx4*^{KO} cells stably overexpressing hFSP1-HA or

mFsp1-HA with icFSP1 and 0.5 μM Lip-1 for 48 h. **i.** Lipid peroxidation was measured by C11-BODIPY 581/591 staining after treating Pfa1 *Gpx4*^{KO} cells stably overexpressing Fsp1-HA with DMSO or 2.5 μM icFSP1 and 0.5 μM Lip-1 for 3 h. Representative plots of one out of 3 independent experiments (left) and quantified median values (right, mean ± SEM) of 3 independent experiments are shown. **j.** Cell viability was measured after treating Pfa1 *Gpx4*^{WT} cells stably overexpressing FSP1 from different species (i.e., *Homo sapiens* (human), *Mus musculus* (mouse), *Rattus norvegicus* (rat), *Gallus gallus* (chicken), and *Xenopus laevis* (frog)) with RSL3 for 24 h. **k.** Representative immunoblot analysis of GPX4, HA (FSP1) and VCP expression in Pfa1 *Gpx4*^{WT} and *Gpx4*^{KO} cells stably overexpressing orthogonal FSP1 from one out of 2 independent experiments. **l.** Cell viability was measured after treating Pfa1 *Gpx4*^{KO} cells stably expressing FSP1 with icFSP1 for 24 h. Data represents the mean ± SD of 3 wells of a 96 well plate from one out of 2 independent experiments (f,g,h,j,l). Heatmaps represent the mean of 3 independent experiments (a-c).

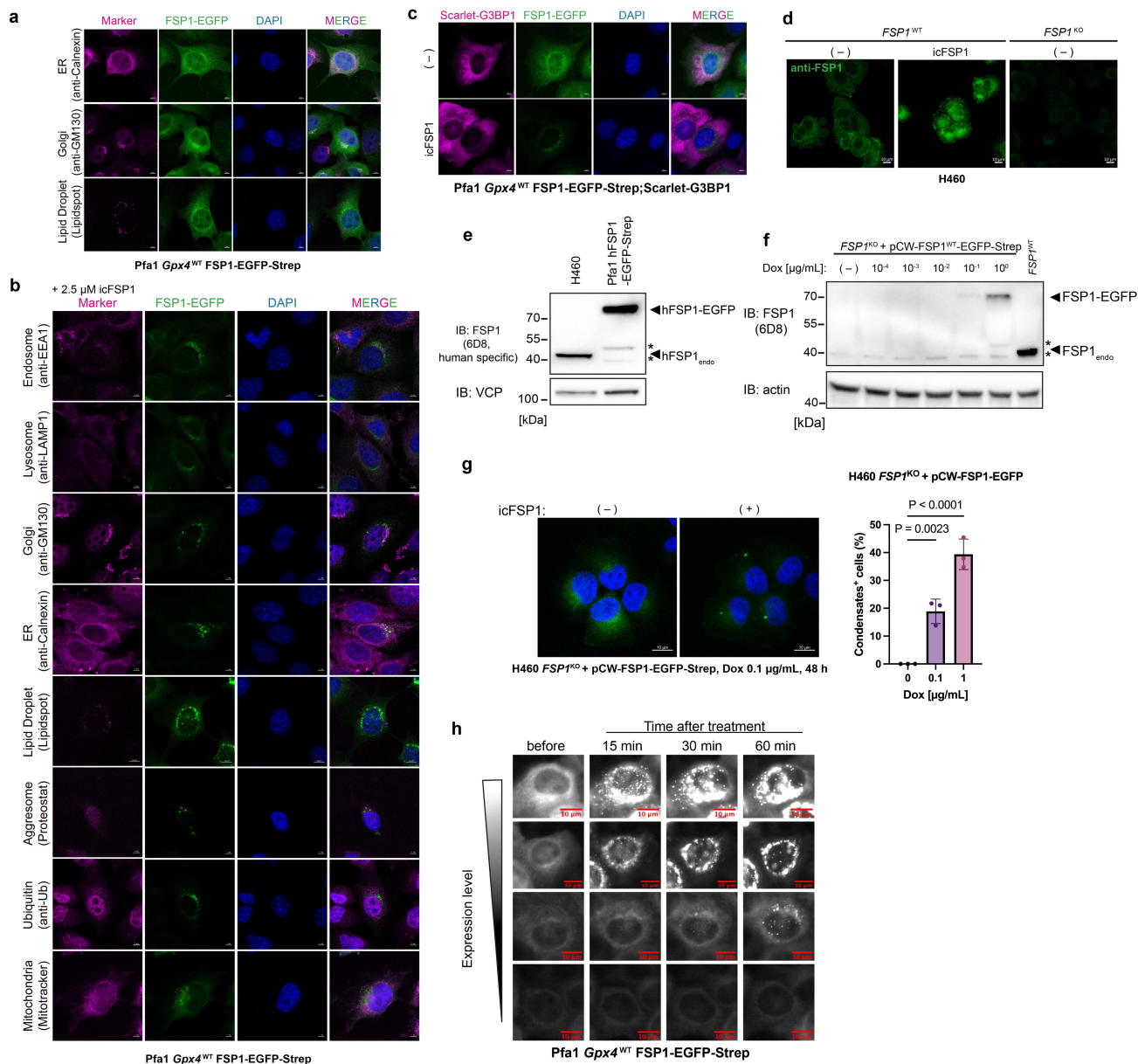


Extended Data Fig. 3 | See next page for caption.

Article

Extended Data Fig. 3 | icFSP1 has no impact on FSP1 enzyme activity and expression. **a.** Representative reaction curves of *in vitro* assay. iFSP1 toward recombinant hFSP1 activity was assessed by fluorescent (FL) intensity of reduced form of resazurin. **b.** Representative reaction curves of *in vitro* assay. icFSP1 toward recombinant hFSP1 activity was assessed by FL intensity of reduced form of resazurin. Data represents the mean of 3 wells of a 96 well plate from one out of 3 independent experiments (**a,b**). **c.** Schematic representation of the FSP1 enzyme activity assay using menadione as a substrate. **d.** NADH consumption assay *in vitro*. Representative reaction curves of the FSP1 enzyme activity assay for measuring NADH consumption. iFSP1 toward recombinant hFSP1 activity was assessed by determining the absorbance of NADH. **e.** NADH consumption assay *in vitro*. Representative reaction curves of the FSP1 enzyme activity assay for measuring NADH consumption. icFSP1 toward recombinant hFSP1 activity were assessed by determining the absorbance of NADH. Data represents the curve fitting line and an original single value of one well of a 96-well plate from one out of 3 independent experiments. 0 μ M and DMSO samples represent the same samples (**d,e**). **f.** Schematic representation of the FSP1 enzyme activity assay using CoQ₀ as the substrate. **g.** NADH consumption assay *in vitro*. Representative reaction curves of the FSP1 enzyme activity assay for measuring NADH consumption. iFSP1 toward recombinant hFSP1 activity was assessed by determining the absorbance of NADH. **h.** NADH consumption assay *in vitro*. Representative reaction curves of the FSP1 enzyme activity assay for measuring NADH consumption. icFSP1 toward recombinant hFSP1 activity were assessed by determining the absorbance of NADH. Data represents the curve fitting line and an original single value of one well of a 96-well plate from

one out of 3 independent experiments. 0 μ M and DMSO samples represent the same samples (**g, h**). **i.** Cell viability was measured after treating Pfa1 *Gpx4*^{KO} cells stably overexpressing hFSP1-HA with iFSP1 or icFSP1 for 24 h. **j.** Lactate dehydrogenase (LDH) release was determined after treating Pfa1 *Gpx4*^{KO} hFSP1-HA overexpressing cells with DMSO, 2.5 μ M iFSP1 or icFSP1 or 0.5 μ M Lip-1 for 24 h. Data represents the mean \pm SD of 3 wells of a 96 well plate from one out of 3 independent experiments. P values were calculated by two-way ANOVA followed by Bonferroni's multiple comparison test (i, j). **k.** Lipid peroxidation was evaluated by C11-BODIPY 581/591 staining after treating *Gpx4*^{KO} cells stably overexpressing hFSP1-HA with DMSO, 2.5 μ M iFSP1 or icFSP1 and 0.5 μ M Lip-1 for 3 h. Representative plots of one out of 3 independent experiments (left) and quantified median values of 3 independent experiments (right) are shown. Data represents the mean \pm SEM of 3 independent experiments (k). one-way ANOVA followed by Tukey's multiple comparison test. **l.** Representative immunoblot analysis of GPX4, FSP1 and VCP expression after treating H460 cells with iFSP1 or icFSP1 for 48 h. **m.** Representative immunoblot analysis of GPX4, FSP1 and VCP expression after treating HT-1080 cells with iFSP1 or icFSP1 for 48 h. **n.** Immunoblot analysis of GPX4, FSP1 and VCP expression after treating HT-1080 cells with iFSP1 or icFSP1 for 72 h. **o.** Confocal microscopy fluorescence images after treating Pfa1 *Gpx4*^{WT} cells stably overexpressing hFSP1-EGFP-Strep with 2.5 μ M icFSP1 or iFSP1 for 4 h. Scale bars, 10 μ m. **p.** Confocal microscopy fluorescence images after treating Pfa1 *Gpx4*^{WT} cells stably overexpressing hFSP1-EGFP-Strep or mFsp1-EGFP-Strep with 2.5 μ M icFSP1 or iFSP1 treatment for 4 h. Scale bars, 10 μ m. Representative results are from one out of 2 independent experiments (l-p).

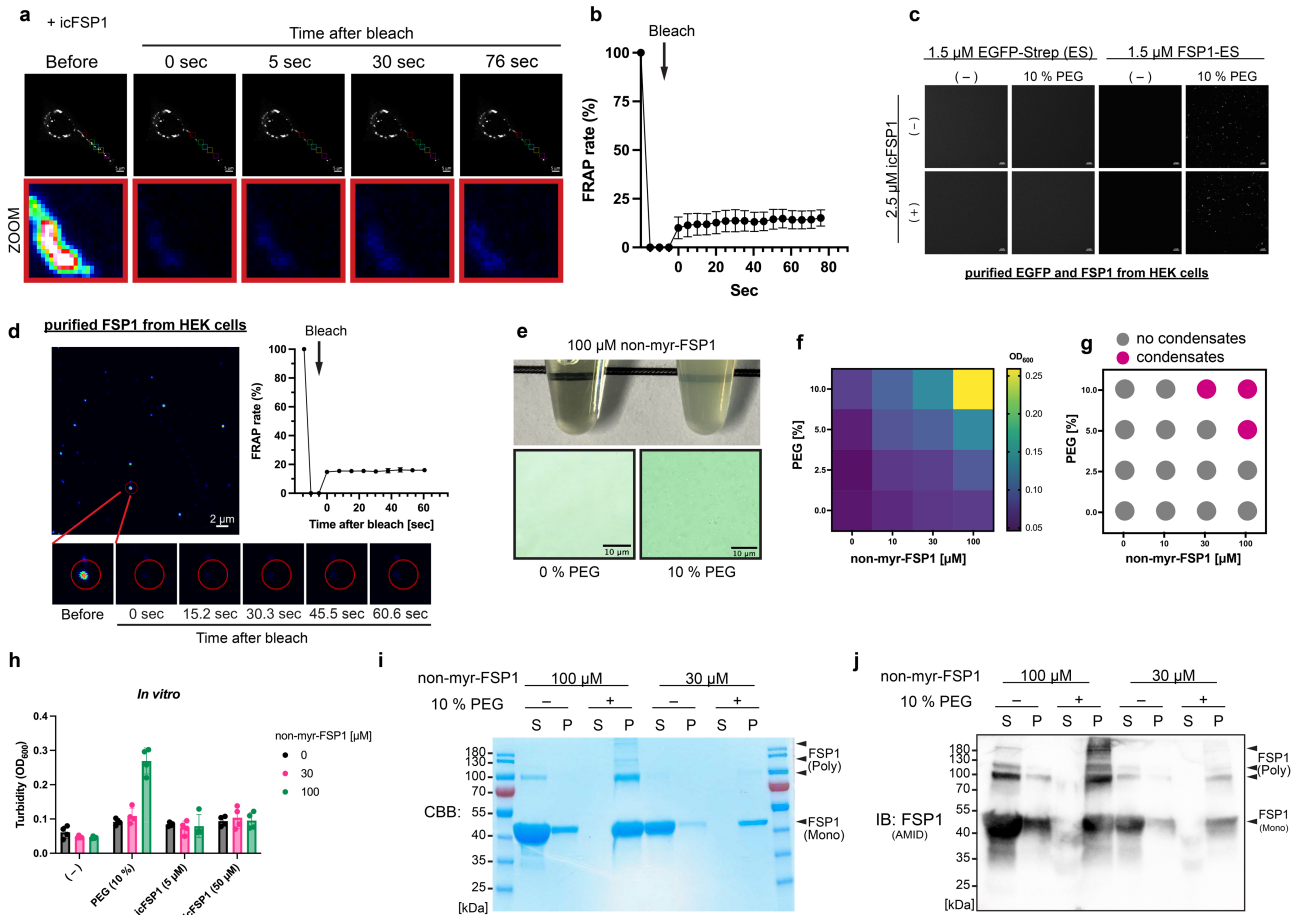


Extended Data Fig. 4 | FSP1 condensates do not localize to specific

organelles. **a.** Confocal microscopy images of FSP1-EGFP-Strep overexpressing Pfa1 *Gpx4*^{WT} cells stained with ER, Golgi and lipid droplet markers under normal cell culture conditions. Scale bars, 5 μm. **b.** Confocal microscopy images of FSP1-EGFP-Strep overexpressing Pfa1 *Gpx4*^{WT} cells after treating with 2.5 μM icFSP1 for 120 min, and subsequently stained with markers for endosome, lysosome, Golgi, ER, lipid droplet, aggresome, ubiquitin and mitochondria. Scale bars, 5 μm. **c.** Confocal microscopy images of FSP1-EGFP-Strep and Scarlet-G3BP1 overexpressing Pfa1 *Gpx4*^{WT} cells after treating with 0 or 2.5 μM icFSP1 for 120 min. Scale bars, 5 μm. **d.** Confocal microscopy images of H460 or *FSP1*^{KO} H460 cells after treating with 0 or 10 μM icFSP1 for 4 h, following stained with FSP1 antibody (14D7). Scale bars, 10 μm. Representative results are from one out of 2 independent experiments (a-d). **e.** Representative immunoblot analysis of FSP1 and VCP expression in H460 cells and hFSP1-EGFP-Strep

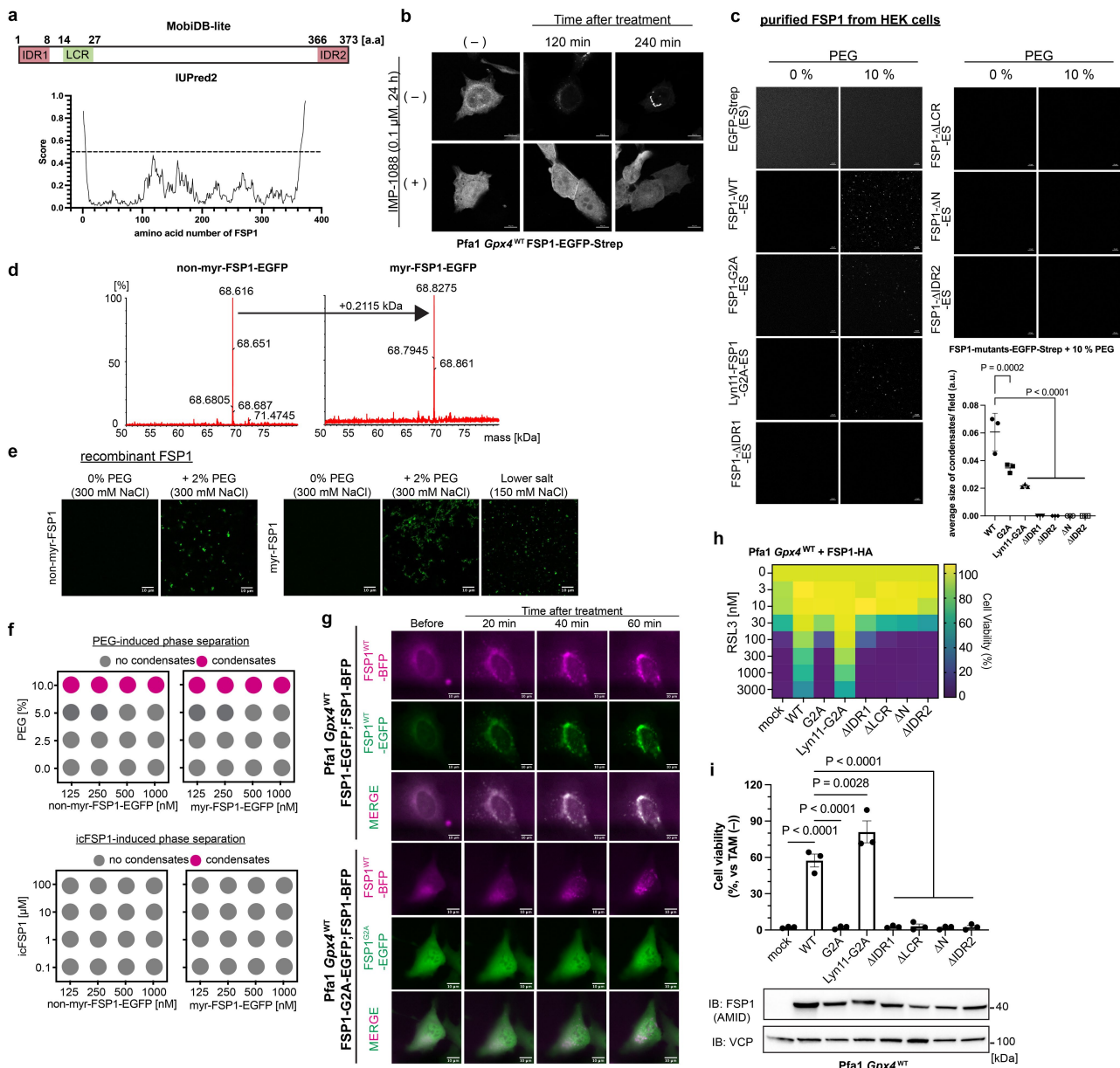
overexpressing Pfa1 *Gpx4*^{WT} cells from one out of 2 independent experiments. **f.** Representative immunoblot analysis of FSP1 and actin expression in H460 WT cells and Dox-inducible hFSP1-EGFP-Strep overexpressing H460 *FSP1*^{KO} cells after treating with Dox for 48 h from one out of 2 independent experiments. **g.** Confocal microscopy images of Dox-inducible hFSP1-EGFP-Strep overexpressing H460 *FSP1*^{KO} cells after treating with 0.1 μg/mL for 48 h and followed by treating with 0 or 10 μM icFSP1 for 4 h. Scale bars, 10 μm. Representative images from one out of 2 independent experiments (left) and quantified values (right, mean ± SD of 3 independent fields) are shown. One-way ANOVA followed by Dunnett's multiple comparison test. **h.** Time-lapse fluorescent images of Pfa1 *Gpx4*^{WT} cells stably overexpressing hFSP1-EGFP-Strep before and immediately after treatment with 2.5 μM icFSP1 for the indicated time. Scale bars, 10 μm. Representative results are from one out of 2 independent experiments.

Article



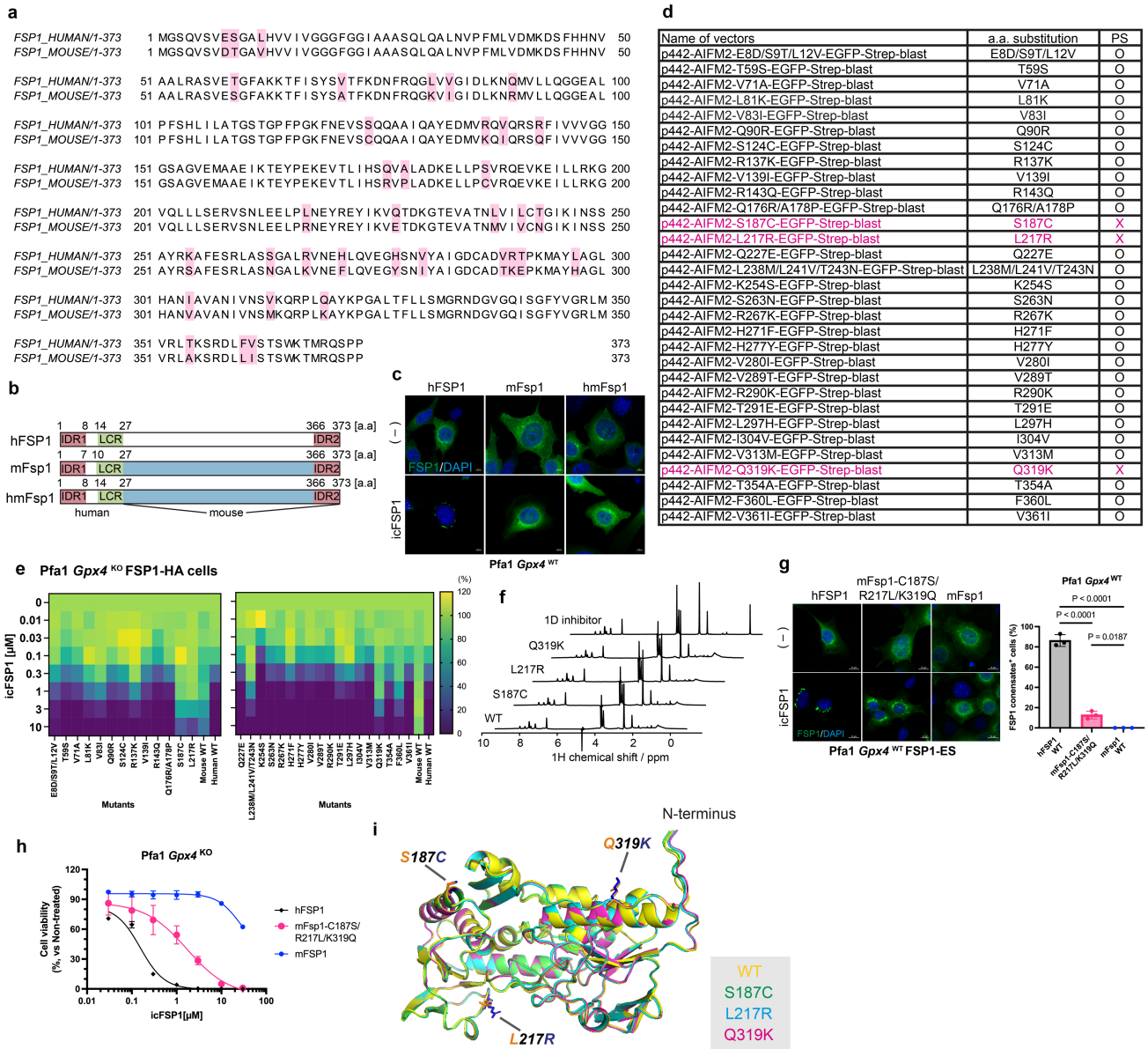
Extended Data Fig. 5 | FSP1 forms viscoelastic material. **a.** Fluorescence recovery after photobleaching (FRAP) assay after treating Pfa1 *Gpx4*^{WT} cells stably overexpressing hFSP1-EGFP-Strep with 2.5 μ M icFSP1 for 240 min. Greyscale images show representative FRAP images right before and at indicated time points after photo-bleaching. Lookup Table (LUT) images show enlarged red rectangle areas of upper FRAP images. Scale bars, 5 μ m. Representative results from one out of 2 independent experiments. See also Supplementary Video 6. **b.** Quantified FRAP rate of each condensate. Data represents the mean \pm SD of 4 condensates from Extended Data Fig. 5a. Representative results from one out of 2 independent experiments are shown. **c.** FSP1 condensation *in vitro*. Representative confocal microscopy images of 1.5 μ M EGFP-Strep and hFSP1-EGFP-Strep purified from transfected HEK29T cells were obtained immediately after mixing with 2.5 μ M icFSP1 with or without 10% PEG. Scale bars, 10 μ m. Representative results are shown from one out of 2 independent experiments. **d.** FRAP assay after incubating 0.5 μ M hFSP1-EGFP-Strep with 10% PEG. LUT images show enlarged red rectangle areas of FRAP images (left and below). Scale bars, 2 μ m. Representative results from one out of 2 independent experiments. Quantified FRAP rate of each condensate (right). Data represents the mean \pm SD of 4 independent condensates. **e.** Recombinant non-myristoylated FSP1 (non-myrist-FSP1) condensation *in vitro*. Representative bright field images of

100 μ M non-myrist-FSP1 expressed and purified from *E. coli* right after mixing with or without 10% PEG in PCR tubes (top). Representative bright field images (bottom) were obtained using the microscope. Scale bars, 10 μ m. Representative results are from one out of 2 independent experiments. **f.** Absorbance of 600 nm was measured for different concentrations of PEG and non-myrist-FSP1. Heatmaps represent the mean of 2 independent experiments. **g.** Phase diagram of the presence of condensates was determined by microscopy after absorbance measurement (f). **h.** Absorbance of 600 nm was measured for different concentrations of PEG and icFSP1, non-myrist-FSP1. Data represents the mean \pm SD from 4 wells of 384 well plates from one out of 2 independent experiments. **i.** Sedimentation assay of non-myrist-FSP1. Representative Coomassie brilliant blue (CBB) staining of non-myrist-FSP1 fraction after centrifugation in the presence or absence of 10% PEG. S: supernatant, P: re-suspended pellet. Monomer (Mono, ~42 kDa) and estimated oligomerized FSP1 (Poly, ~90 kDa) can be observed. **j.** Immunoblot analysis of non-myrist-FSP1 fraction after centrifugation in the presence or absence of 10% PEG. S: supernatant, P: re-suspended pellet. Monomer (Mono, ~42 kDa) and estimated oligomerized FSP1 (Poly, ~90 kDa) can be observed. The same samples but different gels were used for CBB staining (i) and immunoblot analysis (j). Representative results from one out of 2 independent experiments (i, j).



Extended Data Fig. 6 | Myristoylation, IDRs, and LCR are required for the anti-ferroptotic role of FSP1 as well as condensations. **a.** IDR and LCR prediction from FSP1 sequence. From MobiDB-lite prediction (top), there are 2 IDRs (1–8, 366–373 amino acid [a.a.]) and one LCR (14–27 a.a.) in FSP1. IUPred2 scores are visualized, and the dashed line shows the threshold; 0.5 (bottom). **b.** Confocal microscopy images of hFSP1-EGFP-Strep overexpressing Pfa1 *Gpx4*^{WT} cells after pre-treating with or without 0.1 μ M IMP-1088 for 24 h and subsequently treating with or without 2.5 μ M icFSP1 for the indicated time. Scale bars, 10 μ m. Representative results from one out of 2 independent experiments. **c.** FSP1 condensation *in vitro*. Fluorescent images of 1.5 μ M EGFP-Strep and hFSP1-EGFP-Strep mutants purified from transfected HEK29T cells were obtained right after mixing with or without 10% PEG. Scale bars, 10 μ m. Representative results from one out of 2 independent experiments of 3 different fields. Quantification results are shown as mean \pm SD of $n = 3$ from one out of 2 independent experiments. Average sizes of condensates were calculated by Fiji/ImageJ. **d.** Mass spectrometry analysis of recombinant non-myristoylated FSP1-EGFP (non-myristoylated FSP1-EGFP) and myristoylated FSP1-EGFP (myristoylated FSP1-EGFP) purified from *E. coli*. **e.** FSP1 condensation *in vitro*. Representative fluorescent images represent 15 μ M recombinant non-myristoylated or myristoylated FSP1-EGFP with 0% or

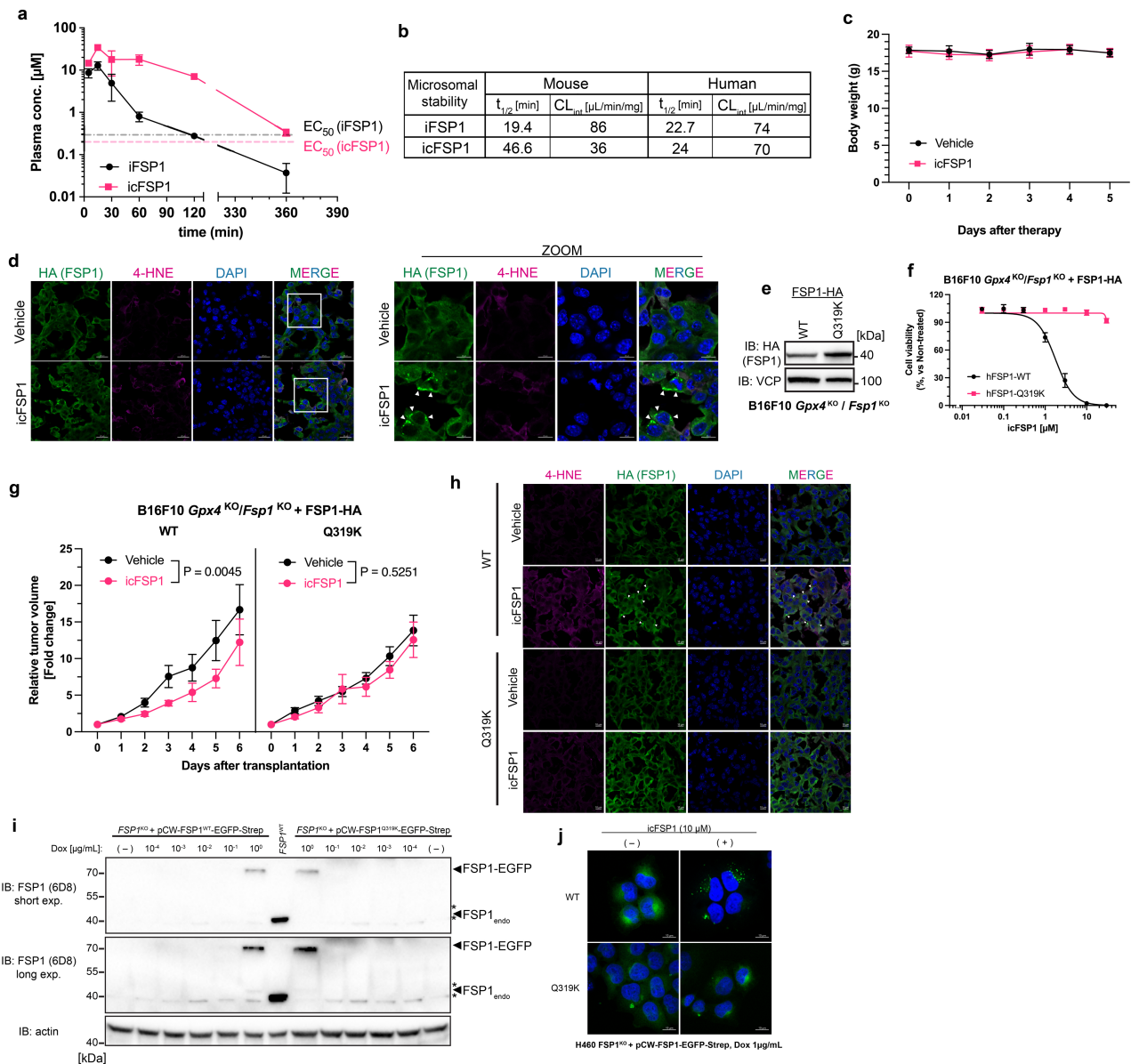
2% PEG in 300 mM NaCl PBS or 10 μ M recombinant myristoylated FSP1-EGFP with 150 mM NaCl in PBS as a lower salt from one out of 2 independent experiments. **f.** Phase diagram of the presence of condensates was determined by microscopy from one out of 2 independent experiments. **g.** Time-lapse fluorescent images of Pfa1 *Gpx4*^{WT} cells stably overexpressing hFSP1-EGFP-Strep; hFSP1-mTagBFP or hFSP1-G2A-EGFP-Strep; hFSP1-mTagBFP before and immediately after treatment with 2.5 μ M icFSP1 for the indicated times. Scale bars, 10 μ m. Representative results are from one out of 2 independent experiments. **h.** Cell viability was measured after treating Pfa1 *Gpx4*^{WT} cells stably overexpressing hFSP1 mutants with RSL3 for 24 h. The heatmap represents the mean of 3 wells of 96 well plates from one out of 2 independent experiments. **i.** Cell viability (top) was measured after treating Pfa1 *Gpx4*^{WT} cells stably overexpressing hFSP1 mutants with or without 1 μ M TAM for 72 h TAM. Data were normalized by each group of non-treatment with TAM. Immunoblot analysis (bottom) of FSP1 and VCP expression in Pfa1 *Gpx4*^{WT} cells stably overexpressing hFSP1 mutants in cells from one out of 2 independent experiments. Data represents mean \pm SEM of 3 independent experiments (i). P values were calculated by one-way ANOVA followed by Dunnett's multiple comparison test (c, i).



Extended Data Fig. 7 | Mutational analysis of human FSP1 resistant to icFSP1.

a. Protein sequence alignment of human and mouse FSP1 using Jalview (v2.11.2.6). **b.** Schematic model of chimeric FSP1 mutants. From MobiDB-lite prediction, there are 2 IDRs (1–7, 366–373 a.a.) and one LCR (10–27 a.a.) in FSP1. Chimeric hmFsp1 was generated from human FSP1 (1–27 a.a.) and mouse Fsp1 (28–373 a.a., marked as blue). **c.** Confocal microscopy images after treating Pfa1 *Gpx4*^{WT} cells stably overexpressing FSP1-EGFP-Strep mutants with and without 2.5 μM icFSP1 for 240 min. Scale bars, 5 μm. Representative results from one out of 2 independent experiments. **d.** Summary of the viability assay using single point mutations (as indicated) from human to mouse in FSP1-EGFP-Strep expressing constructs. After treating cells with 2.5 μM icFSP1 for overnight, the presence of condensates was determined using a microscope. Human FSP1 is sensitive to icFSP1 (O), while mouse Fsp1 is resistant to icFSP1 (X). 3 mutants show complete resistance (X). This screening was performed once using a 96 well plate. **e.** Cell viability was measured after treating Pfa1 *Gpx4*^{KO} cells stably overexpressing hFSP1 mutants with icFSP1 for 24 h. Heatmaps represent the

mean of 3 wells of 96 well plate from one out of 2 independent experiments. **f.** Saturation transfer difference (STD) spectra of WT hFSP1 or its mutants S187C, L217R and Q319K show binding of icFSP1 (bottom to top). Top spectrum shows a 1D ¹H reference spectrum of icFSP1. **g.** Confocal microscopy images after treating Pfa1 *Gpx4*^{WT} cells stably overexpressing human and mouse FSP1-EGFP-Strep or the combination mutant (mFSP1-C187S/R217L/K319Q) with and without 2.5 μM icFSP1 for 240 min. Scale bars, 10 μm. Representative images (left) and quantitative results (right, mean ± SD of 3 different fields) from one out of 2 independent experiments. One-way ANOVA followed by Bonferroni’s multiple comparison test. **h.** Cell viability was measured after treating Pfa1 *Gpx4*^{KO} cells stably overexpressing human and mouse FSP1-HA or the combination mutant with icFSP1 for 24 h. Data represents the mean ± SD of 3 wells of a 96 well plate from one out of 2 independent experiments. **i.** Predicted cartoon structure of hFSP1 WT (yellow) S187C (green), L217R (cyan), and Q319K (magenta) by AlphaFold2 or ColabFold. Each mutant amino acid residue represents human FSP1 (orange) and mouse FSP1 (dark blue) as sticks.



Extended Data Fig. 8 | Targeting of FSP1 by icFSP1 as potential anti-cancer therapy using mouse cells.

a. Pharmacokinetic (PK) parameters of icFSP1 and iFSP1. Plasma concentration was measured after single i.p. administration (10 mg/kg). Data represents mean \pm SD from 4 mice of one experiment.

b. Summary of microsomal stability analysis of icFSP1 and iFSP1.

c. Body weight of tumor-bearing mice during the treatment of mice with icFSP1 (50 mg/kg i.p. twice a day, $n = 6$) and vehicle ($n = 6$) as a control. These mice are the same as in Fig. 4f. Data represents mean \pm SD from one out of 2 independent experiments.

d. At the end of the *in vivo* pharmacological studies, tumors were dissected, cryosectioned and stained with anti-HA to visualize hFSP1 and with anti-4-HNE to visualize the lipid peroxidation breakdown product. Representative confocal microscopy images are shown from one out of 2 independent experiments. Arrowheads indicate FSP1 condensates. Scale bars, 20 μ m or 10 μ m.

e. Immunoblot analysis of HA (FSP1) and VCP expression of B16F10 *Gpx4*^{ko}/*Fsp1*^{ko} cells stably overexpressing FSP1-WT or the Q319K mutant. Representative results from one out of 2 independent experiments.

f. Cell viability was measured after treating B16F10 *Gpx4*^{ko}/*Fsp1*^{ko} cells stably overexpressing FSP1-WT or Q319K mutants with icFSP1 for 48 h. Data represent mean \pm SD of 3 wells from one out of 2 independent experiments.

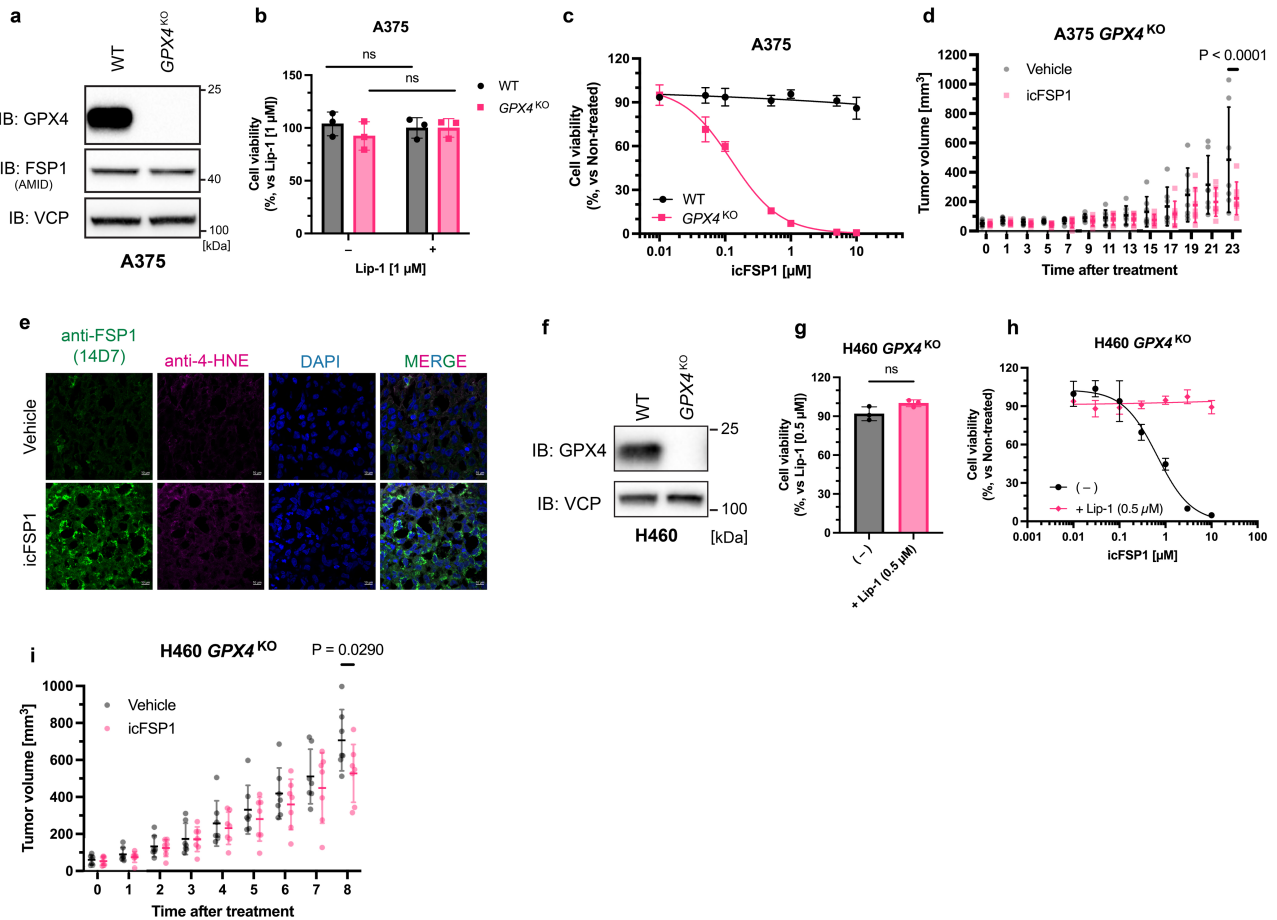
g. icFSP1 inhibits tumor growth of hFSP1 WT but not of FSP1-Q319K expressing cells *in vivo*. B16F10

Gpx4^{ko}/*Fsp1*^{ko} cells stably expressing hFSP1 WT or Q319K were subcutaneously implanted into C57BL/6j mice ($n = 33$, in total). Treatment with vehicle ($n = 10$ for WT and 8 for Q319K) or icFSP1 (50 mg/kg i.p. twice a day, $n = 8$ for WT and 7 for Q319K) was started from day 6 after randomization. Data represents the mean \pm SEM from one out of 2 experiments. P values were calculated by two-way ANOVA followed by Tukey's multiple comparison test.

h. At the end of the *in vivo* pharmacological studies, tumors were dissected, cryosectioned and stained with anti-HA to visualize hFSP1 and with anti-4-HNE to visualize the lipid peroxidation breakdown product. Representative confocal microscopy images are shown from one out of 2 independent experiments. Arrowheads indicate FSP1 condensates.

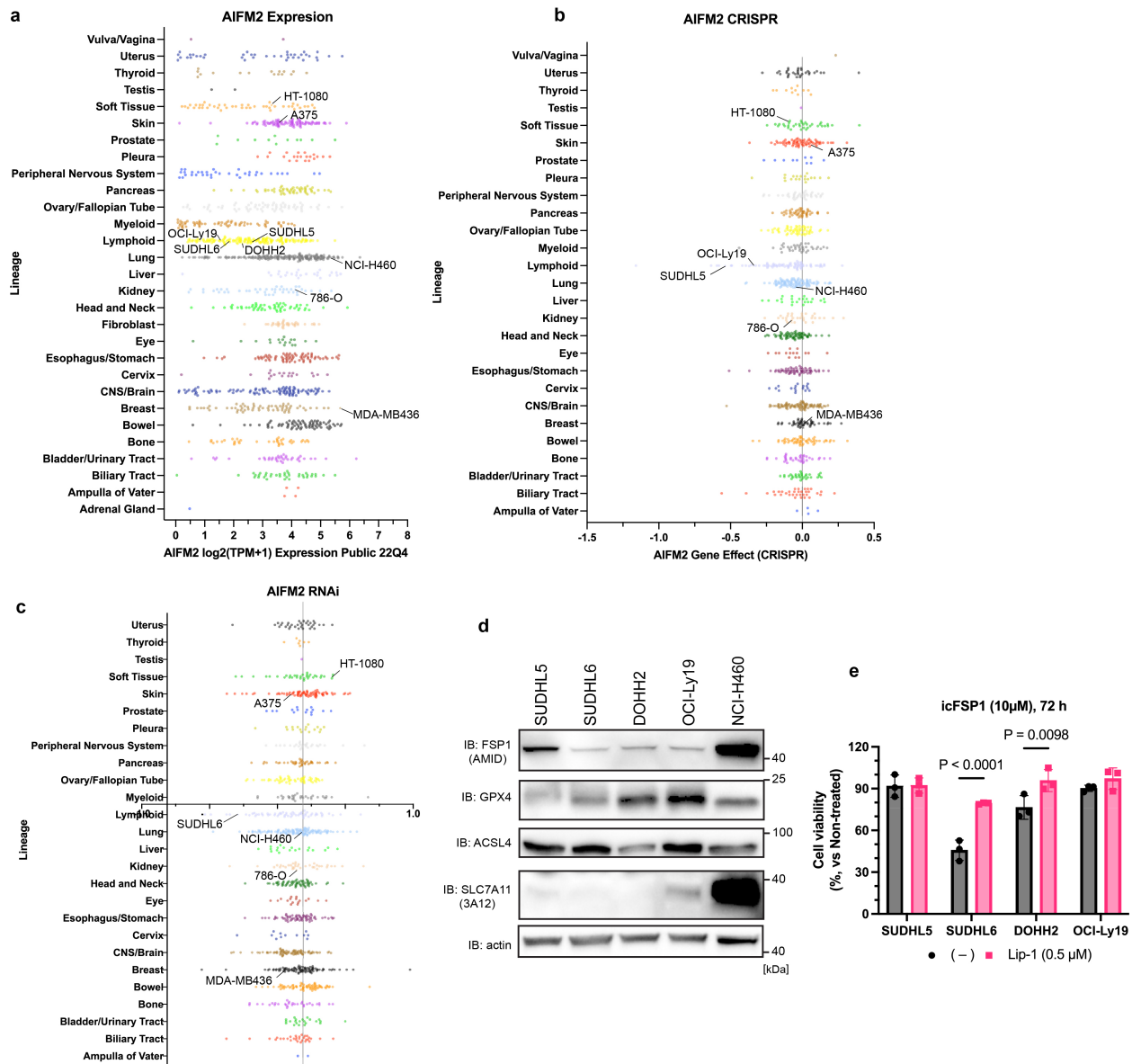
i. Immunoblot analysis of FSP1 and actin expression of H460 WT and *Fsp1*^{ko} cells with doxycycline (Dox)-inducible FSP1-WT or the Q319K mutant after Dox induction with indicated concentrations for 48 h. The left part of the blot is already shown in Extended Data Fig. 4f. Representative results from one out of 2 independent experiments.

j. Confocal microscopy images after treating H460 *Fsp1*^{ko} cells with doxycycline-inducible FSP1-WT or the Q319K mutant with 1 μ M of Dox for 48 h, followed by treatment with and without 10 μ M icFSP1 for 240 min. Scale bars, 10 μ m. Representative images from one out of 2 independent experiments.



Extended Data Fig. 9 | Targeting of FSP1 by icFSP1 as potential anti-cancer therapy using human cells. **a.** Immunoblot analysis of GPX4, FSP1 and VCP expression of A375 WT and *GPX4*^{KO} cells. Representative images from one out of 2 independent experiments. **b.** Cell viability was measured after Lip-1 withdrawal for 72 h in A375 WT and *GPX4*^{KO} cells. Data represent the mean ± SD of 3 wells from one out of 2 independent experiments. **c.** Cell viability was measured after treating A375 WT and *GPX4*^{KO} cells with icFSP1 for 48 h. Data represents the mean ± SD of 3 wells from one out of 2 independent experiments. **d.** icFSP1 inhibits tumor growth *in vivo*. A375 *GPX4*^{KO} cells (a human melanoma cell line) were subcutaneously implanted into the flanks of Athymic Nude mice. After tumors became palpable (day 3), mice were randomized and treatment was started with icFSP1 (50 mg/kg i.p. twice a day for beginning 4 days and once a day afterward, n = 7) or vehicle (n = 7). Data represents the mean ± SD from one experiment. P value was calculated by two-way ANOVA followed by Bonferroni's multiple comparison. **e.** At the end of the *in vivo* pharmacological studies, tumors were dissected, cryosectioned and stained with anti-FSP1 (14D7) to

visualize hFSP1 and with anti-4-HNE to visualize the lipid peroxidation breakdown product. Representative confocal microscopy images of 3 different samples from a single experiment are shown. **f.** Immunoblot analysis of GPX4, and VCP expression of H460 WT and *GPX4*^{KO} cells from one out of 2 independent experiments. **g.** Cell viability was measured after Lip-1 withdrawal for 72 h in H460 WT and *GPX4*^{KO} cells. Data represents the mean ± SD of 3 wells from one out of 2 independent experiments. Two-tailed unpaired t-test. **h.** Cell viability was measured after treating H460 WT and *GPX4*^{KO} cells with icFSP1 for 48 h. Data represents the mean ± SD of 3 wells from one out of 2 independent experiments. **i.** icFSP1 inhibits tumor growth *in vivo*. H460 *GPX4*^{KO} cells (a human lung cancer cell line) were subcutaneously implanted into the flanks of Athymic Nude mice. After tumors became palpable (day 8), mice were randomized and treatment was started with icFSP1 (50 mg/kg i.p. twice a day, n = 7) or vehicle (n = 7). Data represents the mean ± SD from one experiment. P value was calculated by two-way ANOVA followed by Sidak's multiple comparison tests.



Extended Data Fig. 10 | FSP1 is a potential target in multiple cancer cells.

a. AIFM2 (FSP1) expression in different cancer cells from different origins. **b.** AIFM2 gene effect (CRISPR) in different cancer cells from different origins. **c.** AIFM2 gene effect (RNAi) in different cancer cells from different origins. Data were mined from <https://depmap.org/portal/> and cell lines used in this study were highlighted with the names of cancer cell lines. **d.** Representative

immunoblot analysis of GPX4, FSP1, ACSL4, XCT (SLC7A11) and actin expression of indicated cell lines from one out of 2 independent experiments. **e.** Cell viability in lymphoma (SUDHL5, SUDHL6, DOHH2, OCI-Ly19) cells treated with icFSP1 in the presence or absence of 0.5 μM Lip-1 for 72 h. Data represents the mean ± SD of 3 wells from one out of 2 independent experiments. P values were calculated by two-way ANOVA followed by Tukey's multiple comparison tests.

Reporting Summary

Nature Portfolio wishes to improve the reproducibility of the work that we publish. This form provides structure for consistency and transparency in reporting. For further information on Nature Portfolio policies, see our [Editorial Policies](#) and the [Editorial Policy Checklist](#).

Statistics

For all statistical analyses, confirm that the following items are present in the figure legend, table legend, main text, or Methods section.

n/a Confirmed

- The exact sample size (n) for each experimental group/condition, given as a discrete number and unit of measurement
- A statement on whether measurements were taken from distinct samples or whether the same sample was measured repeatedly
- The statistical test(s) used AND whether they are one- or two-sided
Only common tests should be described solely by name; describe more complex techniques in the Methods section.
- A description of all covariates tested
- A description of any assumptions or corrections, such as tests of normality and adjustment for multiple comparisons
- A full description of the statistical parameters including central tendency (e.g. means) or other basic estimates (e.g. regression coefficient) AND variation (e.g. standard deviation) or associated estimates of uncertainty (e.g. confidence intervals)
- For null hypothesis testing, the test statistic (e.g. F , t , r) with confidence intervals, effect sizes, degrees of freedom and P value noted
Give P values as exact values whenever suitable.
- For Bayesian analysis, information on the choice of priors and Markov chain Monte Carlo settings
- For hierarchical and complex designs, identification of the appropriate level for tests and full reporting of outcomes
- Estimates of effect sizes (e.g. Cohen's d , Pearson's r), indicating how they were calculated

Our web collection on [statistics for biologists](#) contains articles on many of the points above.

Software and code

Policy information about [availability of computer code](#)

Data collection CytExpert v2.4 (Beckman Coulter), Eve v1.8.2 (Nanolive), Image Lab v6.0 (Biorad), SoftMax Pro v7 (Molecular Devices), VisiView v4.0 (Visitron System), ZEN Black v2.3 (ZWISS).

Data analysis CellProfiler v4.1.3 (Broad Institute), Flow Jo v10 software (Treestar, Inc), GraphPad Prism v9 (GraphPad Software), Image J v1.52 & 1.53 (NIH), Masslynx V4.2 (Waters), MetaboAnalyst online platform v5.0 (PMID 31756036), ZEN Blue v3.2 (ZWISS), Topspin 4.0.6 (Bruker).

For manuscripts utilizing custom algorithms or software that are central to the research but not yet described in published literature, software must be made available to editors and reviewers. We strongly encourage code deposition in a community repository (e.g. GitHub). See the Nature Portfolio [guidelines for submitting code & software](#) for further information.

Data

Policy information about [availability of data](#)

All manuscripts must include a [data availability statement](#). This statement should provide the following information, where applicable:

- Accession codes, unique identifiers, or web links for publicly available datasets
- A description of any restrictions on data availability
- For clinical datasets or third party data, please ensure that the statement adheres to our [policy](#)

All data are available in the Article and the Supplementary Information, and from the corresponding author on reasonable request. Gel source images are shown in

Supplementary Fig. 2. All source data are provided in this paper. Cancer cell line data were mined from <https://depmap.org/portal/>. The prediction for phase separation of FSP1 was conducted by <https://iupred2a.elte.hu> and <https://mobidb.bio.unipd.it>.

Research involving human participants, their data, or biological material

Policy information about studies with [human participants or human data](#). See also policy information about [sex, gender \(identity/presentation\), and sexual orientation](#) and [race, ethnicity and racism](#).

Reporting on sex and gender	N/A
Reporting on race, ethnicity, or other socially relevant groupings	N/A
Population characteristics	N/A
Recruitment	N/A
Ethics oversight	N/A

Note that full information on the approval of the study protocol must also be provided in the manuscript.

Field-specific reporting

Please select the one below that is the best fit for your research. If you are not sure, read the appropriate sections before making your selection.

Life sciences Behavioural & social sciences Ecological, evolutionary & environmental sciences

For a reference copy of the document with all sections, see [nature.com/documents/nr-reporting-summary-flat.pdf](https://www.nature.com/documents/nr-reporting-summary-flat.pdf)

Life sciences study design

All studies must disclose on these points even when the disclosure is negative.

Sample size	For in vitro experiments, sample sizes were determined based on previous similar studies that have given statistically significant results (PMID: 31634899, 35922516). The number of animals studied per treatment group was determined based on our preliminary data and previous similar studies that have given statistically significant results (PMID: 35922516 and 25402683), and respects the limited use of animal models in line with the 3R recommendations: Replacement, Reduction, Refinement.
Data exclusions	No data exclusions.
Replication	The experimental findings were reproduced as validated by at least three independent experiment in Fig 1c-f, Fig 2b-e, Fig 3a-e, Fig 4b-c and e, Extended Fig 2a-c and i, Extended Fig 3a-k; and at least two independent experiments in Fig 1b and g, Fig 4f-h, Extended Fig 1b-i,k and l, Extended Fig 2d-h and j-l, Extended Fig 3l-p, Extended Fig 4a-h, Extended Fig 5, Extended Fig 6, Extended Fig 7c and e-h, Extended Fig 8c-j, Extended Fig 9a-c and f-h, and Extended Fig 10d-e.
Randomization	For animal studies, mice were randomized into separate cages. For in vitro studies, randomization is not relevant since cells come in millions of populations and are automatically randomized and seeded to different wells for treatment.
Blinding	For animal study, mice were given a number prior to data collection and analysis. Data was collected and analyzed blindly. For in vitro experiments, investigators were not blinded, as standard in this manner of study, which contained multiple steps requiring distinct operations for accuracy and precision precluding blinding to experimental variables.

Reporting for specific materials, systems and methods

We require information from authors about some types of materials, experimental systems and methods used in many studies. Here, indicate whether each material, system or method listed is relevant to your study. If you are not sure if a list item applies to your research, read the appropriate section before selecting a response.

Materials & experimental systems

n/a	Involved in the study
<input type="checkbox"/>	<input checked="" type="checkbox"/> Antibodies
<input type="checkbox"/>	<input checked="" type="checkbox"/> Eukaryotic cell lines
<input checked="" type="checkbox"/>	<input type="checkbox"/> Palaeontology and archaeology
<input type="checkbox"/>	<input checked="" type="checkbox"/> Animals and other organisms
<input checked="" type="checkbox"/>	<input type="checkbox"/> Clinical data
<input checked="" type="checkbox"/>	<input type="checkbox"/> Dual use research of concern
<input checked="" type="checkbox"/>	<input type="checkbox"/> Plants

Methods

n/a	Involved in the study
<input checked="" type="checkbox"/>	<input type="checkbox"/> ChIP-seq
<input type="checkbox"/>	<input checked="" type="checkbox"/> Flow cytometry
<input checked="" type="checkbox"/>	<input type="checkbox"/> MRI-based neuroimaging

Antibodies

Antibodies used	GPX4 (1:1000 for WB, ab125066, Abcam), 4-HNE (0.5 g/mL for IF, MHN-20P, JaiCA), human FSP1 (1:1000, sc-377120, Santa Cruz Biotechnology), human FSP1(1:5 for WB, clone AIFM2 6D8, rat IgG2a, developed in-house: available from Sigma, Cat#MABC1638-25UL), mouse FSP1 (1:100 for WB, clone AIFM2 1A1 rat IgG2a, developed in-house), mouse FSP1(1:5 for WB and undilute or 1:1 for ICC and IF, clone AIFM2 14D7 IgG2b, developed in-house), human SLC7A11 (1:10; Rat IgG2a monoclonal antibody against an N-terminal peptide of hXCT, clone 3A12-1-1, developed in-house) mouse SLC7A11 (1:1000, Cell Signaling Technology, Cat#98051S), ACSL4 (1:1000, clone A-5, Santa Cruz, Cat#sc-271800), β -actin-HRP (1:50000, A3854, Sigma-Aldrich), valosin containing protein (VCP, 1:10000, ab11433 or ab109240, Abcam), Calnexin (1:100 for ICC, ab22595, Abcam), GM130 (1:100 for ICC, Clone: EP892Y, ab52649, Abcam), EEA1 (1:100 for ICC, Clone: C45B10, 3288S, Cell SignalingTechnology), and LAMP1 (1:100 for ICC, Clone: H4A3, sc20011, Santa Cruz Biotechnology), HA tag (YPYDVPDYA, 1:1000 for WB and 1:10 for IF, clone 3F10 rat IgG1, developed in-house), FLAG tag (DYKDDDDK, 1:5000, 2368S, Cell Signaling Technology), Goat anti-Rat Alexa Fluor 488 IgG (H+L) (1:500, A-11006, Invitrogen), Goat Anti-Mouse IgG H&L Alexa Fluor 647 (1:500, ab150115, Abcam), Donkey anti-rat IgG alexa fluor 555 (1:500, ab150154, Abcam) were used in this study.
Validation	GPX4 (ab125066), VCP (ab11433 or ab109240), Human FSP1 (sc-377120), HA tag (clone 3F10), FLAG tag (2368S), β -actin-HRP (A3854), ACSL4 (sc-271800), human SLC7A11 (clone 3A12) antibodies were validated for WB using mouse and human cells samples in previous publications (PMID: 35922516, 31634899, and 27842070). 4-HNE (MHN-20P) antibody was validated for IHC using mouse samples in a previous publication (PMID: 35922516) and for IF in this study in Extended Fig 8d,h. FSP1 antibody (clone AIFM2 1A1/6D8 rat IgG2a, and clone AIFM2 14D7 IgG2b, developed in-house) has been validated for WB in previous study (PMID: 35922516), and for ICC/IF in this study in Extended Fig 4d. Calnexin antibody (ab22595) was validated for ICC using human and mouse cell samples on Cell Signaling Technology website. GM130 antibody (ab52649) was validated for WB using mouse embryonic fibroblasts on Abcam website and for ICC in this study in Extended Fig 4b. mouse xCT/SLC7A11 antibody (98051S) was validated for WB using mouse cell samples on Cell Signaling Technology website. EEA1 antibody (3288S) was validated for ICC using human and mouse cell samples on Cell Signaling Technology website. LAMP1 antibody (sc20011) was validated for ICC using human and mouse cell samples on Santa Cruz Biotechnology website. Secondary antibodies were validated for ICC/IF on each provider on website (Cell Signaling Technology, Invitrogen, Abcam).

Eukaryotic cell lines

Policy information about [cell lines and Sex and Gender in Research](#)

Cell line source(s)	4-OH-TAM-inducible Gpx4 ^{-/-} murine immortalized fibroblasts (Pfa1) were reported previously (PMID: 18762024). HT-1080 (CCL-121), 786-O (CRL-1932), A375 (CRL-1619), B16F10 (CRL-6475), HEK293T (CRL-3216), HT-29 (HTB-38), NCI-H460 (HTB-177), MDA-MB-436 (HTB-130), and 4T1 (CRL-2539) cells were obtained from ATCC. THP-1 cells were obtained from DSMZ (Germany). Human PBMC cells were purchased from Tebu-bio (Cat#088SER-PBMC-F). SUDHL5, SUDHL6, DOHH2, and OCI-Ly19 cells (available from DSMZ) were kindly gifted from Dr. Stephan Hailfinger. Rat1 cells (available from Thermo Fisher) were kindly gifted from Medizinische Hochschule Hannover.
Authentication	None of the cell lines used were authenticated.
Mycoplasma contamination	All cell lines were tested negative for mycoplasma contamination.
Commonly misidentified lines (See ICLAC register)	No commonly misidentified cell lines were used.

Animals and other research organisms

Policy information about [studies involving animals; ARRIVE guidelines](#) recommended for reporting animal research, and [Sex and Gender in Research](#)

Laboratory animals	Five to six-weeks-old female C57BL6/J and athymic nude mice were obtained from Charles River and six to seven weeks-old mice were used for experiments. All mice were kept under standard conditions with water and food ad libitum and in a controlled environment (22 ± 2°C, 55 ± 5% humidity, 12 h light/dark cycle) in Helmholtz Munich animal facility under SPF-IVC standard conditions.
--------------------	--

Wild animals	The study did not involve wild animals.
Reporting on sex	Experiments were performed on only female mice.
Field-collected samples	The study did not involve field-collected samples.
Ethics oversight	All experiments were performed in compliance with the German Animal Welfare Law and have been approved by the institutional committee on animal experimentation and the government of Upper Bavaria (ROB-55.2-2532.Vet_02-17-167).

Note that full information on the approval of the study protocol must also be provided in the manuscript.

Flow Cytometry

Plots

Confirm that:

- The axis labels state the marker and fluorochrome used (e.g. CD4-FITC).
- The axis scales are clearly visible. Include numbers along axes only for bottom left plot of group (a 'group' is an analysis of identical markers).
- All plots are contour plots with outliers or pseudocolor plots.
- A numerical value for number of cells or percentage (with statistics) is provided.

Methodology

Sample preparation	100,000 cells per well were seeded on a 12-well plate one day prior to the experiments. On the next day, cells were treated with 2.5 μ M icFSP1 for 3 h, and then incubated with 1.5 μ M C11-BODIPY 581/591 (Invitrogen, Cat#D3861) for 30 min in a 5% CO ₂ atmosphere at 37°C. Subsequently, cells were washed by PBS once and trypsinized, and then resuspended in 500 μ L PBS. Cells were passed through a 40 μ m cell strainer and analyzed by a flow cytometer (CytoFLEX, Beckman Coulter) with a 488-nm laser for excitation. Data was collected from the FITC detector (for the oxidized form of BODIPY) with a 525/40nm bandpass filter and from the PE detector (for the reduced form of BODIPY) with a 585/42 nm bandpass filter.
Instrument	CytoFLEX (Beckman Coulter)
Software	CytExpert v2.4 was used for data collection. FlowJo v10 was used for data analysis.
Cell population abundance	At least 10,000 cells were analyzed for each sample.
Gating strategy	Cell populations were separated from cellular debris using FSC and SSC.

Tick this box to confirm that a figure exemplifying the gating strategy is provided in the Supplementary Information.



Integrated chemical and genetic screens unveil FSP1 mechanisms of ferroptosis regulation

Received: 3 March 2023

Accepted: 25 September 2023

Published online: 13 November 2023

Check for updates

Toshitaka Nakamura ¹, Eikan Mishima ^{1,2}, Naoya Yamada¹, André Santos Dias Mourão³, Dietrich Trümbach ¹, Sebastian Doll¹, Jonas Wanninger¹, Elena Lytton¹, Peter Sennhenn⁴, Tamara Nishida Xavier da Silva ⁵, José Pedro Friedmann Angeli ⁵, Michael Sattler ^{3,6}, Bettina Proneth ^{1,7} & Marcus Conrad ^{1,7} ✉

Ferroptosis, marked by iron-dependent lipid peroxidation, may present an Achilles heel for the treatment of cancers. Ferroptosis suppressor protein-1 (FSP1), as the second ferroptosis mainstay, efficiently prevents lipid peroxidation via NAD(P)H-dependent reduction of quinones. Because its molecular mechanisms have remained obscure, we studied numerous FSP1 mutations present in cancer or identified by untargeted random mutagenesis. This mutational analysis elucidates the FAD/NAD(P)H-binding site and proton-transfer function of FSP1, which emerged to be evolutionarily conserved among different NADH quinone reductases. Using random mutagenesis screens, we uncover the mechanism of action of next-generation FSP1 inhibitors. Our studies identify the binding pocket of the first FSP1 inhibitor, iFSP1, and introduce the first species-independent FSP1 inhibitor, targeting the NAD(P)H-binding pocket. Conclusively, our study provides new insights into the molecular functions of FSP1 and enables the rational design of FSP1 inhibitors targeting cancer cells.

Since the recognition of ferroptosis as a distinct iron-dependent form of cell death characterized by the oxidative destruction of cellular membranes, the process has attracted tremendous interest, likely owing to its high relevance in human diseases, such as neurodegenerative disorders, tissue ischemia–reperfusion injury and malignancies¹. In particular, certain cancer-cell states, including cancer stem cells and therapy-resistant and disseminating cancer cells, have been reported to exhibit an inherent vulnerability to ferroptosis, providing a rationale for selective induction of ferroptosis as a next-generation cancer therapy approach^{2–7}. Recently, FSP1 was identified as a powerful backup

system for a key regulator of ferroptosis called glutathione peroxidase 4 (GPX4)^{8–11}. By reducing quinones, such as extra-mitochondrial ubiquinone (CoQ₁₀) or vitamin K at the expense of NAD(P)H, the NAD(P)H–CoQ₁₀–vitamin K–FSP1 axis averts the lipid-peroxidation chain reaction and associated ferroptosis on the level of phospholipid radicals. FSP1 is expressed in numerous cancer cell lines, and knockout of the FSP1-encoding gene, apoptosis-inducing factor mitochondria associated 2 (*Aifm2*), has no impact on embryo development and does not cause any overt phenotype in adult mice^{10,12,13}. Therefore, FSP1 might be preferred as a target in tumor cells compared with GPX4 (refs. 14–17),

¹Institute of Metabolism and Cell Death, Molecular Target and Therapeutics Center, Helmholtz Munich, Neuherberg, Germany. ²Division of Nephrology, Rheumatology and Endocrinology, Tohoku University Graduate School of Medicine, Sendai, Japan. ³Institute of Structural Biology, Molecular Target and Therapeutics Center, Helmholtz Munich, Neuherberg, Germany. ⁴transMedChem, Munich, Germany. ⁵Rudolf Virchow Zentrum (RVZ), Center for Integrative and Translational Bioimaging, University of Würzburg, Würzburg, Germany. ⁶Bavarian NMR Center, Department of Bioscience, School of Natural Sciences, Technical University of Munich, Garching, Germany. ⁷These authors contributed equally: Bettina Proneth, Marcus Conrad.

✉ e-mail: marcus.conrad@helmholtz-munich.de

which is known to be essential for early embryogenesis and tissue homeostasis in a variety of organs, such as the kidneys, liver and brain¹⁸.

Although FSP1's central role in ferroptosis prevention has been established, detailed molecular and structural mechanisms underlying the process have remained elusive, and studies investigating mutations of FSP1 occurring in certain cancer types are still in their infancy. The first reported inhibitor for FSP1 (that is, iFSP1)⁸ is specific for the human enzyme^{19,20}, and this specificity precludes in-depth studies on its precise mechanism of action (MoA), thus hindering the analysis of organismal differences and similarities among different FSP1 orthologs. In light of these limitations and shortcomings, we conducted comprehensive chemical and genetic screenings both to understand the molecular and structural basis of FSP1 function and FSP1's role in cellular ferroptosis vulnerability and to identify FSP1 inhibitors that can target FSP1 enzymes across different organisms.

Results

G244 is essential for the predicted NAD(P)H-binding site

To understand the molecular and structural basis of FSP1's functions, we surveyed consensus sequences and sequence motifs of FSP1 orthologs and nicotinamide adenine dinucleotide (NADH)-quinone reductases across various organisms. Among these, type II NADH-quinone reductases (NDH-2s) are well-characterized membrane proteins involved in the respiratory chain^{21,22}, and like FSP1 are flavoproteins that can efficiently reduce quinones using NADH. NDH-2s contain two conserved NADH-binding motifs (GXGXXGXE, WXXG) and one flavin adenine dinucleotide (FAD)-binding motif (GD)²³. Interestingly, these consensus amino acid sequences in FSP1 are well-conserved among species (Fig. 1a,b and Extended Data Fig. 1a,b). Previously, the E156A and D285N substitutions, located within the GXGXXGXE and GD binding sites of human FSP1, respectively, have been reported to affect the enzymatic activity of FSP1 (refs. 9,24), although the functional relevance of G244 (WXXG motif) in FSP1 has remained unclear. In addition, a substitution (that is, p.G244D) within the NAD-binding motif is registered in the database of somatic mutations in human cancer (<https://cancer.sanger.ac.uk/cosmic>)²⁵ (Extended Data Fig. 2a,b). Thus, we first analyzed whether substituting G244 with aspartic acid affects the enzymatic activity of FSP1 in vitro^{8,10}. The G244D substitution in fact abrogates its oxidoreductase activity to a much greater extent than does the E156A substitution (Fig. 1c,d). This loss in enzyme activity is very similar to that of the inactive D285N mutant, which lacks the prosthetic group, flavin adenine dinucleotide (FAD) (Fig. 1c,d). We then investigated the cellular relevance of these substitutions in ferroptosis suppression using mouse embryonic fibroblast cells with 4-hydroxytamoxifen (Tam)-inducible deletion of *Gpx4* (that is, Pfa1 cells)²⁶, and in cells treated with the GPX4 inhibitor (1S,3R)-RSL3 (RSL3)². We included cells with the somatic substitutions V148L and S187F, which are also reported in the database, as a direct comparison, as well as other well-studied alterations such as G2A and Lyn11 membrane-anchoring sequence (Lyn11)-tagged G2A (Extended Data Fig. 2c–f). The G2A variant is known to be the myristoylation-defective mutant and strongly affects FSP1 localization, thereby abrogating its ferroptosis-suppressive function⁸. By contrast, the Lyn11-G2A mutant has a membrane-targeting sequence attached to the N-terminus of FSP1-G2A, and therefore can suppress ferroptosis⁹. Although the other reported somatic substitutions (V148L and S187F) and the Lyn11-G2A mutant enable FSP1 to protect against ferroptosis to some extent, the G244D mutant showed complete loss of its ferroptosis-suppressive function in the same way as the D285N and G2A variants (Fig. 1e,f and Extended Data Fig. 2d,e). To further validate these consensus motifs, we took advantage of the protein structure of FSP1 predicted by AlphaFold2 (refs. 27,28), which perfectly aligns with the crystal structure of the yeast NDH-2 enzyme known as Ndi1 (ref. 29) (Extended Data Fig. 1b), resulting in the superimposed, modeled structure of FSP1 with putative binding sites for FAD, NADH and CoQ₅ (Extended Data Fig. 2g)¹⁹. According to this modeled FSP1

structure, G244 is an essential constituent of the NADH-binding domain (Fig. 1g), similar to other NDH-2s (Extended Data Fig. 1b), further supporting the findings that the somatic substitution G244D abrogates the ferroptosis-suppressive role of FSP1.

Genetic screens unravel the proton-transfer function of FSP1

To gain further insights into the molecular mechanisms underlying how FSP1 reduces quinones at the expense of NAD(P)H, we established a random mutagenesis screen as an unbiased approach (Fig. 2a). Using error-prone PCR, up to three DNA mutations, on average, were introduced into the FSP1 gene *AIFM2*, resulting in one to three amino acid substitutions per FSP1 molecule. The resulting pool of genetic material was subsequently cloned into a lentivirus-based expression vector using seamless cloning. This plasmid pool was then transduced into Pfa1 cells with a very low infection ratio (the multiplicity of infection was approximately 0.1), according to genome-wide CRISPR screening approaches performed by our group and others^{30–32}, allowing each cell to express one FSP1 mutant. Transduced cells were divided into two groups: one was collected immediately after blasticidin selection, and the other was treated with 500 nM RSL3 for 2 d before collection. After cells were collected, genomic DNA was extracted and *AIFM2* was amplified by high-fidelity PCR and subjected to next-generation sequencing (NGS), with the goal of identifying possible mutations. Then, the complete sequence of *AIFM2* was analyzed, and the RSL3-treated group was compared with the control group. By calculating the Z score of each DNA sequence and annotating amino acid alterations in FSP1, we retrieved several expected loss-of-function mutations that corresponded to residues in the myristoylation motif (MGXXXS)³³, the NADH-binding motif (GXGXXGXE, WXXG) and the FAD-binding motif (GD) (Fig. 2b), substantiating the validity of our approach. To further validate the screening results, we cloned the majority of detected mutations and stably expressed them in Pfa1 cells. Indeed, several mutants are sensitive to RSL3- and tamoxifen-induced ferroptosis (Fig. 2c–e and Extended Data Fig. 3a), indicating that they fail to confer the ferroptosis-suppressive function of FSP1. However, without a three-dimensional (3D) structure of FSP1, we cannot formally exclude that a fraction of these mutations not only directly impact the enzymatic activity, but also affect the binding affinity of substrates, expression levels in cells and/or proper protein folding and localization. Nonetheless, to further investigate the role of the aforementioned amino acid residues, we again took advantage of the modeled structure of FSP1 (Extended Data Fig. 2g). According to this model, D41 and C286, located in close proximity to FAD or the predicted GD motif, respectively (Figs. 1b and 2b), are suggested to be important for FAD binding (Fig. 2f). Additionally, our mutagenesis screen identified E160 and K355 as critical amino acid residues for enzyme activity of ferroptosis suppression (Fig. 2b–e). Mechanistically, NDH-2s and other members of the two-dinucleotide binding domains flavoprotein (tDBDF) superfamily, such as dihydrolipoamide dehydrogenases (DLDs), coenzyme A-glutathione reductases (GRs), apoptosis-inducing factor mitochondria associated 1 (AIFM1), ferredoxin reductases (FNRs), nitrite reductases (NIRs), NADH peroxidases and sulfide-quinone oxidoreductases (SQRs), have the glutamic acid residue (Glu) as a catalytic site, like E172 in *Staphylococcus aureus* (Fig. 2g), as well as a nearby glutamic acid and/or lysine, like K379 in *S. aureus*³⁴. In line with this mechanism, E156 and K355 of FSP1 are structurally well conserved. Additionally, sequential acidic amino acid residues in close proximity to the glutamic acid have been proposed to be part of a conserved proton-transfer function during quinone reduction²³. This proton-transfer function presumably consists of a proton transfer through sequential, conserved carboxylic residues in the α -helix (that is E172, E176, D179 and E183 for *S. aureus* (Fig. 2g), E169, E173, D176 and E180 for *C. thermarum*, and E242, E246, D249 and D254 for *S. cerevisiae*, respectively), and a residue for hydrogen bond formation and subsequent protonation of the quinone upon reduction in the active site (that is, K379 for *S. aureus*, K376 for *C. thermarum*,

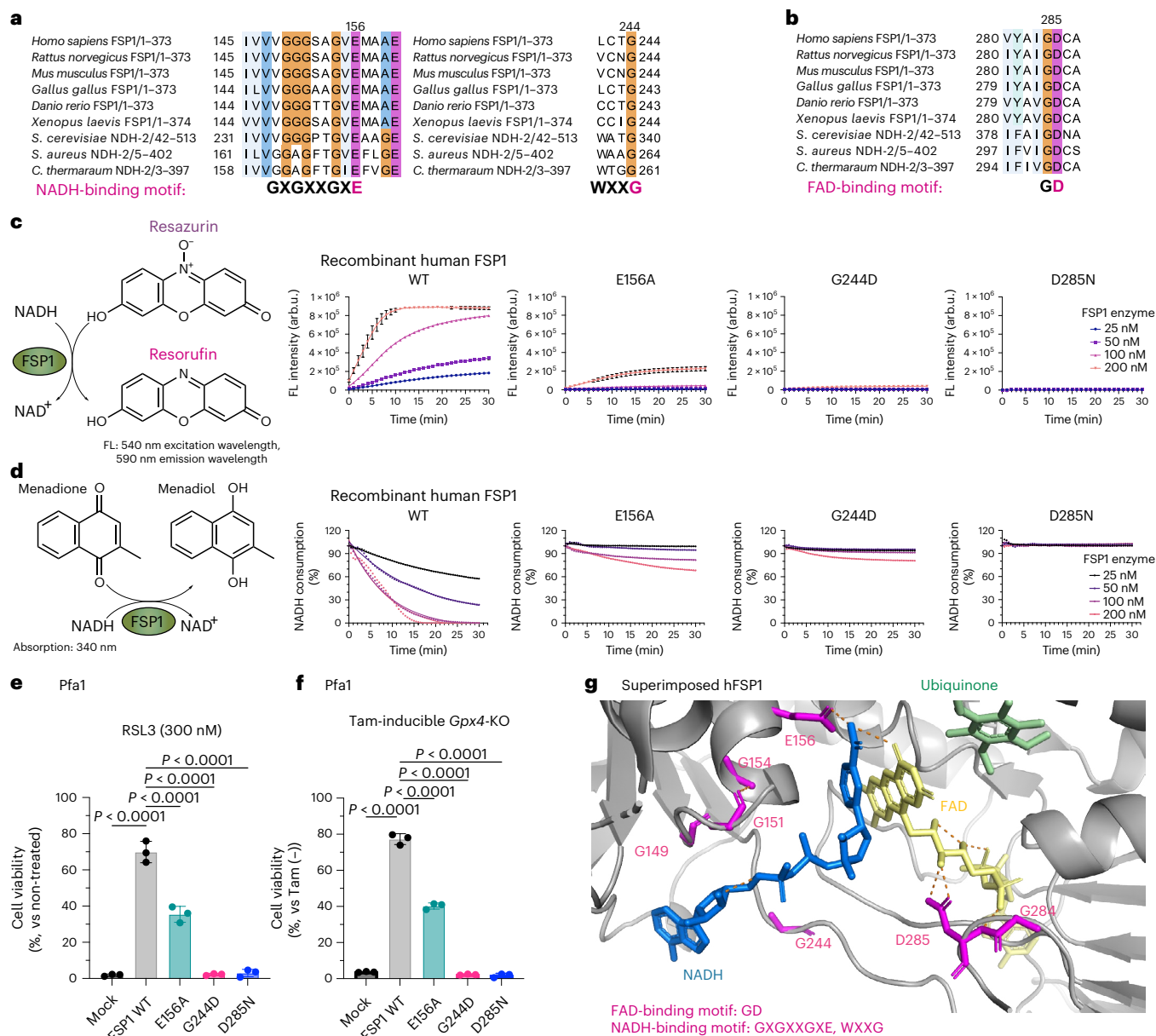


Fig. 1 | G244 is essential for the predicted NAD(P)H-binding site of FSP1. **a**, Conserved NADH-binding site (GXGXXGXE and WXXG). Protein alignment of FSP1 from different species: *Homo sapiens* (human), *Mus musculus* (mouse), *Rattus norvegicus* (rat), *Gallus gallus* (chicken), *Xenopus laevis* (frog), *Danio rerio* (zebrafish), *Saccharomyces cerevisiae* Ndi1 (PDB: 4G73), *Caldalkalibacillus thermarum* NDH-2 (PDB: 5NA1), and *Staphylococcus aureus* NDH-2 (PDB: 4NWZ). The numbers next to the organisms indicate the range of the amino acids of each gene used for generating the protein alignment. **b**, Conserved FAD-binding site (GD). Protein alignment of FSP1 from different species. **c**, Schematic representation of the FSP1 enzyme activity assay with resazurin used as the substrate (left). Reduction of resazurin in the presence of wild-type (WT) FSP1, FSP1-E156A, FSP1-G244D, or FSP1-D285N at the indicated concentrations. Data are shown as the mean ± s.d. of 3 wells of a 96-well plate, from 1 of 3 independent experiments. FL, fluorescence. **d**, Schematic representation of FSP1 enzyme activity assay, with menadione used as the substrate (left). Oxidation of NADH in the presence of WT FSP1, FSP1-E156A, FSP1-G244D, or FSP1-D285N at the

indicated concentrations. Data are from a single well of a 96-well plate from 1 of 3 independent experiments. **e**, Viability of Pfa1 cells stably overexpressing WT HA-tagged human FSP1 (hFSP1-HA) or FSP1 mutants, treated with 300 nM RSL3 for 24 h. Data are shown as the mean ± s.d. of 3 wells of a 96-well plate from 1 of 3 independent experiments. **f**, Viability was measured in Pfa1 cells stably overexpressing WT hFSP1 or one of the mutants with or without treatment with Tam (1 μM) for 72 h. Data were normalized to each group that was not treated with Tam. Data are shown as the mean ± s.d. of 3 wells of a 96-well plate from 1 of 3 independent experiments. *P* values were calculated using a one-way analysis of variance (ANOVA) followed by Dunnett’s multiple-comparison test (**e, f**). **g**, Predicted FSP1 structure, with consensus NADH- and FAD-binding motifs, from the AlphaFold2 database (<https://alphafold.ebi.ac.uk>). The co-factors, FAD (yellow), NADH (blue) and CoQ₃ (green), were embedded from the structure of the yeast ortholog, NDH-2 (Ndi1) (PDB: 4G73). The expected hydrogen bond was generated by Pymol.

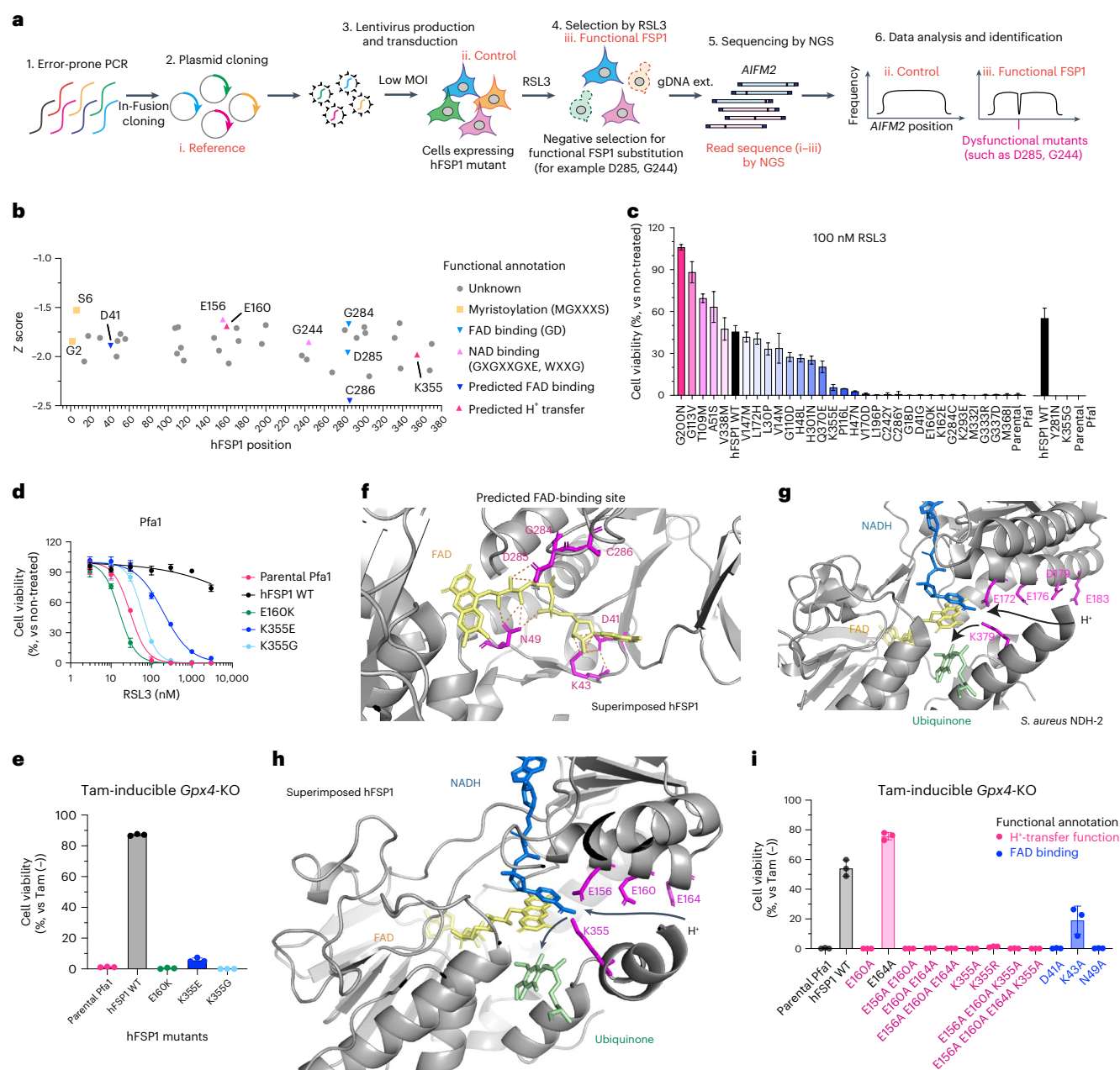


Fig. 2 | An unbiased genetic screen uncovers the proton-transfer function of FSP1. **a**, Schematic of the mutational screen. *AIFM2* was mutated using error-prone PCR (Step 1). PCR fragments were then cloned into plasmids (i. Reference) using the seamless cloning enzyme “in-Fusion” (Step 2). Lentivirus pools using randomly mutated plasmids were transduced into Pfa1 cells (ii. Control) with low multiplicity of infection (MOI) (Step 3). Cells overexpressing mutated FSP1 were selected by RSL3 (iii. Functional FSP1) (Step 4). Surviving clones were harvested and genomic DNA was extracted and followed by NGS sequencing (Step 5). Sequencing results were analyzed and mutations were identified (Step 6). gDNA ext., genomic DNA extraction. **b**, Representative summary of dysfunctional FSP1 substitutions after Z-score calculation. Mutated residues in the myristoylation motif (MGXXXS, yellow), NADH-binding motif (GXGXXGXE, WXXG, light pink) or FAD-binding motif (GD, light blue), and those predicted to affect proton-transfer function (E160 and K355, pink) or FAD binding (D41 and C286, blue), are shown. **c**, Viability of Pfa1 cells stably overexpressing hFSP1-HA or mutant FSP1 that were treated with 100 nM RSL3 for 24 h or that were not treated. Data are shown as the mean ± s.d. of 3 wells of a 384-well plate (left) or a 96-well plate (right) from one experiment. **d**, Viability of Pfa1 cells stably overexpressing WT hFSP1-HA or mutant FSP1 that were treated with RSL3 for 24 h or that were not treated.

e, Viability of Pfa1 cells stably overexpressing WT hFSP1 or a mutant that were treated with 1 μM Tam for 72 h or that were not treated. Data were normalized to each group that was not treated with Tam (Tam (-)). Data are shown as the mean ± s.d. of 3 wells of a 96-well plate from 1 of 3 independent experiments (**d,e**). **f**, Superimposed hFSP1 structure with FAD (yellow) and FAD-binding residues. FAD was embedded from the structure of *S. aureus* NDH-2 (PDB: 5NA1), and expected hydrogen bonds were generated using Pymol. **g**, Superimposed *S. aureus* NDH-2 structure (PDB: 5NA1) with the co-factors FAD (yellow), NADH (blue) and CoQ₃ (green). The proton transfer through sequential carboxylic residues in the α-helix (that is, E172, E176, D179 and E183) and subsequent final protonation from K379 to ubiquinone are indicated with black arrows. **h**, Proposed FSP1 proton transfer through sequential carboxylic residues in the α-helix (that is, E156, E160 and E164) and subsequent final protonation from K355 to ubiquinone are indicated with black arrows. **i**, Viability was measured in Pfa1 cells stably overexpressing WT hFSP1 or mutants after treatment with 1 μM Tam for 72 h or without treatment. Data were normalized to each group that was not treated with Tam. Data are shown as the mean ± s.d. of 3 wells of a 96-well plate from 1 of 2 independent experiments.

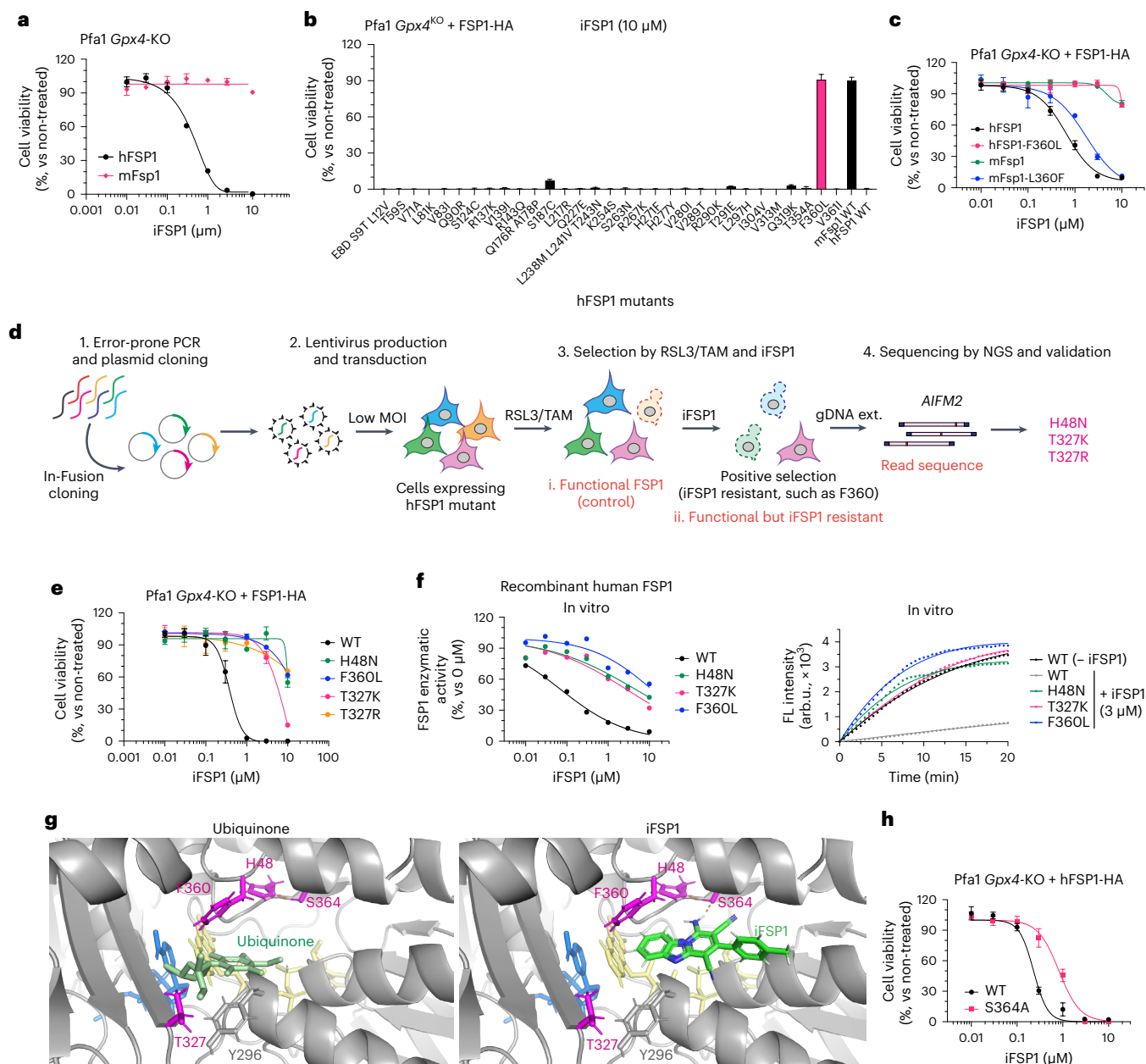


Fig. 3 | iFSP1 targets the quinone-binding pocket. a, Viability of Pfa1 *Gpx4*-KO cells stably overexpressing hFSP1-HA or mouse (mFsp1)-HA treated with iFSP1 for 24 h. **b**, Viability of Pfa1 *Gpx4*-KO cells stably overexpressing WT FSP1-HA or an FSP1 mutant, treated with 10 μM iFSP1 for 24 h. **c**, Viability of Pfa1 *Gpx4*-KO cells stably expressing hFSP1, hFSP1-F360L, mFsp1, or mFsp1-L360F, treated with iFSP1 for 24 h. **d**, Schematic representation of the mutational screen. **e**, Viability of Pfa1 *Gpx4*-KO cells stably expressing WT FSP1-HA or an FSP1 mutant, treated with iFSP1 for 24 h. **f**, Representative dose–response curves for the effect of iFSP1 on the activity of FSP1 mutants, using recombinant purified hFSP1 protein (left). Representative reaction curve for the effect of 3 μM iFSP1 or 0 μM iFSP1 on the

activity of WT FSP1 and the mutant variants (right). Data are from a single well of a 96-well plate from 1 of 3 independent experiments. arb.u., arbitrary units. **g**, Comparison between iFSP1 and quinone in the binding pocket. H48, T327, S364 and F360 are highlighted in magenta. In silico simulation identified the interaction between S364 and iFSP1 using a hydrogen bond, and H48 is expected to stabilize its orientation. Each interaction is depicted by the dashed line in orange. **h**, Cell viability of Pfa1 *Gpx4*-KO cells stably overexpressing WT hFSP1 or hFSP1-S364A, treated with iFSP1 for 24 h. Data are shown as the mean ± s.d. of 3 wells of a 96-well plate from 1 of 3 independent experiments (**a–c,e,h**).

and Y482 for *S. cerevisiae*, respectively) (Fig. 2g and Extended Data Fig. 3b,c). In accordance with this protonation pathway, E156, E160 and E164 are present in the α-helix, and K355 is in close proximity to the catalytic site in FSP1 (Fig. 2h). Thus, this highly conserved proton-transfer mechanism involving sequential carboxylic acid and lysine residues is most likely crucial for the quinone protonation function of FSP1. Therefore, amino acid mutations identified by random

mutagenesis, namely E160K, K355E and K355G, can be considered detrimental because they potentially interrupt the proton-transfer chain. To validate these FAD and proton-transfer functions, we generated corresponding alanine mutants and overexpressed them in Pfa1 cells. Except for the E164A and K43A mutants, all remaining Ala substitutions failed to rescue from ferroptosis induced by either knockout (KO) of *Gpx4* or pharmacological inhibition of GPX4,

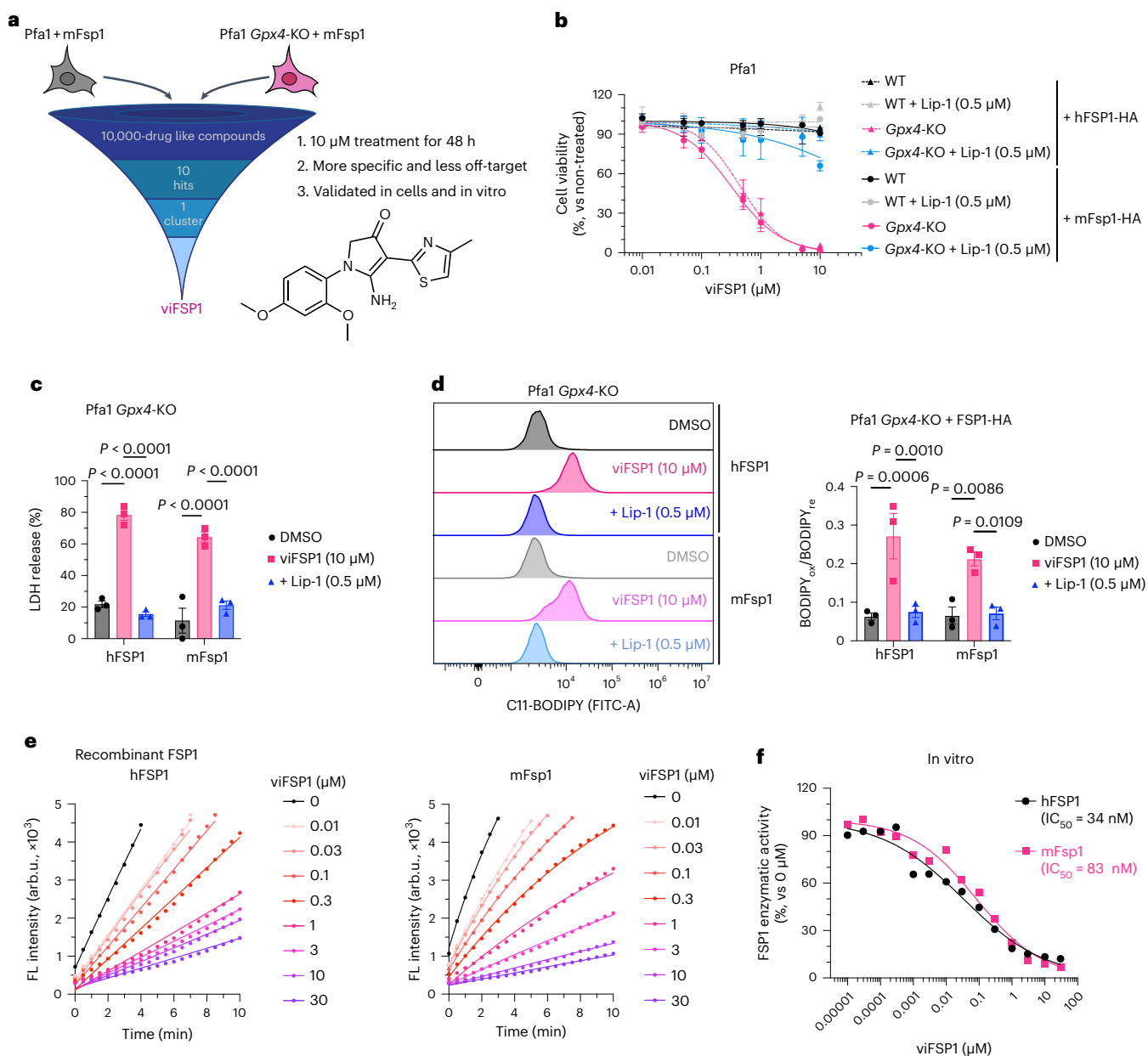


Fig. 4 | Identification of viFSP1 as a species-independent FSP1 inhibitor.

a, Schematic of the compound screen to identify new mFSP1 inhibitors, and the chemical structure of viFSP1. Survival of Pfa1 *Gpx4*-KO + mFSP1 cells relies on mFSP1 function. **b**, Viability of Pfa1 *Gpx4*-WT and *Gpx4*-KO cells stably overexpressing human or mouse FSP1-HA, treated with viFSP1 for 24 h. Lip-1 was used to inhibit ferroptosis. **c**, Lactate dehydrogenase (LDH) release was determined after treating Pfa1 *Gpx4*-KO cells overexpressing hFSP1-HA or mFSP1-HA with DMSO, 10 μ M viFSP1 or 0.5 μ M Lip-1 for 24 h. **d**, Lipid peroxidation was evaluated by C11-BODIPY 581/591 staining after treating *Gpx4*-KO cells stably overexpressing hFSP1-HA or mFSP1-HA with DMSO, 10 μ M viFSP1 or 0.5 μ M Lip-1

for 3 h. The plot is representative of three independent experiments (left), and quantified median values of three independent experiments (right) are shown. BODIPY_{ox}, fluorescence of oxidized BODIPY. BODIPY_{re}, fluorescence of reduced BODIPY. Data are shown as the mean \pm s.e.m. of three independent experiments (**b–d**). *P* values were calculated using a one-way ANOVA followed by Tukey’s multiple-comparison test (**c,d**). **e**, Representative assays of the inhibitory effect of different concentrations of viFSP1 on hFSP1 (left) or mFSP1 (right), using recombinant purified proteins. **f**, Representative dose–response curves for the effect of viFSP1 on hFSP1 and mFSP1 activity. Data are from a single well of a 96-well plate from 1 of 2 independent experiments (**e,f**).

suggesting that these positions are essential for FSP1 function (Fig. 2i and Extended Data Fig. 3d,e).

iFSP1 targets the quinone-binding pocket

We previously discovered iFSP1, the first FSP1 inhibitor⁸, although the mode of inhibition and the binding site remained unknown. First, we focused on the inherent differences in half-maximal inhibitory concentration (IC₅₀) values between human and mouse FSP1 isoforms, because

iFSP1 is specific for the human protein^{19,20}. Indeed, Pfa1 *Gpx4*-KO cells stably overexpressing human FSP1 are sensitive to iFSP1 treatment, whereas mouse-Fsp1-expressing cells are resistant to it (Fig. 3a). To identify the possible amino acids residue or residues that is or are targeted by iFSP1, we first site-directly altered all human FSP1 residues to their mouse Fsp1 counterparts in a step-by-step fashion and confirmed that their expression levels were sufficient to confer potential resistance to ferroptosis by Tam-inducible KO of *Gpx4* in Pfa1 cells (Extended Data

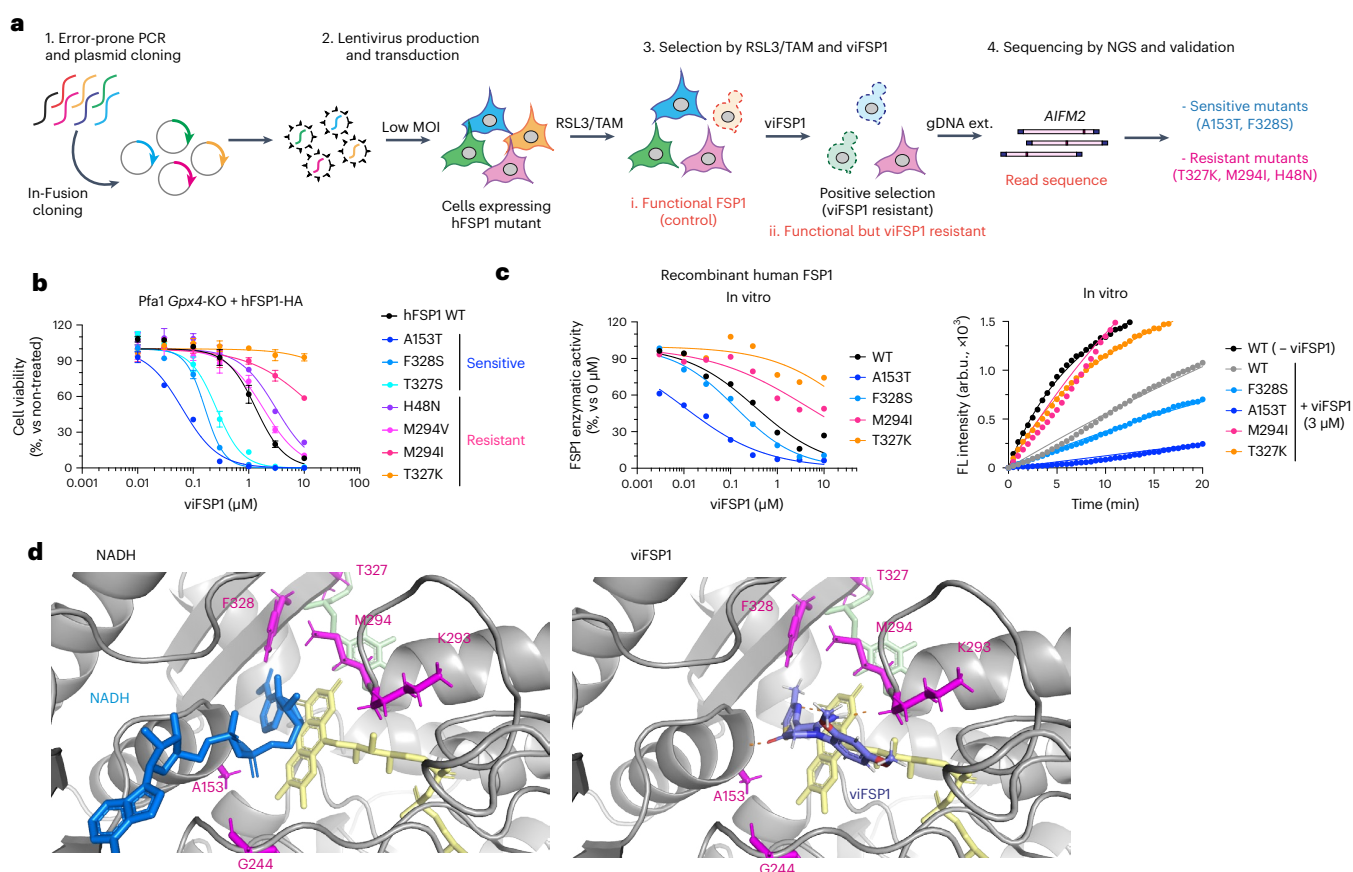


Fig. 5 viFSP1 targets the NAD(P)H-binding pocket of FSP1. **a**, Schematic of the mutational screen to identify the responsible sites affecting viFSP1 activity in hFSP1. **b**, Viability in Pfa1 *Gpx4*-KO cells stably overexpressing mutant hFSP1-HA, treated with viFSP1 for 24 h. Data are shown as the mean \pm s.d. of 3 wells of a 96-well plate from 1 of 3 independent experiments (See also Supplementary Videos 1–4). **c**, Representative dose–response curves for the effect of viFSP1 on the activity of WT FSP1 or its mutants, using recombinant purified hFSP1 protein

(left). Representative in vitro assays of inhibition of WT FSP1 and the mutant variants by 3 μM viFSP1 or 0 μM viFSP1 (right). Data are from a single well of a 96-well plate from 1 of 3 independent experiments. **d**, Comparison between viFSP1 and NADH in respective binding pockets. A153, G244, M294, T327 and F328 are highlighted in magenta. In silico simulation identified the interaction between the main chains of A153, K293 and viFSP1 using a hydrogen bond. Each interaction is depicted by the dashed line in orange.

Fig. 4a,b). Cells stably expressing the mutated human FSP1 enzyme were then treated with iFSP1 for 24 h. Surprisingly, the F360L mutant emerged to be as resistant to iFSP1 treatment as was murine FSP1, and vice versa in murine Fsp1 (Fig. 3b,c)²⁰. Thus, we hypothesized that F360 and its surrounding residues are part of the putative binding pocket of iFSP1. To further pinpoint the actual binding site, we performed a random PCR mutagenesis screen to identify iFSP1-resistant mutants (Fig. 3d). Similar to the RSL3 screening method described above (Fig. 2a), the randomly mutated FSP1 pool was overexpressed in Pfa1 cells and selected with RSL3 for 2 d. Afterwards, cells were treated with Tam to remove dysfunctional FSP1 mutants. Then, TAM/RSL3-selected cells were treated for 7 d with iFSP1 to establish iFSP1-resistant clones, followed by NGS analysis. After data analysis and validation, we identified H48N, T327K and T327R as iFSP1-resistant mutants. For validation, the viability of Pfa1 *Gpx4*-KO cells expressing F360L, H48N, T327K or T327R was determined 24 h after iFSP1 treatment, which showed that they indeed are all resistant to iFSP1 (Fig. 3e and Extended Data Fig. 4c).

To confirm that iFSP1 directly inhibits human FSP1 and does not act up- or downstream in the NAD(P)H–CoQ₁₀–vitamin K–FSP1 axis, we heterologously expressed FSP1 harboring either the H48N, T327K or F360L substitution in *Escherichia coli* and purified recombinant FSP1 variants. We found that, when tested in the classical FSP1 enzyme assay, F360L, H48N and T327K mutants are resistant to iFSP1, corroborating that iFSP1 is a direct inhibitor of human FSP1 (Fig. 3f and Extended Data

Fig. 4d). Interestingly, human, *Gallus gallus* (Chicken), and *Xenopus laevis* (frog) all contain a phenylalanine at position 360 (human FSP1 numbering), whereas mouse, rat (*Rattus norvegicus*) and *Danio rerio* (zebrafish) have a leucine at the corresponding position (Extended Data Fig. 4e). Moreover, human FSP1-T327S, which reflects the serine residue found in *X. laevis*, is also sensitive to iFSP1 (Extended Data Fig. 4f). Thus, we selected and examined F360 (human and chicken) and L360 (mouse and rat), and, as expected, Pfa1 *Gpx4*-KO cells overexpressing human or chicken FSP1 were sensitive to iFSP1, whereas those expressing rat or mouse FSP1 were resistant to iFSP1 (Extended Data Fig. 4g,h). In light of the fact that these mutants face the expected membrane-attaching surface and quinone-binding pocket (Extended Data Fig. 2g), it can be assumed that iFSP1 targets the quinone-binding site (Fig. 3g)^{19,20}. According to this model, iFSP1 would bind to FSP1 via the hydrogen bond between S364 and iFSP1 and the π – π interaction between F360, Y296 and iFSP1 (Fig. 3g,h).

viFSP1 is a species-independent FSP1 inhibitor

iFSP1 is not applicable for FSP1-inhibition studies in experimental rodent models (Extended Data Fig. 4g). Thus, to better understand the role of FSP1 in a broader context, including species-specific differences, inhibitors targeting FSP1 in species besides humans are highly warranted. To this end, we screened a library of 10,000 drug-like small molecules in murine-FSP1-expressing Pfa1 cells (Fig. 4a) and identified a

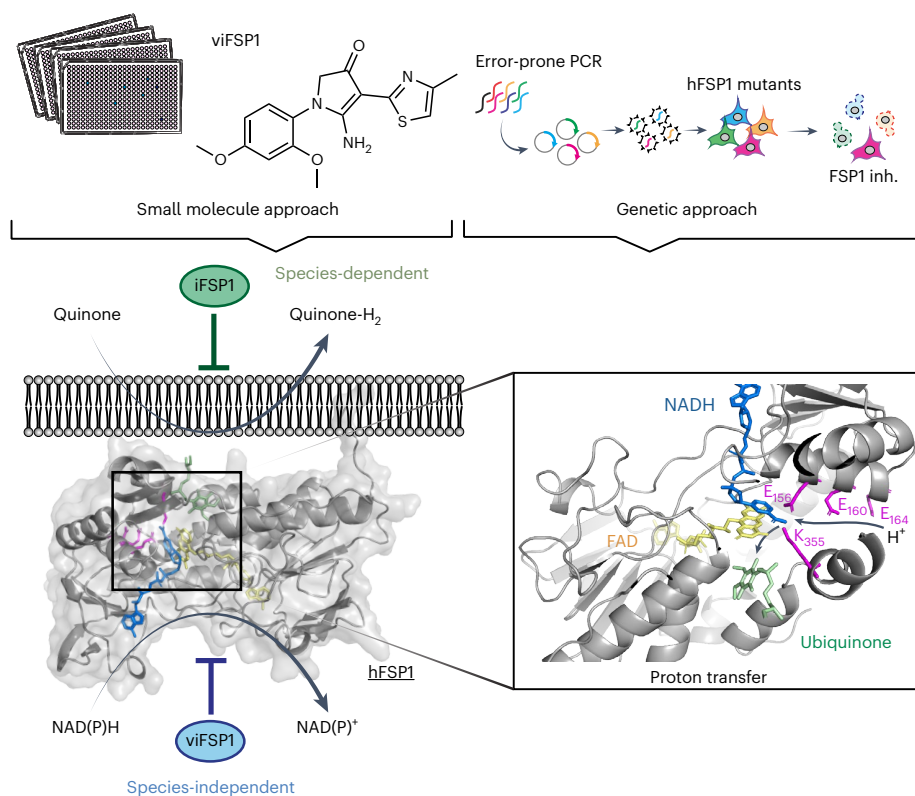


Fig. 6 | Mechanistic insights into FSP1 and its different target sites using FSP1 inhibitors. The chemical approach using the compound library and the genetic approach using targeted and untargeted mutagenesis uncover the mechanism of action of two representative FSP1 inhibitors. Human-specific iFSP1 targets

the quinone-binding pocket, whereas species-independent viFSP1 targets the NAD(P)H-binding pocket. Besides, a well-conserved proton transfer function is critical for the anti-ferroptotic activity of FSP1.

compound, referred to hereafter as versatile inhibitor of FSP1 (viFSP1), that is a new inhibitor of human and murine FSP1. Treatment with viFSP1 causes marked lipid peroxidation and associated ferroptotic cell death in Pfa1 cells stably expressing either murine Fsp1 or human FSP1 (Fig. 4b–d). viFSP1-induced cell death was rescued by the ferroptosis inhibitor liproxstatin-1 (Lip-1)³⁵, confirming that viFSP1 indeed causes ferroptotic cell death in cells whose survival depends on FSP1 (Extended Data Fig. 5a). To address whether viFSP1 may also kill (cancer) cells by targeting FSP1, co-treatment of viFSP1 with pharmacological inhibitors of GPX4 (RSL3 (ref. 36) and JKE-1674 (ref. 37)) or genetic deletion of GPX4 synergistically^{38,39} induced ferroptosis in a number of human and murine cancer cell lines as well as rat fibroblast (Rat1) and Pfa1 cells overexpressing FSP1 from different species (Extended Data Fig. 5b–h and Extended Data Fig. 6a–j). To perform an initial structure–activity relationship study (SAR), we obtained a handful of commercially available analogs of viFSP1 in addition to custom-made ones, indicating that the substitution pattern of methoxy-groups around the phenyl ring influences human/mouse selectivity. The compound structures and corresponding half-maximal effective concentration (EC_{50}) values are depicted in Extended Data Figure 5c. We then studied whether this next-generation FSP1 inhibitor acts as a direct inhibitor of FSP1 using recombinant hFSP1 and mFsp1 enzymes in the resazurin reduction assay^{8,10} (Fig. 4e,f). Indeed, both hFSP1 and mFsp1 enzyme activity are equally sensitive to viFSP1 in a cell-free target-based system, and calculated IC_{50} values do not show a major difference among human and murine enzymes (Fig. 4f). Thus, this set of data strongly indicates that viFSP1 is a direct species-independent FSP1 inhibitor.

To further investigate the competitive mechanism of action of viFSP1, the relationship of FSP1 enzymatic activity and its substrates was analyzed using an in vitro assay. Taking advantage of the fact that

FSP1 can also bind and reduce resazurin at the expense of NADH⁸, we calculated the velocity of the enzyme-catalyzed reaction at infinite concentration of substrate (V_{max}) and the Michaelis constant (K_m) in the presence of FSP1 inhibitors using increasing amounts of either NADH or resazurin (Extended Data Figs. 4i and 7a). From the Lineweaver-Burk and Dixon plots⁴⁰, it can be speculated that iFSP1 and viFSP1 are both non-competitive inhibitors, which means that these FSP1 inhibitors can bind the enzyme in the presence or absence of a substrate; however, this should be investigated experimentally when the 3D structure of FSP1 becomes available.

viFSP1 targets the NAD(P)H-binding pocket of FSP1

To understand the inhibitory mechanism of viFSP1 in more detail, we performed a random mutagenesis screen to identify a viFSP1-resistant mutant version of FSP1 (Fig. 5a). Akin to the iFSP1 screen described above (Fig. 3), Pfa1 *Gpx4*-KO cells stably overexpressing randomly mutated yet functional FSP1 enzymes were selected by viFSP1 for 7 d, followed by NGS analysis. After data analysis and validation, we identified A153T and F328S as viFSP1-sensitive mutants, and H48N, M294I, M294V, T327K and T327R as viFSP1-resistant mutants (Fig. 5b and Extended Data Figs. 4c and 7b). Pfa1 *Gpx4*-KO cells overexpressing A153T or F328S were at least ten times more sensitive to viFSP1 treatment than were cells overexpressing wild-type FSP1; cells overexpressing the H48N, M294I, M294V, T327K or T327R variants were approximately five to ten times more resistant to viFSP1 treatment (Fig. 5b). In addition to the T327K variant of FSP1, the A153T, F328S and M294I variants were examined in the in vitro FSP1 enzyme assay using purified recombinant human FSP1. Thereby, we could observe the same tendency for FSP1 inhibition in the cell-free system using viFSP1 as in cell culture, showing that viFSP1 is a direct inhibitor of FSP1

(Fig. 5c and Extended Data Fig. 7b). Because these amino acids are located in the NAD(P)H-binding site and are highly conserved among species (Extended Data Fig. 7c–f), it can be assumed that viFSP1 targets the NAD(P)H-binding pocket (Fig. 5d).

Discussion

Using a series of targeted and untargeted chemical–genetic screens, we report here unprecedented insights into contributions of the NAD(P)H-binding motif and the proton-transfer function to FSP1 activity (Fig. 6), in addition to the identification of a species-independent FSP1 inhibitor, viFSP1. A number of point mutations in the *AIFM2* gene are present as somatic mutations in people with cancer, including those encoding p.G244D, p.E160D, p.E160 stop, p.K355R and p.D285N (Extended Data Fig. 8a). In light of the loss of function of these mutants, cancer cells harboring these somatic mutations (heterozygous mutations) might be more vulnerable to ferroptosis. Given that some cancer cells are resistant to GPX4-inhibition-induced ferroptosis, and that FSP1 inhibitors sensitize a number of cancer cells to ferroptosis induced by sublethal GPX4 inhibition, the combination therapy of FSP1 inhibitors with canonical ferroptosis inducers, such as GPX4 and system x_c^- inhibitors, ideally in a tumor-specific manner, could potentially be a new anticancer therapy. Depmap analysis (<https://depmap.org/portal/>, v23Q2) revealed that ovarian cancer cells (SKOV3 cells) and endometrial/uterine cancer cells (RL952 cells) harbor G337D and S6L substitutions, respectively, in FSP1 (Extended Data Fig. 8b,c). Considering that S6 is part of the myristoylation consensus motif (Fig. 2b)³³, and that G337D fails to protect against ferroptosis (Fig. 2c), these cancer cell lines might be more vulnerable to ferroptosis induction.

Although iFSP1 was reported as the first FSP1 inhibitor⁸ and it was predicted to target the quinone-binding site in an in silico simulation¹⁹, its MoA, including a potential binding pocket, has remained obscure. The combination of hypothesis-driven and unbiased approaches using site-directed and error-prone PCR mutagenesis, respectively, has now enabled us to pinpoint H48, F360 and T327 as being necessary for iFSP to bind and inhibit human FSP1, which was also reported in a recent independent study²⁰. Considering that some of these amino acid residues can differ substantially among species, this knowledge could be used to develop FSP1 inhibitors to achieve species-specific selectivity. Moreover, bioinformatic analyses of people with cancer harboring T327M mutations in FSP1 (Extended Data Fig. 6b)²⁵ suggest that certain individuals might be resistant to treatment with FSP1 inhibitors, thus likely necessitating personalized treatment approaches.

Because iFSP1 is specific for human FSP1, we introduce here a species-independent FSP1 inhibitor, viFSP1, that will prove useful when studying the functions of FSP1 orthologs. Notably, FSEN15 (ref. 41), a compound based on a similar scaffold, was recently reported by another group, although neither a detailed SAR analysis nor a comprehensive characterization of the interaction site have been presented. In any case, we now characterize viFSP1, which is by far more potent in cultured cells and in a cell-free system, as a direct inhibitor targeting the NADH-binding pocket surrounding residues A153, F328, M294 and T327 of FSP1.

By using random mutagenesis screens with error-prone PCR to identify the binding pocket of FSP1 inhibitors, we infer that the screening strategy described herein can be applied to other compounds when searching for the binding pocket of related target proteins⁴². Thanks to recent advances in artificial-intelligence technologies, and when combined with the predicted structures from AlphaFold2 and other docking simulations, the identification of pharmacological inhibitors will become more accurate, straightforward and reliable. We confirmed that all mutants that are resistant or sensitive to FSP1 inhibitors indeed afford survival of cells after genetic deletion of *Gpx4*, suggesting that these mutants must be functional. However, as experimental data on the 3D structure of FSP1 remain elusive at this stage, we cannot formally exclude the possibility that amino acid alterations can affect

folding and/or other unrecognized post-translational modifications of FSP1. As shown above, this kind of information can be very useful; however, caution must be taken when interpreting data on the basis of modeling approaches. An experimentally validated 3D structure of FSP1 is needed in the near future. As a showcase, we applied these genetics and bioinformatics approaches to FSP1 and identified a series of mutations, which ultimately dictate the sensitivity of cells to ferroptosis. The information collected from the mutational analysis might prove highly beneficial in pharmacogenetic studies to predict the efficacy of ferroptosis therapy for each individual patient in clinical settings in the future.

Online content

Any methods, additional references, Nature Portfolio reporting summaries, source data, extended data, supplementary information, acknowledgements, peer review information; details of author contributions and competing interests; and statements of data and code availability are available at <https://doi.org/10.1038/s41594-023-01136-y>.

References

1. Jiang, X., Stockwell, B. R. & Conrad, M. Ferroptosis: mechanisms, biology and role in disease. *Nat. Rev. Mol. Cell Biol.* **22**, 266–282 (2021).
2. Dixon, S. J. et al. Ferroptosis: an iron-dependent form of nonapoptotic cell death. *Cell* **149**, 1060–1072 (2012).
3. Viswanathan, V. S. et al. Dependency of a therapy-resistant state of cancer cells on a lipid peroxidase pathway. *Nature* **547**, 453–457 (2017).
4. Hangauer, M. J. et al. Drug-tolerant persister cancer cells are vulnerable to GPX4 inhibition. *Nature* **551**, 247–250 (2017).
5. Ubellacker, J. M. et al. Lymph protects metastasizing melanoma cells from ferroptosis. *Nature* **585**, 113–118 (2020).
6. Muller, S. et al. CD44 regulates epigenetic plasticity by mediating iron endocytosis. *Nat. Chem.* **12**, 929–938 (2020).
7. Mai, T. T. et al. Salinomycin kills cancer stem cells by sequestering iron in lysosomes. *Nat. Chem.* **9**, 1025–1033 (2017).
8. Doll, S. et al. FSP1 is a glutathione-independent ferroptosis suppressor. *Nature* **575**, 693–698 (2019).
9. Bersuker, K. et al. The CoQ oxidoreductase FSP1 acts parallel to GPX4 to inhibit ferroptosis. *Nature* **575**, 688–692 (2019).
10. Mishima, E. et al. A non-canonical vitamin K cycle is a potent ferroptosis suppressor. *Nature* **608**, 778–783 (2022).
11. Jin, D. Y. et al. A genome-wide CRISPR–Cas9 knockout screen identifies FSP1 as the warfarin-resistant vitamin K reductase. *Nat. Commun.* **14**, 828 (2023).
12. Mei, J., Webb, S., Zhang, B. & Shu, H. B. The p53-inducible apoptotic protein AMID is not required for normal development and tumor suppression. *Oncogene* **25**, 849–856 (2006).
13. Tonnus, W. et al. Dysfunction of the key ferroptosis-surveillance systems hypersensitizes mice to tubular necrosis during acute kidney injury. *Nat. Commun.* **12**, 4402 (2021).
14. Muller, F. et al. Elevated FSP1 protects KRAS-mutated cells from ferroptosis during tumor initiation. *Cell Death Differ.* **30**, 442–456 (2023).
15. Koppula, P. et al. A targetable CoQ–FSP1 axis drives ferroptosis- and radiation-resistance in KEAP1 inactive lung cancers. *Nat. Commun.* **13**, 2206 (2022).
16. Pontel, L. B. et al. Acute lymphoblastic leukemia necessitates GSH-dependent ferroptosis defenses to overcome FSP1-epigenetic silencing. *Redox Biol.* **55**, 102408 (2022).
17. Nakamura, T. et al. Phase separation of FSP1 promotes ferroptosis. *Nature* **619**, 371–377 (2023).
18. Conrad, M., Lorenz, S. M. & Proneth, B. Targeting ferroptosis: new hope for as-yet-incurable diseases. *Trends Mol. Med.* **27**, 113–122 (2020).

19. Mishima, E. et al. DHODH inhibitors sensitize to ferroptosis by FSP1 inhibition. *Nature* **619**, E9–E18 (2023).
20. Xavier da Silva, T. N., Schulte, C., Alves, A. N., Maric, H. M. & Friedmann Angeli, J. P. Molecular characterization of AIFM2/FSP1 inhibition by iFSP1-like molecules. *Cell Death Dis.* **14**, 281 (2023).
21. Kaila, V. R. I. & Wikstrom, M. Architecture of bacterial respiratory chains. *Nat. Rev. Microbiol.* **19**, 319–330 (2021).
22. Melo, A. M., Bandejas, T. M. & Teixeira, M. New insights into type II NAD(P)H:quinone oxidoreductases. *Microbiol. Mol. Biol. Rev.* **68**, 603–616 (2004).
23. Marreiros, B. C. et al. Structural and functional insights into the catalytic mechanism of the type II NADH:quinone oxidoreductase family. *Sci. Rep.* **7**, 42303 (2017).
24. Nguyen, H. P. et al. Aifm2, a NADH oxidase, supports robust glycolysis and is required for cold- and diet-induced thermogenesis. *Mol. Cell* **77**, 600–617 (2020).
25. Tate, J. G. et al. COSMIC: the Catalogue Of Somatic Mutations In Cancer. *Nucleic Acids Res.* **47**, D941–D947 (2018).
26. Seiler, A. et al. Glutathione peroxidase 4 senses and translates oxidative stress into 12/15-lipoxygenase dependent- and AIF-mediated cell death. *Cell Metab.* **8**, 237–248 (2008).
27. Jumper, J. et al. Highly accurate protein structure prediction with AlphaFold. *Nature* **596**, 583–589 (2021).
28. Varadi, M. et al. AlphaFold Protein Structure Database: massively expanding the structural coverage of protein-sequence space with high-accuracy models. *Nucleic Acids Res.* **50**, D439–D444 (2022).
29. Feng, Y. et al. Structural insight into the type-II mitochondrial NADH dehydrogenases. *Nature* **491**, 478–482 (2012).
30. Nakamura, T. et al. The mitochondrial Ca²⁺ uptake regulator, MICU1, is involved in cold stress-induced ferroptosis. *EMBO Rep.* **22**, e51532 (2021).
31. Sanjana, N. E., Shalem, O. & Zhang, F. Improved vectors and genome-wide libraries for CRISPR screening. *Nat. Methods* **11**, 783–784 (2014).
32. Doll, S. et al. ACSL4 dictates ferroptosis sensitivity by shaping cellular lipid composition. *Nat. Chem. Biol.* **13**, 91–98 (2017).
33. Meinnel, T., Dian, C. & Giglione, C. Myristoylation, an ancient protein modification mirroring eukaryogenesis and evolution. *Trends Biochem. Sci.* **45**, 619–632 (2020).
34. Sousa, F. M. et al. The key role of glutamate 172 in the mechanism of type II NADH:quinone oxidoreductase of *Staphylococcus aureus*. *Biochim. Biophys. Acta Bioenerg.* **1858**, 823–832 (2017).
35. Friedmann Angeli, J. P. et al. Inactivation of the ferroptosis regulator Gpx4 triggers acute renal failure in mice. *Nat. Cell Biol.* **16**, 1180–1191 (2014).
36. Yang, W. S. et al. Regulation of ferroptotic cancer cell death by GPX4. *Cell* **156**, 317–331 (2014).
37. Eaton, J. K. et al. Selective covalent targeting of GPX4 using masked nitrile-oxide electrophiles. *Nat. Chem. Biol.* **16**, 497–506 (2020).
38. Wooten, D. J., Meyer, C. T., Lubbock, A. L. R., Quaranta, V. & Lopez, C. F. MuSyC is a consensus framework that unifies multi-drug synergy metrics for combinatorial drug discovery. *Nat. Commun.* **12**, 4607 (2021).
39. Meyer, C. T. et al. Quantifying drug combination synergy along potency and efficacy axes. *Cell Syst.* **8**, 97–108 (2019).
40. Cornish-Bowden, A. A simple graphical method for determining the inhibition constants of mixed, uncompetitive and non-competitive inhibitors. *Biochem. J.* **137**, 143–144 (1974).
41. Hendricks, J.M. et al. Identification of structurally diverse FSP1 inhibitors that sensitize cancer cells to ferroptosis. *Cell Chem. Biol.* **21**, 1090–1103 (2023).
42. Stockwell, B. R. Chemical genetics: ligand-based discovery of gene function. *Nat. Rev. Genet.* **1**, 116–125 (2000).

Publisher's note Springer Nature remains neutral with regard to jurisdictional claims in published maps and institutional affiliations.

Open Access This article is licensed under a Creative Commons Attribution 4.0 International License, which permits use, sharing, adaptation, distribution and reproduction in any medium or format, as long as you give appropriate credit to the original author(s) and the source, provide a link to the Creative Commons license, and indicate if changes were made. The images or other third party material in this article are included in the article's Creative Commons license, unless indicated otherwise in a credit line to the material. If material is not included in the article's Creative Commons license and your intended use is not permitted by statutory regulation or exceeds the permitted use, you will need to obtain permission directly from the copyright holder. To view a copy of this license, visit <http://creativecommons.org/licenses/by/4.0/>.

© The Author(s) 2023

Methods

Chemicals

Liproxstatin-1 (Lip-1; Selleckchem, cat. no. S7699), (1*S*,3*R*)-RSL3 (RSL3; Cayman, cat. no.19288), iFSP1 (ChemDiv, cat. no. 8009-2626 or Cayman cat. no. Cay29483), viFSP1 (ChemDiv, cat. no. D715-1847 or Vitas M Laboratory, cat. no. STK626779), deferoxamine mesylate salt (DFO; Sigma, cat. no. 138-14-7), ferrostatin-1 (Fer-1; Sigma, cat. no. SML0583), zVAD-FMK (zVAD; Enzo Life Sciences, cat. no. ALX-260-02), necrostatin-1s (Nec-1s; Enzo Life Sciences, cat. no. BV-2263-5), MCC950 (Sigma, cat. no. 5381200001), olaparib (Selleckchem, cat. no. S1060) and JKE-1674 (Cayman, cat. no. Cay30784-1) were used in this study. Custom-made compounds were obtained from Intonation Research Laboratories.

Cell lines

4-hydroxytamoxifen (Tam)-inducible *Gpx4*^{-/-} murine immortalized fibroblasts (referred to as Pfa1 cells) have been reported previously²⁶. Genomic *Gpx4* deletion can be achieved using Tam-inducible Cre recombinase and the CreER¹²-LoxP system. HT-1080 (CCL-121), HEK293T (CRL-3216), 786-O (CRL-1932), A375 (CRL-1619), B16F10 (CRL-6475), LLC (CRL-1642), MDA-MB-436 (HTB-130), SW620 (CCL-227), NCI-H460 (HTB-177) and 4T1 (CRL-2539) cells were obtained from ATCC. SKOV3 (91091004) cells were obtained from Sigma-Aldrich. HEC151 cells (JCRB1122-A) were obtained from Tebubio. MC38 cells (available from Sigma) were a gift from P. Agostinis (KU Leuven, Belgium). Rat1 cells (available from Thermo Fisher) were a gift from Medizinische Hochschule Hannover. Huh7 cells (available from Thermo Fisher) were a gift from R. Schneider (Helmholtz Munich). Pfa1, 786-O, A375, SW620, Huh7, HT-1080, Rat1, MC38, LLC and B16F10 cells were cultured in DMEM-high glucose (4.5 g glucose L⁻¹) with 10% fetal bovine serum (FBS), 2 mM L-glutamine and 1% penicillin-streptomycin. MDA-MB-436, HEC151, SKOV3, H460 and 4T1 cells were cultured in RPMI GlutaMax with 10% FBS and 1% penicillin-streptomycin. To generate cell lines stably overexpressing FSP1, antibiotics (puromycin 1 μg mL⁻¹ and blasticidin 10 μg mL⁻¹) were used for selection. For culturing GPX4-deficient cells, 1 μM Lip-1 was supplemented. All cells were cultured at 37 °C with 5% CO₂ and verified to be negative for mycoplasma.

Production and isolation of FSP1 enzyme

Recombinant human and mouse FSP1 proteins and FSP1 mutants were produced in BL21*E. coli* and purified by affinity chromatography with a Ni-NTA system⁸.

FSP1 enzyme activity and inhibition assay

For the resazurin assay, enzyme reactions in TBS buffer (50 mM Tris-HCl, 150 mM NaCl) containing 15–200 nM recombinant human or mouse FSP1 and their mutants, 200 μM NADH and the inhibitors (iFSP1 and viFSP1) were prepared. After the addition of 100 μM resazurin sodium salt (Sigma, cat. no. R7017), the fluorescence intensity (FL intensity, excitation/emission wavelengths (Ex/Em) = 540 nm/590 nm) was recorded every 30 or 60 s using SpectraMax M5 or SpectraMaxiD5 microplate reader with SoftMax Pro v7 (Molecular devices) at 37 °C. Reactions without resazurin (inhibitor) were used to normalize and calculate FSP1 enzymatic activity and IC₅₀ values. Curve fitting and calculation of IC₅₀ values were performed using GraphPad Prism v9.

For the NADH-consumption assay, enzyme reactions in PBS (Gibco, cat. no. 14190094) containing 25–200 nM recombinant human FSP1 (or its mutants) and 50 μM menadione (Sigma, cat. no. M5625) were prepared. After the addition of 200 μM NADH, the absorbance at 340 nm at 37 °C was measured every 30 s using SpectraMax M5 Microplate Reader (Molecular Devices). Reactions without NADH or without enzyme were used to normalize the results. Curve fitting was done using GraphPad Prism v9.

For analysis of enzyme kinetics, reactions in PBS (Gibco, cat. no. 14190094) containing 100 nM recombinant human FSP1 and 0.04–500 μM NADH with 100 μM resazurin sodium salt or 0.03–100 μM resazurin with 200 μM NADH were mixed; then, FL intensity

(Ex/Em = 540/590 nm) was recorded every 60 s using the Spectra MaxiD5 microplate reader (Molecular Devices) at 37 °C. The initial slope of FL intensity was used for following the calculations of K_m and V_{max} using GraphPad Prism v9.

Cell viability assay

Cells were seeded on 96-well plates (2,000–10,000 cells per well for ferroptosis inducers and 500 cells per well for TAM) or 384-well plates (800 cells per well) and cultured overnight. The next day, the medium was changed and the following compounds were added: RSL3, iFSP1, viFSP1, Lip-1, DFO, Fer-1, zVAD, Nec-1s, MCC950 and olaparib, at the indicated concentrations in each figure. Cell viability was determined after 24–48 h (for RSL3, iFSP1, and viFSP1) or 72 h (for TAM) upon treatment, using AquaBluer (MultiTarget Pharmaceuticals, cat. no.6015) or 0.004% resazurin as an indicator of viable cells.

As readout, fluorescence was measured at Ex/Em = 540/590 nm using a SpectraMax M5 microplate reader with SoftMax Pro v7 (Molecular devices) after 4–6 h of incubation in normal cell-culture medium. Cell viability (%) was normalized and calculated using untreated conditions, which is in the absence of ferroptosis inducers or tamoxifen.

The synergistic effect was assessed using MuSyC (<https://musyc.lolab.xyz>)^{38,39}.

LDH release assay

For the LDH release assay, 2,500 cells per well were seeded on 96-well plates and cultured overnight. On the following day, the medium was changed to the fresh DMEM containing inhibitors and incubated for another 24 h. Necrotic cell death was determined using the Cytotoxicity Detection kit (LDH) (Roche, cat. no. 11644793001) following the manufacturer's protocol. In brief, cell-culture supernatant was collected as a sample of the medium, and cells were then lysed with 0.1% Triton X-100 in PBS as a lysate sample. Medium and lysate samples were individually mixed with reagents on the 96-well plate, and the reaction mixture was incubated for 15–30 min at room temperature. Then, the absorbance was measured at 492 nm using the SpectraMax M5 microplate reader (Molecular Devices). The cell death ratio was calculated by LDH release (%) as follows: (absorbance (abs) of medium sample) / ((abs of lysate) + (abs of medium samples)) × 100.

Lipid peroxidation assay

One day before the experiments, 100,000 cells per well were seeded on a 12-well plate. On the next day, cells were treated with 10 μM viFSP1 for 3 h and were then incubated with 1.5 μM C11-BODIPY 581/591 (Invitrogen, cat. no. D3861) for 30 min in a 5% CO₂ atmosphere at 37 °C. Subsequently, cells were washed with PBS once and trypsinized at 37 °C. Then, cells were resuspended in 500 μL PBS and passed through a 40-μm cell strainer, followed by analysis using a flow cytometer (CytOFLEX with the software (CytExpert v2.4), Beckman Coulter) with a 488-nm laser for excitation. Data were collected from the fluorescein isothiocyanate (FITC) detector (for the oxidized form of BODIPY) with a 525/40 nm bandpass filter, or from the phycoerythrin (PE) detector (for the reduced form of BODIPY) with a 585/42 nm bandpass filter. At least 10,000 events were analyzed per sample. Data were analyzed using FlowJo Software. The ratio of fluorescence of C11-BODIPY 581/591 (lipid peroxidation) (FITC/PE ratio (oxidized/reduced)) was calculated using the median value of each channel³⁰.

Live-cell imaging

Pfa1 cells (5,000–10,000 cells) were seeded on a μ-Dish 35 mm, low (ibidi, cat. no. 80136), and incubated overnight. The next day, the cell culture medium was changed to fresh medium. Live-cell imaging was performed using 3D Cell Explorer (Nanolive) with the software Evv1.8.2. During imaging, the cells were maintained at 37 °C and a 5% CO₂ atmosphere using a temperature-controlled incubation chamber. After recording one image, a 100-fold concentration of viFSP1 in DMEM

was added to the dishes (the final concentration was 10 μM viFSP1), and then recording was continued. For ferroptosis suppression, cells were pretreated 0.5 μM Lip-1 for 15 min before recording. Images were taken every 5 min for more than 6 h.

Cell lysis and immunoblotting

Cells were lysed in LCW lysis buffer (0.5% Triton X-100, 0.5% sodium deoxycholate salt, 150 mM NaCl, 20 mM Tris-HCl, 10 mM EDTA, 30 mM Na-pyrophosphate tetrabasic decahydrate), supplemented with protease and phosphatase inhibitor cocktail (cOmplete and phoSTOP, Roche, cat. no. 04693116001 and cat. no. 4906837001), and centrifuged at 20,000g, 4 °C, for 30 min to 1 h. The cell lysate was sampled by dissolved with 6 \times SDS loading buffer (375 mM Tris-HCl, 9% SDS, 50% glycerol, 9% β -mercaptoethanol, 0.03% bromophenol blue, pH 6.8). After boiling at 95 °C for 3 min, the samples were resolved on 12% SDS-PAGE gels (Bio-Rad, cat. no. 4568043 or cat. no. 4568046) and subsequently electroblotted onto a polyvinylidene difluoride (PVDF) membrane (Bio-Rad, cat. no. 1704156 or cat. no. 1704274), following the manufacturer's protocol. The membranes were incubated in the blocking buffer, 5% milk (Roth, cat. no. T145.2) in TBS-T (20 mM Tris-HCl, 150 mM NaCl, and 0.1% Tween-20), then probed with the primary antibodies. The primary antibodies were diluted in antibody-dilution buffer (5% BSA, 0.1% NaN_3 (Sigma, cat. no. S2002) in TBS-T) and were against GPX4 (1:1000, Abcam, cat. no. ab125066), valosin containing protein (VCP, 1:10,000, Abcam, cat. no. ab109240), HA tag (1:1,000, rat IgG1, clone 3F10, developed in-house), human FSP1 (1:1,000, Santa Cruz, cat. no. sc-377120, AMID) or human FSP1 (1:5, rat IgG2a, clone AIFM2 6D8, developed in-house), human and mouse FSP1 (1:5, rat IgG2a, clone AIFM2 1A1-1, developed in-house) and human and mouse FSP1 (1:5, rat IgG2b, clone AIFM2 14D7, developed in-house), or were diluted in 5% milk in TBS-T against horseradish-peroxidase-conjugated β -actin (1:50,000, Sigma, cat. no. A3854) overnight. After the membrane was washed once, it was probed with secondary antibodies (1:1,000–1:5,000, Cell Signaling, cat. no. 7074S for rabbit; cat. no. 7076S for mouse, and 1:1,000 for anti-rat IgG1b and 2a/b, developed in-house) diluted in 5% skim milk in TBS-T. The antibody-antigen complexes were detected by the ChemiDoc Imaging System with Image Lab v6.0 (Bio-Rad). Representative images are shown after being adjusted to the appropriate brightness and angle using ImageJ/Fiji software (ver.1.53).

Construction of expression plasmids

All plasmids in this study were constructed using standard molecular biology techniques, and were verified by sequencing: human *AIFM2* cDNA (NM_001198696.2, C>T:1008) and codon-optimized *Mus musculus* (mouse) FSP1 (NP_001034283.1), *Rattus norvegicus* (rat) FSP1 (NP_001132955.1) and *Gallus gallus* (chicken) FSP1 (XP_421597.1) were cloned or synthesized into p442-IRES-blast vectors^{8,17}. For generating mutants or subcloning, DNA was first amplified by KOD One (Sigma, cat. no. KMM-201NV), and PCR products were purified by Wizard SV Gel&PCR Clean-up System (Promega, cat. no. A9285). Ligation reactions of PCR products with digested vectors were performed using In-Fusion cloning enzymes (Takara Bio, cat. no. 639649 or 638948). Subsequently, reaction mixtures were transformed into NEB stable competent cells (NEB, cat. no. C3040H). Plasmids were isolated using the QIAprep Spin Miniprep Kit (QIAGEN, cat. no. 27106), followed by sequencing.

Lentiviral production and transduction

HEK293T cells were used to produce lentiviral particles. The ecotropic envelope protein of the murine leukemia virus (MLV) was used for murine-derived cells. A third-generation lentiviral packaging system consisting of transfer plasmids, envelope plasmids (pEcoEnv-IRES-puro or pHCMV-EcoEnv (Addgene, cat. no. 15802) (ecotropic particles)) and packaging plasmids ((pMDLg_pRRE and pRSV_Rev, or psPAX2 (Addgene, cat. no. 12260)) were co-lipofected into HEK293T cells using transfection reagents (PEI MAX (Polysciences, cat. no. 24765)

or X-tremeGENE HP agent (Roche, cat. no. 06366236001)). Cell culture supernatants containing viral particles were collected at 2–3 d post-transfection and filtered through a 0.45- μm PVDF filter (Millipore, cat. no. SLHV033RS), and were then stored at -80°C .

Cells were seeded on 12- or 6-well plates with lentivirus supplemented with 10 $\mu\text{g mL}^{-1}$ protamine sulfate overnight. On the next day, the cell-culture medium was replaced with fresh medium containing appropriate antibiotics, such as puromycin (Gibco, cat. no. A11138-03; 1 $\mu\text{g mL}^{-1}$) and blasticidin (Invitrogen, cat. no. A1113903; 10 $\mu\text{g mL}^{-1}$), and transduced cells were selected until non-transduced cells were completely dead.

Mutational screens

Mutated *AIFM2* cDNA (NM_001198696.2, C>T:1008) with the adapter sequence for p442 was amplified from the virus expression vector p442-hFSP1-IRES-Blast⁸ by error-prone PCR using the GeneMorph II Random Mutagenesis Kits (Agilent cat. no. 200550). The optimal mutagenesis rate (3–5 DNA mutations per gene) was achieved using PCR under the following conditions: (1) 95 °C for 120 s, (2) 95 °C 30 s, (3) 60 °C 30 s, (4) 72 °C for 75 s, (5) 72 °C 10 min; the cycles in steps 2–4 were repeated 25 times, and all other steps were performed once. After the isolation of PCR products using agarose electrophoresis and clean-up using the Wizard SV Gel&PCR Clean-up System, the FSP1 fragment was ligated into a digested p442-IRES-blast vector using In-Fusion enzyme (Takara, cat. no. 639649) under the following conditions: 400 ng DNA insert, 200 ng vector and 8 μL enzyme in 40 μL reaction volume, at 50 °C for 15 min. Then, the insert-vector mixture was transformed into NEB stable cells, which were incubated at 37 °C for 1 h. After the induction of antibiotic-resistant genes, cells were applied to 8 plates (Thermo Fisher, cat. no. 240835) and cultured with ampicillin selection growth medium at 30 °C overnight. On the next day, colonies were collected, and DNA was isolated using the QIAGEN Plasmid Maxi Kit (Qiagen, cat. no. 12163).

As described above, a third-generation lentiviral packaging system consisting of FSP1 mutant library plasmids, envelope plasmids (pEcoEnv-IRES-puro) and packaging plasmids (pMDLg_pRRE and pRSV_Rev) were co-lipofected into HEK293T cells using transfection reagents (X-tremeGENE HP agent). Cell culture supernatants containing viral particles were collected at 2 d post-transfection and filtered through a 0.45- μm PVDF filter, and were then stored at -80°C .

Pfa1 cells were seeded into ten T-175 flasks (1.0×10^6 cells per flask, 2.0×10^7 cells in total) with medium containing 10 $\mu\text{g mL}^{-1}$ protamine and lentivirus containing FSP1 mutants and were transduced with extremely low infection efficiency (MOI = approximately 0.1, calculated as previously described⁴³). The next day, the medium was replaced with the fresh medium containing blasticidin (12.5 $\mu\text{g mL}^{-1}$) and puromycin (1 $\mu\text{g mL}^{-1}$). After selection using blasticidin for 3 d, 10 million cells were collected as a control group; at the same time, 20 million cells were seeded into five flasks (2.0×10^6 cells per flask, 2.0×10^7 cells in total) with 500 nM RSL3. After the induction of ferroptosis by RSL3 for 2 d, 10 million cells were collected as the RSL3-treated group. Then, 10 million cells per condition were treated with individual FSP1 inhibitors (5 μM for the first 5 d and 10 μM thereafter) and with 500 nM RSL3 and 1 μM 4-OH Tam so that the Pfa1 cells became fully resistant to FSP1 inhibitors while still expressing functional FSP1. Then, surviving Pfa1 *Gpx4*-KO cells overexpressing resistant FSP1 mutants were expanded, and 10 million cells per condition were collected and stored at -80°C .

After collecting cells from all conditions, cells were lysed in lysis buffer (50 mM Tris, 50 mM EDTA, 1% SDS, pH 8) with proteinase K (100 $\mu\text{g mL}^{-1}$) at 55 °C overnight. On the next day, RNase A (50 $\mu\text{g mL}^{-1}$) was added and incubated for 30 min at 37 °C to digest RNA. Then, the equivalent volume of phenol:chloroform:isoamyl alcohol (25:24:1) (Roth, cat. no. A156.2) was added. The solution was briefly vortexed and centrifuged for 10 min at 16,000g to separate DNA from RNA and proteins. The top phase of the DNA-containing solution was carefully collected in the new tubes and DNA was precipitated by the 2 \times volumes

of 75 mM NaCl in ethanol by centrifugation for 10 min at 16,000g. The pellet was then washed with 70% ethanol, followed by centrifugation. After drying the remaining ethanol, the pellet was dissolved in 200 μ L TE buffer per condition and incubated at 65 °C for 1 h. Finally, the DNA of the *AIFM2* region (approximately 1,500 base pairs) was amplified by KOD One (Sigma, Cat. no. KMM-201NV) and purified as described above.

NGS library preparation was performed using ThruPLEX DNA-Seq HV PLUS kit (Takara, cat. no. R400782) with minor optimization. After the preparation of the library, the DNA was purified using NucleoMag NGS Clean-up and Size Select (Th. Geyer, cat. no. 11833159) for subsequent NGS. NGS was performed by the core facility in Helmholtz Munich.

NGS data analysis of human *AIFM2* cDNA

Paired-end sequencing was performed in different conditions using an Illumina NovaSeq 6000 instrument using ThruPLEX DNA-Seq HV PLUS kit (see Supplementary Table 1). The program FastQC (v0.11.7) (<http://www.bioinformatics.babraham.ac.uk/projects/fastqc>) was applied to the resulting FASTQ files to identify sequences that were over-represented (Illumina adapter) and to exclude them from further analysis. We used the Trimmomatic V.0.39 tool⁴⁴ with the following options (ILLUMINACLIP:TruSeq2-PE_extended.fa:2:30:10 LEADING:3 TRAILING:3 SLIDINGWINDOW:4:15 MINLEN:36) to trim paired-end data (see Supplementary Table 1). Trimmed paired-end reads (original length, 151 bp) were aligned to the reference *AIFM2* cDNA sequence of 1,210 bp with the Burrows-Wheeler Alignment Tool (BWA), version 0.7.17-r1188 (ref. 45). First, an index was generated for the reference sequence using the command 'bwa index'. Then, by applying the subcommand 'mem', BWA outputs the final alignment in the SAM (Sequence Alignment/Map) format. Aligned reads were converted to the BAM (Binary Alignment Map) format and sorted by leftmost chromosomal coordinates with the program SAMtools version 1.2 (ref. 46) using the commands 'samtools view' and 'samtools sort', respectively. From sorted BAM files, the coverage information per base for the FSP1 reference sequence was extracted by applying IGVtools of the Integrative Genomics Viewer (IGV), version 2.11.9 (ref. 47). The command 'igvtools count' with the options (-w 1 and -bases) was used to produce an output file in the WIG (wiggle) format for each sorted BAM file. The mutation frequency at each position (Xi) of the FSP1 reference sequence was calculated from the sum of mutated nucleotides at the corresponding position of the reference sequence in the alignment divided by the sum of all nucleotides (A,C,G,T,N) at this location. The count information per base stored in the wiggle files served as input for a custom written R script for the calculation of the mutation frequency. The tab-delimited output file of the R script contains the number of each nucleotide and deletions and insertions, as well as the sum of all nucleotides and the mutation frequency from the alignment (columns) at each position of the FSP1 sequence (rows).

$$\text{Mutation frequency (Xi)} = N_{\text{mut}}(\text{Xi})/N_{\text{all}}(\text{Xi})$$

Where Xi is the position of *AIFM2*, N_{mut} the sum of mutated nucleotides at Xi and N_{all} is the sum of all nucleotides at Xi. The Z score was calculated using mean (μ) and standard deviation (σ) as follows:

$$Z = [Xi - \mu_{\text{RSL3 or iFSP1s}}] / \sigma_{\text{RSL3 or iFSP1s}}$$

$$\mu_{\text{RSL3}} = \text{Mean}(\text{Mutationfrequency}_{\text{RSL3}} / \text{Mutationfrequency}_{\text{ctrl}})$$

$$\mu_{\text{iFSP1s}} = \text{Mean}(\text{Mutationfrequency}_{\text{iFSP1s}} / \text{Mutationfrequency}_{\text{RSL3}})$$

$$\sigma_{\text{RSL3}}$$

$$= \text{Standard Deviation}(\text{Mutationfrequency}_{\text{RSL3}} / \text{Mutationfrequency}_{\text{ctrl}})$$

$$\sigma_{\text{iFSP1s}}$$

$$= \text{Standard Deviation}(\text{Mutationfrequency}_{\text{iFSP1s}} / \text{Mutationfrequency}_{\text{RSL3}})$$

Where iFSP1s represents iFSP1 or viFSP1, and ctrl is the control. Then, amino acid substitutions were investigated in light of the possible DNA alternation using the codon table (Supplementary Table 1).

Screening of mouse FSP1 inhibitors

Pfa1 and Pfa1 *Gpx4*-KO cells stably overexpressing murine FSP1 were seeded on separate 384-well plates (500 cells per well), and screened with a library of small-molecule inhibitor compounds, as reported previously⁸. Viability of the different cell lines was assessed 48 h after treatment using AquaBlue. Compounds showing selective lethality in Pfa1 *Gpx4*-KO cells stably overexpressing murine FSP1 were then validated in cell viability and in vitro FSP1 enzymatic assays, as described above.

CRISPR-Cas9-mediated gene knockout

Single guide RNAs (sgRNA) vectors for human GPX4, mouse Gpx4 and mouse Fsp1 were established, and KO cells were generated as previously reported^{10,17}. SW620 *GPX4*-KO cells were transiently co-transfected with the desired sgRNAs expressing lentiCRISPRv2-blast or lentiCRISPRv2-puro using the X-tremeGENE HP. One day after transfection, cells were selected with puromycin (1 μ g mL⁻¹) and blasticidin (10 μ g mL⁻¹) until non-transfected cells were dead. Single-cell clones were isolated in serial dilutions, and KO clones were confirmed by immunoblotting.

Stable expression of genes by transfection

4T1 *Gpx4*-KO cells and B16F10 *Gpx4-KO Fsp1*-KO (DKO) cells were transfected with 141-IRES-puro, 141-hFSP1-IRES-puro, 141-mFsp1-IRES-puro, 141-mGpx4-IRES-puro or 141-mGpx4 U46C-IRES-puro vectors using the X-tremeGENE HP agent. One day after transfection, cells were selected and cultured in the presence of puromycin (1 μ g mL⁻¹) and absence of Lip-1 to select for stable FSP1- or GPX4-expressing cells.

In silico modeling and structural analysis

A predicted human FSP1 structure was obtained from the AlphaFold2 database (<https://alphafold.ebi.ac.uk>)²⁸. To yield the superimposed structure of FSP1 with its cofactor flavin adenine dinucleotide (FAD), NADH and ubiquinone, the structure of the FSP1 ortholog NDH-2 (PDB: 4G73 ref. 29 or SNA1 ref. 48) was aligned to FSP1 using Pymol v2.5.2 (Schrödinger), and the positions of FAD, NADH and ubiquinone were extracted and embedded into FSP1 structure¹⁹ or another NDH-2 (PDB: 4NWZ ref. 49). The in silico modeling for iFSP1 and viFSP1 were conducted by modeling software SeeSAR v12.1 (BioSolveIT)¹⁹. After visual inspection, the most viable poses were selected, and then docking molecules were exported as PDB files. Depictions of all docking or superimposed structures were made using Pymol.

Protein alignment of FSP1 orthologues

The human FSP1 sequence and its orthologues were obtained from UniProt (<https://www.uniprot.org>), NCBI (<https://www.ncbi.nlm.nih.gov/gene/>) and the PDB (<https://www.rcsb.org>), then aligned and visualized using JalView⁵⁰ (v2.11.2.6).

Genome DNA extraction and sequencing

Genomic DNA from SKOV3 was extracted using DNAzol (Fisher Scientific, cat. no.15413379), according to the manufacturer's instructions. Sequencing was performed by Eurofins genomics.

Statistics and reproducibility

All data shown are the mean \pm s.e.m. or mean \pm s.d., and the numbers (n) in each figure legend represents biological replicates or technical replicates. All experiments (except for the mutational analysis) were performed independently at least twice. One-way or two-way ANOVA followed by Dunnett's or Tukey's multiple-comparisons test were performed using GraphPad Prism 9 (GraphPad Prism) (see the figure legends for more details). The results of the statistical analyses are represented in each figure. $P < 0.05$ was considered statistically

significant. No statistical method was used to predetermine sample size. No data were excluded from the analyses. The experiments were not randomized. The investigators were not blinded to allocation during experiments or outcome assessment.

Reporting summary

Further information on research design is available in the Nature Portfolio Reporting Summary linked to this article.

Data availability

All data are available in the article and the supplementary information, and from the corresponding author on reasonable request. Gel source images are shown in Supplementary Figure 2. Human cancer cell line data were mined from the DepMap (<https://depmap.org/portal/>) or COSMIC (<https://cancer.sanger.ac.uk/cosmic>) databases. Murine cancer cell line data was mined from the TISMO database (<http://tismo.cis-trome.org>)⁵¹. The sequence data from this study have been submitted to NCBI BioProject (<https://www.ncbi.nlm.nih.gov/bioproject>) under BioProject ID [PRJNA942499](https://www.ncbi.nlm.nih.gov/bioproject/PRJNA942499). Source data are provided with this paper.

References

- Pan, D. et al. A major chromatin regulator determines resistance of tumor cells to T cell-mediated killing. *Science* **359**, 770–775 (2018).
- Bolger, A. M., Lohse, M. & Usadel, B. Trimmomatic: a flexible trimmer for Illumina sequence data. *Bioinformatics* **30**, 2114–2120 (2014).
- Li, H. Aligning sequence reads, clone sequences and assembly contigs with BWA-MEM. Preprint at <https://arxiv.org/abs/1303.3997> (2013).
- Li, H. et al. The sequence alignment/map format and SAMtools. *Bioinformatics* **25**, 2078–2079 (2009).
- Robinson, J. T. et al. Integrative genomics viewer. *Nat. Biotechnol.* **29**, 24–26 (2011).
- Sena, F. V. et al. Type-II NADH:quinone oxidoreductase from *Staphylococcus aureus* has two distinct binding sites and is rate limited by quinone reduction. *Mol. Microbiol.* **98**, 272–288 (2015).
- Heikal, A. et al. Structure of the bacterial type II NADH dehydrogenase: a monotopic membrane protein with an essential role in energy generation. *Mol. Microbiol.* **91**, 950–964 (2014).
- Waterhouse, A. M., Procter, J. B., Martin, D. M. A., Clamp, M. & Barton, G. J. Jalview Version 2—a multiple sequence alignment editor and analysis workbench. *Bioinformatics* **25**, 1189–1191 (2009).
- Zeng, Z. et al. TISMO: syngeneic mouse tumor database to model tumor immunity and immunotherapy response. *Nucleic Acids Res.* **50**, D1391–D1397 (2022).

Acknowledgements

We are grateful to all current and former members of the Conrad Laboratory for providing valuable materials and fruitful discussions.

This work was supported by Deutsche Forschungsgemeinschaft (DFG) (CO 291/7-1 and the Priority Program SPP 2306 (CO 291/9-1, no. 461385412; CO 291/10-1, no. 461507177)) and PR 1752/3-1 to B.P., the German Federal Ministry of Education and Research (BMBF) FERROPATH (01EJ2205B), and the European Research Council (ERC) under the European Union's Horizon 2020 research and innovation program (grant agreement no. GA 884754) to M.C. MC38 cells were kindly gifted from P. Agostinis (KU Leuven, Belgium). Rat1 cells were kindly gifted from Medizinische Hochschule Hannover. Huh7 cells were kindly gifted from R. Schneider (Helmholtz Munich).

Author contributions

T.N., M.S., B.P. and M.C. conceived the study and wrote the manuscript. T.N., E.M., N.Y., J.W. and E.L. performed in vitro and cell experiments. A.S.D.M. expressed FSP1 in cells and purified recombinant FSP1. T.N. and P.S. performed in silico analysis. T.N., S.D. and D.T. designed and performed mutational screens and analyzed the resulting data. T.N.X.d.S. and J.P.F.A. made murine FSP1 expression cells for compound screening. All authors read and agreed on the content of the paper.

Funding

Open access funding provided by Helmholtz Zentrum München - Deutsches Forschungszentrum für Gesundheit und Umwelt (GmbH).

Competing interests

M.C., B.P. and P.S. are co-founders and shareholders of ROSCUE Therapeutics. The other authors declare no competing interests.

Additional information

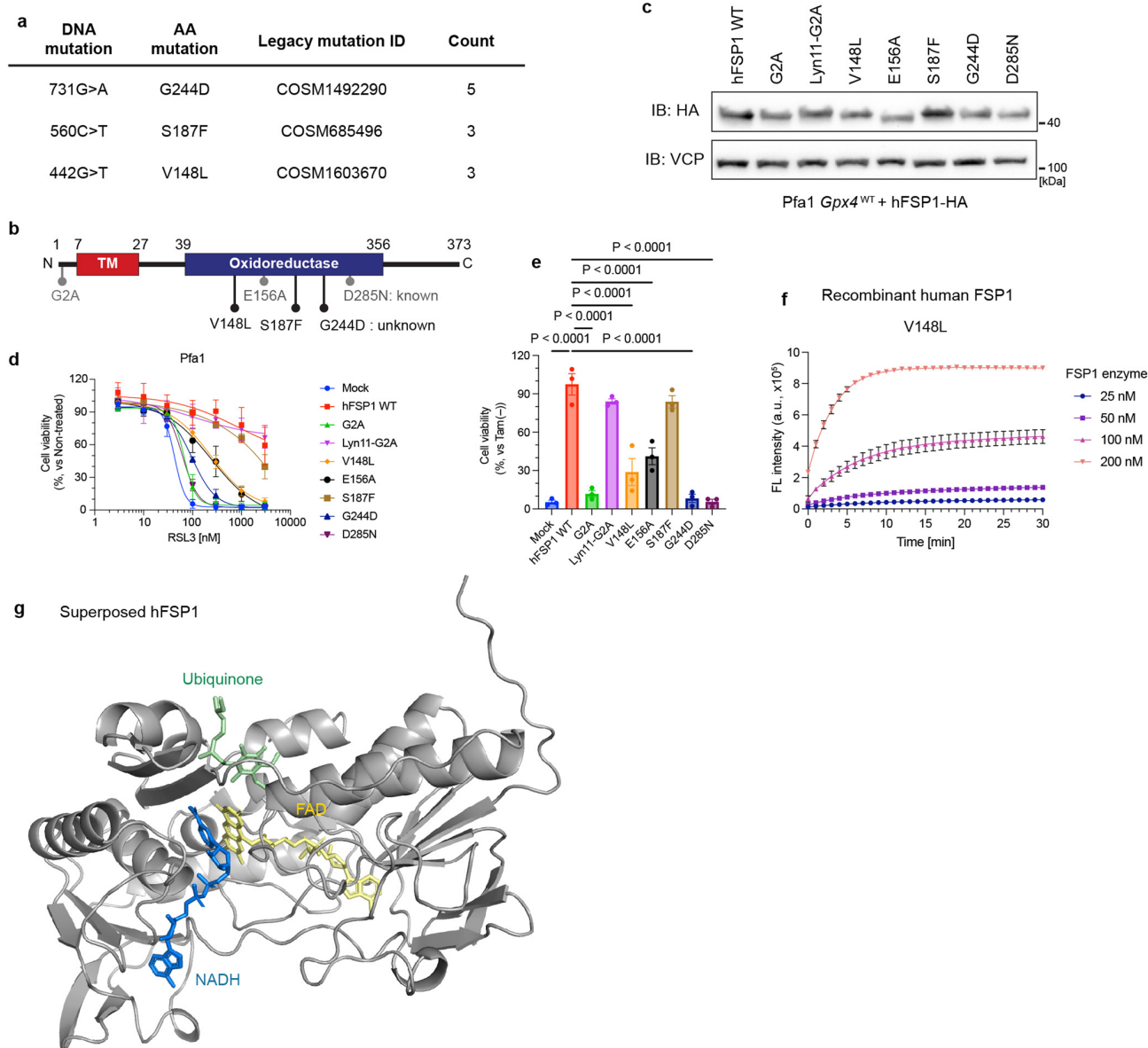
Extended data is available for this paper at <https://doi.org/10.1038/s41594-023-01136-y>.

Supplementary information The online version contains supplementary material available at <https://doi.org/10.1038/s41594-023-01136-y>.

Correspondence and requests for materials should be addressed to Marcus Conrad.

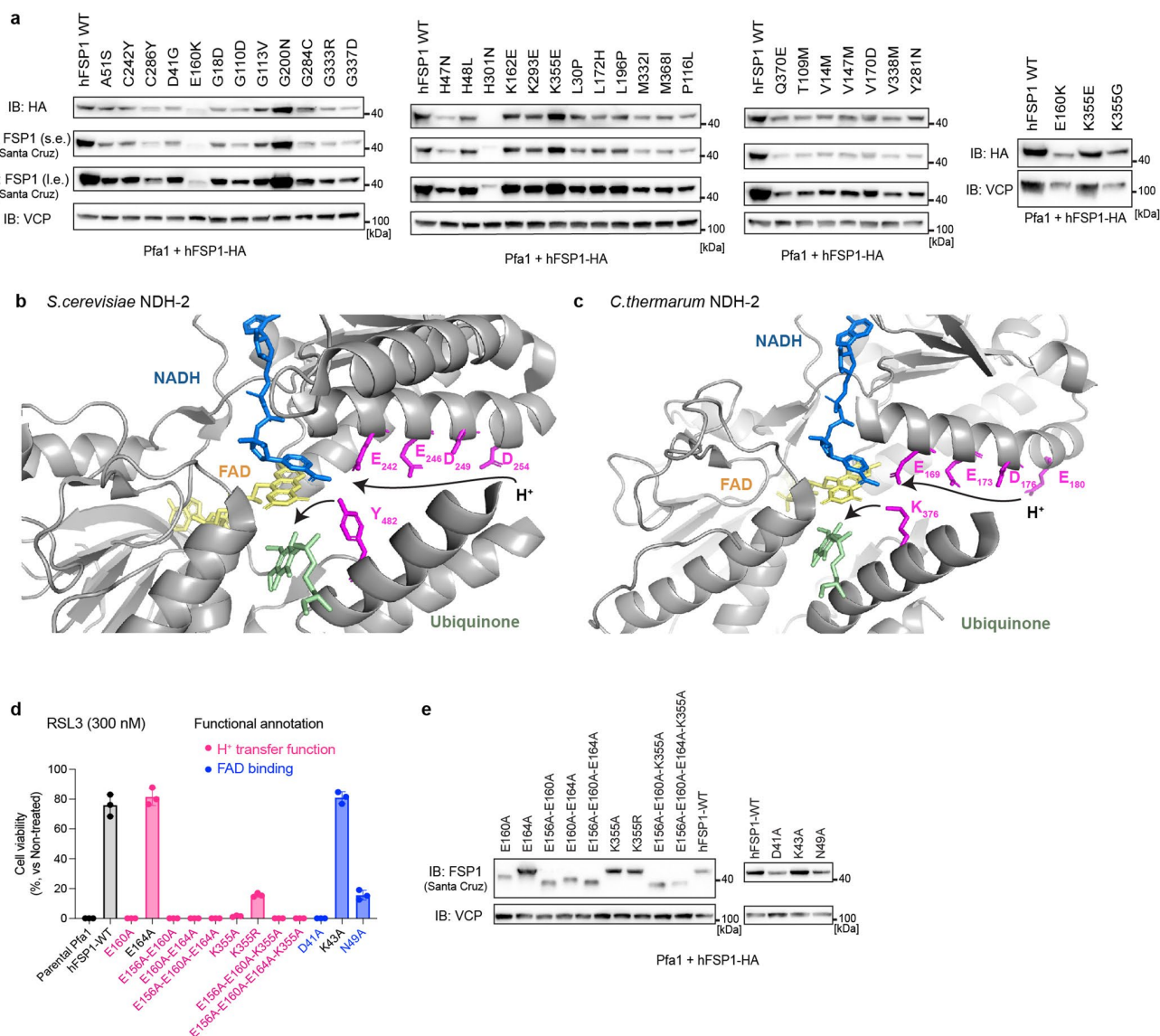
Peer review information *Nature Structural & Molecular Biology* thanks Raphaël Rodriguez, Silvia Von Karstedt and the other, anonymous, reviewer(s) for their contribution to the peer review of this work. Primary handling editor Carolina Perdigoto, in collaboration with the *Nature Structural & Molecular Biology* team. Peer reviewer reports are available.

Reprints and permissions information is available at www.nature.com/reprints.



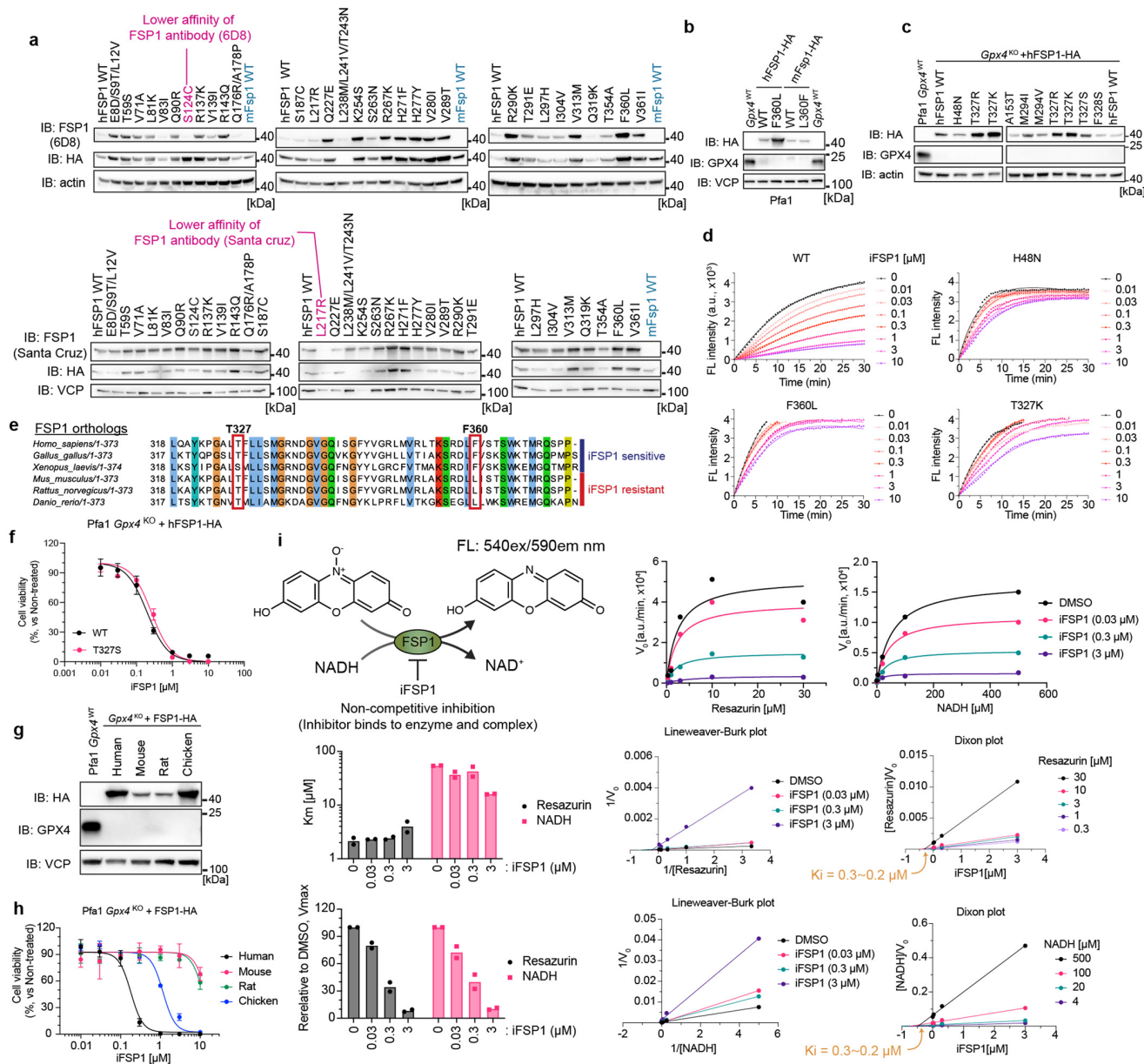
Extended Data Fig. 2 | Analysis of somatic FSP1 mutations reported in cancer patients. a. Somatic mutations of *AIFM2* found in cancer patients using the COSMIC database. b. Schematic FSP1 enzyme representation with annotated functional mutations as reported. c. Immunoblot analysis of FSP1 and VCP expression in Pfa1 cells stably overexpressing wildtype hFSP1 or its mutant variants from a single experiment. d. Cell viability in Pfa1 cells stably overexpressing wildtype hFSP1 or its mutant variants treated with RSL3 for 24 h. e. Cell viability was measured after treating Pfa1 cells stably overexpressing wildtype hFSP1 or its mutant variants with or without 1 μ M Tam for 72 h. Data was normalized by each group of non-treatment with Tam. Data represents the

mean \pm SEM of 3 wells of a 96-well plate from one out of 4 (d) or 3 (e) independent experiments. p values were calculated from one-way ANOVA followed by Dunnett's multiple comparison test. f. Reduction of resazurin in the presence of FSP1 V148L at the indicated concentrations. Data represents the mean \pm SD of 3 wells of a 96-well plate from one out of 3 independent experiments. g. Superimposed human FSP1 structure from AlphaFold2 database (<https://alphafold.ebi.ac.uk>). The cofactors, flavin adenine dinucleotide (FAD, yellow), nicotinamide adenine dinucleotide (NADH, blue) and ubiquinone (CoQ₉, green) were embedded from the structure of the yeast orthologue, NDH-2 (Ndi1) (PDB: 4G73).



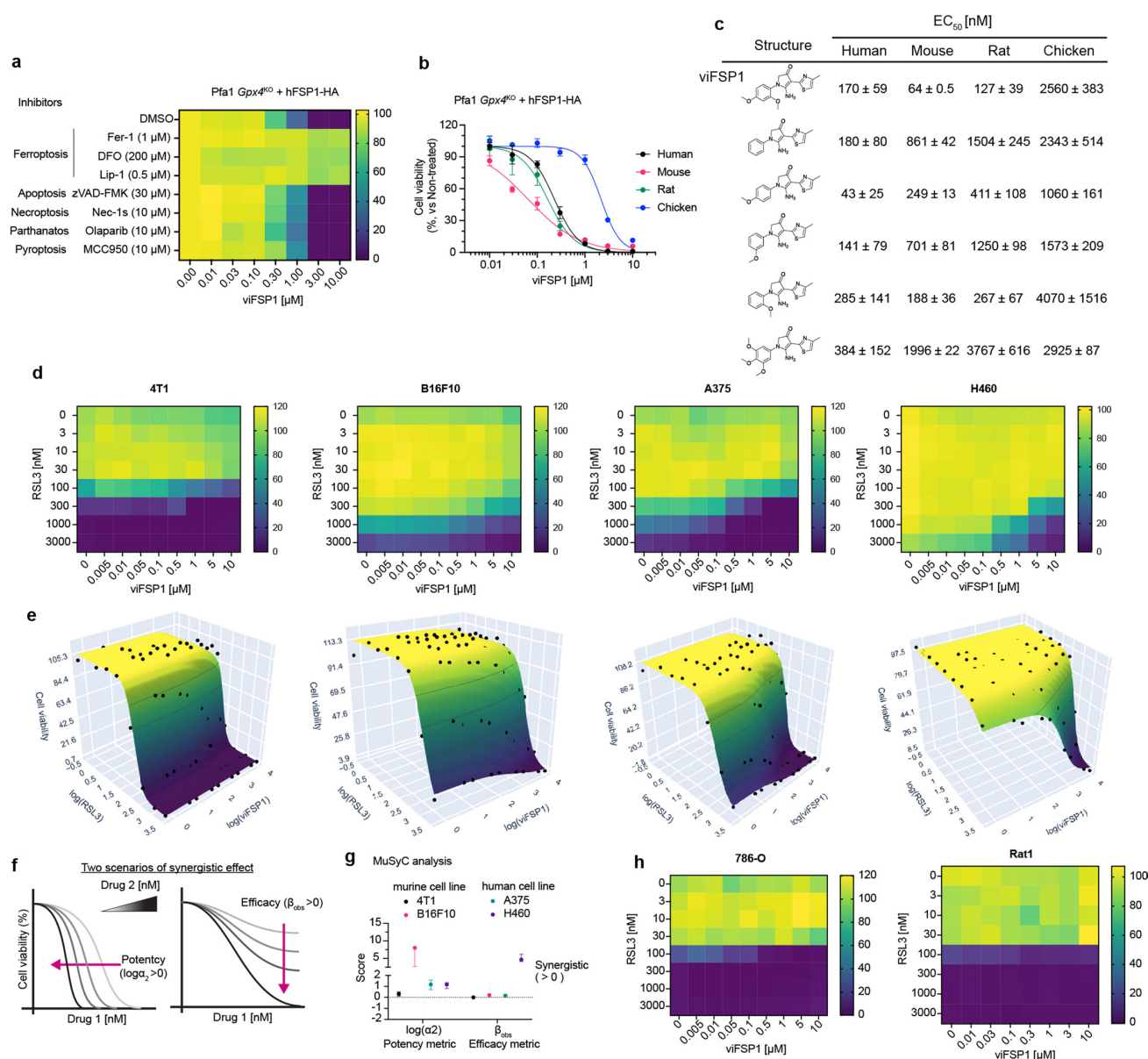
Extended Data Fig. 3 | Dysfunctional FSP1 mutations and proposed proton transfer function in NDH-2s. a. Immunoblot analysis of FSP1 (using AMID (Santa Cruz) and HA antibodies) and VCP expression in Pfa1 cells stably overexpressing wildtype hFSP1 or its mutant variants. For immunoblot of FSP1, s.e. and l.e. represent short and long exposure, respectively. b. Crystal structure of *Saccharomyces cerevisiae* (*S. cerevisiae*) NDH-2 (PDB: 4G73) with its cofactors, FAD (yellow), NADH (blue), and CoQ₃ (green). The proton transfer via sequential carboxylic residues in the α -helix (that is, E242/E246/D249/D254) and subsequent final protonation from Y482 to ubiquinone are indicated with black arrows. c. Crystal structure of *Caldalkalibacillus thermarum* (*C. thermarum*)

NDH-2 (PDB: 4NWZ) with its cofactors, FAD (yellow), NADH (blue), and CoQ₃ (green). The proton transfer via sequential carboxylic residues in the α -helix (that is, E169/E173/D176/E180) and subsequent final protonation from K376 to ubiquinone are indicated with black arrows. d. Cell viability was measured after treating Pfa1 cells stably overexpressing wildtype hFSP1 or its mutant variants with or 300 nM RSL3 for 24 h. Data was normalized by each group of non-treatment with RSL3. Data represents the mean \pm SD of 3 wells of a 96-well plate from one out of 3 independent experiments. e. Immunoblot analysis of FSP1 (Santa Cruz) and VCP expression in Pfa1 cells stably overexpressing wildtype hFSP1 or its mutant variants in cells. Data is shown from a single experiment (a,e).



Extended Data Fig. 4 | Identification of the iFSP1 binding pocket via site-directed mutagenesis. a. Immunoblot analysis of FSP1 (clone 6D8, AMID: Santa Cruz, and HA), actin, and VCP expression in Pfa1 cells stably overexpressing wildtype hFSP1 or its mutant variants. Each human specific FSP1 antibody (6D8 and Santa Cruz) showed a lower affinity against the highlighted human FSP1 mutants similar to mouse wildtype FSP1. b. Immunoblot analysis of GPX4, FSP1 (HA), and VCP expression in Pfa1 cells stably overexpressing wildtype hFSP1 and its mutant variants. c. Immunoblot analysis of GPX4, FSP1 (HA), and actin expression in Pfa1 cells stably overexpressing wildtype hFSP1 and its mutant variants. Data is shown from a single experiment (a-c). d. Representative resazurin reduction assay in the presence of wildtype FSP1 or its mutant variants with the indicated concentrations of iFSP1. Data represents a single well of a 96-well plate from one out of 3 independent experiments. e. Alignment of different FSP1 orthologues. Note, T327 and F360 (in human position) are different among species. f. Cell viability of Pfa1 *Gpx4*-KO cells stably expressing wildtype hFSP1

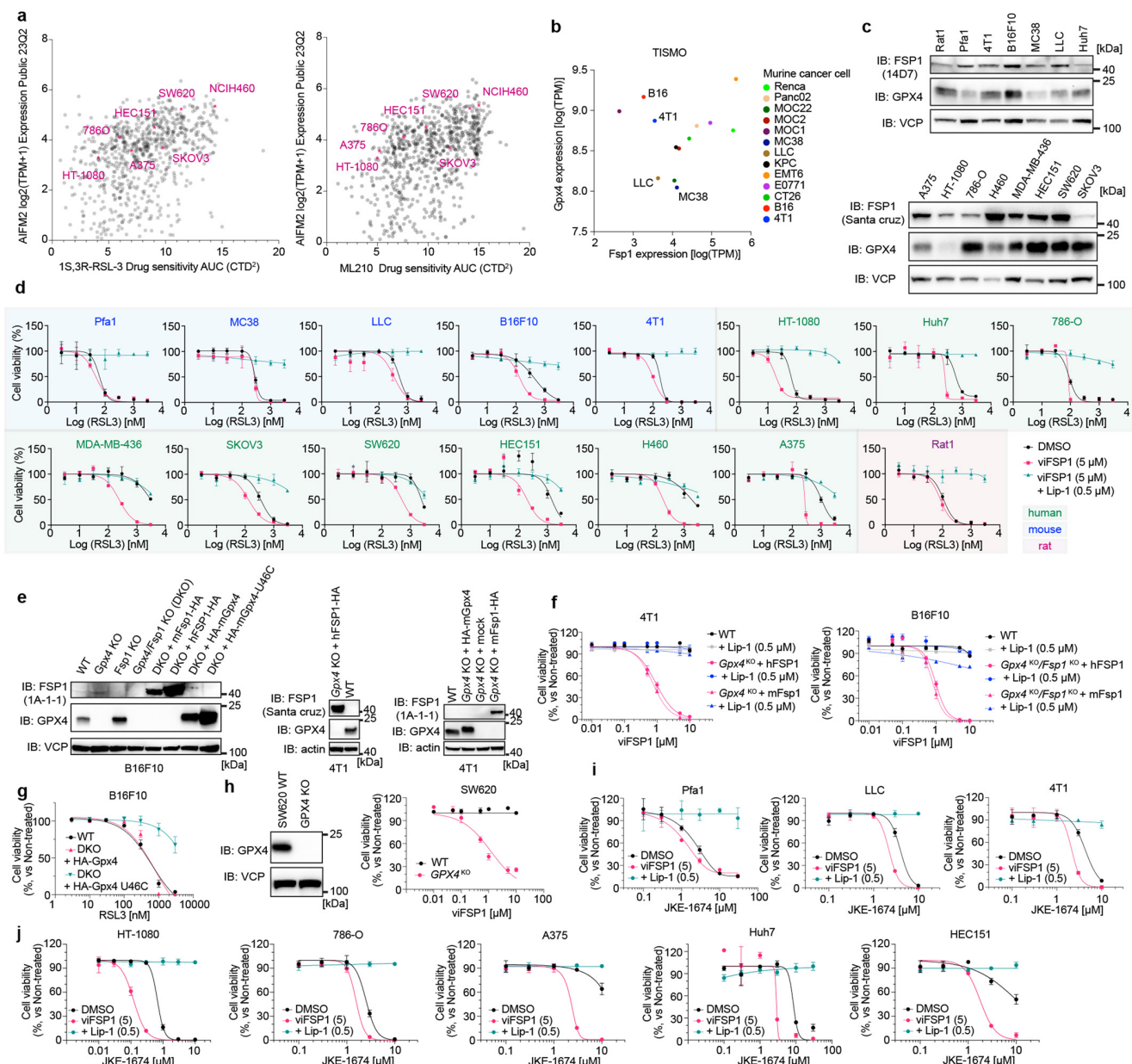
or the T327 mutant treated with iFSP1 for 24 h. Data represents the mean \pm SD of 3 wells of a 96-well plate from one out of 2 independent experiments. g. Immunoblot analysis of GPX4, FSP1 (HA), and VCP expression in Pfa1 cells stably overexpressing wildtype FSP1 orthologues from a single experiment. h. Cell viability of Pfa1 *Gpx4*-KO cells stably expressing the different wildtype FSP1 orthologues treated with iFSP1 for 24 h. Data represents the mean \pm SD of 3 wells of a 96-well plate from one out of 3 independent experiments. i. Enzyme kinetics in vitro assay. Schematic representation of the FSP1 enzyme activity assay using resazurin and NADH as the substrates. Representative reduction kinetics of resazurin, bar plots of the K_m and relative V_{max} values, Lineweaver-Burk plot, and Dixon plot in the presence of different concentrations of either NADH or resazurin with iFSP1 at indicated concentrations. Reduction kinetics, Lineweaver-Burk plot, and Dixon plot represent a single well of a 96-well plate from one out of 2 independent experiments. Bar plots represent the mean from 2 independent experiments.



Extended Data Fig. 5 | viFSP1 is a potent FSP1 inhibitor in different cell lines.

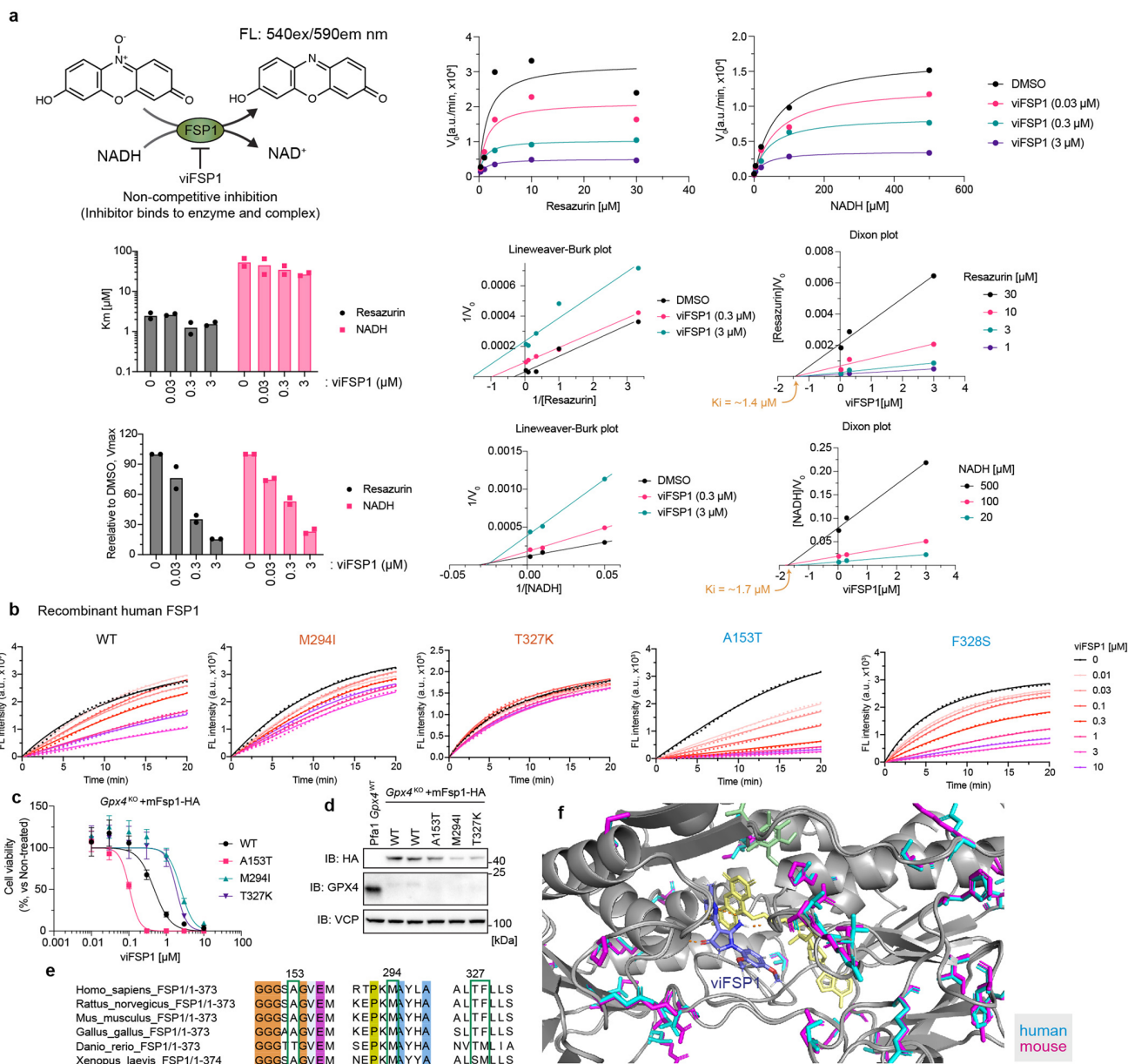
a. Cell viability of Pfa1 *Gpx4*-KO cells stably overexpressing hFSP1 mutants treated with viFSP1 for 48 h with indicated cell death inhibitors. Ferrostatin-1 (Fer-1), deferoxamine (DFO) and liproxstatin-1 (Lip-1) were used as ferroptosis inhibitors. b. Cell viability of Pfa1 *Gpx4*-KO cells stably overexpressing wildtype FSP1 enzyme from different organisms treated with viFSP1 for 48 h. Data represents the mean \pm SD of 3 wells of a 96-well plate from one out of 2 independent experiments (See also Supplementary Videos 1-8). c. An initial structure-activity relationship study (SAR) for viFSP1. Pfa1 *Gpx4*-KO cells stably expressing wildtype FSP1 from different species were treated with the different viFSP1 analogs for 48 h. EC₅₀ values were obtained from 3 wells of a 96-well plate

from a single experiment and calculated by GraphPad Prism9. d. Heat maps represent cell viability of 4T1, B16F10, A375, and H460 cells treated with viFSP1 and RSL3 for 48 h. Data represents the mean of 4 wells of a 384-well plate from 3 independent experiments. e. 3D-Heat maps represent the same data as d and are visualized by MuSyC (<https://musyc.lolab.xyz>)^{38,39}. f. Schematic models for the synergistic effect of 2 given compounds. g. Synergistic potency and efficacy. Data is calculated by MuSyC using the data from d. Data represent the mean \pm 95% confidence intervals of three independent experiments. h. Heat map represents cell viability of 786-O and Rat1 cells treated with viFSP1 and RSL3 for 48 h. Data represents the mean of 4 wells of a 384-well plate (786-O) or a single well of a 96-well plate (Rat1) from one out of 3 or 2 independent experiments.



Extended Data Fig. 6 | viFSP1 shows the synergistic effect toward ferroptosis in numerous cancer cells. a. DepMap database analysis. *AIFM2* (*FSP1*) expression and sensitivity of GPX4 inhibitors (RSL3 and ML210) are shown and cell lines used in this study are highlighted. b. TISMO data analysis. The baseline expression of *Gpx4* and *Fsp1* are shown and cell lines used in this study are highlighted. c. Immunoblot analysis of GPX4, FSP1, and VCP expression in various cell lines (from a single experiment). d. Cell viability of various cell lines treated with RSL3 and/or viFSP1 for 24 h. Lip-1 was used as a ferroptosis inhibitor. e. Immunoblot analysis of GPX4, FSP1, actin and VCP expression in B16F10 and 4T1 cells from a single experiment. DKO: *Gpx4*-KO/*Fsp1*-KO. f. Cell viability of 4T1 *Gpx4*-KO cells

stably expressing hFSP1 or mFSP1, and B16F10 DKO cells stably expressing hFSP1 or mFSP1 treated with viFSP1 for 48 h. Lip-1 was used as ferroptosis inhibitor. g. Cell viability of B16F10 DKO cells stably expressing mGPX4 or mGPX4 U46C treated with RSL3 for 24 h. h. Representative immunoblot analysis of GPX4, and VCP expression in SW620 cells from a single experiment (left). Cell viability of SW620 wildtype cells or *GPX4*-KO treated with viFSP1 for 48 h (right). i. Cell viability of murine cell lines treated with JKE-1674 and/or viFSP1 (5 μ M) and Lip-1 (0.5 μ M) for 24 h. j. Cell viability of human cancer cell lines treated with JKE-1674 and/or viFSP1 (5 μ M) and Lip-1 (0.5 μ M) for 24 h. Data represents the mean \pm SD of 3 wells of a 96-well plate from one out of 2 independent experiments (d,f,g,h,i,j).



Extended Data Fig. 7 | Mechanism of action of viFSP1. a. Enzyme kinetics in vitro assay. Schematic representation of the FSP1 enzyme activity assay using resazurin and NADH as the substrates. Representative reduction kinetics of resazurin, bar plots of the K_m and relative V_{max} values, Lineweaver-Burk plot, and Dixon plot in the presence of different concentrations of either NADH or resazurin with viFSP1 at indicated concentrations. Reduction kinetics, Lineweaver-Burk plot, and Dixon plot represent a single well of a 96-well plate from one out of 2 independent experiments. Bar plots represent the mean from 2 independent experiments. b. Representative resazurin reduction assay in the presence of FSP1 mutants with indicated concentrations of viFSP1.

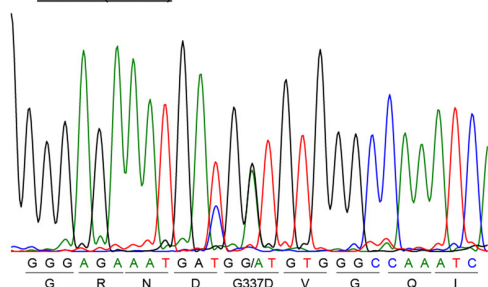
Data represents a single well of a 96-well plate from one out of 3 independent experiments. c. Cell viability of Pfa1 *Gpx4*-KO cells stably overexpressing wildtype mouse FSP1 or its mutants treated with viFSP1 for 24 h. Data represents the mean \pm SD of 3 wells of a 96-well plate from one out of 2 independent experiments. d. Immunoblot analysis of GPX4, FSP1 (HA), and VCP expression in Pfa1 cells stably overexpressing wildtype FSP1 or its mutants from a single experiment. e. Alignment of different FSP1 orthologues. f. Comparison between predicted human (blue) and mouse (magenta) FSP1 structures in the respective viFSP1 binding pocket. Amino acid differences are highlighted in magenta/blue.

a COSMIC analysis

Position	DNA mutation	AA mutation	Legacy mutation ID	Count
244	c.731G>A	p.G244D	COSM1492290	5
160	c.480G>T	p.E160D	COSM4660640	2
160	c.478G>T	p.E160*	COSM8475894	1
355	c.1064A>G	p.K355R	COSM5969878	1
285	c.853G>A	p.D285N	COSM3807587	1
327	c.980C>T	p.T327M	COSM8368094	1

b DepMap analysis

Cell Line	Depmap ID	Cancer type	Protein change
SKOV3	AH-000811	Ovarian	p.G337D
RL952	AH-000965	Endometrial/Uterine	p.S6L

c SKOV3 (G337D)**Extended Data Fig. 8 | Reported *AIFM2* mutations in different cancer types.**

a. COSMIC database analysis. *AIFM2* somatic mutations (heterozygous) are found in cancer patients. Mutations can affect the enzymatic activity of FSP1, such as the proton transfer function (E160, K355), NADH binding (G244), and FAD

binding (D285), and may affect the efficacy of FSP1 inhibitors (T327). b. DepMap database analysis. The S6 mutation likely affects FSP1 enzymatic activity via altered myristoylation (consensus motif: MGxxxS). c. Representative sequence data for genomic DNA of *AIFM2* surrounding G337G/D extracted from SKOV3.

Reporting Summary

Nature Portfolio wishes to improve the reproducibility of the work that we publish. This form provides structure for consistency and transparency in reporting. For further information on Nature Portfolio policies, see our [Editorial Policies](#) and the [Editorial Policy Checklist](#).

Statistics

For all statistical analyses, confirm that the following items are present in the figure legend, table legend, main text, or Methods section.

n/a Confirmed

- The exact sample size (n) for each experimental group/condition, given as a discrete number and unit of measurement
- A statement on whether measurements were taken from distinct samples or whether the same sample was measured repeatedly
- The statistical test(s) used AND whether they are one- or two-sided
Only common tests should be described solely by name; describe more complex techniques in the Methods section.
- A description of all covariates tested
- A description of any assumptions or corrections, such as tests of normality and adjustment for multiple comparisons
- A full description of the statistical parameters including central tendency (e.g. means) or other basic estimates (e.g. regression coefficient) AND variation (e.g. standard deviation) or associated estimates of uncertainty (e.g. confidence intervals)
- For null hypothesis testing, the test statistic (e.g. F , t , r) with confidence intervals, effect sizes, degrees of freedom and P value noted
Give P values as exact values whenever suitable.
- For Bayesian analysis, information on the choice of priors and Markov chain Monte Carlo settings
- For hierarchical and complex designs, identification of the appropriate level for tests and full reporting of outcomes
- Estimates of effect sizes (e.g. Cohen's d , Pearson's r), indicating how they were calculated

Our web collection on [statistics for biologists](#) contains articles on many of the points above.

Software and code

Policy information about [availability of computer code](#)

Data collection

Data analysis

For manuscripts utilizing custom algorithms or software that are central to the research but not yet described in published literature, software must be made available to editors and reviewers. We strongly encourage code deposition in a community repository (e.g. GitHub). See the Nature Portfolio [guidelines for submitting code & software](#) for further information.

Data

Policy information about [availability of data](#)

All manuscripts must include a [data availability statement](#). This statement should provide the following information, where applicable:

- Accession codes, unique identifiers, or web links for publicly available datasets
- A description of any restrictions on data availability
- For clinical datasets or third party data, please ensure that the statement adheres to our [policy](#)

All data is available in the Article, the Supplementary Information, and also from the corresponding author on reasonable request. Gel source images are shown in Supplementary Fig. 2. All source data is provided in this paper. Human cancer cell line data was mined from DepMap (<https://depmap.org/portal/>) or COSMIC

(<https://cancer.sanger.ac.uk/cosmic>) databases. Murine cancer cell line data was mined from TISIMO database (<http://tismo.cistrome.org>). The sequence data from this study has been submitted to NCBI BioProject (<https://www.ncbi.nlm.nih.gov/bioproject>) under BioProject ID PRJNA942499.

Human research participants

Policy information about [studies involving human research participants and Sex and Gender in Research](#).

Reporting on sex and gender	<input type="text" value="n.a."/>
Population characteristics	<input type="text" value="n.a."/>
Recruitment	<input type="text" value="n.a."/>
Ethics oversight	<input type="text" value="n.a."/>

Note that full information on the approval of the study protocol must also be provided in the manuscript.

Field-specific reporting

Please select the one below that is the best fit for your research. If you are not sure, read the appropriate sections before making your selection.

Life sciences Behavioural & social sciences Ecological, evolutionary & environmental sciences

For a reference copy of the document with all sections, see [nature.com/documents/nr-reporting-summary-flat.pdf](https://www.nature.com/documents/nr-reporting-summary-flat.pdf)

Life sciences study design

All studies must disclose on these points even when the disclosure is negative.

Sample size	Sample sizes in vitro experiments were determined based on the numbers required to achieve statistical significance using indicated statistics, as well as considering of previous publications on similar experiments (PMID: 31634899 and 35922516).
Data exclusions	No data exclusions.
Replication	The experimental findings were reproduced as validated by at least two independent experiment in Fig. 1-5 and Extended Data Fig. 2-7 except for the mutational analysis.
Randomization	Randomization is not relevant to the in vitro experiments since cells come in millions of populations and are automatically randomized and seeded to different wells for treatment.
Blinding	In the in vitro experiments, the investigators were not blinded, which is standard in this type of study due to the multiple steps involved that require precise operations for accuracy and precision precluding blinding to experimental variables.

Reporting for specific materials, systems and methods

We require information from authors about some types of materials, experimental systems and methods used in many studies. Here, indicate whether each material, system or method listed is relevant to your study. If you are not sure if a list item applies to your research, read the appropriate section before selecting a response.

Materials & experimental systems

n/a	Involvement in the study
<input type="checkbox"/>	<input checked="" type="checkbox"/> Antibodies
<input type="checkbox"/>	<input checked="" type="checkbox"/> Eukaryotic cell lines
<input checked="" type="checkbox"/>	<input type="checkbox"/> Palaeontology and archaeology
<input checked="" type="checkbox"/>	<input type="checkbox"/> Animals and other organisms
<input checked="" type="checkbox"/>	<input type="checkbox"/> Clinical data
<input checked="" type="checkbox"/>	<input type="checkbox"/> Dual use research of concern

Methods

n/a	Involvement in the study
<input checked="" type="checkbox"/>	<input type="checkbox"/> ChIP-seq
<input type="checkbox"/>	<input checked="" type="checkbox"/> Flow cytometry
<input checked="" type="checkbox"/>	<input type="checkbox"/> MRI-based neuroimaging

Antibodies

Antibodies used	GPX4 (1:1000 for WB, ab125066, Abcam), human FSP1 (1:1000, sc-377120, Santa Cruz Biotechnology), human FSP1(1:5 for WB, clone AIFM2 6D8, rat IgG2a, developed in-house: available from Sigma,
-----------------	---

Cat#MABC1638-25UL), mouse FSP1 (1:100 for WB, clone AIFM2 1A1 rat IgG2a, developed in-house), mouse FSP1(1:5 for WB, clone AIFM2 14D7 IgG2b, developed in-house), β -actin-HRP (1:50000, A3854, Sigma-Aldrich), valosin containing protein (VCP, 1:10000, ab11433 or ab109240, Abcam), HA tag (YPYDVPDYA, 1:1000 for WB, clone 3F10 rat IgG1, developed in-house) were used in this study. The appropriate secondary antibodies (1:1000-5000, Cell Signaling, Cat#7074S for rabbit; 7076S for mouse, and 1:1000 for anti-rat IgG1b and 2a/b, developed in-house) diluted in 5% skim milk in TBS-T.

Validation

GPX4 (ab125066), VCP (ab11433 or ab109240), human FSP1 (sc-377120), HA tag (clone 3F10), β -actin-HRP (A3854) antibodies were validated for WB using mouse and human cell samples in previous publications (PMID: 35922516, 31634899, and 27842070). FSP1 antibody (clone AIFM2 1A1/6D8 rat IgG2a, and clone AIFM2 14D7 IgG2b, developed in-house) has been validated for WB in previous study (PMID: 35922516).

Eukaryotic cell lines

Policy information about [cell lines and Sex and Gender in Research](#)

Cell line source(s)

4-OH-TAM-inducible Gpx4^{-/-} murine immortalized fibroblasts (Pfa1) were established in our lab as reported previously (PMID: 18762024). HT-1080 (CCL-121), HEK293T (CRL-3216), 786-O (CRL-1932), A375 (CRL-1619), B16F10 (CRL-6475), LLC (CRL-1642), MDA-MB-436 (HTB-130), SW620 (CCL-227), NCI-H460 (HTB-177) and 4T1 (CRL-2539) cells were obtained from ATCC. MC38 cells (SCC172) and SKOV3 (91091004) were obtained from Sigma-Aldrich. HEC151 cells (JCRB1122-A) were obtained from Tebubio. Rat1 cells (available from Thermo Fisher) were kindly gifted from Medizinische Hochschule Hannover. Huh7 cells (available from Thermo Fisher) were kindly gifted from Dr. Robert Schneider, Helmholtz Munich. MC38 cells (available from Sigma) were kindly gifted from Dr. Patrizia Agostinis (KU Leuven, Belgium).

Authentication

None of the cell lines used were authenticated.

Mycoplasma contamination

All cell lines were tested negative for mycoplasma contamination.

Commonly misidentified lines
(See [ICLAC](#) register)

No commonly misidentified cell lines were used.

Flow Cytometry

Plots

Confirm that:

- The axis labels state the marker and fluorochrome used (e.g. CD4-FITC).
- The axis scales are clearly visible. Include numbers along axes only for bottom left plot of group (a 'group' is an analysis of identical markers).
- All plots are contour plots with outliers or pseudocolor plots.
- A numerical value for number of cells or percentage (with statistics) is provided.

Methodology

Sample preparation

100,000 cells per well were seeded on a 12-well plate one day prior to the experiments. On the next day, cells were treated with 2.5 μ M icFSP1 for 3 h, and then incubated with 1.5 μ M C11-BODIPY 581/591 (Invitrogen, Cat#D3861) for 30 min in a 5% CO₂ atmosphere at 37°C. Subsequently, cells were washed by PBS once and trypsinized, and then resuspended in 500 μ L PBS. Cells were passed through a 40 μ m cell strainer and analyzed by a flow cytometer (CytoFLEX, Beckman Coulter) with a 488-nm laser for excitation. Data was collected from the FITC detector (for the oxidized form of BODIPY) with a 525/40nm bandpass filter and from the PE detector (for the reduced form of BODIPY) with a 585/42 nm bandpass filter.

Instrument

CytoFLEX (Beckman Coulter)

Software

CytExpert v2.4 was used for data collection. FlowJo v10 was used for data analysis.

Cell population abundance

At least 10,000 cells were analyzed for each sample.

Gating strategy

Cell populations were separated from cellular debris using FSC and SSC.

- Tick this box to confirm that a figure exemplifying the gating strategy is provided in the Supplementary Information.


DHODH inhibitors sensitize to ferroptosis by FSP1 inhibition

<https://doi.org/10.1038/s41586-023-06269-0>

Received: 13 September 2022

Accepted: 30 May 2023

Published online: 5 July 2023

 Check for updates

Eikan Mishima^{1,2,5}, Toshitaka Nakamura^{1,5}, Jiashuo Zheng^{1,5}, Weijia Zhang¹, André Santos Dias Mourão³, Peter Sennhenn⁴ & Marcus Conrad^{1✉}

ARISING FROM C. Mao et al. *Nature* <https://doi.org/10.1038/s41586-021-03539-7> (2021)

Ferroptosis, a form of non-apoptotic cell death that is hallmarked by lipid peroxidation of cellular membranes, has gained considerable attention as it is considered a potential therapeutic target for breaking cancer therapeutic resistance¹. In their recent Article, Mao et al.² identified mitochondrially localized dihydroorotate dehydrogenase (DHODH) as an additional enzyme that mediates suppression of ferroptosis, implying that inhibition of DHODH may present a promising strategy to overcome ferroptosis resistance in cancer cells. Here we show that the contribution of DHODH in ferroptosis suppression appears to be small and context-dependent, because the ferroptosis-sensitizing effect of DHODH inhibitors is apparent only at high concentrations that also efficiently inhibit ferroptosis-suppressor protein 1 (FSP1), which has an important role in ferroptosis defence³. The observed effects on ferroptosis sensitization with this concentration of inhibitors cannot be attributed to DHODH inhibition per se. Thus, applying compounds that modulate ferroptosis at appropriate concentrations is mandatory to avoid off-target effects.

Canonically, DHODH catalyses the ubiquinone (CoQ₁₀)-dependent oxidation of dihydroorotate to orotate. Orotate is an essential building block for the de novo pyrimidine biosynthesis that is required during cell proliferation, and therefore DHODH presents a promising target for tumour therapy⁴ (Extended Data Fig. 1a). Mao et al.² concluded that in addition to the mitochondrial form of glutathione peroxidase 4 (GPX4), DHODH is able to suppress ferroptosis at the inner mitochondrial membranes by reducing CoQ₁₀ to ubiquinol. Ubiquinol in turn facilitates the scavenging of phospholipid radicals, which implies that DHODH may constitute a druggable target for ferroptosis sensitization². Substantiating their conclusions, the authors showed that cancer cell lines with genetic deletion of *DHODH* were more sensitive to ferroptosis-inducing agents, including the GPX4 inhibitor (1S,3R)-RSL3 (RSL3). Moreover, they showed that brequinar, a potent and selective inhibitor of DHODH, also sensitized cancer cells towards ferroptosis. Although a comprehensive mechanistic framework explaining the molecular events that ultimately determine the cells' sensitivity to ferroptosis is an important goal for the ferroptosis field, the study by Mao et al.² contains several weaknesses and misinterpretations, strongly arguing against the conclusion that inhibition of DHODH is a promising target to overcome ferroptosis resistance in cancer cells.

First, the authors used extremely high concentrations of brequinar (500 μM), far exceeding the reported half-maximal inhibitory concentration (IC₅₀) of 7 nM, to inhibit DHODH^{4,5}. Although we could indeed observe a synergistic effect of brequinar and ferroptosis inducers, including RSL3, in various cancer cells (Fig. 1a and Extended Data

Fig. 1b–d), the sensitizing effect of brequinar was only evident at a concentration (IC₅₀ = 61 μM; Fig. 1a) much higher than that required for DHODH inhibition (Fig. 1b and Extended Data Fig. 1e). DHODH is a CoQ₁₀-reducing flavoprotein similar to FSP1, which suppresses ferroptosis by reducing extramitochondrial CoQ₁₀ and vitamin K^{3,6}, thereby preventing lipid peroxidation in a wide array of cancer cell lines independently of the cysteine–glutathione–GPX4 axis. Thus, we tested whether the ferroptosis-sensitizing effect of brequinar was actually mediated by inhibition of FSP1. Indeed, cell-free assays using recombinant FSP1 revealed that high concentrations of brequinar inhibited FSP1 activity (IC₅₀ = 24 and 14 μM for human and mouse FSP1, respectively), similar to the human FSP1-specific inhibitor iFSP1³ (Fig. 1c and Extended Data Fig. 2a–c). In line with this result, the high concentration of brequinar also induced ferroptosis in mouse fibroblast Pfa1 cells with genetic deletion of *Gpx4* and stably overexpressing human FSP1, whose survival depends solely on FSP1 activity³ (Fig. 1d). Notably, the ferroptosis-sensitizing effect of brequinar was retained regardless of the genetic ablation of *DHODH* (Fig. 1e and Extended Data Fig. 2d), whereas it was lost in *FSP1*-knockout cells (Fig. 1f). Of note, other DHODH inhibitors (for example, vidofludimus) also showed FSP1 inhibitory effects and sensitized cells to ferroptosis (Extended Data Fig. 2e–h), whereas BAY-2402234, a DHODH inhibitor seemingly lacking FSP1 inhibitory activity, did not sensitize cells towards ferroptosis (Extended Data Fig. 2h). Predictive structural analysis suggested that brequinar fitted well in the putative CoQ₁₀-binding pocket of FSP1 (Fig. 1g and Extended Data Fig. 2i). Together, these results demonstrate that the ferroptosis-sensitizing effect of brequinar (and several other DHODH inhibitors) is mediated via inhibition of FSP1 and not via DHODH.

Second, Mao et al.² report that genetic deletion of *DHODH* potentially sensitized human cancer cells, including HT-1080 cells, to ferroptosis induced by RSL3². Nonetheless, in our hands this sensitizing effect by deletion of *DHODH* was minor and far smaller than the effect of *FSP1* deletion (Fig. 1h and Extended Data Fig. 3a). This tendency was even more apparent in other cancer cell lines (Fig. 1h). In addition, unlike *FSP1*, overexpression of *DHODH* invariably did not protect Pfa1 cells from ferroptosis induced by genetic deletion of *Gpx4* or by inhibition of GPX4 with RSL3 (Fig. 1i and Extended Data Fig. 3b,c). By stark contrast, overexpression of *FSP1* alone was sufficient to prevent ferroptosis even in the absence of GPX4 and *DHODH* expression (Extended Data Fig. 3d,e). As such, the contribution of *DHODH* to ferroptosis resistance seems to be rather subtle.

Third, the concentration of RSL3 used by Mao et al.² to induce ferroptosis in HT-1080 cells was very high. HT-1080 is among the most

¹Institute of Metabolism and Cell Death, Helmholtz Zentrum München, Neuherberg, Germany. ²Division of Nephrology, Rheumatology and Endocrinology, Tohoku University Graduate School of Medicine, Sendai, Japan. ³Institute of Structural Biology, Helmholtz Zentrum München, Neuherberg, Germany. ⁴transMedChem, Munich, Germany. ⁵These authors contributed equally: Eikan Mishima, Toshitaka Nakamura, Jiashuo Zheng. ✉e-mail: marcus.conrad@helmholtz-munich.de

Matters arising

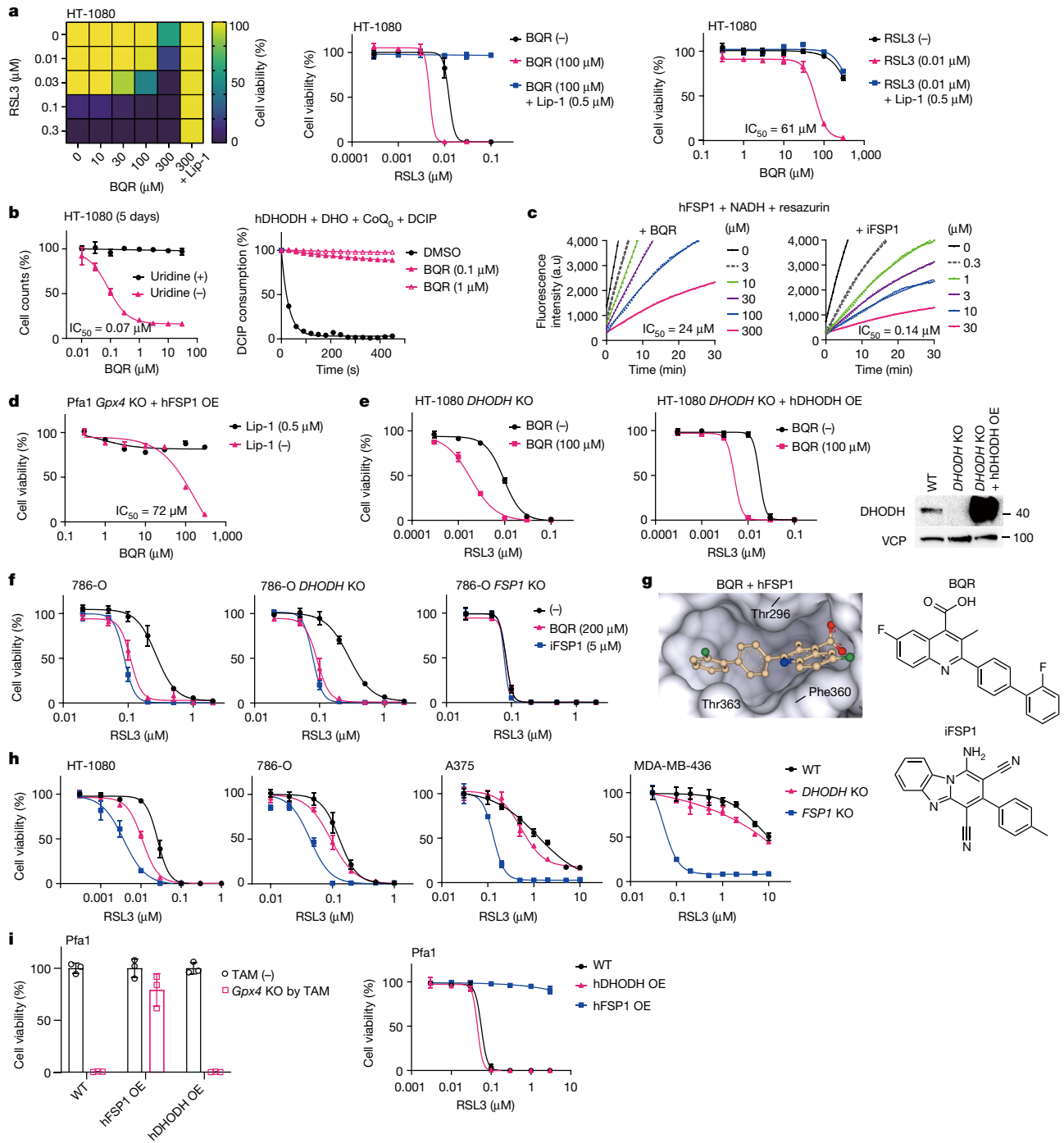


Fig. 1 | Brequinarsensitizes cancer cells to ferroptosis via FSP1 inhibition.

a, Left, heat map of viability of HT-1080 cells showing the synergistic lethal effects of brequinar (BQR) and RSL3. The well-established ferroptosis inhibitor liproxstatin-1 (Lip-1, 0.5 μ M) was used as a positive control to prevent ferroptosis. Viability was measured after treatment with RSL3 for 24 h. Middle, viability of HT-1080 cells treated with varying concentrations of RSL3 and a fixed concentration of BQR (100 μ M) for 24 h. Right, viability of HT-1080 cells treated with increasing concentrations of BQR and a sub-lethal dose of RSL3 (0.01 μ M) for 24 h. **b**, Left, relative cell counts of BQR-treated HT-1080 cells incubated with or without uridine (100 μ M) for 5 days. Right, in vitro assays showing the inhibitory effect of BQR (0.1 and 1 μ M) on DHODH enzyme activity. Recombinant human DHODH (hDHODH, 25 nM), dihydroorotate (DHO), coenzyme Q₀ (CoQ₀) and 2,6-dichloroindophenol (DCIP) were used. **c**, In vitro assays showing the inhibitory effect of BQR and iFSP1 towards FSP1 enzyme activity. Recombinant human FSP1 (hFSP1, 50 nM) was used. a.u., arbitrary units. **d**, The effect of BQR on

the viability of Pfa1 mouse embryonic fibroblasts with *Gpx4* knockout (KO) and stable overexpression (OE) of human FSP1. **e**, The synergistic effect of BQR (100 μ M) and RSL3 (24 h) on the viability of *DHODH*-knockout HT-1080 cells with or without overexpression of human DHODH. WT, wild type. The effect of BQR (200 μ M) and iFSP1 (5 μ M) on the viability of wild-type and *DHODH*- or *FSP1*-knockout 786-O cells treated with RSL3 for 24 h. **g**, Chemical structures of BQR and iFSP1 and the predicted binding site of BQR in the hFSP1 enzyme. **h**, The effects of genetic deletion of *DHODH* or *FSP1* on the viability of HT-1080, 786-O, A375 and MDA-MB-436 cancer cell lines treated with RSL3 for 24 h. **i**, Viability of wild-type or 4-hydroxytamoxifen (TAM)-induced *Gpx4*-knockout Pfa1 cells stably overexpressing haemagglutinin-tagged hFSP1 or hDHODH. Left, viability was measured three days after TAM treatment. Right, viability was measured after treatment with RSL3 for 24 h. Data are mean \pm s.d. of $n = 3$ independent experiments (a, b (left), d-f, h, i). Data are representative of two (b, right) or three (c) independent experiments.

ferroptosis-sensitive human cancer cell lines and is thus widely used in ferroptosis research. On the basis of our own results as well as those from other groups, 300 nM of RSL3 is generally sufficient to induce ferroptosis in these cells (although fetal bovine serum contained in the culture medium may have an effect on ferroptosis sensitivity owing to variable concentrations of selenium, vitamin E and/or other micronutrients). The authors used more than 10 μ M RSL3 to induce ferroptosis in HT-1080 cells². These high concentrations were apparently necessary because the authors worked with very high cell densities, seeding 20,000 cells per well in a 96-well plate. It should be highlighted that high cell densities can indeed desensitize cells to ferroptosis and even protect *Gpx4*-knockout cells from dying^{7,8} (Extended Data Fig. 3f). Besides GPX4, RSL3 targets most of the 25 human selenoproteins owing to the strong preference of the chloroacetamide group of RSL3 towards selenocysteine⁹ (which probably becomes even more relevant at the higher concentrations as used here (over 10 μ M)), therefore we assumed that the confluent cell culture conditions seem to be suboptimal when examining the ferroptosis sensitivity of the cells against RSL3.

Finally, the role of the mitochondrial form of GPX4 in ferroptosis prevention claimed by Mao et al.² is unclear. Here, it is important to mention that GPX4 is expressed in three distinct isoforms (Extended Data Fig. 4a). Transcription of the short form of GPX4 (the cytosolic form) is driven by its promoter 5' of exon 1, whereas the mitochondrial matrix form is driven by a distal promoter that allows translation of a cognate mitochondrial targeting signal at its N terminus. Transcription of nuclear GPX4 is mediated by its own promoter in an alternative exon¹⁰. The short form of GPX4 is abundantly expressed in all tissues and is enriched in the cytoplasm and the extra-matrix space of mitochondria of somatic cells, whereas the mitochondrial matrix and nuclear forms are abundantly expressed in the mitochondrial matrix and nucleus of testicular cells, respectively^{11,12} (Extended Data Fig. 4b). Earlier studies using isoform-specific knockout and transgenic mice as well as cells showed that the mitochondrial matrix and nuclear form are both important for spermatogenesis, but are otherwise dispensable for cytoprotection^{12–14}, although the influence of the knockout of the mitochondrial matrix-targeted variant of GPX4 in cancer cells has not been determined. Of note, although Mao et al. first reported that mitochondrial GPX4 has a role in ferroptosis prevention², a subsequent report by the same group reconciled their findings by showing that ferroptosis induced by *GPX4* deletion can only be prevented by overexpression of cytosolic GPX4 (that is, the short form) but not the mitochondrial matrix form¹⁵, which is in agreement with our data (Extended Data Fig. 4c). In addition, the mitochondrial matrix form of GPX4 was expressed at a much lower level than the short form across a range of cancer cell lines, as determined by quantitative PCR with reverse transcription (RT-qPCR), the only way to unequivocally discriminate between the two forms (Extended Data Fig. 4d), similar to results from an earlier study performed on mouse tissues¹¹.

In summary, DHODH inhibitors, including high concentrations of brequinar, sensitize cancer cells to ferroptosis via inhibition of FSP1 and not DHODH. Appropriate concentrations of ferroptosis-inducing and -sensitizing compounds are needed to avoid off-target effects. Although a number of DHODH inhibitors have been developed and are in clinical development against solid and haematological malignancies⁴, our study shows that the concentration and target engagement of DHODH inhibitors need to be carefully evaluated. Furthermore, we reiterate the importance of cell density in the study of ferroptosis and the seemingly irrelevant role of mitochondrial matrix GPX4 in ferroptosis prevention. The contribution of DHODH in ferroptosis, however, seems to be minor and context-specific.

Methods

Chemicals

Brequinar (SML0113), uridine (U3750), resazurin sodium salt (R7017), NADH (N8129), coenzyme Q₀ (D9150), 2,6-dichloroindophenol (DCIP,

D1878), L-dihydroorotic acid (D7128), L-buthionine sulfoximine (BSO; B2515), menadione (M5625) and ferrostatin-1 (Fer-1, SML0583) were purchased from Sigma Aldrich. (1S,3R)-RSL3 (19288), ML210 (23282), vidofludimus (18377), BAY-2402234 (33259), and ASLAN003 (33516) were purchased from Cayman. The following chemicals were obtained as indicated: erastin (329600, Merck Millipore), iFSP1 (8009-2626, ChemDiv), liproxstatin-1 (Lip-1, S7699, Selleckchem), PCT299 (HY-124593, MedChemExpress).

Cell lines

TAM-inducible *Gpx4*^{-/-} murine immortalized fibroblasts (Pfa1) were reported previously⁷. HT-1080 (CCL-121), 786-O (CRL-1932), A375 (CRL-1619), MDA-MB-436 (HTB-130), A549 (CCL-185), H460 (HTB-177), SW620 (CCL-227) and HEK293T (CRL-3216) cells were obtained from ATCC. LOX-IMVI was obtained from NCI/NIH. Cell lines, except for MDA-MB-436 and H460, were maintained in DMEM high glucose (4.5 g l⁻¹ glucose, 21969-035, Gibco) supplemented with 10% fetal bovine serum (FBS), 2 mM L-glutamine, and 1% penicillin/streptomycin at 37 °C with 5% CO₂. MDA-MB-436 and H460 cells were maintained in RPMI 1640 medium (61870-010, GlutaMAX supplemented, Gibco) supplemented with 10% FBS and 1% penicillin/streptomycin. *DHODH*-knockout cells and *Dhodh*-knockout Pfa1 cells were maintained in a medium containing uridine (100 and 50 μ M, respectively). *GPX4*-knockout cells were maintained in a medium containing Lip-1 (1 μ M) or Fer-1 (5 μ M). All cells were regularly tested for mycoplasma contamination.

Cell viability assays

Cells were seeded on 96-well plates at the following cell number per well and allowed to adhere overnight. For RSL3 treatment, 3,000 cells (HT-1080, 786-O and A375), 5,000 cells (MDA-MB-436) and 1,500 cells (Pfa1) were seeded. For the viability assay shown in a heat map, cells were seeded at 2,500 cells (HT-1080, 786-O, A375 and A549) and 5,000 cells (MDA-MB-436) for RSL3, ML210 and erastin treatment; and 1,000 cells of HT-1080 per well for BSO treatment. On the next day, cells were treated with the ferroptosis inducers. In the co-treatment experiments, brequinar, iFSP1 or Lip-1 were added alongside the ferroptosis inducers. When brequinar was used in the assay, uridine (100 μ M) was supplemented in the media to avoid the effect of the depletion of intracellular pyrimidines as well as to maintain *DHODH*-knockout cells. Cell viability was assessed 24 h (RSL3 and ML210), 48 h (erastin) and 72 h (BSO) after the treatment using AquaBluer (MultiTarget Pharmaceuticals) or 0.004 % Resazurin sodium salt (Sigma Aldrich) diluted in the culture medium unless stated otherwise. The cell viability was expressed as relative values compared to the control sample, which was defined as 100%. To induce the knockout of *Gpx4* in Pfa1 cells, the cells were seeded on 96-well plates (500 cells/well) and treated with 1 μ M TAM. Cell viability of TAM-treated Pfa1 cells was assessed 72 h after the treatment. To evaluate the effect of the confluency of cells towards ferroptosis sensitivity, HT-1080 cells were seeded on 96-well plates at 3,000, 8,000 and 20,000 cells per well, and then treated with RSL3 on the following day.

Cell proliferation assays

HT-1080 and Pfa1 cells were seeded on 96-well plates at 200 cells per well and incubated with or without uridine (100 and 50 μ M, respectively) for 5 days. After the incubation, relative cell counts were evaluated using AquaBluer.

Preparation of lentiviral particles

Lentiviral packaging system consisting of a transfer plasmid, psPAX2 (12260, Addgene), with pMD2.G (for human cells, 12259, Addgene) or pHCMV-EcoEnv (for mouse cells, 15802, Addgene) was co-lipofected into HEK293T cells using PEI-MAX (Polysciences). Cell culture supernatants containing viral particles were collected 48 h after the transfection and used to transduce the cell line of interest after filtration using a 0.45 μ m low protein binding syringe filter.

Matters arising

CRISPR–Cas9-mediated gene knockout

Sequences of single guide RNA (sgRNA), vectors for expression of Cas9 and sgRNA, and Cas9 expression system are listed in Supplementary Table 1. For transient expression of the CRISPR–Cas9 system, cells were transiently co-transfected with the sgRNA-cloned Cas9 expression plasmids (listed in Supplementary Table 1) using the X-tremeGENE HP agent (Roche). One day after transfection, cells were selected by treatment with puromycin ($1 \mu\text{g ml}^{-1}$), blasticidin ($10 \mu\text{g ml}^{-1}$) and/or geneticin (1 mg ml^{-1}). After selection, single-cell clones were picked and knockout clones were identified by immunoblotting. For stable expression of the CRISPR–Cas9 system, cells were infected with lentiviral particles containing the sgRNA-cloned lentiCRISPR v2-neo plasmid (98292, Addgene) with protamine sulfate ($8 \mu\text{g ml}^{-1}$). One day after transfection, cells were treated with geneticin (1 mg ml^{-1}). After the selection, the loss of expression of the targeted protein was confirmed by immunoblotting of batch cultures. For doxycycline-inducible Cas9 expression system, doxycycline-inducible Cas9 expressing cells were generated by transducing lentiviral particles containing pCW-Cas9-Blast (83481, Addgene)⁵. pCW-Cas9-Blast expressing cells were infected with lentiviral particles containing the sgRNA-cloned LentiGuide-Neo (139449, Addgene) or pKLV-U6gRNA(*BbsI*)-PGKpuro2aBFP vector (50946, Addgene). One day after transfection, cells were treated with geneticin (1 mg ml^{-1}) or puromycin ($1 \mu\text{g ml}^{-1}$), and then incubated with doxycycline ($10 \mu\text{g ml}^{-1}$) for 5 days to express Cas9. After the selection and the Cas9 induction, single-cell clones were picked and knockout clones were identified by immunoblotting.

Overexpression of DHODH, FSP1 and GPX4 isoforms

Codon-optimized human *DHODH* gene with a C-terminal HA tag was synthesized (Twist Bioscience) and cloned in the expression vector pLV-EF1a-IRES-Neo (85139, Addgene). Human *FSP1*-coding original sequence (NM_001198696.2) with a C-terminal HA tag was cloned in the expression vector p442-Blast. Coding sequences of the short form (NM_001367832.1) and mitochondrial matrix form (NM_002085.5) of human *GPX4* were amplified by PCR using cDNA produced from A375 cells, and they were cloned into the expression vector p442-Blast. Cells were infected with lentiviral particles containing the transfer plasmids. One day after infection, cells were selected with geneticin (1 mg ml^{-1}) or blasticidin ($10 \mu\text{g ml}^{-1}$). Reconstitution of DHODH, FSP1 and GPX4 isoforms expression was verified by immunoblotting. *GPX4*-knockout HT-1080 cells overexpressing each form of GXP4 were maintained with Fer-1 ($5 \mu\text{M}$) after the selection.

Western blotting

Cells were lysed in LCW lysis buffer pH 7.5 (0.5% Triton X-100, 0.5% sodium deoxycholate salt, 150 mM NaCl, 20 mM Tris-HCl, 10 mM EDTA, 30 mM Na-pyrophosphate tetrabasic decahydrate) containing protease and phosphatase inhibitor mixture (cOmplete and phoSTOP, Roche), and centrifuged at $15,000g$, $4 \text{ }^\circ\text{C}$ for 20 min. The supernatant was collected and used as the protein sample. Western blotting was performed by standard immunoblotting procedure with 12% SDS–PAGE gel, PVDF membrane, and primary antibodies against human FSP1 (1:1,000, sc-377120, Santa Cruz), DHODH (1:1,000, sc-166348, Santa Cruz), GPX4 (1:1,000, ab125066, Abcam), HA (1:1,000, clone 3F10, rat IgG1, developed in-house), and valosin containing protein (VCP) for loading control (1:10,000, ab109240, Abcam). Images were analysed with Image Lab 6.0 software (Bio-Rad).

Expression and purification of recombinant FSP1 and DHODH

Recombinant human and mouse FSP1 protein containing an N-terminal 6-histidine tag were produced in *Escherichia coli*, and purified by affinity chromatography with a Ni-NTA system as described previously³. The codon-optimized DNA sequence corresponding to the mitochondrial

intermembrane region of human DHODH 29–395 was synthesized as a gBlocks gene fragment (Integrated DNA Technologies) and cloned into a petM11 vector that contains an N-terminal 6-histidine tag. Expression and purification were done as previously reported¹⁶. In short, *E. coli* BL21 cells were transformed with the prepared DHODH vector and grown in TB at $37 \text{ }^\circ\text{C}$. When the cells reached OD 2.0, 0.5 mM IPTG was added and expression was performed at $20 \text{ }^\circ\text{C}$ overnight. Cells were collected, dissolved in the lysis buffer (PBS supplemented with 10 mM imidazole) and lysed using a sonicator. After centrifugation, the supernatant fraction was applied to a prepacked nickel column and washed extensively with the lysis buffer. The protein was eluted with PBS supplemented with 350 mM imidazole followed by concentration and final purification step over a size exclusion chromatography column pre-equilibrated with PBS. Protein was aliquoted, frozen in liquid nitrogen and stored at $-80 \text{ }^\circ\text{C}$ until further usage.

FSP1 enzyme inhibitor assay

Enzyme reactions in PBS pH 7.4 containing 50 nM hFSP1 or mFSP1 enzyme, 200 μM NADH (freshly prepared in water) and the inhibitors were prepared⁶. After the addition of 100 μM resazurin sodium salt, fluorescent intensity (excitation 540, emission 590 nm) was measured every 30 s on a 96-well plate using a SpectraMax M5 Microplate Reader and SoftMAX pro 7 (Molecular devices).

Determination of FSP1 activity by measuring NADH consumption

Enzyme reactions in PBS pH 7.4 containing 25 nM hFSP1 and 50 μM of menadione with or without 300 μM of brequinar were prepared⁶. After the addition of 200 μM NADH, the absorbance at 340 nm was measured every 30 s on a 96-well plate. Reactions without NADH or without enzyme were used to normalize the results.

DHODH enzyme inhibitor assay

DHODH activity was measured as reported previously¹⁷. The reaction was performed at pH 8.0 at $32 \text{ }^\circ\text{C}$ in a buffer containing 50 mM Tris, 0.1% Triton X-100, 150 mM NaCl, 25 nM recombinant human DHODH protein, 500 μM L-dihydroorotic acid, 100 μM coenzyme Q₀ and 120 μM DCIP with the inhibitors. DHODH activity was measured kinetically as a function of decreased DCIP absorbance at 600 nm.

In silico modelling

The predicted human FSP1 structure was obtained from the AlphaFold2 database (<https://alphafold.ebi.ac.uk>)¹⁸. To yield the superposed structure of FSP1 with its cofactor flavin adenine dinucleotide (FAD), the structure of the yeast orthologue NDH-2 (Ndi1)¹⁹ (PDB: 4G73) was aligned to FSP1 using Pymol v2.5.2 (Schrödinger), and the position of FAD was extracted and embedded into FSP1 structure as a template for modelling. The modelling software SeeSAR v12.1 (BioSolveIT) was used to dock the selected molecules into the hFSP1 protein. The binding site was detected and defined employing the integrated DoGSiteScorer module embedded in SeeSAR. Molecules were uploaded as SD files without any further preparation. For docking, the number of poses for each molecule was set to 500, and clash tolerance was set to high to allow a comparably tolerant generation of poses. The subsequent HYDE scoring function within SeeSAR was used to post-optimize the docking poses and to assess the estimated affinity. After visual inspection, the most viable poses were selected and filtered for favourable torsion quality and docking poses with unfavourable intra- and intermolecular clashes were removed.

RT–qPCR

Total RNA was extracted from the cells using RNeasy Mini kit (Qiagen) with genomic DNA removal by RNase-Free DNase set (Qiagen) and was reverse-transcribed using the QuantiTect Reverse Transcription Kit (Qiagen). Human testis mRNA was purchased from Takara-bio (636533)

and was reverse-transcribed. RT-qPCR was performed using PowerUp SYBR Green Master Mix (Thermo Fisher Scientific) with qTOWER3 G (Analytikjena). All samples were run with triplicates under the following condition: 1, 50 °C for 2 min; 2, 95 °C for 2 min; 3, 95 °C for 15 s; 4, 59.5 °C for 15 s; 5, 72 °C for 1 min; 6, 95 °C 1 s and cycle from 3 to 5 was repeated for 40 times. Sequences of the primers were the following: 5'-TGCTCTGTGGGGCTCTG and 5'-ATGTCCTTGGCGGAAAACCTC for detecting the short and mitochondrial matrix forms of *GPX4*; and 5'-ATTGGTCGGCTGGACGAG and 5'-ATGTCCTTGGCGGAAAACCTC for specific detection of the mitochondrial matrix form. The expression ratio of (the mitochondrial matrix form)/(the short and mitochondrial matrix forms) of *GPX4* was calculated using the $\Delta\Delta C_t$ method.

Quantification and statistical analysis

Statistical information for individual experiments can be found in the corresponding figure legends. Values are presented as mean \pm s.d. Statistical comparisons between groups were analysed by a two-tailed Student's *t*-test or one-way ANOVA with Dunnett's post hoc test. Statistical analyses were conducted using GraphPad Prism 9 (GraphPad Software).

Online content

Any methods, additional references, Nature Portfolio reporting summaries, source data, extended data, supplementary information, acknowledgements, peer review information; details of author contributions and competing interests; and statements of data and code availability are available at <https://doi.org/10.1038/s41586-023-06269-0>.

Reporting summary

Further information on research design is available in the Nature Portfolio Reporting Summary linked to this article.

Data availability

All data are available within the article and the Supplementary Information. Gel source images are shown in Supplementary Fig. 1. Source data are provided with this paper.

1. Jiang, X., Stockwell, B. R. & Conrad, M. Ferroptosis: mechanisms, biology and role in disease. *Nat. Rev. Mol. Cell Biol.* **22**, 266–282 (2021).
2. Mao, C. et al. DHODH-mediated ferroptosis defence is a targetable vulnerability in cancer. *Nature* **593**, 586–590 (2021).
3. Doll, S. et al. FSP1 is a glutathione-independent ferroptosis suppressor. *Nature* **575**, 693–698 (2019).
4. Zhang, L. et al. Recent advances of human dihydroorotate dehydrogenase inhibitors for cancer therapy: current development and future perspectives. *Eur. J. Med. Chem.* **232**, 114176 (2022).

5. Baumgartner, R. et al. Dual binding mode of a novel series of DHODH inhibitors. *J. Med. Chem.* **49**, 1239–1247 (2006).
6. Mishima, E. et al. A non-canonical vitamin K cycle is a potent ferroptosis suppressor. *Nature* **608**, 778–783 (2021).
7. Seiler, A. et al. Glutathione peroxidase 4 senses and translates oxidative stress into 12/15-lipoxygenase dependent- and AIF-mediated cell death. *Cell Metab.* **8**, 237–248 (2008).
8. Wu, J. et al. Intercellular interaction dictates cancer cell ferroptosis via NF2-YAP signalling. *Nature* **572**, 402–406 (2019).
9. Chen, Y. et al. Quantitative profiling of protein carbonylations in ferroptosis by an aniline-derived probe. *J. Am. Chem. Soc.* **140**, 4712–4720 (2018).
10. Moreno, S. G., Laux, G., Brielmeier, M., Bornkamm, G. W. & Conrad, M. Testis-specific expression of the nuclear form of phospholipid hydroperoxide glutathione peroxidase (PHGPx). *Biol. Chem.* **384**, 635–643 (2005).
11. Schneider, M. et al. Embryonic expression profile of phospholipid hydroperoxide glutathione peroxidase. *Gene Expr. Patterns* **6**, 489–494 (2006).
12. Liang, H. et al. Short form glutathione peroxidase 4 is the essential isoform required for survival and somatic mitochondrial functions. *J. Biol. Chem.* **284**, 30836–30844 (2009).
13. Conrad, M. et al. The nuclear form of phospholipid hydroperoxide glutathione peroxidase is a protein thiol peroxidase contributing to sperm chromatin stability. *Mol. Cell. Biol.* **25**, 7637–7644 (2005).
14. Schneider, M. et al. Mitochondrial glutathione peroxidase 4 disruption causes male infertility. *FASEB J.* **23**, 3233–3242 (2009).
15. Wu, S. et al. A ferroptosis defense mechanism mediated by glycerol-3-phosphate dehydrogenase 2 in mitochondria. *Proc. Natl. Acad. Sci. USA* **119**, e2121987119 (2022).
16. Walse, B. et al. The structures of human dihydroorotate dehydrogenase with and without inhibitor reveal conformational flexibility in the inhibitor and substrate binding sites. *Biochemistry* **47**, 8929–8936 (2008).
17. Christian, S. et al. The novel dihydroorotate dehydrogenase (DHODH) inhibitor BAY 2402234 triggers differentiation and is effective in the treatment of myeloid malignancies. *Leukemia* **33**, 2403–2415 (2019).
18. Varadi, M. et al. AlphaFold Protein Structure Database: massively expanding the structural coverage of protein-sequence space with high-accuracy models. *Nucleic Acids Res.* **50**, D439–D444 (2022).
19. Feng, Y. et al. Structural insight into the type-II mitochondrial NADH dehydrogenases. *Nature* **491**, 478–482 (2012).

Acknowledgements The authors would like to thank A. Wahida for critical reading of the manuscript. This work was supported by funding from the Deutsche Forschungsgemeinschaft (DFG) (CO 291/7-1) and the DFG Priority Program SPP 2306 (CO 291/9-1, 461385412 and CO 291/10-1, 461507177), the German Federal Ministry of Education and Research (BMBF) FERROPath (01EJ2205B), and the European Research Council (ERC) under the European Union's Horizon 2020 research and innovation programme (grant agreement no. GA 884754) to M.C.; JSPS KAKENHI (20KK0363) to E.M.; Alexander von Humboldt Post-Doctoral Fellowship to J.Z.; and China Scholarship Council to W.Z.

Author contributions E.M., T.N., J.Z., and M.C. conceived the study and wrote the manuscript. E.M., T.N., J.Z., and W.Z. performed the experiments and analysis. A.S.D.M. expressed and purified recombinant FSP1 and DHODH. P.S. performed in silico modelling. All authors read and agreed on the content of the paper.

Competing interests M.C. and P.S. hold patents for some of the compounds described herein, and are co-founders and shareholders of ROSCUE Therapeutics.

Additional information

Supplementary information The online version contains supplementary material available at <https://doi.org/10.1038/s41586-023-06269-0>.

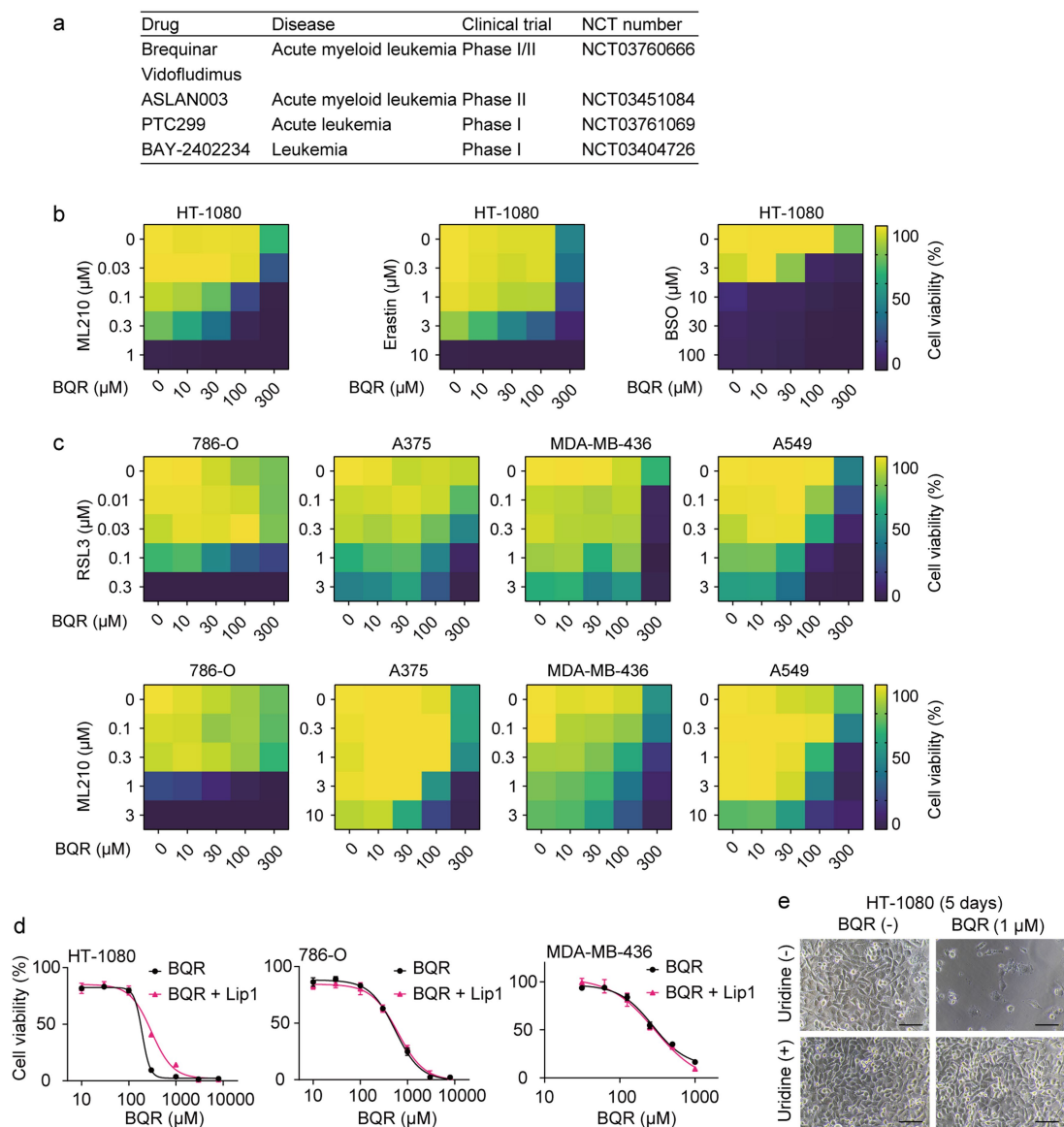
Correspondence and requests for materials should be addressed to Marcus Conrad.

Reprints and permissions information is available at <http://www.nature.com/reprints>.

Publisher's note Springer Nature remains neutral with regard to jurisdictional claims in published maps and institutional affiliations.

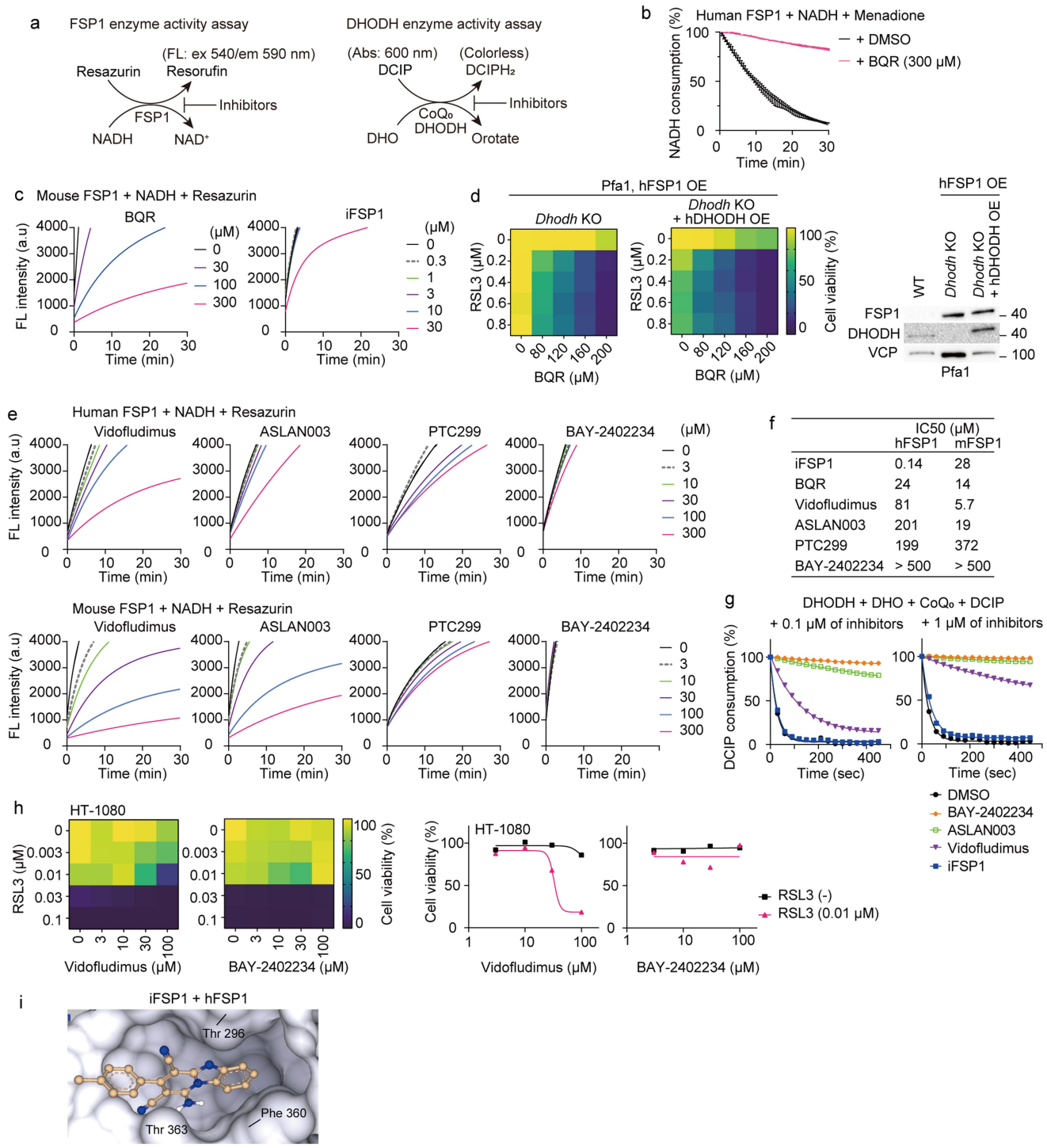
© The Author(s), under exclusive licence to Springer Nature Limited 2023

Matters arising

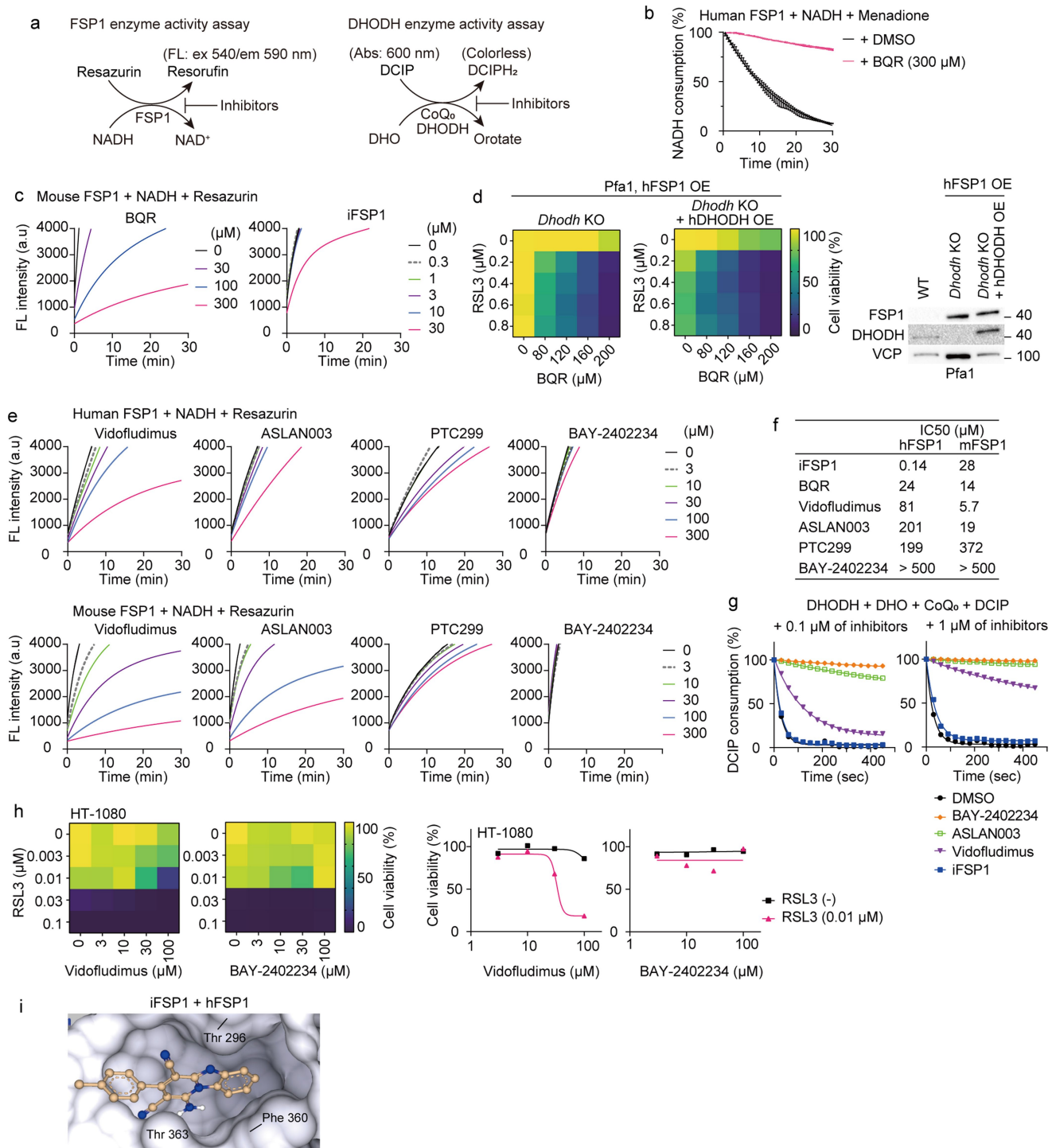


Extended Data Fig. 1 | The synergistic effect of brequinar with ferroptosis inducers in a panel of cancer cell lines. a. Known DHODH inhibitors in cancer-related clinical trials. Sourced from <https://clinicaltrials.gov/>, August 2022. **b.** Heatmaps of cell viability showing the synergistic effects of brequinar (BQR) with ML210, erastin and BSO in HT-1080 cells. Viability was measured after 48 h (ML210 and erastin) and 72 h treatment (BSO). **c.** Heatmaps of cell viability showing the synergistic effects of BQR with RSL3 and ML210 in 786-O, A375, MDA-MB-436 and A549 cells. Viability was measured after 48 h. **d.** Evaluation of

cellular toxicity of brequinar. HT-1080, 786-O and MDA-MB-436 cells were treated with the indicated concentrations of BQR in the presence or absence of the ferroptosis inhibitor liproxstatin-1 (Lip1, 1 μ M) for 24 h. BQR treatment alone was not sufficient to induce ferroptosis. **e.** Representative images of HT-1080 cells treated with or without BQR (1 μ M) and uridine (100 μ M) for 5 days. The cells were seeded at a density of 200 cells/well in a 96-well plate. Scale, 100 μ m. Data is mean \pm s.d. of $n = 3$ (d). Data is representative of two independent experiments (b-e).



Extended Data Fig. 2 | See next page for caption.

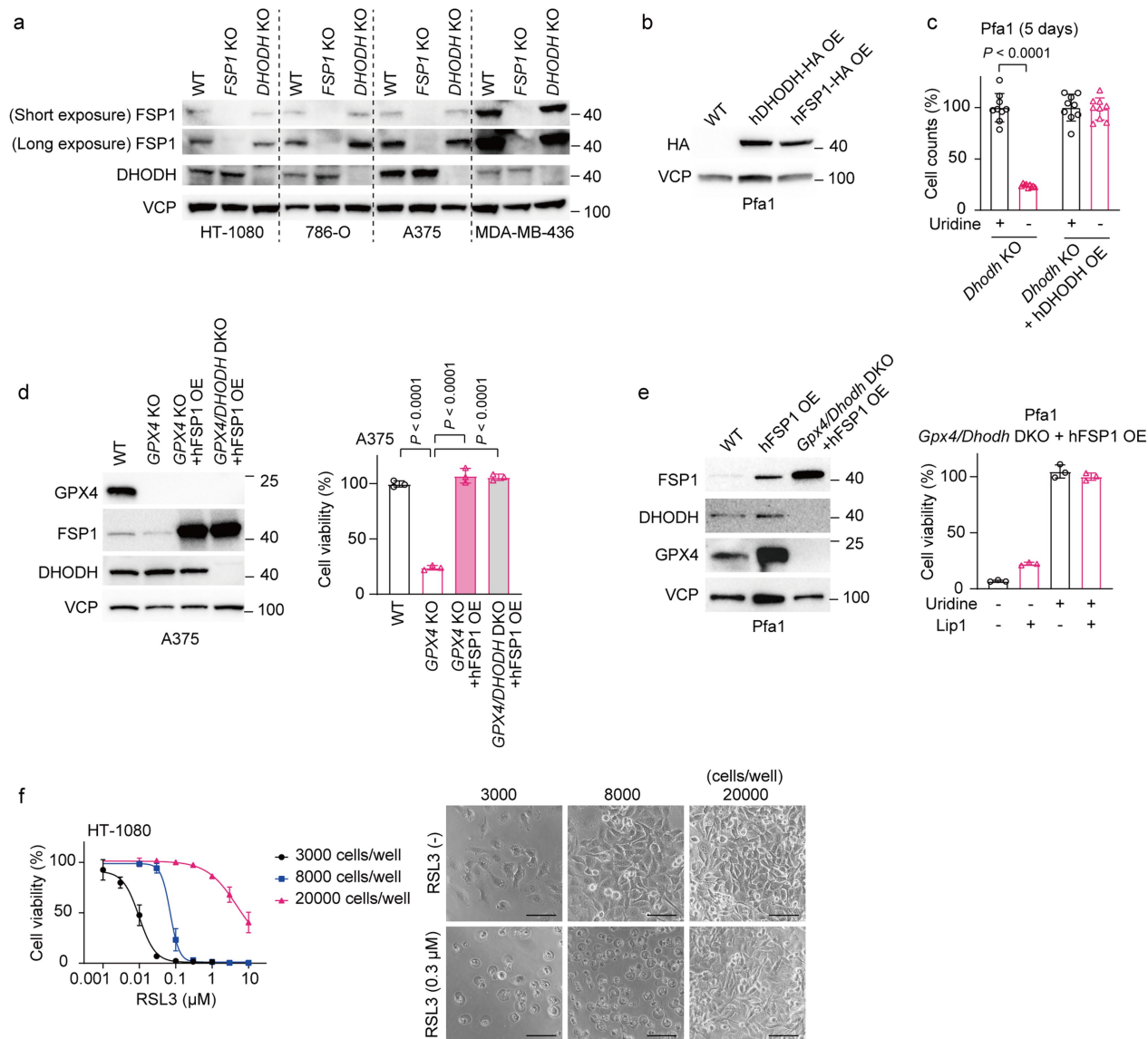


Extended Data Fig. 2 | See next page for caption.

Matters arising

Extended Data Fig. 2 | Inhibitory effects of DHODH inhibitors against FSP1 enzyme activity. **a.** (Left) Scheme of the FSP1 enzyme activity assay. Resazurin (100 μM), a substrate of FSP1, is reduced to resorufin by incubation with recombinant FSP1 protein (50 and 40 nM of human and mouse FSP1, respectively) and NADH (200 μM). The amount of resorufin evaluated by fluorescent intensity (ex 540/em 590 nm) indicates FSP1 enzymatic activity. (Right) Scheme of the DHODH enzyme activity assay. Enzyme reaction of recombinant human DHODH (25 nM), dihydroorotate (DHO, 500 μM) and CoQ_0 (100 μM) reduces an electron acceptor 2, 6-dichlorophenolindophenol (DCIP, 120 μM) to DCIPH_2 . The change in absorbance of DCIP (at absorbance 600 nm) indicates DHODH enzyme activity. **b.** NADH consumption assay using recombinant human FSP1 protein (25 nM) in combination with or without brequinar (BQR, 300 μM). Menadione (50 μM) was used as a substrate of FSP1. Brequinar inhibited the FSP1-dependent NADH consumption. **c.** The inhibitory effect of BQR and iFSP1

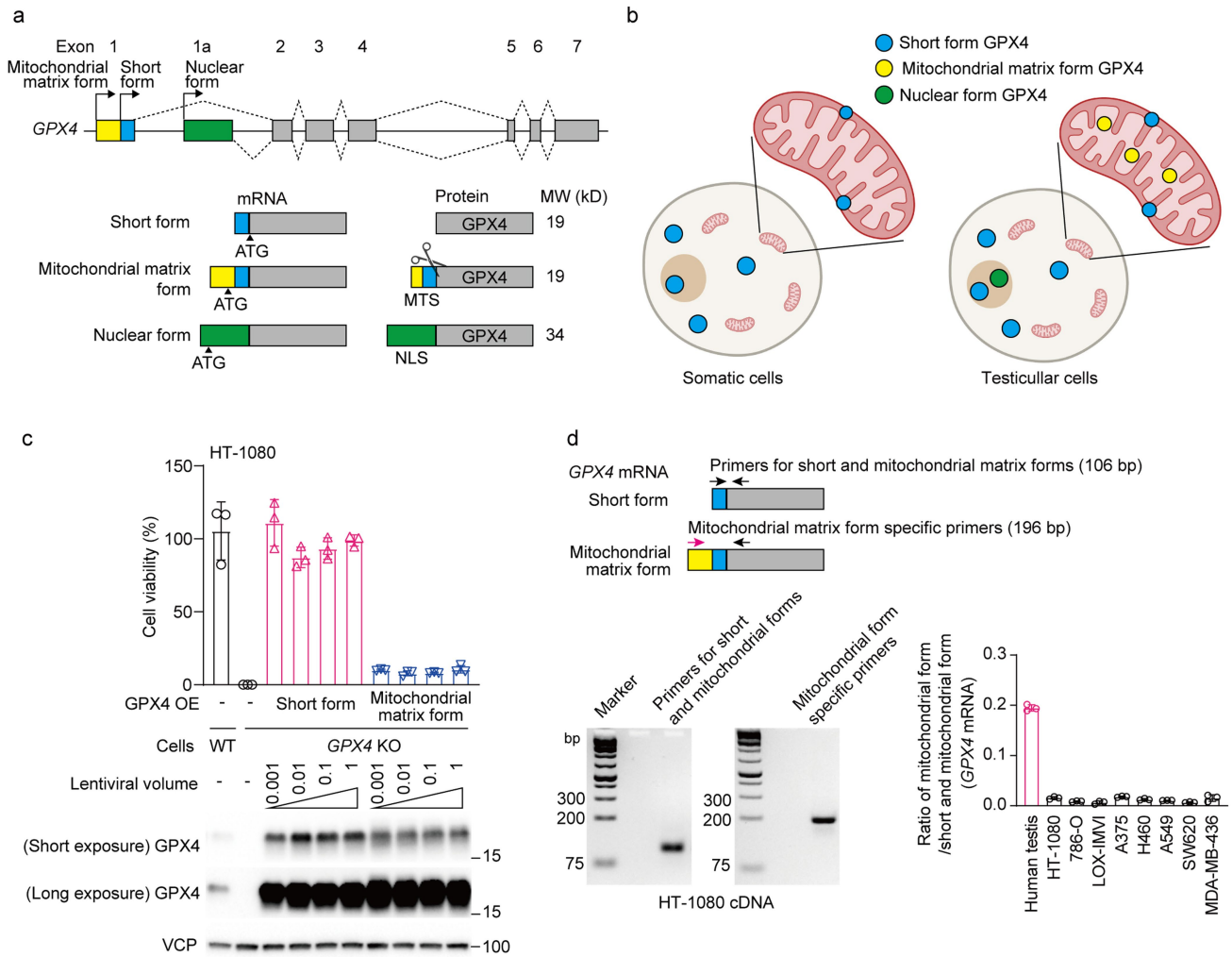
on mouse FSP1 enzymatic activity. **d.** Heatmaps showing the viability and immunoblotting of hFSP1-overexpressed (OE) and *Dhodh* KO-Pfa1 cells with or without overexpression of hDHODH. Viability was measured after treatment with RSL3 for 24 h. Combination of RSL3 with BQR synergistically induced cell death in both cell lines. **e.** The inhibitory effect of known DHODH inhibitors on human and mouse FSP1 enzyme activity. **f.** Calculated IC_{50} values of iFSP1 and DHODH inhibitors against recombinant human and mouse FSP1. **g.** The inhibitory effect of DHODH inhibitors and iFSP1 against human DHODH enzymatic activity. **h.** Heatmaps showing the viability of HT-1080 cells (5,000 cells per well) treated with RSL3 in combination with vidofludimus or BAY-2402234 for 24 h. The values of the groups treated with zero or 0.01 μM of RSL3 are also shown in the right graphs. **i.** The binding prediction of iFSP1 in human FSP1 protein. Data is mean \pm s.d. of $n = 3$ (b). Data is representative of three (b, c and e) and two independent experiments (d, g and h), respectively.



Extended Data Fig. 3 | Immunoblotting of genetic deletion or overexpression of FSP1 and DHODH, and the effect of cell confluency on ferroptosis sensitivity. **a.** Immunoblotting of lysates of *FSP1* KO and *DHODH* KO cells using HT-1080, 786-O, A375 and MDA-MB-436 cell lines. Each parental cell was used as wild type (WT). **b.** Immunoblotting of lysates of Pfa1 cells with stable overexpression (OE) of C-terminally HA-tagged human DHODH (hDHODH) or FSP1 (hFSP1). One experiment was performed (a, b). **c.** Relative cell counts of *Dhodh* KO Pfa1 cells with or without stable OE of hDHODH seeded 200 cells/well in a 96-well plate and incubated with or without uridine (50 μ M) for 5 days. hDHODH OE rescued the suppression of cell growth in *Dhodh* KO Pfa1 cells without uridine supplementation. **d.** Immunoblotting of lysate and viability of A375 cells of WT, *GPX4* KO, *GPX4* KO with hFSP1 OE and *GPX4/DHODH* double KO

with hFSP1 OE. For the measurement of the viability, 500 cells/well were seeded in a 96-well plate and incubated with or without Lip1 (1 μ M) for 4 days. Viability of the cells incubated with Lip1 (1 μ M) was taken as 100%. **e.** Immunoblotting of lysate and viability of *Gpx4* and *Dhodh* double KO Pfa1 cells with stable OE of hFSP1. The cells were seeded at a density of 300 cells/well in a 96-well plate and incubated with or without uridine (50 μ M) and Lip1 (1 μ M) for 5 days. The *Gpx4* and *Dhodh* double KO Pfa1 cells with OE of hFSP1 cells can survive without Lip1. **f.** The effect of cell density of HT-1080 cells on RSL3-induced cell death. The cells were seeded at densities of 3,000, 8,000 or 20,000 cells/well in a 96-well plate. On the next day, the cells were treated with RSL3 for 6 h and viability was determined. Scale, 100 μ m. Data is mean \pm s.d. of $n = 9$ (c) and $n = 3$ (d-f). Two-tailed *t*-test (c); one-way ANOVA with Dunnett's test (d).

Matters arising



Extended Data Fig. 4 | Expression pattern and subcellular localization of GPX4 isoforms. **a.** Structural organization of the *GPX4* gene, mRNA and protein of the GPX4 isoforms. Arrows indicate the transcription initiation sites. The dashed lines indicate the different splicing variants. ATG indicates the initiation codon of methionine. MTS, mitochondrial targeting sequence; NLS, nuclear localization signal. NLS also functions for stretching of DNA binding motifs. **b.** A scheme depicting the reported subcellular localization of each GPX4 isoform in somatic and testicular cells. The short form is abundantly expressed in the cytoplasm and mitochondrial extra-matrix space of somatic cells, while the mitochondrial matrix form is abundantly expressed in the mitochondrial matrix of testicular cells. The illustration was created using BioRender.com (a, b). **c.** Viability of *GPX4* KO HT-1080 cells (500 cells/well)

overexpressing the short or mitochondrial matrix form of GPX4 for three days after withdrawal of ferrostatin-1 (a ferroptosis inhibitor). The cells were prepared by infection with the indicated serial dilution of lentiviral particles containing the expression plasmids. Immunoblotting validated the overexpression of each form. Viability of the cells incubated with Lip1 (1 μ M) was taken as 100%. **d.** The design of the primer pairs detecting both the short and mitochondrial matrix forms (106 bp) and specific for the mitochondrial matrix form (196 bp). Agarose gel images show the amplification of the specific single band. The ratio of the mitochondrial matrix form/short and mitochondrial matrix forms of *GPX4* mRNA expression in the cancer cell lines was calculated as $2^{-\Delta\Delta CT}$ in quantitative RT-PCR. Data is representative of two independent experiments (c and d). Data is mean \pm s.d. of $n = 3$ (c and d).

Reporting Summary

Nature Portfolio wishes to improve the reproducibility of the work that we publish. This form provides structure for consistency and transparency in reporting. For further information on Nature Portfolio policies, see our [Editorial Policies](#) and the [Editorial Policy Checklist](#).

Statistics

For all statistical analyses, confirm that the following items are present in the figure legend, table legend, main text, or Methods section.

n/a Confirmed

- The exact sample size (n) for each experimental group/condition, given as a discrete number and unit of measurement
- A statement on whether measurements were taken from distinct samples or whether the same sample was measured repeatedly
- The statistical test(s) used AND whether they are one- or two-sided
Only common tests should be described solely by name; describe more complex techniques in the Methods section.
- A description of all covariates tested
- A description of any assumptions or corrections, such as tests of normality and adjustment for multiple comparisons
- A full description of the statistical parameters including central tendency (e.g. means) or other basic estimates (e.g. regression coefficient) AND variation (e.g. standard deviation) or associated estimates of uncertainty (e.g. confidence intervals)
- For null hypothesis testing, the test statistic (e.g. F , t , r) with confidence intervals, effect sizes, degrees of freedom and P value noted
Give P values as exact values whenever suitable.
- For Bayesian analysis, information on the choice of priors and Markov chain Monte Carlo settings
- For hierarchical and complex designs, identification of the appropriate level for tests and full reporting of outcomes
- Estimates of effect sizes (e.g. Cohen's d , Pearson's r), indicating how they were calculated

Our web collection on [statistics for biologists](#) contains articles on many of the points above.

Software and code

Policy information about [availability of computer code](#)

Data collection

Data analysis

For manuscripts utilizing custom algorithms or software that are central to the research but not yet described in published literature, software must be made available to editors and reviewers. We strongly encourage code deposition in a community repository (e.g. GitHub). See the Nature Portfolio [guidelines for submitting code & software](#) for further information.

Data

Policy information about [availability of data](#)

All manuscripts must include a [data availability statement](#). This statement should provide the following information, where applicable:

- Accession codes, unique identifiers, or web links for publicly available datasets
- A description of any restrictions on data availability
- For clinical datasets or third party data, please ensure that the statement adheres to our [policy](#)

Human research participants

Policy information about [studies involving human research participants and Sex and Gender in Research](#).

Reporting on sex and gender	<input type="text" value="n.a."/>
Population characteristics	<input type="text" value="n.a."/>
Recruitment	<input type="text" value="n.a."/>
Ethics oversight	<input type="text" value="n.a."/>

Note that full information on the approval of the study protocol must also be provided in the manuscript.

Field-specific reporting

Please select the one below that is the best fit for your research. If you are not sure, read the appropriate sections before making your selection.

Life sciences Behavioural & social sciences Ecological, evolutionary & environmental sciences

For a reference copy of the document with all sections, see [nature.com/documents/nr-reporting-summary-flat.pdf](https://www.nature.com/documents/nr-reporting-summary-flat.pdf)

Life sciences study design

All studies must disclose on these points even when the disclosure is negative.

Sample size	<input type="text" value="Sample sizes in vitro experiments were determined based on the numbers required to achieve statistical significance using indicated statistics, as well as considering of previous publications on similar experiments (PMID: 31634899 and 35922516)."/>
Data exclusions	<input type="text" value="No data exclusions."/>
Replication	<input type="text" value="The experimental findings were reproduced as validated by at least two independent experiment in Fig1 and Extended fig 1-4."/>
Randomization	<input type="text" value="Randomization is not relevant to the in vitro experiments since cells come in millions of populations and are automatically randomized and seeded to different wells for treatment."/>
Blinding	<input type="text" value="In the in vitro experiments, the investigators were not blinded, which is standard in this type of study due to the multiple steps involved that require precise operations for accuracy and precision precluding blinding to experimental variables."/>

Reporting for specific materials, systems and methods

We require information from authors about some types of materials, experimental systems and methods used in many studies. Here, indicate whether each material, system or method listed is relevant to your study. If you are not sure if a list item applies to your research, read the appropriate section before selecting a response.

Materials & experimental systems

n/a	Involved in the study
<input type="checkbox"/>	<input checked="" type="checkbox"/> Antibodies
<input type="checkbox"/>	<input checked="" type="checkbox"/> Eukaryotic cell lines
<input checked="" type="checkbox"/>	<input type="checkbox"/> Palaeontology and archaeology
<input checked="" type="checkbox"/>	<input type="checkbox"/> Animals and other organisms
<input checked="" type="checkbox"/>	<input type="checkbox"/> Clinical data
<input checked="" type="checkbox"/>	<input type="checkbox"/> Dual use research of concern

Methods

n/a	Involved in the study
<input checked="" type="checkbox"/>	<input type="checkbox"/> ChIP-seq
<input checked="" type="checkbox"/>	<input type="checkbox"/> Flow cytometry
<input checked="" type="checkbox"/>	<input type="checkbox"/> MRI-based neuroimaging

Antibodies

Antibodies used	<input type="text" value="GPX4 (1:1000 for WB, ab125066, Abcam), FSP1 (1:1000 for WB, sc-377120, Santa Cruz Biotechnology), DHODH (1:1000 for WB, sc-166348, Santa Cruz Biotechnology), HA antibody (1:1000 for WB, clone 3F10, rat IgG1, developed in-house), valosin containing protein (VCP, 1:10000 for a loading control in WB analysis, ab109240, Abcam)."/>
Validation	<input type="text" value="GPX4 antibody (ab125066, Abcam) and human FSP1 antibody (sc-377120, Santa Cruz Biotechnology) were validated for WB in"/>

Validation

previous publications (PMID: 31634899 and 35922516).
HA antibody was validated for WB in a previous publication (PMID: 31634899).
VCP antibody (ab109243, Abcam) was validated for WB on the manufacturer's website (<https://www.abcam.com/vcp-antibody-epr33072-ab109240.html>).
DHODH antibody (c-166348, Santa Cruz Biotechnology) was validated for WB on the manufacturer's website (<https://www.scbt.com/p/dhodh-antibody-e-8>).

Eukaryotic cell lines

Policy information about [cell lines and Sex and Gender in Research](#)

Cell line source(s)

4-OH-TAM-inducible Gpx4^{-/-} murine immortalized fibroblasts (Pfa1) were originally established in our lab and were reported previously (PMID: 18762024). HT-1080 (CCL-121), 786-O (CRL-1932), A375 (CRL-1619), MDA-MB-436 (HTB-130), A549 (CCL-185), H460 (HTB-177), SW620 (CCL-227) and HEK293T (CRL-3216) cells were obtained from ATCC. LOX-IMVI was obtained from NCI/NIH.

Authentication

None of the cell lines used were authenticated.

Mycoplasma contamination

All cell lines were tested negative for mycoplasma contamination.

Commonly misidentified lines
(See [ICLAC](#) register)

No commonly misidentified cell lines were used.